DESIGN AND EXPERIMENTAL INVESTIGATION OF A LARGE DIAMETER ELECTRON CYCLOTRON RESONANT PLASMA SOURCE

By

Fan Cheung Sze

A DISSERTATION

Submitted to
Michigan State University
in partial fulfillment of the requirements
for the degree of

DOCTOR OF PHILOSOPHY

Department of Electrical Engineering

1993

New
for U
cyclo
recen
915 M
whic
Expe
plasm
ion e
unifo
MPD
evalu
ion a
featur
cm di
with a
Etchi
Etch p

ABSTRACT

DESIGN AND EXPERIMENTAL INVESTIGATION OF A LARGE DIAMETER ELECTRON CYCLOTRON RESONANT PLASMA SOURCE

By

Fan Cheung Sze

New plasma sources are needed to meet the stringent processing condition for Ultra Large Scale Integrated circuit (ULSI) fabrication. Two electron cyclotron resonant Microwave Plasma Disk Reactors (MPDRs) have recently been developed. The first one is the MPDR 20, which is operated at 915 MHz and has a 20 cm discharge diameter. The other is the MPDR 325, which is operated at 2.45 GHz and has a 24 cm discharge diameter. Experimental measurements showed that the two plasma sources had high plasma density (about 10^{11} cm^{-3}), low plasma potential (8-12 volts) and low ion energies (8-15 eV). With downstream magnetic confinement, plasma uniformity of 2.6% (1σ) over 18 cm has been achieved. Performances of five MPDRs with discharge diameter varying from 5 cm to 24 cm were evaluated. The MPDR 325 had an ion production efficiency of 220 eV per ion and power density of 0.1 Watt/cm^3. Etching of 0.1 μm to 0.5 μm features in silicon using an SF_6-argon plasma was performed in a similar 24 cm diameter discharge reactor. Anisotropic (90^o) etch results were achieved with an etch rate of 200-280 Å/min. No microloading effect was observed. Etching results indicated that the etching process was limited by gas flow. Etch performances versus other operation parameters were also studied.

To my mother, A-Ngo Chan, sisters (Siu-Ying, Siu-Chu,
Siu-Hung, Sin-Man and Sin-Fan) and Wai-Ying,
for their love and care.

1421 L, Spartan Village
East Lansing

Chai
resea
appr
labor
house
etchi
Profe
would
Salbe
resear
from
μm to

Michig

ACKNOWLEDEGMENTS

I would like to thank my adviser, Dr. J. Asmussen, Professor and Chairperson of the Department of Electrical Engineering, for his guidance in research and support over the last four and a half years. I enjoyed and appreciated all the moments with him, from those weekends in the laboratory talking about experiments to the discussion of my thesis in his house. I would like to thank Professor D.K. Reinhard for his guidance in the etching work and his comment in my thesis. Also I would like to thank Professor T. Grotjohn who reorganized the clean room in the laboratory. I would like to thank Mr. R. Fritz, Mr. L. Mahoney, Dr. J. Hopwood, Dr. G. Salbert and Mr. B. Musson for their assistance during the early stage of my research. Thanks must also be extended to Dr. Alers and Professor Golding from the Department of Physics and Astronomy for the preparation of 0.1 μm to 0.5 μm patterns in the submicron etching experiments.

Research funding was provided in part by Wavemat Inc. and Michigan State Research Excellent Fund.

TABLE OF CONTENTS

3.1
3.2
3.3
3.4
3.5

§ 3.6

4.1
4.2
4.3

5.1
5.2

LIST OF TABLES

Figur

Figur

Figur

Figur

Figure

Figure

Figure

Figure 2

Figure 2

LIST OF FIGURES

Figur

Figur

Figur

Figur

Figure

Figure

Figure

Figure

Figure 5

Figure 5.

Figure 5.3

Figure 7.

Figure 7.

Figure 7.

Figure 7.

Figure 7.

Figure 7.1

CHAPTER ONE

INTRODUCTION

§ 1.1 Introduction

§ 1.2 Research objective

§ 1.3 Research history

§ 1.4 Outline of thesis

§ 1.1

[187].
five y
compu
improv
develo
memor
memor
design
μm or
both in
understa
fabricati

H
developm
fabricatio
tools no
to provi
especially

Red
plasma too
ideal tool i
so that cont

§ 1.1 Introduction

In 1947, the world's first transistor was fabricated at Bell Laboratories [187]. The evolution of integrated circuit technology during the last forty-five years has changed people's lives so much that people sometimes trust computers more than themselves. The fabrication technology has been improved dramatically last ten years. One typical example is the development of high speed and high density dynamic random access memory (DRAM). In 1984, 64 k-bit DRAM chips were the most advanced memory chips in the market. Today, 4 Mbit DRAM chips, using 0.8 μm design rule, are in mass production. 64 Mbit DRAM prototypes, using 0.25 μm or less design rule have already been produced in research laboratories both in the United States and Japan. This rapid development involves better understanding of the fabrication process as well as an improvement of the fabrication tools.

Hundreds of papers have been published in recent years about the development and performance of new plasma sources for single wafer fabrication. As the feature size shrinks, conventional parallel plate plasma tools no longer serve the need. A better dry (plasma) etching tool is needed to provide better anisotropic etching profiles and with low damage, especially for electronic devices using III-V materials.

Reduction of the feature size to the submicron range requires better plasma tools for the manufacturing process to eliminate undercutting. The ideal tool is one that can produce a dense, broad and low ion energy plasma so that controllable, uniform and highly anisotropic etching can be achieved.

A number of tools, which are intended to meet all these goals, have been proposed and studied in the United States and in other industrial countries. These include electron cyclotron resonant (ECR) plasma sources and non-ECR plasma sources. Examples of the non-ECR sources are the parallel plate plasma source which has been used for many years, the Triode source [74] which is a modification of the parallel plate source, the Helicon source from Australia [29], the Inductively Coupled Plasma (ICP) [49] source and the newest Transmission Couple Plasma (TCP) [153] source from Lam Research Corporation. Examples of the ECR sources are the Axial Divergent Field ECR source [17] which was originated from Japan but has also been studied intensively in the United States, the microwave plasma disk reactor (MPDR) developed at Michigan State University [32], the Leybold source from Germany [26] and the Distributed ECR source from France [24]. All these plasma sources are different in structure and principle of operation. The potential usefulness of these different sources in the IC industries is mainly governed by their performance. However, compatibility of the new source to other commercial processing equipment, the initial capital cost and ease of automation will determine the future role of these sources in semiconductor industry.

While the discussion of the usefulness of the above different plasma sources for future ultra-large scale integrated circuit (ULSI) application still continues, this research investigates the scale up of the MPDR and evaluates the experimental performance of large diameter electron cyclotron resonant sources.

§1.2 Research objectives

The objectives of the research described in this thesis were (1) to design and build a large diameter electron cyclotron resonant MPDR, (2) to experimentally measure the plasma parameters of the large diameter MPDR, (3) to evaluate the performance of different MPDR prototypes in terms of electron temperature versus CPΛ, ion production energy cost, microwave coupling efficiency and power density, and (4) to investigate the performance of the large diameter MPDR in submicron etching application.

§1.3 Research history

The research described in this dissertation was carried out over the period of 1988 to 1993 at Michigan State University under the direction of Dr. Asmussen, Professor and Chairperson of the Department of Electrical Engineering. The experimental work took place in the Microwave Plasma & Microwave Material Processing Laboratories at Michigan State University. Research funding was provided by Wavemat Inc. and Michigan State Research Excellent Fund.

This research builds on previous microwave plasma disk reactor research carried out by Mr. Root [32], Dr. Dahimene [35] and Dr. Hopwood [38]. This past reactor research has lead to MSU owned and patented microwave plasma technologies [32c] that have numerous microwave plasma and microwave material processing application. Much of the knowledge and engineering art used in the thesis to design, build and experimentally investigate the property of the large MPDR was based on

these earlier investigations. A brief history of MPDR development at MSU is given in Chapter Four. Research in this dissertation has been published in part in scientific journals [42,43,45,46] and international conferences [180-190].

§1.3 Outline of thesis

Chapter Two outlines some fundamental properties in electron cyclotron resonant plasmas. Chapter Three is a literature review on all the ECR plasma sources and newly developed non-ECR plasma sources which have been developed in recent years. Structure and operation of these sources are discussed.

Chapter Four gives the general aspects of the MPDR sources: its structure, its development, operations principle and optimal ECR magnetic configuration. Chapter Five presents all the experimental diagnostic techniques and results of two large diameter MPDRs, the MPDR 20 and MPDR 325, and one small plasma source, the MPDR 5. Chapter Six evaluates the performance of five MPDRs in terms of the electron temperature versus the product of pressure and diffusion length of the discharge volume, ion production energy cost, microwave coupling efficiency and power density. One application of the large diameter MPDR is anisotropic etching of submicron features in silicon which is described in detail in Chapter Seven. Etch performances versus various operation conditions are discussed. Finally, Chapter Eight is a summary of research results. Also included are suggestions for future development and research in MPDR.

CHA

CHAPTER TWO

FUNDAMENTALS

§ 2.1 Introduction

§ 2.2 Plasma

2.2.1 Debye - Hückel radius

2.2.2 Mean free path and collision cross-sections

§ 2.3 Motion of charged particles in time-harmonic electric field

§ 2.4 Conductivity in plasma

2.4.1 AC conductivity

2.4.2 Power absorption in plasma

§ 2.5 Sheath and ion energy

§ 2.6 Magnetic confinement of plasma

§ 2.1 Introduction

This chapter reveals some of the fundamental properties of plasmas, which were encountered frequently throughout the research. Some plasma parameters such as Debye radius, plasma frequency, neutral density, mean free path, collision cross sections and so on are first stated in early sections. These parameters will be useful for discussions in other parts of this dissertation.

A general solution for the motion of a charged particle in a time-harmonic electromagnetic field is solved. This general solution describes microscopic charged particle motion in a collisionless plasma and magnetized plasma with a time-harmonic electric field. The energy absorbed by an electron in electron cyclotron resonance is studied. Macroscopic properties such as power absorption in a collisional plasma is also examined in detail. The discussions of sheath potential, ion energy and plasma confinement are also included.

§ 2.2 Plasma

Plasma is the most widespread state of matter in the Universe. It is an ionized gas consisting of three components- free electrons, positive ions and neutral atoms or molecules. The Sun and the stars are enormous lumps of hot plasma. The Earth's atmosphere is surrounded by a plasma envelope known as the ionosphere. In the terrestrial environment, plasmas are encountered in the laboratories and technologies. One typical laboratory plasma is the high-temperature plasma, whose electron and ion energies are in the range of

MeV, in the application of controlled nuclear fusion and magneto-hydrodynamic conversion of heat energy into electric energy. Another kind of plasma is low energy plasma, whose electron and ion energies vary from a few electron-volts to tens of electron-volts. Most of the low energy plasma is found in the fluorescence tubes. In semiconductor industries, low energy plasmas have also been used in the fabrication of microelectronic devices for many years. The development of a low pressure, low ion energy and high density plasma has become one of the important technologies for the fabrication of ultra large scale integrated circuit (ULSI).

Plasma is generated by ionization processes. Two very common processes are photoionization and electric discharge.

In the photoionization process, ionization occurs when the energy of an incident photon is equal to or greater than the ionization potential of the absorbing atoms. For example, the ionization potential of the outermost electron in an atomic oxygen is 13.6 electron-volts, which can be supplied by photon with wavelength less than 910 Å, i.e., in the far ultra violet region. In nature, the Earth's ionosphere is an example of photoionization phenomenon.

Ionization can also be produced, which is found in most laboratory plasma, by applying an electric field across the ionized gas. The electric field accelerates the free electrons to an energy level sufficient to ionize an atom during collisions. One characteristic of this process is that the transfer of energy from the electric field to the electrons is more efficient than to the heavy ions. Such inefficient energy transfer to the ions is because the ions

are much heavier than the electrons. The electrons are accelerated by the applied electric field so quickly that the ions, relatively, seem to be not moving at all. As a result, the temperature of the electrons in a gas discharge is usually much higher than the ion temperature. This is why most laboratory plasma can be modeled as a cold plasma in which the ions are stationary but the electrons are free to move.

The transfer of energy from electrons to the ions during elastic collisions is very inefficient because of the difference in mass. It has been estimated that the energy transfer from an energetic electron to an ion during a collision is no more than a fraction of $4m_e/m_i$, where m_e and m_i are the mass of electron and ion respectively [69]. Beside elastic collisions, inelastic collisions also take place in which energy is transferred from the energetic electrons to the ions and neutral through excitation [74]. The ions or neutral species are elevated to different excited states momentarily and then drop back to lower energy states during which emissions of particular wavelengths take place. Because different species have different emission spectra or "emission signatures", the composition of the species can be determined through optical techniques. Laser induced fluorescence technique is based on these absorption and emission phenomena to examine different species inside the plasma.

If n_e, n_i and N represent the densities of electrons, ions and neutral molecules respectively, then the degree of ionization is defined as [69]:-

$$\alpha_i = n/(n+N)$$

where n equals to n_e and n_i. When α_i is larger than 10^{-4}, the plasma is regarded as a strongly ionized gas in which coulomb interactions become dominant [70]. Plasma encountered in this research, in fact, belongs this category. For example in a 24 cm diameter discharge such as the MPDR 325 plasma source, the argon plasma density at 0.6 mTorr was 1.44 x 10^{11} cm^{-3} using 500 watts 2.45 GHz microwave. The neutral density according to equation (2.4) is 1.93 x 10^{13} cm^{-3} if the neutrals are at room temperature 300K. The corresponding value of α_i is 0.0075. That means the plasma in this study is a highly ionized plasma.

Important plasma parameters, which can be found in most plasma text [54, 55, 60-63, 67-73] are briefly studied below. These parameters help to understand some plasma phenomena and are useful for discussion in later sections.

2.2.1 Debye -Hückel radius

In an ideal cold plasma, when a test charge is introduced inside the plasma, the fast moving electrons will redistribute themselves around the test charge. Such phenomenon is called plasma screening. The potential around the test charge will drop exponential due to this screening effect. In polar coordinates, the potential drop with respect to the radial distance, r, is given as [67]:

$$\Phi(r) = Q \exp(- r/r_D) /(4\pi\epsilon_o r) \qquad (2.1)$$

where Q is the test charge, ϵ_o is the permittivity and r_D is the Debye-Hückel radius or more commonly called Debye length, which is defined below:

$$r_D = [\epsilon_o k_b T_e/(n_e e^2)]^{1/2}$$
$$\approx 69\ (T_e/n_e)^{1/2} \qquad (2.2)$$

where n_e is the plasma density in m^{-3}, k_b is the Boltzmann constant, T_e is the electron temperature in K and e is the electronic charge. This cold plasma model assumes the ions do not move around because of zero temperature. Figure 2.1 shows the variations of the Debye length with electron temperature at different plasma densities. The Debye lengths shown in the figure give the order of thickness of a sheath which is formed next to a boundary.

If we were able to take a snap shot of the plasma, the average distance between the species of an ideal gas is $n^{-1/3}$ where n is the concentration of the gas. Therefore, the "average" distance between two electrons is $n_e^{-1/3}$. For a numerical example, if a plasma density of 10^{11} cm^{-3} and 5 eV electron temperature is formed at 0.6 mTorr, the Debye length is about 53 μm. The "average" distance between two electrons or two ions is 2.2 μm. To shield the electric field of the test charge, the sheath has to be thicker than the Debye length so that sufficient amounts of opposite charged species are inside the sheath to reduce the electric field due to the test charge. For example, according to equation (2.1), less than 0.1% of the potential due to the test charge remains at a distance of about 7 times of the Debye length.

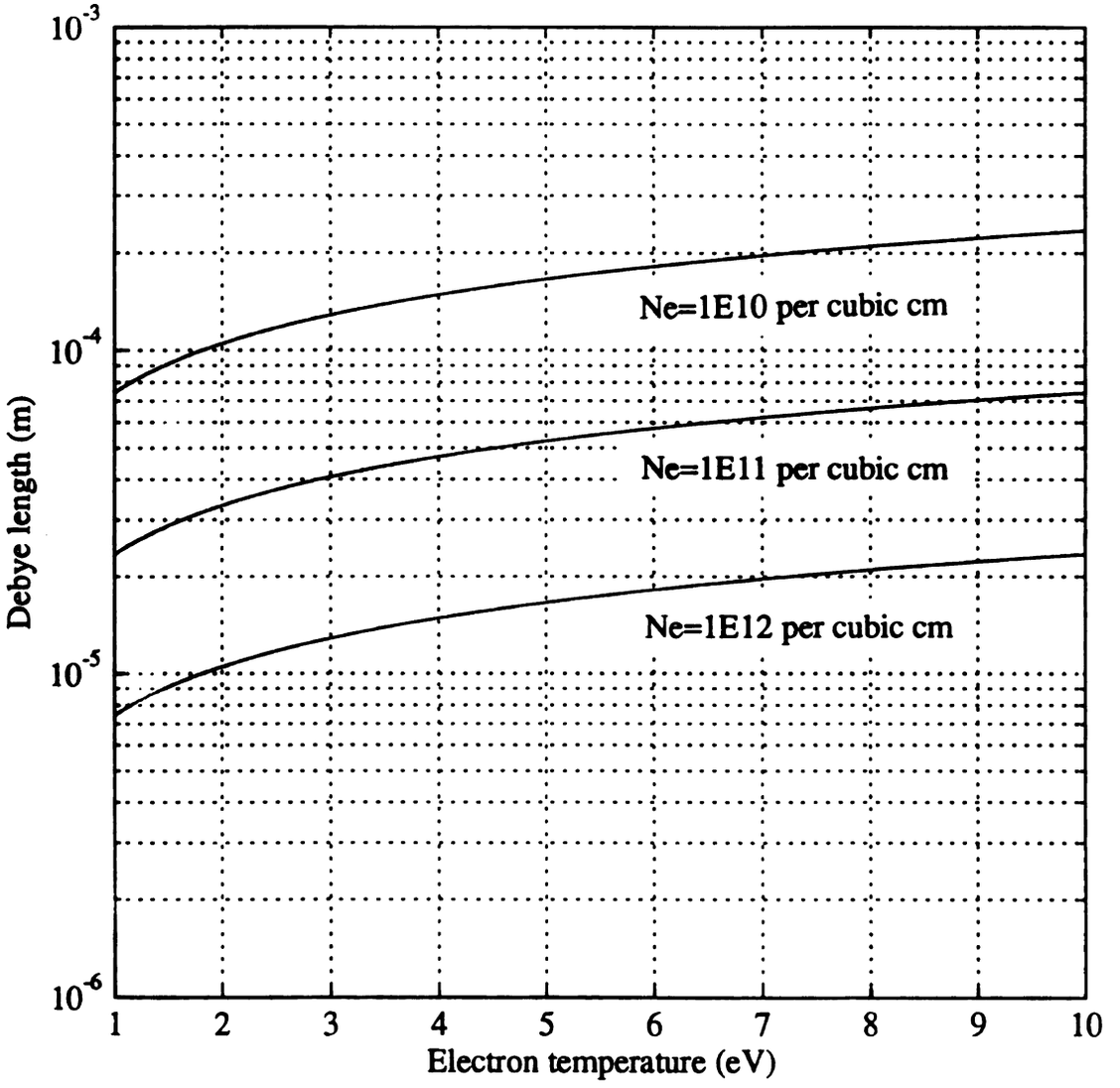

Figure 2.1 Variations of Debye length with electron temperature at different plasma densities

2.2.2 Mean free path and collision cross -sections

Neutral species are also important in plasma process. The relation of neutral density, n_n, to the pressure is given as [63]:-

$$n_n = 9.6564 \times 10^{24} P/T \ (m^{-3}) \tag{2.3}$$

where P is the pressure of the gas expressed in Torr and T is the neutral temperature in Kelvin. The definition of mean free path for a neutral gas is:

$$\lambda_{nn} = 1/(n_n Q_{nn} \sqrt{2}) \tag{2.4}$$

where Q_{nn} is the cross-sections for the neutral-neutral collisions [63]. For argon gas, Q_{nn} is equal to 42×10^{-20} m^2. Figure 2.2 shows the variations of mean free path with pressures and temperature of the neutral argon atoms. Because argon ions have essentially the same mass as the argon atom, the temperature of the argon ion in the bulk of the plasma is assumed to be the same as the neutral argon atoms. Assumng the wall temperature is 300 K and at pressure of 1 mTorr, the mean free path between collisions of the ion and neutral is about 5 cm. Compared with the thickness of the sheath, which is assumed to be ten times the Debye length, it can be concluded that there are very few neutral-ion collisions taking place inside the sheath.

Listed below are the collision frequencies for different species as a function of the collision cross-sections. They are useful in the evaluation of power dissipation in plasma in later sections. Collision frequency between neutrals is given as [63]:

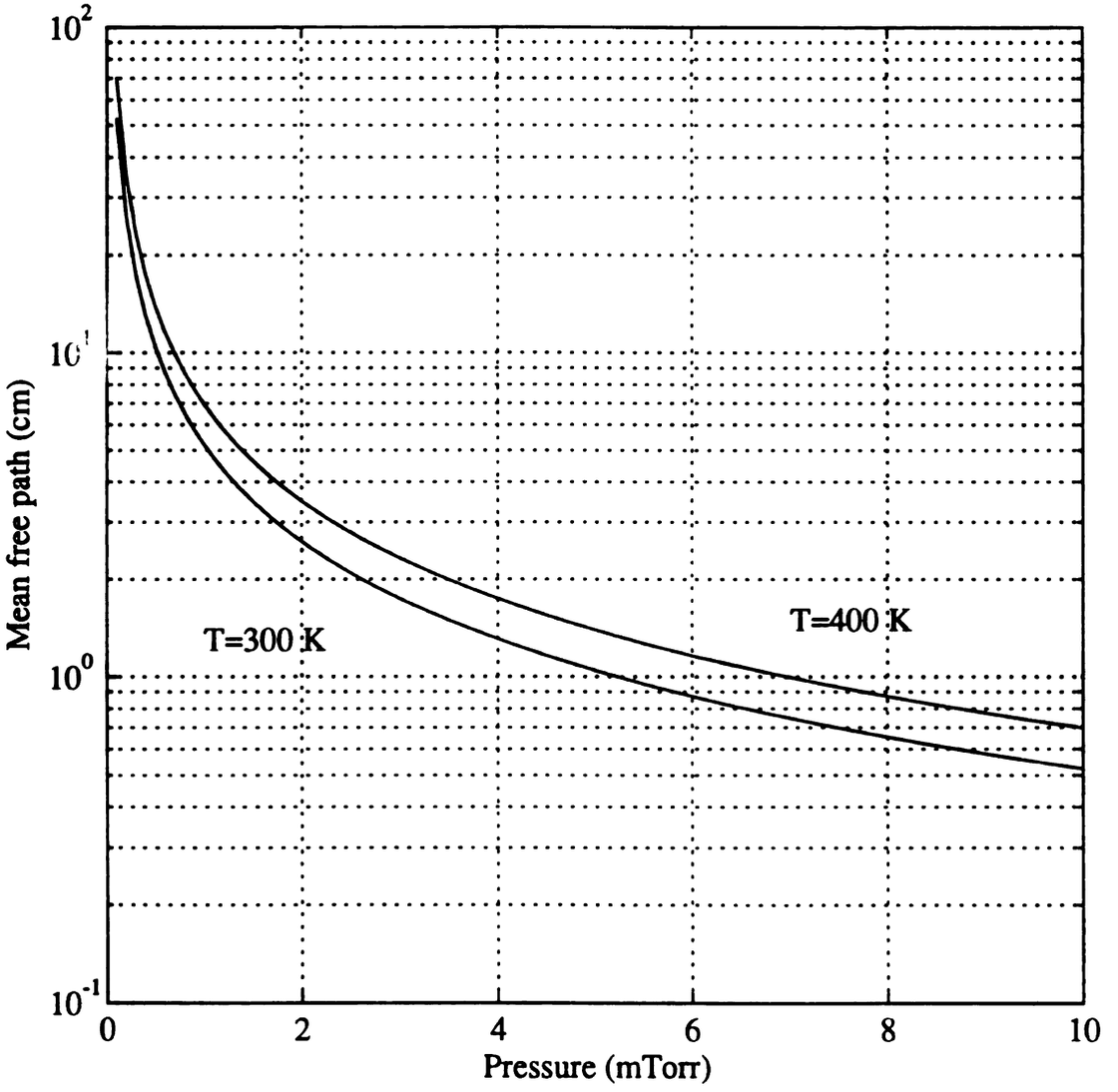

Figure 2.2 Variations of mean free path with pressrue
at different neutral temperatures

$$\nu_{nn} = n_n Q_{nn} \langle v_n \rangle \tag{2.5}$$

while the collision frequencies between electrons and ions, and electrons and neutrals are:

$$\nu_{ei} = 1.94 \times 10^{-12} n_e \ln[1.55 \times 10^{13} (k_b T_e/e)^{3/2}/(n_e)^{1/2}]/(k_b T_e/e) \tag{2.6}$$

$$\nu_{en} = 6.69 \times 10^5 n_n Q_{en} (k_b T_e/e)^{1/2} \tag{2.7}$$

where Q_{en} is the collision cross-section for electron and neutral. However, Kaufman and Robinson pointed out that the collision cross-section often has error of ±20-30%. Thus the numerical data can only represent the order of magnitude of the collision processes.

§ 2.3 Motion of charged particles in time-harmonic electric field

The motion of a charge particle, such as an electron, under the influence of time-harmonic electric field and static magnetic field is a classic problem in electron cyclotron resonant plasma. A closed form solution is possible though complicated.

Figure 2.3 shows a snap shot of the motion of a charge particle in a 3-D space. The orthogonal velocity components of the particle are represented by $v_{//}$, $v_\times$ and $v_\perp$ respectively. $\mathbf{u}_{//}$ denotes the direction of a unit vector whose direction is parallel to the static magnetic field, **B**. $\mathbf{u}_\times$ is a unit vector which is perpendicular to both the static magnetic field and the applied time-

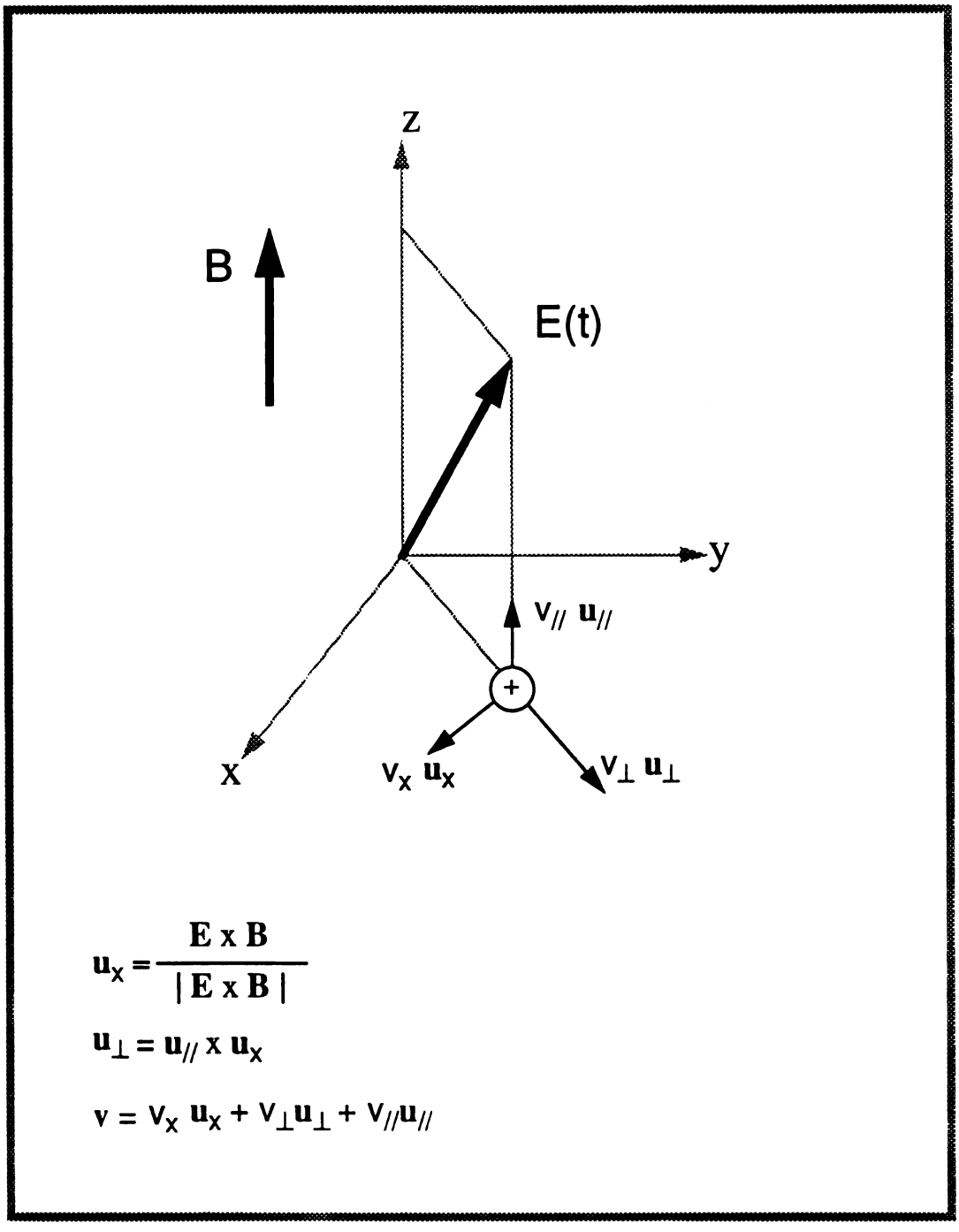

$$u_x = \frac{E \times B}{|E \times B|}$$

$$u_\perp = u_{//} \times u_x$$

$$v = v_x u_x + v_\perp u_\perp + v_{//} u_{//}$$

Figure 2.3 Snap shot of the motion of a charged particle in a time-variant E field and static B field

harmonic electric field, $\mathbf{E}(t)$. $\mathbf{u}_\perp$ is in the direction $\mathbf{u}_{//} \times \mathbf{u}_x$. For the sake of clarity, a positive charge is assumed. The solution derived below, however, can also be applied to the electrons.

The motion of a particle with charge, q, and mass, m, is governed by the following equation:

$$\dot{\mathbf{v}} = (q/m)(\mathbf{E}(t) + \mathbf{v} \times \mathbf{B}) \tag{2.8}$$

As shown in Figure 2.3, the time-harmonic electric field can be decomposed into two components:

$$\mathbf{E}(t) = \mathbf{u}_{//} E_{//} e^{j\omega t} + \mathbf{u}_\perp E_\perp e^{j\omega t} \tag{2.9}$$

After substituting equation (2.9) into (2.8) and rearrangment, we have:

$$\dot{v}_{//} = (q/m) E_{//} e^{j\omega t} \tag{2.10a}$$

$$\dot{v}_\perp = (q/m) E_\perp e^{j\omega t} - \omega_b v_x \tag{2.10b}$$

$$\dot{v}_x = \omega_b v_\perp \tag{2.10c}$$

where ω is the angular frequency of the time-harmonic electric field and ω_b is the cyclotron frequency which is equal to qB/m.

Assuming that the positively charged particle has non-zero velocity at initial state, equations (2.10a-c) are first converted to s-domain by using Laplace Transform:

$$sv_{//}(s) - v_{//}(0) = (q/m)E_{//}/(s-j\omega) \tag{2.11a}$$

$$sv_{\perp}(s) - v_{\perp}(0) = (q/m)E_{\perp}/(s-j\omega) - \omega_b v_x(s) \tag{2.11b}$$

$$sv_x(s) - v_x(0) = \omega_b v_{\perp}(s) \tag{2.11c}$$

The solutions of $v_{//}(s)$, $v_{\perp}(s)$ and $v_x(s)$ can therefore be solved and the final solutions can be obtained by inverse-Laplace Transform. All the intermediate steps are skipped for clarity and the final solutions are:

$$v_{//} = qE_{//}\sin(\omega t)/(m\omega) + v_{//}(0) \tag{2.12}$$

$$v_{\perp} = qE_{\perp}[\omega_b\sin(\omega_b t)-\omega\sin(\omega t)]/[m(\omega_b^2-\omega^2)] + v_{\perp}(0)\cos(\omega_b t) - v_x(0)\sin(\omega_b t) \tag{2.13}$$

$$v_x = qE_{\perp}\omega_b[\cos(\omega t)-\cos(\omega_b t)]/[m(\omega_b^2-\omega^2)] + v_{\perp}(0)\sin(\omega_b t) + v_x(0)\cos(\omega_b t) \tag{2.14}$$

When ω equals to ω_b, it can be shown that both $v_{\perp}$ and v_x will grow with time, a condition for cyclotron resonance:

$$v_{\perp} = qE_{\perp}[(t/2)\cos(\omega_b t)+(\sin(\omega_b t))/(2\omega_b)]/m + v_{\perp}(0)\cos(\omega_b t) - v_x(0)\sin(\omega_b t) \tag{2.15}$$

$$v_x = qE_{\perp}(t/2)[\sin(\omega_b t)]/m + v_{\perp}(0)\sin(\omega_b t) + v_x(0)\cos(\omega_b t) \tag{2.16}$$

For an electron, the cyclotron resonance takes place when the magnetic field strength is 875 Gauss using 2.45 GHz microwave excitation energy. At 915 MHz excitation, the required magnetic field strength is 327 Gauss. The energy gained by an electron under the condition of cyclotron resonance can be obtained by $m_e(v_{//}^2+v_{\perp}^2+v_x^2)/2$. If the initial velocity of the electron is zero, the variation of the energy of the electron with time, t, is:

$$E_e=q^2\{4E_{//}^2\sin^2(\omega_b t)+E_{\perp}^2[t^2\omega_b^2+\sin^2(\omega_b t)+t\omega_b\sin(2\omega_b t)]\}/8m\omega_b^2 \qquad (2.17)$$

Figure 2.4 shows the variation of electron energy with time and $E_{\perp}$, assuming $E_{\perp}= E_{//}$. In the absence of collision, an electron gains an amount of 8.8 eV in 10 nanoseconds when $E_{\perp}$ equals to 2 kV/m.

It should also be noted that equations (2.12-2.14) are the general solutions of the charged particle motion. By setting the frequency of the electric field to zero, a drift velocity of $E_{\perp}/B$ in the direction of **E×B** can be obtained. This drift velocity is the same for both positive and negative charged particles and independent of the mass of the particle. The equations can also be applied to situations such as inhomogeneous static magnetic field in which the magnitude and orientation of the magnetic field are functions of position.

The solution given in this section gives a microscopic view of the motion of a charged particle under the influences of a static magnetic field and time-varying electric field. The macroscopic property of a magnetized plasma is discussed in next section.

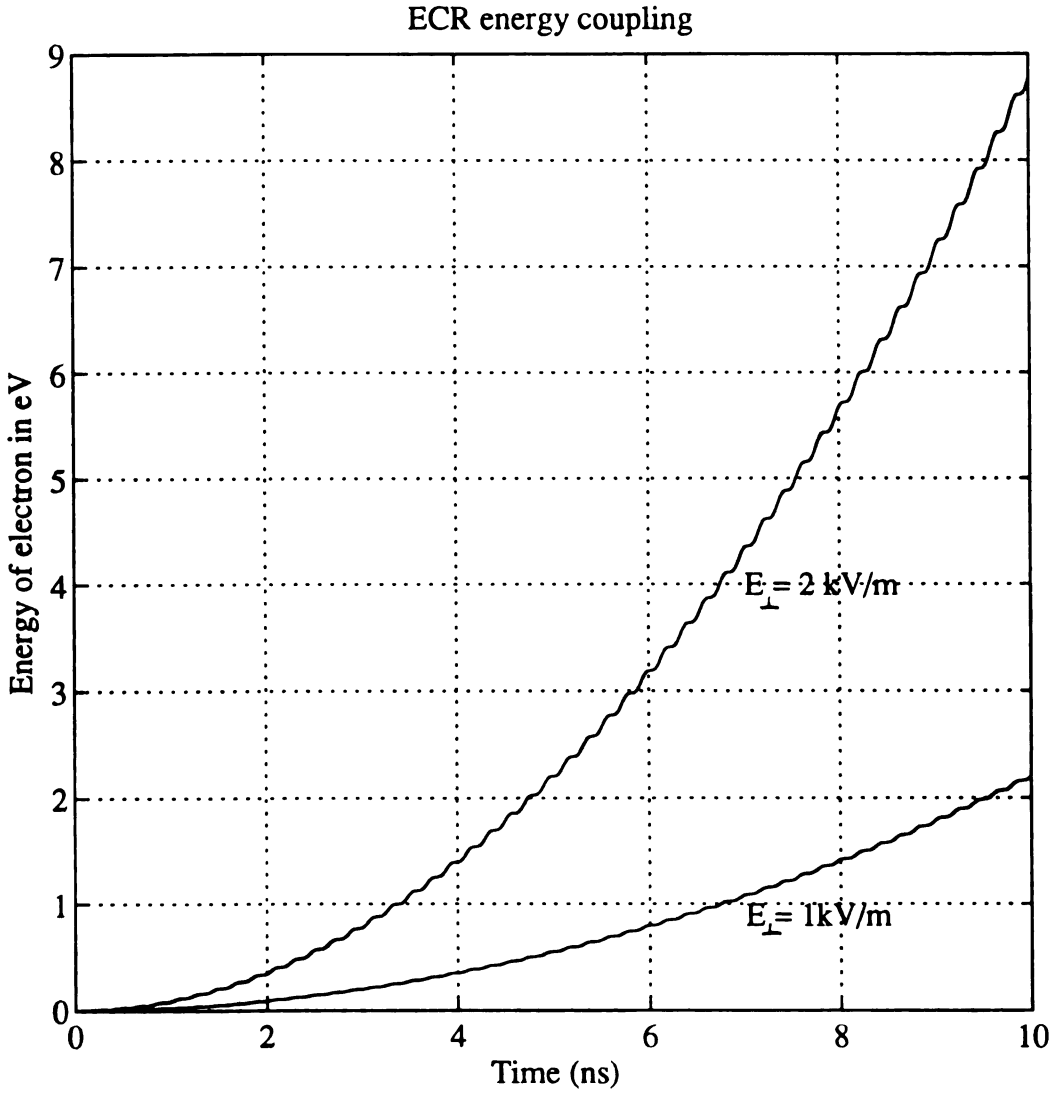

Figure 2.4 Variations of electron energy with time at electron cyclotron resonance at different applied electric field, $E_{\perp}$, strength

§ 2.4 Conductivity in plasma

The absorption of power in a plasma or power dissipation in plasma is the theme in this section. The conductivity of a magnetized plasma is first derived and then the variations of conductivity, which determines the power dissipation, at different static magnetic field strengths and pressures are then studied.

2.4.1 AC conductivity

In the presence of a static magnetic field and collision processes, the macroscopic motion of the electrons under the influence of a time-harmonic electric field is described by the Langevin equation [68,70]:

$$m_e(\partial \mathbf{v}/\partial t) = -e(\mathbf{E} + \mathbf{v}\times\mathbf{B}) - m_e\nu_c\mathbf{v} \qquad (2.18)$$

where $\mathbf{v}$ is the average electron velocity, $\mathbf{E}$ is the electric field and ν_c is the collision frequency between the electrons and the neutrals. It is assumed that the electrons are free to move in a stationary uniform background of ions and neutral which provide a viscous damping force to the motion of the electrons.

Consider both the electron velocity and the electric field vary harmonically with time, $e^{j\omega t}$, equation (2.18) becomes:

$$m_e(j\omega\mathbf{v}) = -e(\mathbf{E} + \mathbf{v}\times\mathbf{B}) - m_e\nu_c\mathbf{v} \qquad (2.19)$$

Becaus

Using t
field sh
field, a
expresse

where

The condu
magnetize
another na
of the elect

Because

$$\mathbf{J} = -en_e\mathbf{v} \tag{2.20}$$

Using the same notations and orientations of the magnetic field and electric field shown in Figure 2.3, the relation of the current to the applied electric field, after substituting (2.20) into (2.19) and rearrangement, can be expressed as:

$$\mathbf{J} = \overset{\approx}{\sigma}\,\mathbf{E} \tag{2.21}$$

where

$$\overset{\approx}{\sigma} = \begin{bmatrix} \sigma_\perp & -\sigma_\times & 0 \\ \sigma_\times & \sigma_\perp & 0 \\ 0 & 0 & \sigma_{//} \end{bmatrix} \tag{2.22}$$

$$\sigma_\perp = (\nu_c+j\omega)^2\sigma_o/[(\nu_c+j\omega)^2+\omega_{ce}^2] \tag{2.23}$$

$$\sigma_\times = (\nu_c+j\omega)\omega_{ce}\sigma_o/[(\nu_c+j\omega)^2+\omega_{ce}^2] \tag{2.24}$$

$$\sigma_{//} \equiv \sigma_o = n_e e^2/[m_e(\nu_c+j\omega)] \tag{2.25}$$

The conductivity, $\tilde{\tilde{\sigma}}$, is a tensor, indicating the anisotropic properties of a magnetized plasma. $\sigma_\perp$ is also called Pederson conductivity [70], $\sigma_\times$ has another name called the Hall conductivity and ω_{ce} is the cyclotron frequency of the electrons which is equal to eB/m_e.

2.4.2

equati

The po
part of

the con
parts of

strengt
should

the sam

A

magneti
the two
Gauss a
microwa
magnetic
perpendi
magnetic
two excit
density is
to be 5 eV

2.4.2 Power absorption in plasma

The ohmic loss or power dissipated in the plasma is given by the equation:

$$P_{diss} = \mathbf{J} \cdot \mathbf{E}$$
$$= \mathrm{Re}(\sigma_{\perp}) |E_{\perp}|^2 + \sigma_{//} |E_{//}|^2 \qquad (2.26)$$

The power absorption by a collisional plasma is thus proportional to the real part of the perpendicular conductivity, $\sigma_{\perp}$, and the parallel components of the conductivity. Figure 2.5 and Figure 2.6 show the variations of the real parts of the conductivity, $\sigma_{\perp}$, with different ratios of ν_c/ω and magnetic field strength at 2.45 GHz and 915 MHz excitation frequency respectively. It should be noted that when the static magnetic field strength is zero, $\sigma_{\perp}$ has the same value as $\sigma_{//}$.

At low ratio of ν_c/ω, maximum power absorption occurs when the magnetic field strength is close to the value required for ECR condition at the two different excitation frequencies, i.e. 327 Gauss at 915 MHz and 875 Gauss at 2.45 GHz. In a real environment, the electric field of the microwave penetrates into the plasma which has a spatial variation of static magnetic field strength. Assuming that the static magnetic field is always perpendicular to the electric field, the variations of conductivity, $\sigma_{\perp}$, with magnetic field strength are then displayed in Figure 2.7 and Figure 2.8 at the two excitation frequencies which were used in the experiments. The plasma density is assumed to be 10^{11} cm^{-3} and the electron temperature is assumed to be 5 eV or 58000 K. Since collision frequencies are related to the neutral

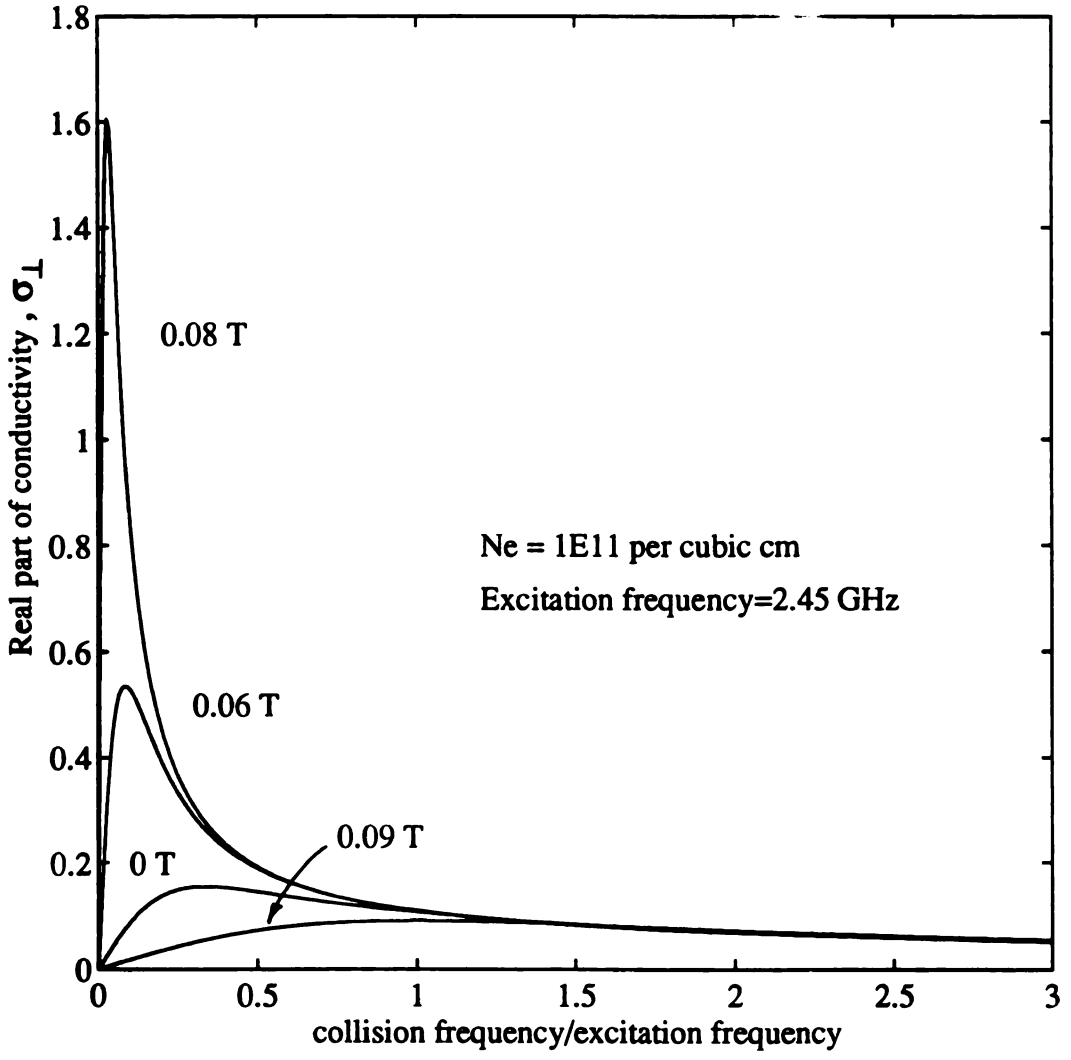

Figure 2.5 Variations of real part of conductivity, $\sigma_{\perp}$, with ratio of collision frequency/excitation frequency at different static magnetic field strength at 2.45 GHz excitation frequency

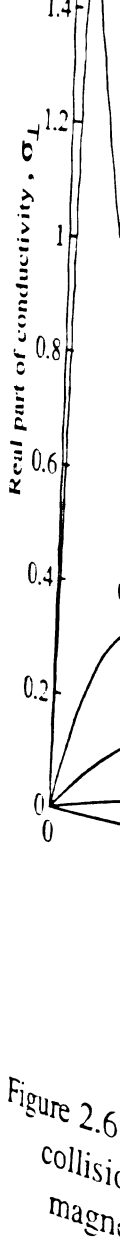

Figure 2.6
collisio
magna

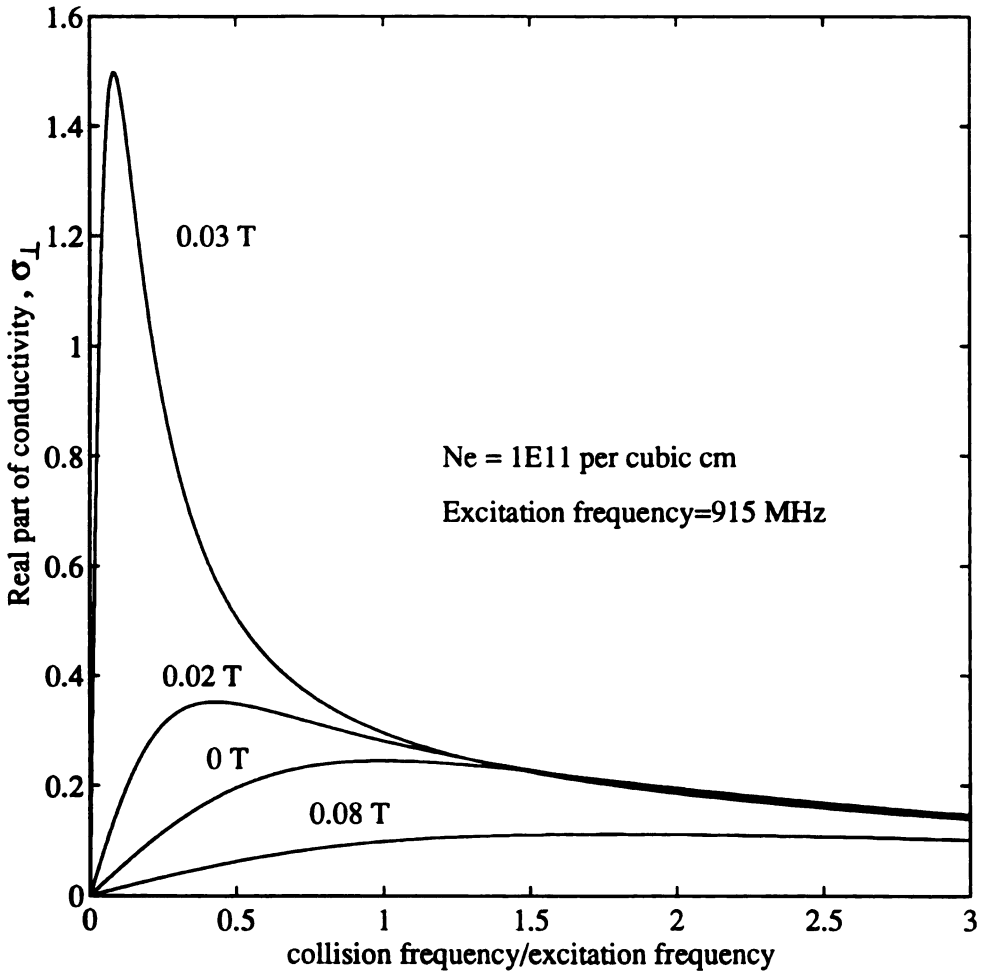

Figure 2.6 Variations of real part of conductivity, $\sigma_{\perp}$, with ratio of collision frequency/excitation frequency at different static magnetic field strength at 915MHz excitation frequency

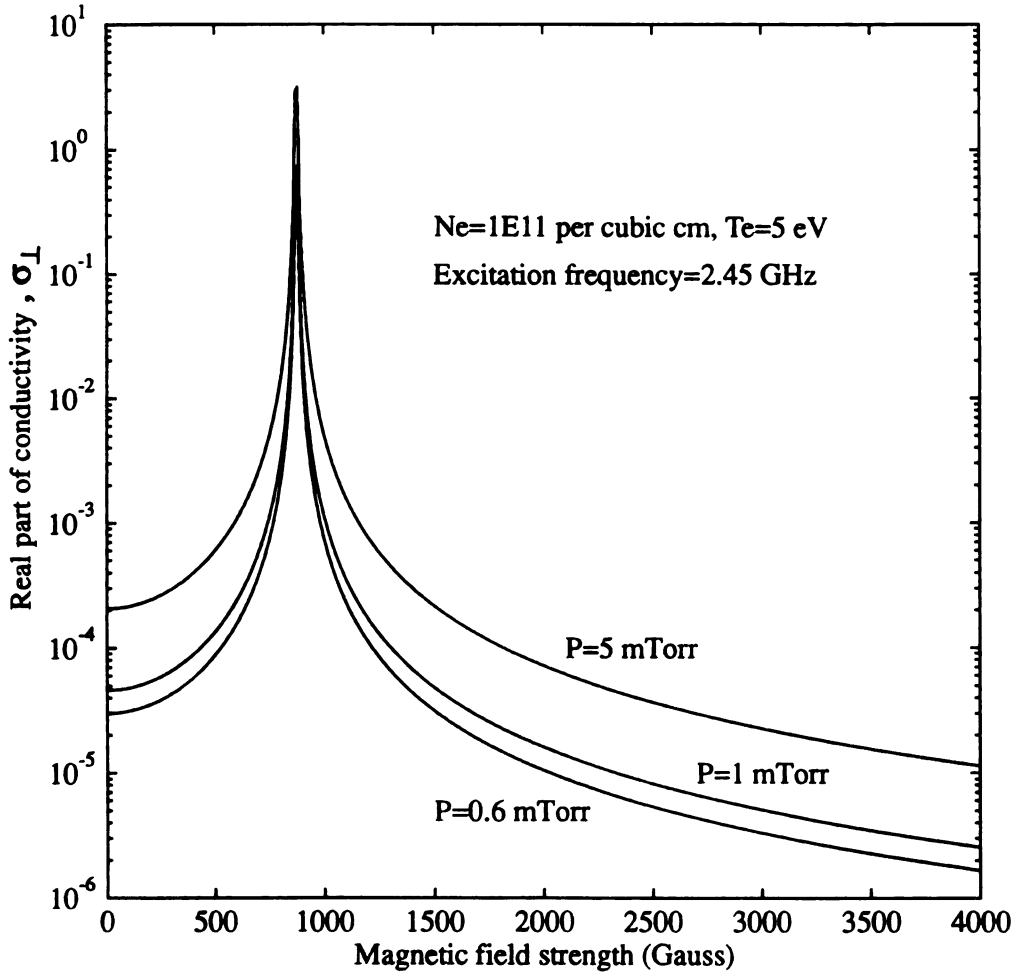

Figure 2.7 Variations of real part of conductivity, $\sigma_{\perp}$, with magnetic field strength at different pressures with 2.45 GHz excitation frequency

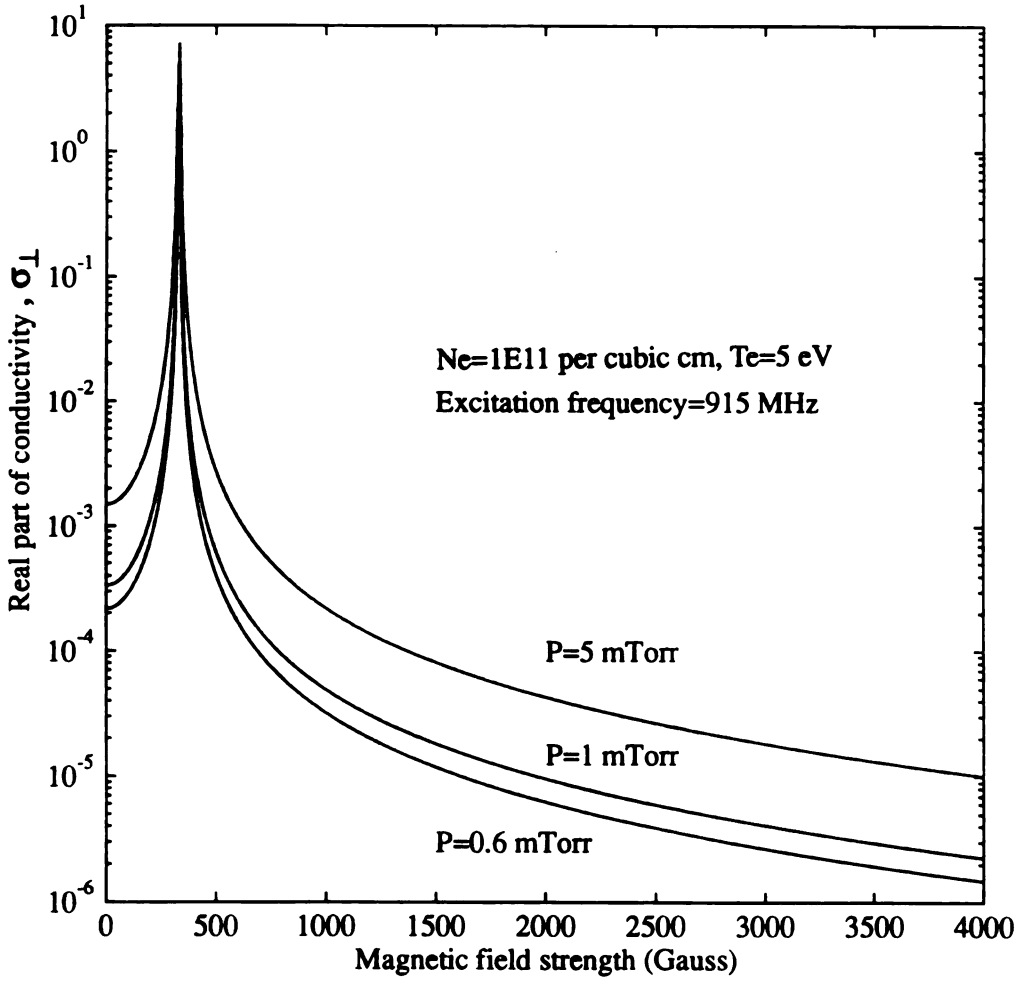

Figure 2.8 Variations of real part of conductivity, $\sigma_\perp$, with magnetic field strength at different pressures with 915 MHz excitation frequency

densit

are th

pressu

absorp

strengt

Figure

shows

shown

sources

reaches

magneti

perpend

the othe

energy a

considere

electric

important

are crucia

The

is readily

density as stated in equations (2.6) and (2.7), the variations of conductivity are therefore related to the pressure. Figures 2.7 and 2.8 show that as the pressure increases, the conductivity increases which means that power absorption by the plasma also increases.

At 0.6 mTorr, the variations of conductivity, $\sigma_{\perp}$, with magnetic field strength at different plasma densities are shown in Figures 2.9 and 2.10. Figure 2.9 show the variations at 2.45 GHz excitation while Figure 2.10 shows the variations at 915 MHz excitation. The plasma densities selected shown are the typical experimental values found in most ECR plasma sources. Figures 2.7 to 2.10 indicate that power absorption by the plasma reaches a maximum when the magnetic field strength is equal to the ECR magnetic strength. This implies that the electric field, which is perpendicular to the static magnetic field, decays faster in ECR region. On the other hand, it also means that a large ECR volume can have a higher energy absorption. These are two of the aspects which are needed to be considered in the design of an ECR plasma source. The orientation of the electric field with respect to the static magnetic field pattern is also important. Other issues such as ion energy, plasma stability and uniformity are crucial in production environment.

The dc conductivity of the electron gas is not used in this analysis but is readily obtained by setting ω to zero in equations (2.23 - 2.25).

Figure 2.9 Var
strength at diff

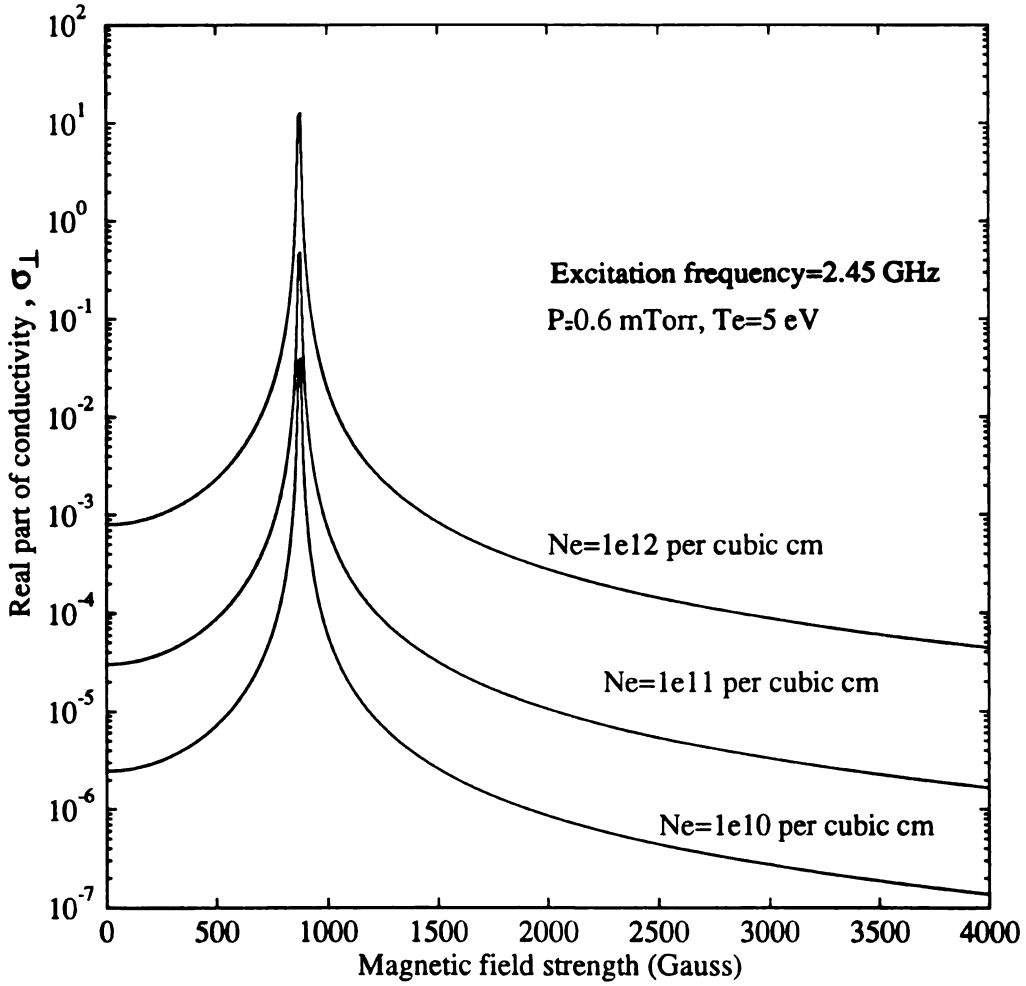

Figure 2.9 Variations of real part of conductivity, $\sigma_{\perp}$, with magnetic field strength at different plasma densities with 2.45 GHz excitation frequency

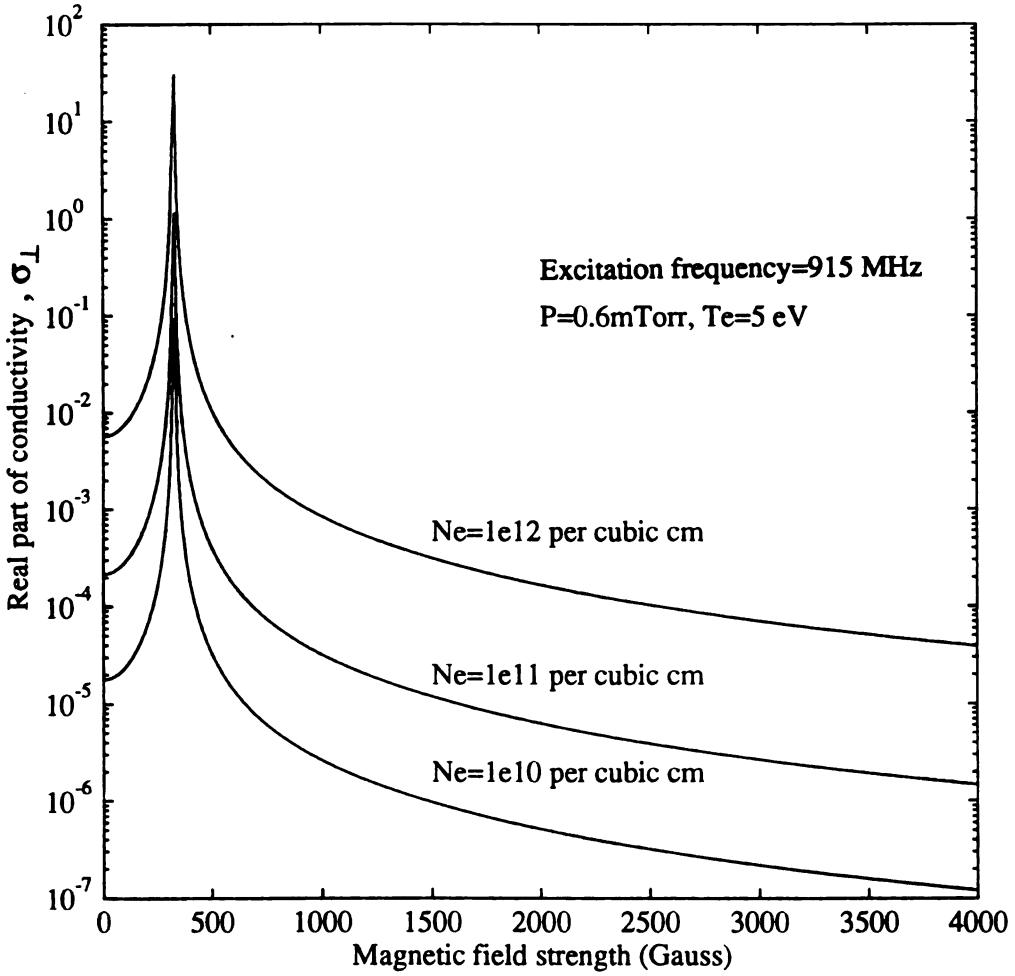

Figure 2.10 Variations of real part of conductivity, $\sigma_{\perp}$, with magnetic field strength at different plasma densities with 915 MHz excitation frequency

§ 2.5

plasma
electron
therefo
accelera
electron
electron
plasma
are prim
tempera
the dow

Bo
differenc
zone. S
imperfec
into the
Bohm's
componer

This is th
computer s

§ 2.5 Sheath and ion energy

Because of small mass and at high temperature, electrons in ECR plasma move much faster than the ions inside plasma. When the fast moving electrons reach a surface, they lower the potential of the surface. A sheath is therefore formed in which low energy electrons are reflected and ions are accelerated. In other words, there is a transfer of energy from the energetic electrons to the ions inside the sheath. Because of the loss of the energetic electrons, the temperature of a discharge, electron temperature, drops as the plasma diffuses away from the generation region. These energetic electrons are primarily lost by diffusion towards the vessel wall. The drop of electron temperature is witnessed experimentally by a drop of plasma potential along the downstream position.

Bohm's criterion states that a plasma itself cannot support potential differences greater than $\approx k_b T_e/2e$ without breaking down into a space-charge zone. Stangeby [71] indicated that the shielding effect of the sheath was imperfect and a small residual field called the pre-sheath penetrated deep into the plasma. The potential drop of this pre-sheath is determined by the Bohm's criterion and therefore the ions enter the sheath with a velocity component towards the surface, which is called the ion acoustic velocity:

$$v_{ia} = (kT_e/M_i)^{1/2} \qquad (2.27)$$

This is the minimum speed of the ions, which is sometimes neglected in computer simulation of ion energy distribution, entering the sheath.

The energy of an ion impinging a surface, such as a substrate, is therefore the summation of its thermal energy in the bulk of the plasma, the pre-sheath potential, the sheath potential between the substrate and the plasma, and the additional negative potential applied to the substrate. When a substrate bias is used, the ions will strike on the substrate surface at nearly 90 degrees. In ion assisted etching, a vertical profile can therefore be achieved. Although the incident angle of the ions impinging the substrate surface can be controlled by the applied bias, a high substrate bias is not desirable because issues such as damages to the etch mask and the substrate surface have to be considered. Therefore an ideal plasma source is one that can create a plasma with a low ion thermal energies and low sheath potential. In experiment, the ion energy distribution can be directly measured by an ion energy analyzer. Details of the measurement techniques and experimental results are discussed in Chapter Five.

§ 2.6 Magnetic confinement of plasma

The concept of magnetic confinement has been implemented by both ECR and non- ECR plasma sources to improve the uniformity and density of the plasma in the processing region. It is an old technique used in plasma research [76-78]. In practice, the plasma pressure always has to be small compared to the pressure of the confinement magnetic field [54]:

$$B^2/2\mu_o >> 2n_eT_ek_b \qquad (2.28)$$

where μ_o is the permeability in vacuum, B is the magnetic strength in Tesla, n_e is the plasma density per m^{-3}, k_b is the Boltzmann constant and T_e is the

electron temperature in Kelvin. Considering that the plasma density equals to 10^{11} cm^{-3} and T_e equals to 5 eV, the required confinement magnetic field is:

$$B >> 6.3 \text{ Gauss} \tag{2.29}$$

Therefore a 100 Gauss magnetic field is sufficient to confine the plasma.

The magnetic field for plasma confinement can be generated either by magnetic coils or permanent magnets. Permanent magnets were used in this research to create a multi-cusp magnetic field for downstream plasma confinement. An improvement of the plasma distribution in the downstream location has been observed [43] and is reported in later chapter.

CHAPTER THREE

ECR PLASMA SOURCES

§ 3.1 Introduction

In 1977, two apparatus [1,2] were announced by the Central Research Laboratory in Hitachi Ltd., Japan. The first one was a microwave ECR ion source [1] which had an antenna inside the discharge region. A strong axial magnetic mirror, whose field intensity was stronger than 890 Gauss, was generated by three electromagnetic coils to prevent erosion of the antenna due to bombardment of charged particles. This ion source was primarily used for ion beam processing [7] such as ion beam sputtering deposition, ion beam etching and non-mass-analyzed ion implantation.

The second apparatus [2] was a modification of the first one. Microwave energy was coupled into a round waveguide and eventually propagated into a 66 mm in inner diameter quartz tube which was placed at the end of the round waveguide. The axial magnetic field near the opening of the quartz tube was adjusted to 875 Gauss. This is the first divergent field microwave electron cyclotron resonance (ECR) plasma source used in semiconductor etching. This source initiated a series of intensive research concerned with the application in semiconductor processing. During the last fifteen years, experiments were carried out first in Japan [3-17] and then more recently in the United States [18-23]. Other ECR sources were also developed worldwide such as the Distributed ECR source (DECR) in France [24,25], the Horn-type ECR source in Germany [26-28] and the multipolar ECR Microwave Plasma Disk Reactor (MPDR) [32-48] in Michigan State University. Even though all the ECR sources use the same principle to generate the plasma, they have different geometries and coupling designs. It was not clear if these different designs resulted in different output plasma

properties. Thus many experimental and theoretical investigations have been devoted to the characterization of each source as well as evaluation of the different sources in specific applications.

This chapter aims to provide a general review of the divergent field ECR source, DECR and Horn-type ECR source. The MPDR source is discussed, separately, in detail in the next three chapters. This chapter also discusses other types of high density plasma sources such as the helicon source [29-31] from Australia and the recent planar radio frequency inductive coupled plasma source (ICP) from IBM [49,152,182,183]. The Transmission Coupled Plasma (TCP) [153,154] source, which looks very similar to the ICP, is now a commercial product for industrial application.

The driving force behind the development of all these new reactors for semiconductor processing, especially etching and deposition, is the demand of high anisotropy, high uniformity, high density, low ion energy and low temperature plasma for fabrication of ULSI devices. Non ECR plasma sources suffer from the fact that the operation pressure has to be above 10 mTorr to maintain a low sheath potential. However, at high pressure, the control of anisotropy is lost. For conventional parallel plate devices, the input power directly determines the energy of the ions impinging the substrate surface. This lack of independent control of ion energy is the main draw back of parallel plate plasma sources. Another important issue which ULSI technology has to deal with is the damage to the substrate. ECR plasma sources, in general, have lower ion energies and can be biased independently so that the energy of the ions impinging on the substrate can

be controlled. This is especially important when processing moderately doped III-V semiconductor materials.

§ 3.2 Axial divergent magnetic field ECR plasma sources

The axial divergent magnetic field ECR plasma source is the most extensively studied high density plasma source. It was the earliest ECR source which was applied to plasma processing application such as silicon etching [2]. Many variations of this source have been made both in Japan and in the United States. Research using this divergent field ECR plasma source includes etching [2-4,5,10,15,17,52,53], deposition [5,11,51], ion beam process [1,8,9,13], sputtering deposition [12], reduction [50], hydrogen annealing [147], wafer cleaning [148] and plasma immersion ion implantation [150,151].

The basic structure of a divergent field ECR plasma source consists of a cylinder with radius, d, and length, L, as shown in the Figure 3.1(a). This defines the discharge region. Two magnetic coils are wrapped around the cylinder to create an axial, static magnetic field. Microwave energy is introduced into the discharge region from a waveguide through a vacuum sealed quartz window. The ions and electrons created in the discharge region then diffuse into the downstream processing region where wafer is being processed.

Variations of magnetic configuration in these ECR plasma sources include gradient field ECR and mirror field ECR [8]. Figure 3.1 shows (a) a gradient field ECR configuration and (b) a mirror field ECR configuration.

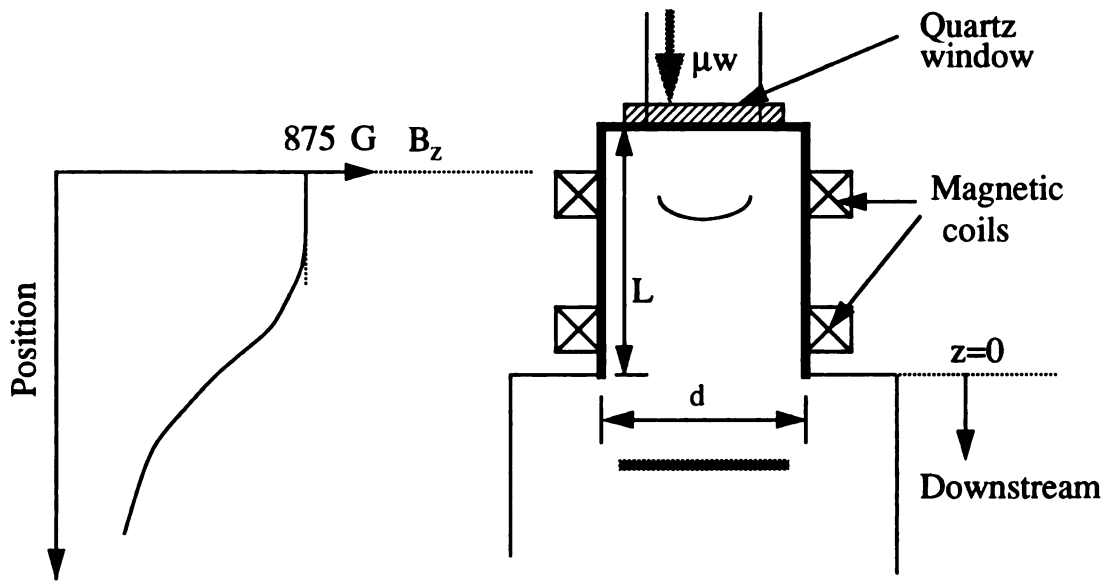

(a) Gradient field ECR configuration

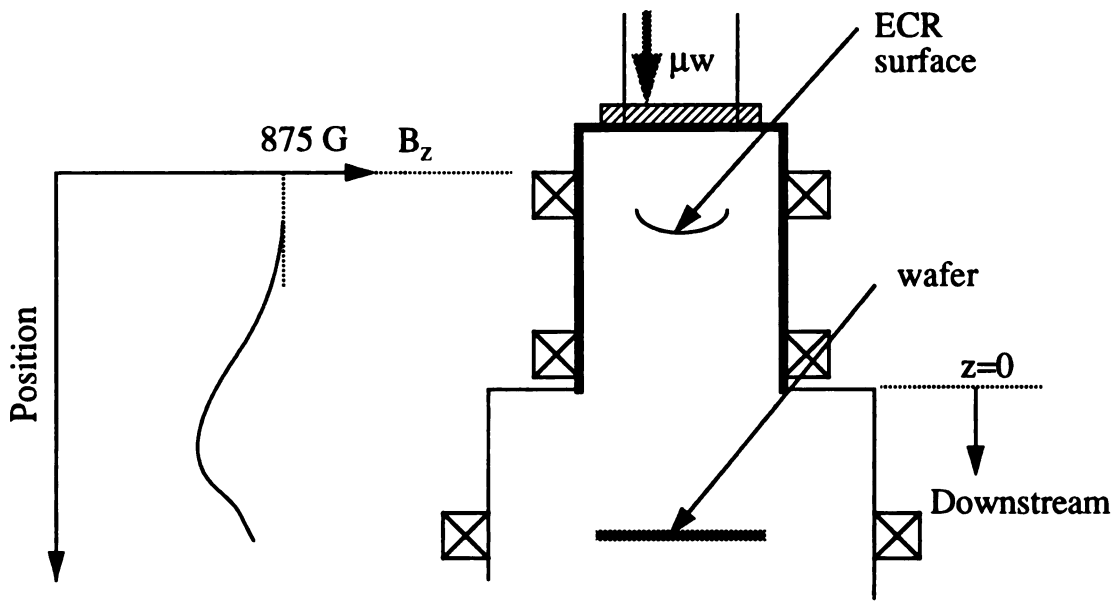

(b) Mirror field ECR configuration

Figure 3.1 Divergent field ECR plasma sources

In the mirror field ECR configuration, a third coil is placed at the same horizontal level of the wafer. As a result, a magnetic mirror is formed as shown in Figure 3.1(b).

The mirror field ECR source has a lower ion energy than the gradient field ECR source. As the third coil current increases from 0 A to 8 A at 0.45 mTorr, the ion energy decreases from about 13 eV to 5 eV and the FWHM (width of ion energy spectrum at 50% maximum) decreases from 8 eV to 5 eV [8]. In the gradient field source, the magnetic field lines penetrate the substrate at different angles. Ions and electrons move along these magnetic flux lines by ambipolar diffusion and impinge on the surface, resulting in different etched profiles in the center and the edge of the wafer [52]. The problem is solved by the third coil in the mirror field ECR configuration, resulting in collimated magnetic flux lines which are perpendicular to the substrate surface. Thus, beside achieving lower ion energy, the mirror field ECR also shows a better etching profile. Samujkawa et al. reported that when a 875 G magnetic strength was maintained right above the substrate, a uniform etched profile could be obtained [52].

The size of the divergent field ECR plasma source has been increased from the original 66 mm in inner diameter and approximately 150 mm high [1,2] to a recent version 200 mm in inner diameter and 197 mm high [5,52]. It is believed that the length of the discharge is critical to create a stable plasma [16]. Several different operation modes, such as TE_{112} [8], TE_{113} [5,12,18] and TM_{01} [23] modes have been reported.

Table 3.1 shows the typical discharge properties of the divergent ECR plasma sources reported in the collected literature. This data represents measurements taken in different sources at different locations. However, all measurements were taken in downstream locations as shown in Figure 3.1.

Etch uniformity is one of the concerns in this divergent field ECR source. Because the motion of the ions and electrons are restricted in the radial direction, any nonuniformity of the plasma densities in the plasma generation region will be projected onto the wafer if it is positioned close to the ECR surface. This was reported by a study made by Iizuka et al. [16]. He suggested that higher TE modes such as TE_{12} and TE_{13} modes might have been excited in his source. Figure 3.2 and Figure 3.3 display the distribution of the electric field strength and its orientation for the TE_{12} and TE_{13} modes respectively. Derivations of the mode equations and their interpretations are discussed in detail in Chapter Four. Therefore they are not repeated here. In each plot, the central axis of the divergent ECR source is represented by the coordinate (41,41). Iizuka reported that a non-uniform etched result was obtained whose pattern matched with the electric field strength patterns shown in the Figure 3.2 and Figure 3.3. Within the discharge region, strong electric field shown in the figures creates more ions. Since lateral diffusion of the ions was restricted because of the axial magnetic field, a non-uniform etch rate was observed when the wafer was placed close to the source [16].

Substrate bias was usually used during etching. However, no self-induced bias can be obtained if the chuck is too close to the discharge generation region. This is because the axial magnetic field prevents the flow of electrons to the grounded side wall. Due to the lack of grounded surface,

TABLE 3.1 PLASMA PARAMETERS FOR DIVERGENT ECR SOURCE

Pressure (mTorr)	Gas	Plasmal Potential(volts)	Power (W)	Ne (cm^{-3})	Te (eV)	Ion energy (eV)	Ref #
3	Ar	-	400-900	2-7 E12	-	-	1
1	H_2	-	400-900	1-2 E12	-	-	1
0.45	Ar	-	100	-	-	12-48	8
0.2- 5	Ar	-	120-600	0.2-1 E11	3-6	-	11
0.6-3	H_2	-	120-600	1.2E10	5-8	-	11
0.3-3	N_2	-	1000	-	-	12-17	15
0.5	Cl_2	-	1000	-	-	14	15
0.4	Ar	10-40	100	3-4 E10	4-4.3	-	16
0.4-30	O_2	12-20	200-300	1-2 E10	-	-	19
0.3	Ar	20-30	500-600	6-8 E10	6-12	-	20

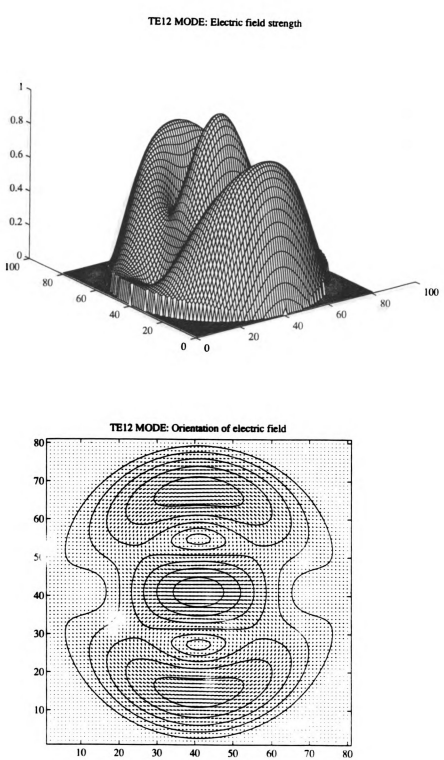

Figure 3.2 Distribution of the electric field (a) strength and (b) orientation in TE_{12} mode

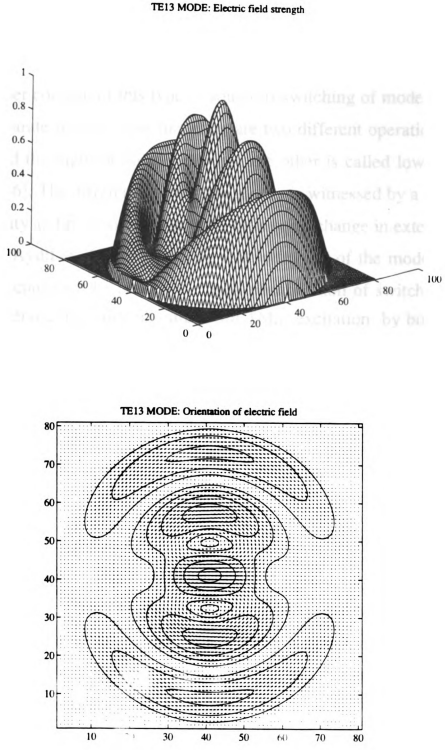

Figure 3.3 Distribution of the electric field (a) strength and (b) orientation in TE_{13} mode

no induced d.c. bias can be estabilished in the chuck which carries the wafer. This phenomenon was reported by Dane et al. [114].

Another concern of this type of source is switching of modes during a process. Separate reports show that there are two different operation modes. One is called the high (density) mode and the other is called low (density) mode [23,146]. The difference of the two modes is witnessed by a change of plasma density and plasma potential with little or no change in external input power [23]. Aydil et al. [146] reported that switching of the modes, during the process, could not be predicted. Such phenomenon of switching mode was also observed in a similar source with TM_{01} excitation by both Carl et al. [23] and Gorbatkin et al. [184]. More work is needed to be done in this source to provide a controllable and repeatable process at specific operation conditions.

§ 3.3 Distributed ECR plasma source

This type of plasma source, originated from a group of French researchers, is one of the two ECR sources developed in Europe. The concept was evolved from another idea called Microwave Multipolar Plasma (MMP) [156]. The MMP, in fact, is a plasma magnetically confined in a chamber. One or more separate plasma sources, such as the divergent field ECR plasma sources, are used to generate the plasma. The idea of the Distributed ECR source is that those magnets used to confine plasma have also an ECR magnetic field strength of 875 Gauss near the pole in each magnet. As shown in Figure 3.4, an antenna is then placed at a nearby position to generate the plasma.

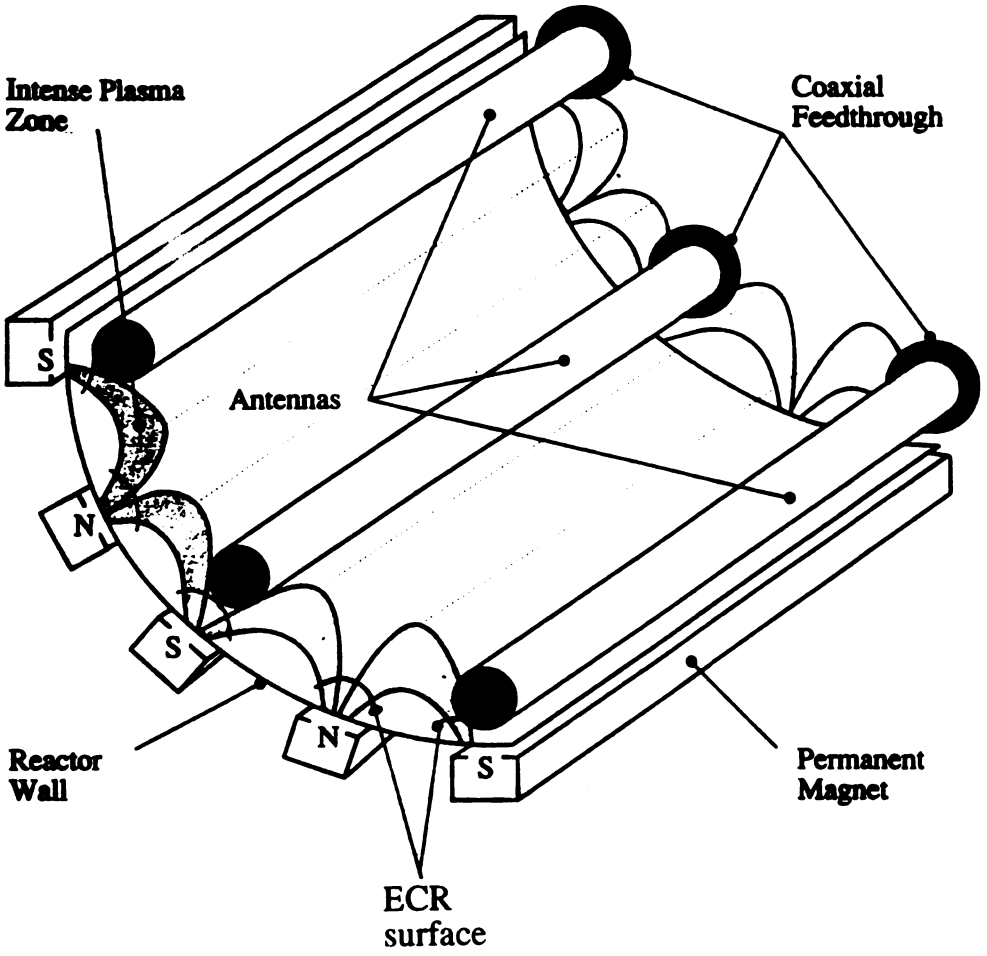

Figure 3.4 Distributed ECR plasma source

As shown in Figure 3.4, eight rows of permanent ferrite magnets with 1500 Gauss pole strength are arranged outside a grounded chamber of 28 cm in diameter [25]. Microwave energy is fed into the chamber through eight 8 mm O.D. tubular stainless steel antennae which are placed inside the plasma. Each antenna has a length of 10 to 40 cm long and is cooled by water. A single microwave generator and a matching device are used to couple the microwave energy to all antennae. Table 3.2 shows some typical plasma density and electron energies that are achieved with this source.

The method of plasma excitation in DECR source suffers from the fact that the antennae embedded inside the plasma will be a constant source of contamination due to the bombardment by the high energy ions or reactive species which reach the surface of the antennae during an etching process. When the source is used in deposition application, the deposited material on the surface of the antennae may degrade the performance of the antennae. Because of these two reasons, the tubular antennae may have to be replaced periodically. Finally, since the wafer is placed inside the chamber and is very close to the antenna array, it is necessary to investigate any damage to the wafer because of the microwave radiation during an etching or deposition process.

§ 3.4 Horn-type ECR plasma sources

These types of horn-type ECR plasma sources were developed in Germany. Two versions have been produced. One is the Elongated-Mirror-Geometry (EMG) plasma source [26] as shown in Figure 3.5. The other, a

TABLE 3.2 PLASMA PARAMETERS OF DISTRIBUTED ECR SOURCE

Pressure (mTorr)	Gas	Plasma Potential (volts)	Power (W)	Ne (cm^{-3})	Te (eV)	Ion energy (eV)	Ref #
0.4-1.8	Ar	24-30	1600	1-1.5 E11	3-3.8	-	25

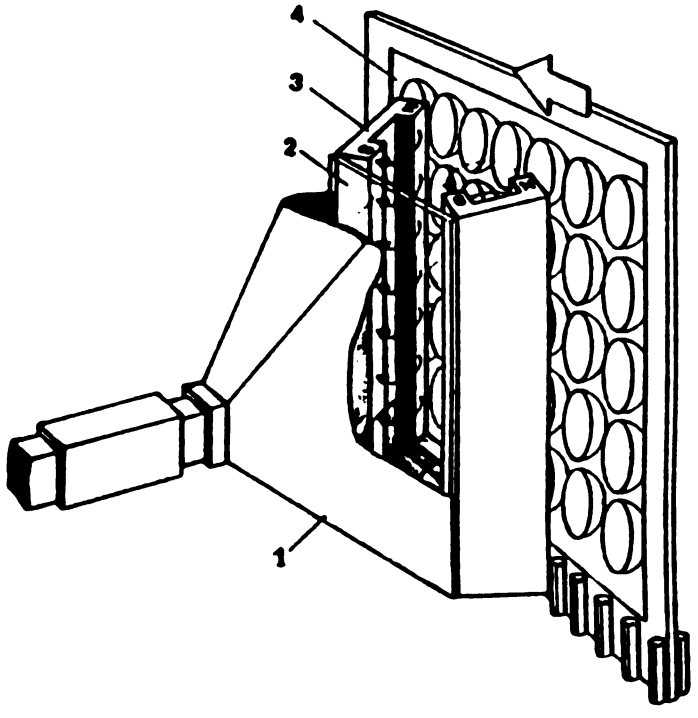

(1) Horn antenna, (2) microwave transparent window, (3) magnetic race-track system, (4) substrate holder.

Figure 3.5 Elongated-Mirror- Geometry (EMG) plasma source

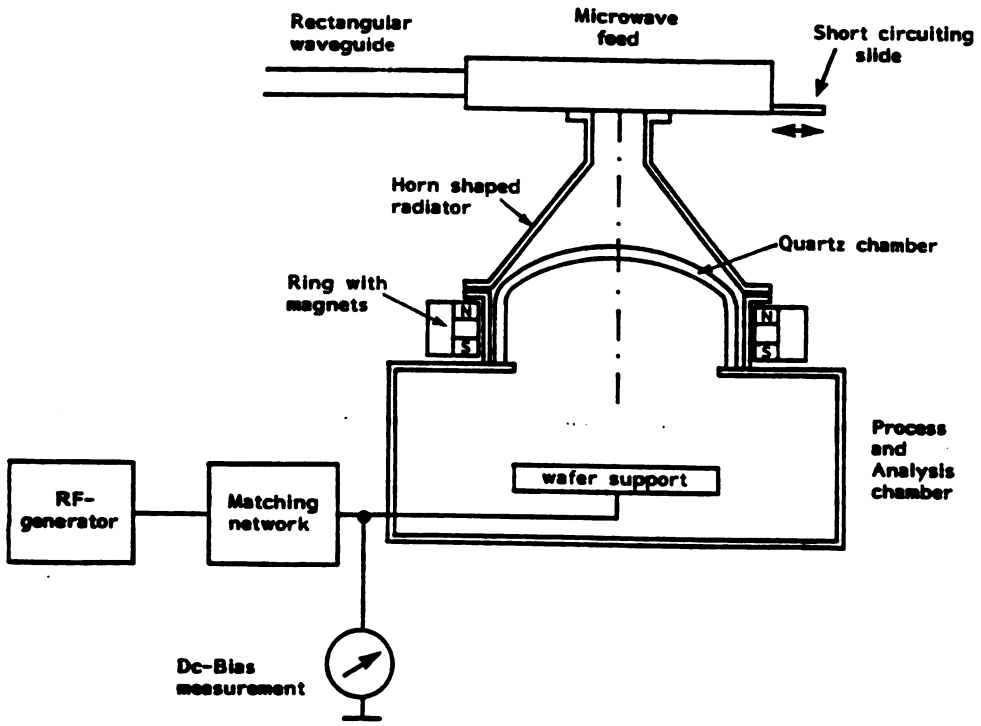

Figure 3.6 Leybold source

cross section of which is shown in Figure 3.6, is here referred as the Leybold source [27,28]. The EMG plasma source uses a rectangular horn of dimension 60 cm x 9 cm. It has been used primarily for deposition such as silicon dioxide [26]. The Leybold source uses a circular horn with 20 cm in diameter and is used for etching [27]. It has a dome-shaped quartz disk which is similar to the MPDR described in the next chapter. Both EMG and Leybold sources use permanent magnets to form the ECR magnetic surface.

A TM_{01} microwave excitation mode is used to generate the plasma. Two "plasma modes", ring mode and bulk mode, have been reported from the Leybold source, which are dependent on pressure and input power [28]. The transition from ring mode to bulk mode is accompanied by a change of plasma density and reflected microwave power. A study of mass spectroscopy of the ring mode and the bulk mode indicates a change of distribution of charged species inside the plasma. For example, in an oxygen plasma at 0.75 mTorr, O_2^+ ions are the majority ions in the ring mode when the microwave power is between 120 watts to 360 watts. When microwave power is higher or equal to 480 watts, the source is operating in bulk mode, whose concentrations of the O^+ and O_2^+ ions are basically the same. Moreover, during the transition from ring mode to bulk mode, the plasma potential changes from 10 volts to 50 volts.

To understand the cause of the ring mode and the bulk mode, the mode diagram of TM_{01} is examined. Figure 3.7 shows the distribution of the transverse electric field in TM_{01} mode. It has a maximum electric field strength off the center, but a zero strength at the center. The longitudinal electric field, however, has a maximum strength at the center as shown in

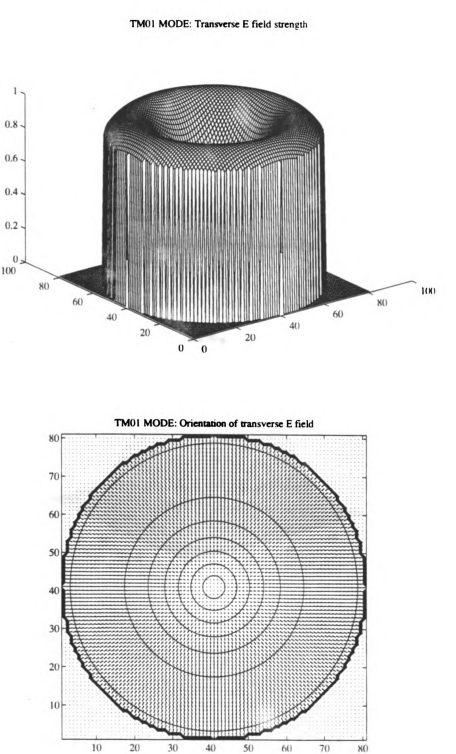

Figure 3.7 Distribution of transverse electric field in TM_{01} mode

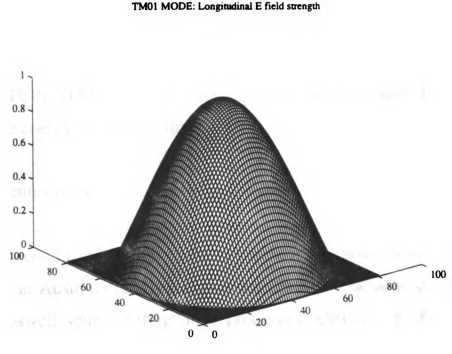

Figure 3.8 Longitudinal E field strength in TM_{01} mode

Figure 3.8. It is believed that in the ring mode, only the transverse electric field is responsible to generate the plasma. In the bulk mode, both the longitudinal and transverse electric fields generate the plasma.

§ 3.5 Other plasma sources

Three types of new sources which are non-ECR plasma sources are also studied both in the industry and universities. They are the Helicon source [29-31,154,157-161], the Helical resonator and the planar rf Inductive Coupled Plasma (ICP) [49,162-164] or Transmission Coupled Plasma (TCP) [153,154]. All these plasma sources use 13.56 MHz microwave energy to generate the plasma.

3.5.1 Helicon source

A second name for the Helicon source is the Boswell source. It was developed in Australia [29-31]. Figure 3.9 shows a schematic drawing of a typical Boswell source sitting on a processing chamber A rf antenna is wrapped around a cylindrical glass chamber in which the plasma is formed. The outer side of the rf antenna is surrounded by magnetic coil that creates a static axial magnetic field inside the glass cylinder. The magnetic coil helps to confine the charged species created inside the glass cylinder, thus reducing the diffusion loss of the ions to the glass wall. Typical dimensions of the glass cylinder are 15 cm in diameter and 22 cm long.

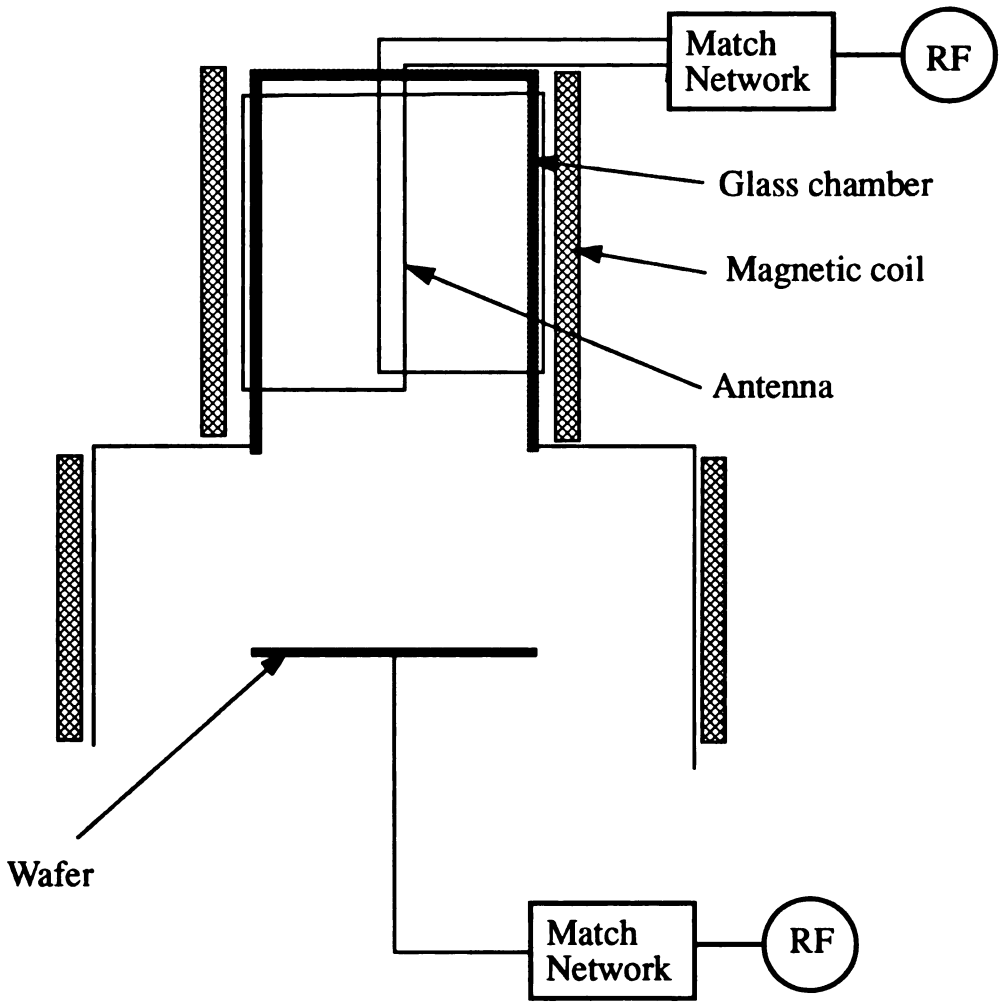

Figure 3.9 Schematic drawing of a Boswell Source

3.5.2 Helical resonator

Another high density rf source is from Prototech in the United States, called Helical Resonator. Figure 3.10 shows the side view of the longitudinal section of a Helicon resonator. Two differences can be found in this source. First, a helical coil is used to surround a quartz tube. Second, there is an electrostatic shield between the quartz tube and the helical coil. Another major difference between this source and the Boswell source is that no magnetic coil is used. Instead, the whole structure is hosted inside a metallic cylinder as shown in Figure 3.10. The function of the electrostatic shield is believed to be the same as the Faraday shield in ICP_2 source which is described in next section.

3.5.3 Inductive coupled plasma (ICP) sources

Inductive coupled plasma sources (ICP) have been used as sources of charged species for mass spectrometers for many years. Figure 3.11 is a schematic diagram of an ICP-Mass Spectrometer constructed by Sciex to detect neutral species. The neutral species are forced to flow through a small diameter glass tube into a second but larger glass tube. A high voltage rf is applied to a coil wrapped around at the end of the second glass tube to form a discharge. The ionized neutral species then enter the mass spectrometer and are analyzed.

The use of planar inductive coupled plasma in semiconductor processing, however, is relatively new. Yet, it gets considerable attention in the industry since its development is supported by a major computer

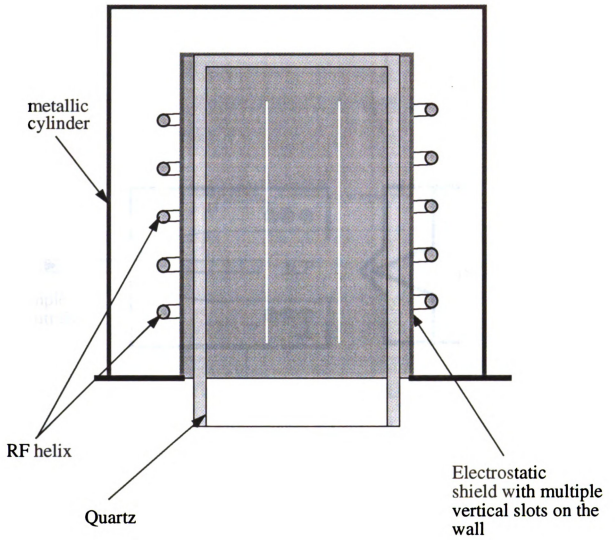

Figure 3.10 Side view of longitudinal section of a Helical Resonator

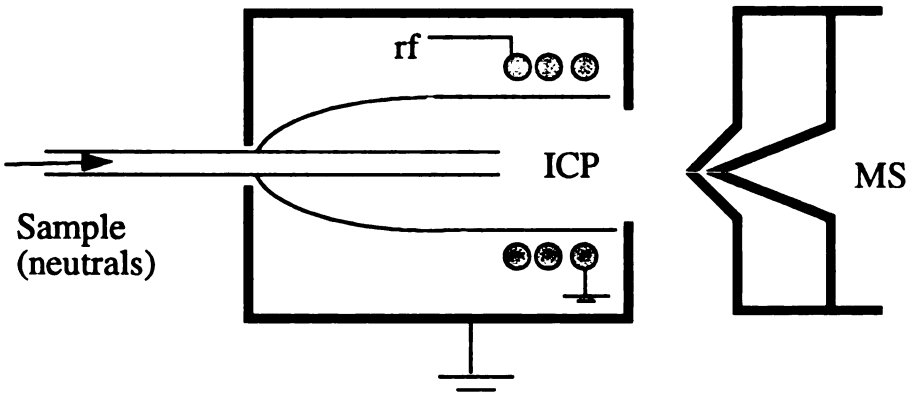

Figure 3.11 Schematic drawing of ICP-MS instrument constructed by Sciex

company and a major semiconductor equipment supplier. More than one version of this type of source have been developed, even though they look very similar to each other. The first one is the planar ICP from IBM [49,164,182,183], hereafter referred as ICP_1. The second version is from University of Wisconsin in Madison [162,163], hereafter referred as ICP_2. The third one is the Transmission Coupled Plasma (TCP) from Lam Research, California [153,154].

Figure 3.12 (a) displays the cross-sectional view of the ICP_1 and the bottom view of the plasma showing the cusp-shaped confined plasma. One characteristic of this source is the use of a rectangular coil on a flat half inch thick quartz plate. The argon plasma density is reported to be increased linearly with power from 10^{11} cm^{-3} at 300 W to 6 x 10^{11} cm^{-3} at 1.2 kW at 1 mTorr [182]. The variation of the induced electric field strength at 2 inches under the coil is shown in Figure 3.12 (b). Typical argon ion production efficiencies are about 175 eV/ion at 1 mTorr [182]. The source has been used for ashing application [49].

The ICP_2 is basically the same as the ICP_1 except two major differences. As shown in Figure 3.13, the first difference is that a circular coil is used instead of a rectangular coil. The second difference is a major improvement of the ICP_1 that a Faraday shield is placed in between the coil and a one inch thick quartz plate as shown in Figure 3.13(b). This Faraday shield serves the same purpose as the shield used in the Helical Resonator that the plasma is created by rf inductive coupling rather than capacitive coupling.

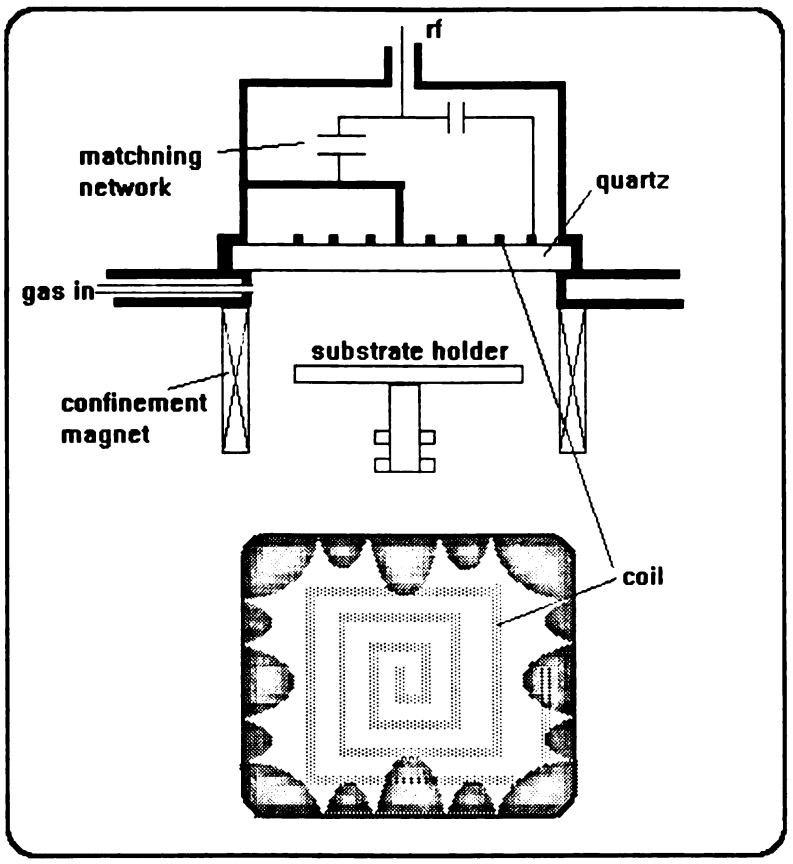

Figure 3.12 (a) A shematic diagram of the ICP_1

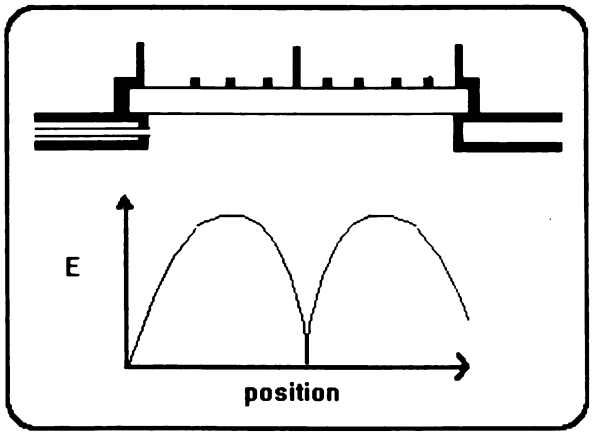

Figure 3.12 (b) Variation of induced electric field 2 inches under the coil

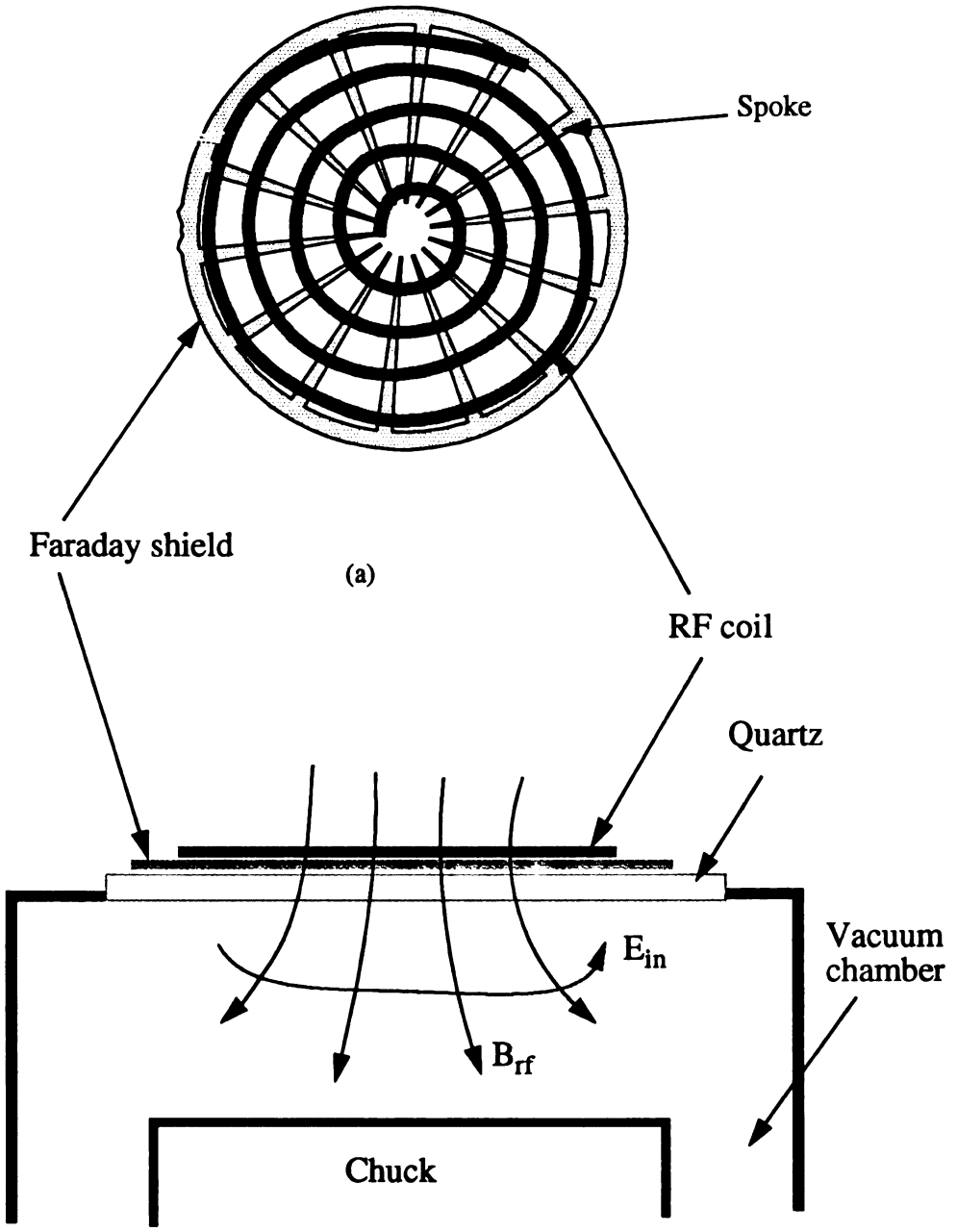

Figure 3.13 Schematic illustration of ICP_2

It is believed that during start up or at low plasma densities, without a Faraday shield as shown in Figure 3.14, the high voltage in the coil and any ground surface in the system including the substrate holder behave like the two electrodes of a capacitor. Plasma is generated in part by the electric field, E_c, between the two "electrodes" and by the electric field, E_{in}, induced by the time varying magnetic field, B_{rf}. The presence of the capacitive electric field, E_c, caused fluctuation of plasma and caused sputtering on those ground surface near to the coil.

With the present of a metallic Faraday shield as shown in Figure 3.13(b). the capacitive electric field, E_c, is isolated from the plasma. In this case, only the induced electric field, E_{in}, is responsible for the generation of the plasma. The vertical drilled through slots in Helical resonator and the radial spokes in the Faraday shield probably serve the purpose of removing power loss due to eddy current in the shield. The ICP_2 has been used for polymer coating using HMDSO (hexamethyldisiloxane) [163] at 13.56 MHz with 1.2-1.6 kW power. Other applications include optical film coating, fluorination of thermal plastic and chemical treatment of synthetic and natural fiber surface [186].

The Transmission Coupled Plasma (TCP) is a planar ICP source marketed by Lam Research. No detailed structure of the source has been published. The source is claimed to be a variation of the previous two ICP sources. It can be operated from 1-10 mTorr while most of the ICP_2 applications are at 20 mTorr or above. The TCP has demonstrated anisotropic etching of 0.3 μm features [153] in polysilicon and has an etching uniformity of 5%, 3 σ over 200 mm wafer probably with

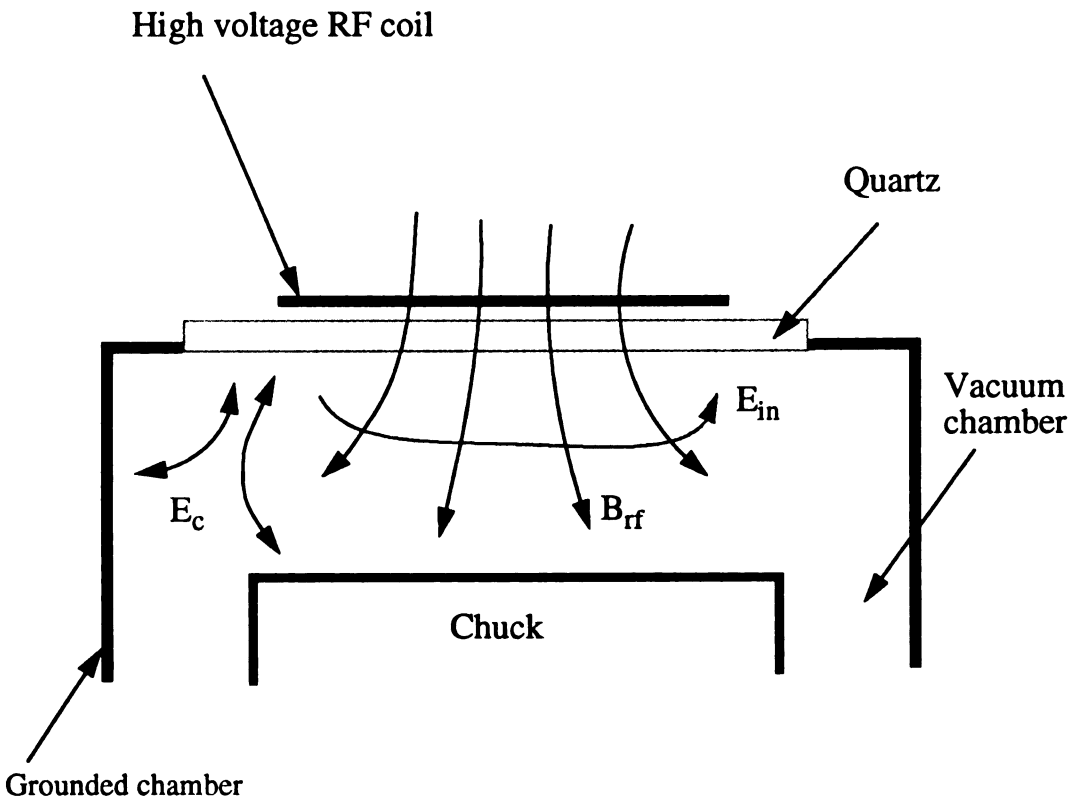

Figure 3.14 Illustration of capacitive and inductive coupling

downstream confinement magnets. The etch rate varies from 0.3 to 1 μm per minute, depending on the gas chemistry and the type of substrate film.

§ 3.6 Summary

All the ECR sources and the non-ECR sources described in this chapter are developed for future ULSI applications. Three, but not the least, important issues which all these plasma sources have to fulfill are low damage, high uniformity and scalability of the source for large area processing. The Microwave Plasma Disk Reactor is one type of ECR source which fulfills all these three requirements. In next three chapters, the structures, operation and performances of the MPDRs will be examined. The capability of the MPDR in etching of silicon features down to 0.1 μm is then presented in Chapter Seven, which demonstrates that the MPDR, especially the large diameter MPDR, may play an important role in semiconductor processing.

CHAPTER FOUR

MICROWAVE PLASMA DISK REACTOR

§ 4.1 Introduction

The Microwave Plasma Disk Reactor (MPDR) is one type of the ECR plasma sources developed for future Ultra Large Scale Integrated circuits (ULSI) application. Five different sizes of ECR Microwave Plasma Disk Reactors have been fabricated and investigated in the MSU laboratories. Investigation of two large diameter reactors, the MPDR 20 and MPDR 325, is one of the major subjects in this dissertation. Properties of other smaller MPDR plasma sources, which have not been investigated, are also included in this dissertation.

Experimental investigations of the MPDR sources are discussed in Chapter Five and Chapter Six. This chapter details the structural and historical development of the MPDR plasma sources. The operation of the MPDRs is also described in detail. Electromagnetic resonant modes in a perfect cylindrical empty cavity are also presented for the illustration of the excitation modes used in most of the MPDRs. They are also used in the discussion of optimal magnetic configuration for the MPDRs.

§ 4.2 Structure of the MPDR

The structure of the large diameter MPDRs, the MPDR 20 and MPDR 325 are described in detail in this section. MPDR 20 has a discharge diameter of 20 cm while the MPDR 325 has a discharge diameter of 24 cm. All the features found in these two reactors can be found in other small prototype reactors developed in the laboratory. All MPDRs share two basic

features: a cylindrical microwave resonant cavity enclosing a quartz discharge chamber and a multicusp ECR magnetic configuration.

§ 4.2.1 Structure of the MPDR 20

MPDR 20 was the first large diameter ECR MPDR developed in the MSU laboratories. It was also the first 915 MHz ECR plasma source developed for plasma processing. Besides operating at 915 MHz microwave frequency, it can also be operated at 2.45 GHz. Figure 4.1(a) displays the longitudinal cross section of the reactor. Microwave energy is coupled into the 45.7 cm diameter x 45.7 cm high aluminum cavity <1> by a microwave input probe <3>. By adjusting the position, Lp, of the microwave input probe and the height, Ls, between the sliding short <2> and the baseplate <4>, the reactor can be tuned to a specific electromagnetic resonant mode with zero reflected power. Illustration of the excitation modes is covered later in this chapter.

The baseplate <4> is 51 cm in diameter. It consists of two pieces: a top brass piece <4a> and a bottom stainless steel piece <4b>. The baseplate hosts 24 of 5.4 cm x 5.4 cm x 2.7 cm rare earth permanent magnets made of neodymium iron boron <9>. The magnets are arranged in alternate poles inside the baseplate by stacking two magnets together. They are kept in position by a magnet keeper <6> made with low carbon steel. A 12-pole multicusp ECR magnetic field is formed as shown in Figure 4.1(b). The ECR surface, which has a field strength of 875 Gauss for 2.45 GHz excitation frequency, is located 2.33 cm from the surface of the magnet. If the excitation frequency is reduced to 915 MHz, then the ECR surface has a

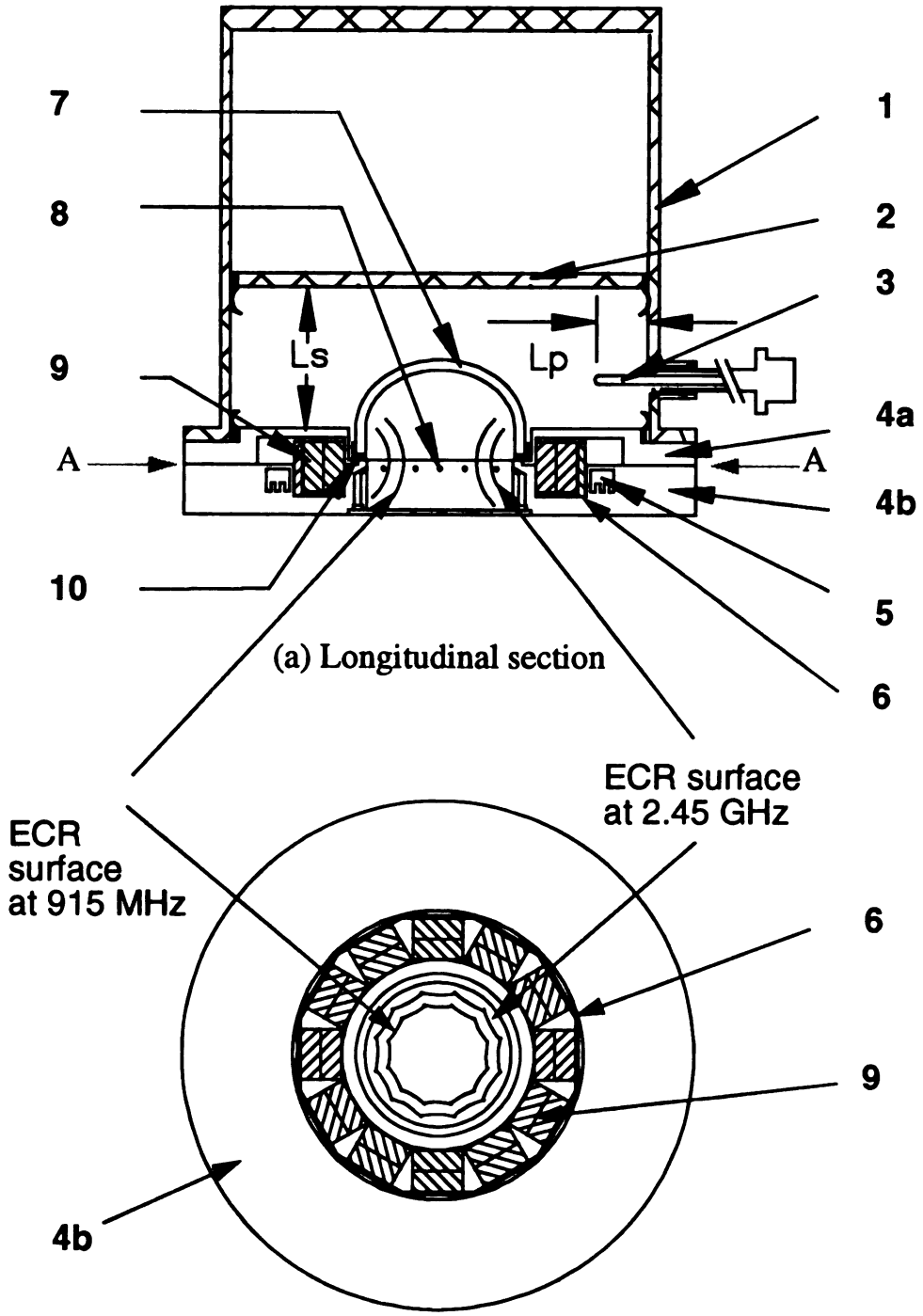

Figure 4.1 Structure of MPDR 20

field strength of 327 Gauss which is located 3.7 cm from the magnet's surface. To protect the magnets from thermal demagnetization, a water channel <5> is used to cool the baseplate.

The discharge volume is defined by the 20 cm diameter opening in the baseplate and the dome-shaped quartz disk <7>. A discharge volume of about 3000 cm^3 is formed. Gas is introduced into the discharge region through twelve gas pin holes <8> drilled on the inner surface of the baseplate. The quartz disk sits on the baseplate <4b> with a L-shaped Viton vacuum gasket <10> in between as shown in Figure 4.1(a).

Figure 4.2(a) is a picture of the components in MPDR 20, showing the aluminum cavity, the probe and the quartz disk. There are two circular rings mounting on the outside of the aluminum cavity. 2 mm in diameter holes are drilled on these rings. They are used for electric field measurement to verify the excitation mode in the reactor. Figure 4.2(b) shows the stainless steel baseplate <4b> with the ECR magnets.

§ 4.2.2 Historical development of MPDR

The historic development of the MPDR can be divided into two stages since 1981. The first seven years was the first stage of development. It was the evolution stage in which major components reached their final form. The next stage of development took about five years. More than five MPDRs were constructed for different applications. Each of these newly developed MPDRs had its own specific features and improvement, but components such as the cylindrical cavity and the baseplate remained the same even though the sizes of these components varied.

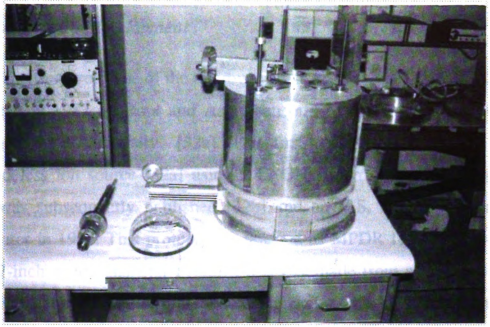

(a) Cylindrical cavity, quartz disk and microwave probe

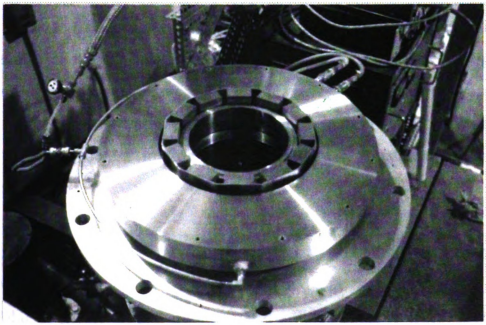

(b) Magnetic ring in the baseplate

Figure 4.2 Photographs showing the components of the MPDR 20

The first stage of development

The first prototype of the microwave plasma disk reactor (MPDR) was presented in 1982 by Root and Asmussen in a MSU/NASA Workshop in Michigan State University [32a]. This first reactor was designed as an electrodeless ion source [32a] using 2.45 GHz microwave excitation. The work was subsequently published [32b] and an U.S. Patent was granted [32c] later in 1985. This prototype is referred as MPDR I in Figure 4.3. It has a 7-inch inside diameter cylindrical cavity made from a brass cylinder. Microwave energy was introduced into the cavity by a side-feed monopole antenna or probe. The plasma was generated and confined in a flat 9-cm diameter cylindrical quartz disk and an ion extraction grid attached to the bottom of the baseplate. This prototype reactor was not an ECR plasma source because there was no static magnetic field inside the quartz disk for the electron cyclotron resonance to take place. The reactor was originally designed to be a high efficiency ion source. Ions were extracted through the grid for either downstream processing such as oxidation of silicon wafer [34] or as an electrodeless microwave electrothermal thruster for spacecraft propulsion [185].

Another paper was published in 1985 by Root and Asmussen [33]. This paper was important because it pointed out the concept of using a multipolar magnetic cusp to reduce plasma diffusion to the wall inside the plasma disk, and the idea of using electron cyclotron resonance to generate plasma for low pressure application. This was the first time when the concept of using rare earth permanent magnet to form a multipolar cusp-

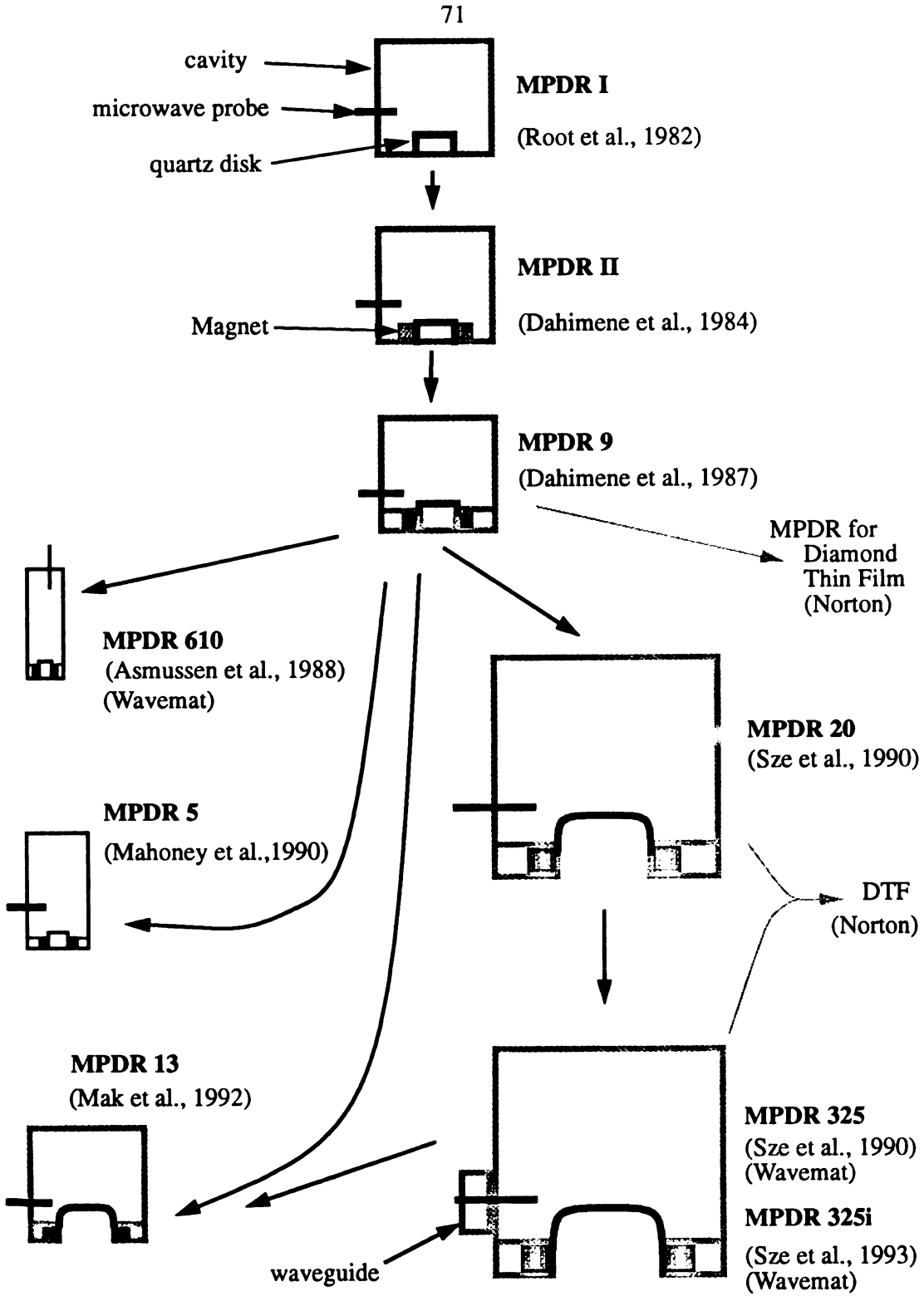

Figure 4.3 Development of MPDRs for ECR plasma Applications

shaped ECR magnetic field to generate a plasma was ever published. About the same year in the MSU laboratories, Dahimene tested the first electron cyclotron resonant MPDR by placing a ring of permanent magnets around the quartz disk. This is referred as MPDR II in Figure 4.3. The worked was first represented in the 19th EPIB conference [35a] and later published in 1986 [35b]. An improved version of the reactor was published in 1987 [36]. The ECR magnets, instead of being exposed to the microwave field, were hosted inside the baseplate. This version of MPDR is referred hereafter as the MPDR 9, as shown in Figure 4.3, because it has a 9 cm diameter of plasma.

Early versions of the MPDR 9 had metal grids attached to the bottom of the baseplate [32-36]. The reactor was operated as a broad ion beam source. The advantage of using a grid is to establish a pressure gradient between the plasma generation region and the downstream processing chamber. Such pressure gradient allows several mTorrs in the region enclosed by the quartz disk and the grid so that a high density plasma can be generated. The processing region below the grid can be maintained at pressure less than 0.1 mTorr so that a mean free path between collision of 52 cm can be obtained. Ions can be accelerated by the grid through proper biasing, forming a broad directed beam to bombard the substrate surface. The disadvantage of using a metal grid or grids is that the processing rate is reduced due to the recombination loss of ions on the grid surface. The grid itself, in addition, may become the source of contaminant due to physical sputtering by energetic ions, or chemical reaction between reactive species in plasma and the grid.

The MPDR 9 can also be operated without a grid for different applications. Examples of these applications are plasma oxidation by G. Salbert [182] and etching by J. Hopwood [60]. In fact all current ECR MPDRs are now operated without any grid attached to baseplate [43, 45-48, 183,184]. A gridless reactor increases the processing rate due to elimination of recombination loss of the ions on the grid. Potential contamination from the grid is also removed. The lowest processing pressure in a gridless MPDR 9 is about 0.3 mTorr depending on how much microwave power is used. However, the amount of microwave power that could be used in the MPDR 9 source was limited to 350 watts at pressure less than 10 mTorr. This is because a Viton O-ring is used in the MPDR 9 as the vacuum seal between the quartz disk and the baseplate. The O-ring will burn if too much microwave power is used.

The second stage of development

Since 1988, a family of MPDR plasma sources was developed with some structural modifications. The original MPDR 9 has a 17.8 cm inside diameter brass cylinder with 9 cm diameter discharge. Eight 2.54 x 2.54 x 2.54 cm Ne-Fe-B magnets are arranged in a multicusp configuration to create the ECR surface. On the basis of the blueprint of the MPDR 9, three different sizes of MPDR prototypes were designed and fabricated.

One reactor was a 3.75 cm diameter discharge reactor designed by Asmussen and Fritz in 1988 and published in 1990 [40]. It was later modified to a commercial product known as MPDR 610 [48,165]. MPDR 610 is an ion, plasma or free radical source designed for molecular beam

epitaxy applications such as superconducting thin film deposition. Both the method of microwave excitation and orientation of the ECR magnetic field in this source are different from the rest of the plasma sources in the MPDR family. Either 915 MHz or 2.45 GHz microwave excitation can be used to create the plasma. It is now being studied by Srivastava [48].

The second reactor has a 5 cm discharge diameter designed by L. Mahoney (hereafter referred as MPDR 5) and was published in 1991 [41]. It has a 8.9 cm inner diameter cavity. Because of the small diameter of the cavity, this reactor can only be operated at TE_{111} mode. The discussion of mode excitation is covered in later section and therefore is not discussed here. Eight 1 cm x 1 cm x 1 cm permanent magnets are used to form an octapolar static magnetic field. This source was previously configured as an ion beam source in Mahoney's work [41,61] using a multi-grid to accelerate the ions. The source can also be operated without a grid as a plasma source, which is studied in this thesis.

The third reactor [42,43] is the MPDR 20. The design of which is one of the major subjects in this dissertation. This reactor is a scale up of the MPDR 9. A twelve-pole multicusp static magnetic field is used. However, the reactor can be run with either 915 MHz or 2.45 GHz excitation. One significant step was achieved in this reactor. It was the first MPDR which was operated with an opening bigger than the cutoff radii of the cylindrical cavity resonant modes. Because the reactor runs very well at 2.45 GHz without a grid as the smaller reactors, a commercial reactor was released later by WAVEMAT with some modifications. This is the MPDR 325 [45] as shown in Figure 4.4(a). This reactor is another important subject in this

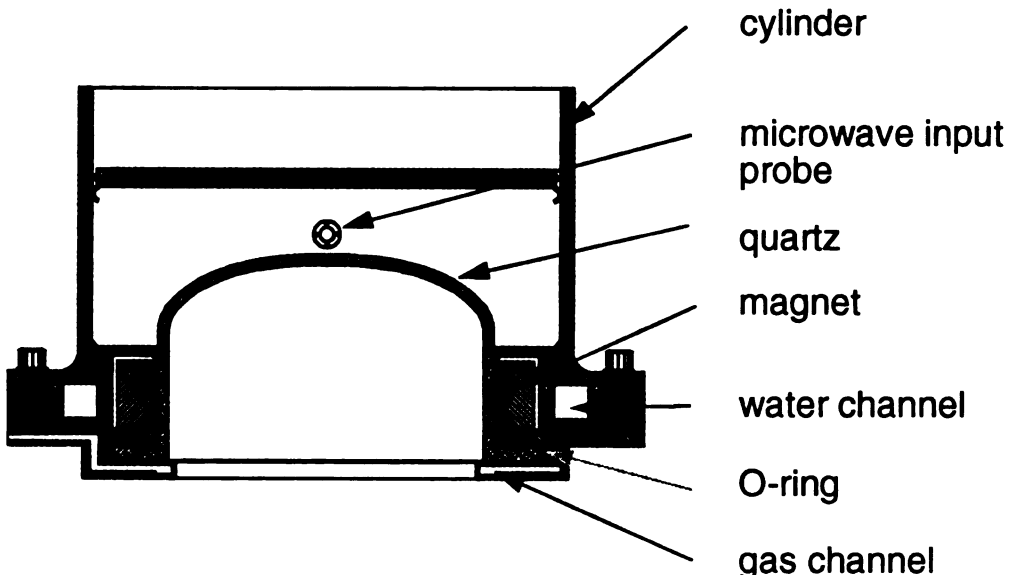

(a)

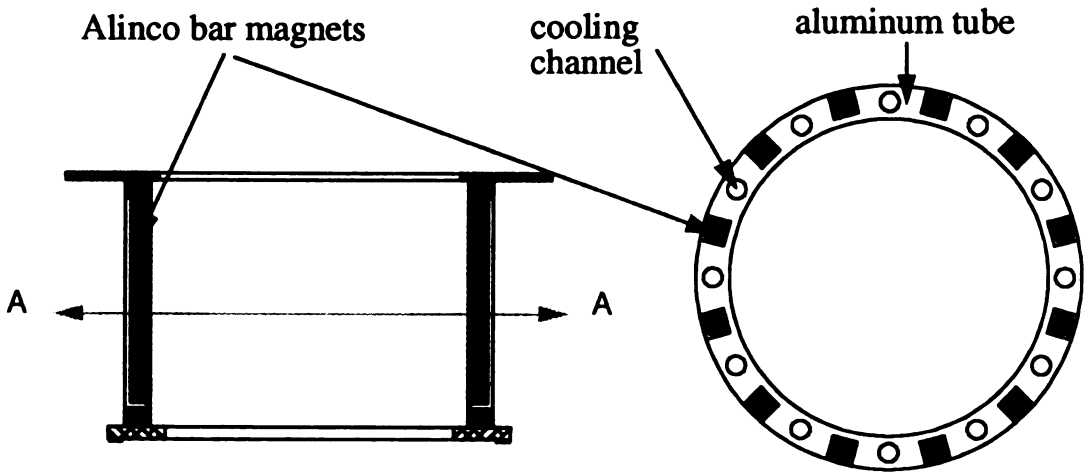

Longitudinal view View of section A-A

(b)

Figure 4.4 (a) MPDR 325 and (b) MPCS

dissertation, especially its performance and application in etching of submicron features in silicon.

Although MPDR 325 looks similar to the MPDR 20, it has several different features which are improvement over the MPDR 20. The inner diameter of the cavity is 35.56 cm which is smaller than the MPDR 20. As indicated in later section, the resonant modes in MPDR 325 are further apart than those in the MPDR 20 if both are operated at 2.45 GHz. As shown in Figure 4.4(a), the long quartz vessel in MPDR 325, which covers most of the baseplate area, reduces contaminant from the metal wall. The whole reactor is made of aluminum. Therefore it is much lighter than the MPDR 20. Unlike the MPDR 20, a waveguide port is used for microwave input. The use of waveguide is better than using a coaxial cable, which is used in MPDR 20, in that power ratings of coaxial cable limit the input power to the cavity.

The baseplate of the MPDR 325 is also water cooled. It has the same magnetic configuration as the MPDR 20. The input gas holes are equally spaced in a metal gas ring near the opening of the quartz vessel as shown in Figure 4.4(a). The 24 cm inner diameter quartz vessel is clamped vacuum tight between the baseplate and the gas ring piece. This forms the plasma generation region with a volume of 3600 cm^3.

The experience of running a large diameter MPDR 325 lead to the modification of the original MPDR 9. A 13 cm inner diameter quartz disk is used in a modified baseplate in MPDR 9 which is hereafter referred as

MPDR 13 [47]. MPDR 13 shares the same 17.8 cm diameter cavity as in MPDR 9, but it uses the same type of quartz disk in MPDR 325. Therefore the differences between MPDR 9 and MPDR 13 are just the size and shape of the quartz disk as shown in Figure 4.3. The MPDR 13 is currently investigated by Mak [47] and King [46].

Three improvements in MPDR 13 and MPDR 325 can be found. One is the use of a longer quartz vessel to reduce contamination by reducing the exposed area of the metal wall to the plasma. The second improvement is moving the O-ring seal away from the plasma so that it would not burn at high microwave power. Microwave input powers up to 1000 watts have been used in these two reactors. It is believed that both reactors can be operated at power over 1000 watts.

The third improvement is the use of a multipolar plasma confinement structure (MPCS) [43] as shown in Figure 4.4(b). The MPCS can be attached underneath the baseplate of the MPDR 20 and MPDR 325. It is made from an aluminum tube which has an outside diameter of 28 cm and length of 22 cm. The inside diameter is 24 cm, which is large enough for 6-inch wafer processing. Twelve slots are located on the outside of the MPCS. A 0.5 x 0.5 x 6 inches Alinco bar magnet with pole strength of 1 kGauss is placed in each of the twelve slots. When attaching to the baseplate, all magnets, both inside the applicator baseplate and those in the MPCS, are oriented in a manner that one of the poles of each magnet is facing toward the central axis of the system and poles of neighboring magnets, either above, below, or side by side, are opposite to each other. Such a configuration creates magnetic cusps oriented horizontally and vertically.

This configuration minimizes the diffusion of ionic species towards the wall, therefore reducing loss of plasma due to surface recombination. The MPCS has a magnetic field strength of 100 Gauss 2 cm from the inner surface and the field strength decays rapidly toward the center of the confinement chamber. The MPCS can be cooled either by gas or water using the cooling channel as shown in Figure 4.4(b), which run parallel to the bar magnets. Experimental observation showed that the MPCS did not heat up at all.

The MPCS improves the uniformity of the plasma for large wafer application. Experimental results showed that a uniformity of 2.6% standard deviation of plasma density over 18 cm diameter was achieved at 12.5 cm downstream in MPDR 20. A similar but shorter MPCS was used by M. Dahimene in MPDR 325 and a 3.0% standard deviation of plasma density at 6 cm downstream was obtained over 15 cm diameter [43]. At 15 cm downstream in MPDR 325, a uniformity of 8.1% (3 σ) was achieved [45]. The downstream plasma confinement structure has already become an integral component in all ECR MPDR applications.

§ 4.3 Operation of the MPDR

4.3.1 Electromagnetic resonant modes in cylindrical cavity

The resonant modes of electromagnetic wave in a cylindrical cavity are represented by two groups [66, 75]. One is called the transverse electric field (TE) mode in which the electric field of the electromagnetic wave lies in the transverse plane of the cylinder. The magnetic field of the

electromagnetic wave in TE mode has both transverse and axial components. The other is called transverse magnetic field (TM) mode which means that the electric field has both transverse and axial components, but the magnetic field only lies in the transverse plane of the cylinder.

Each cylindrical cavity resonant mode is governed by a mode equation. For TE mode, the mode equation is given as [66]:

$$\Psi_{npq} = J_n (x'_{np} r/a)[b \cos(n\phi) + c \sin(n\phi)] \sin(q\pi z/d) \qquad (4.1)$$

where n=0,1,2,...; p=1,2,3,...; q=1,2,3,...; **a** is the radius of the cavity; **d** is the length of the cavity and x'_{np} is the p^{th} zero of the first derivative of Bessel function, J_n.

For TM mode, the mode equation is:

$$\Psi_{npq} = J_n (x_{np} r/a) [b \cos(n\phi) + c \sin(n\phi)] \cos(q\pi z/d) \qquad (4.2)$$

where n=0,1,2,...; p=1,2,3,...; q=0,1,2,...; **a** is the radius of the cavity; **d** is the length of the cavity and x_{np} is the p^{th} zero of Bessel function, J_n.

The relation between the resonant frequency and the geometry of a perfect cylindrical cavity is given by Harrington {66].

For TE mode:

$$d = q\pi a/[4\pi^2 a^2 f^2 \epsilon \mu - x'^2_{np}]^{1/2} \qquad (4.3)$$

For TM mode:

$$d = q\pi a/[4\pi^2 a^2 f^2 \epsilon \mu - x_{np}^2]^{1/2} \qquad (4.4)$$

where f is the frequency, ϵ is the permittivity and μ is the permeability in vacuum. At fixed microwave frequency, the variation of cavity radius versus the resonant length in a cylindrical cavity can be represented by a mode chart. Figure 4.5 and 4.6 show the mode chart for the TE and TM modes at 2.45 GHz respectively. In these two mode charts, there are repeated patterns. These repeated patterns represent higher order modes. For example, in a 10 cm diameter cylindrical cavity, the TE_{11} mode can be excited at cavity lengths about 9 cm, 18 cm and 27 cm which are represented by TE_{111}, TE_{112} and TE_{113} in Figure 4.5 respectively. These mode charts give the theoretical relation between cavity radius and the resonant length for an empty perfect cylindrical cavity. In a non-perfect cavity such as the one in MPDR, the resonant lengths of these cavity modes shift. The presence of the quartz disk and the hole in the baseplate shortens the resonant length. With the presence of a discharge, the protruded plasma lengthens the resonant length. These resonant lengths also change as the plasma densities change with input microwave power and pressure.

The number of resonant modes which exist in a cylindrical cavity is determined by its radius and length. A large diameter cavity such as the MPDR 20 has resonant modes close to each other as shown in Figure 4.5. A small diameter cavity such as MPDR 9 has its resonant modes widely separated. As a result, single mode excitation is possible in small diameter

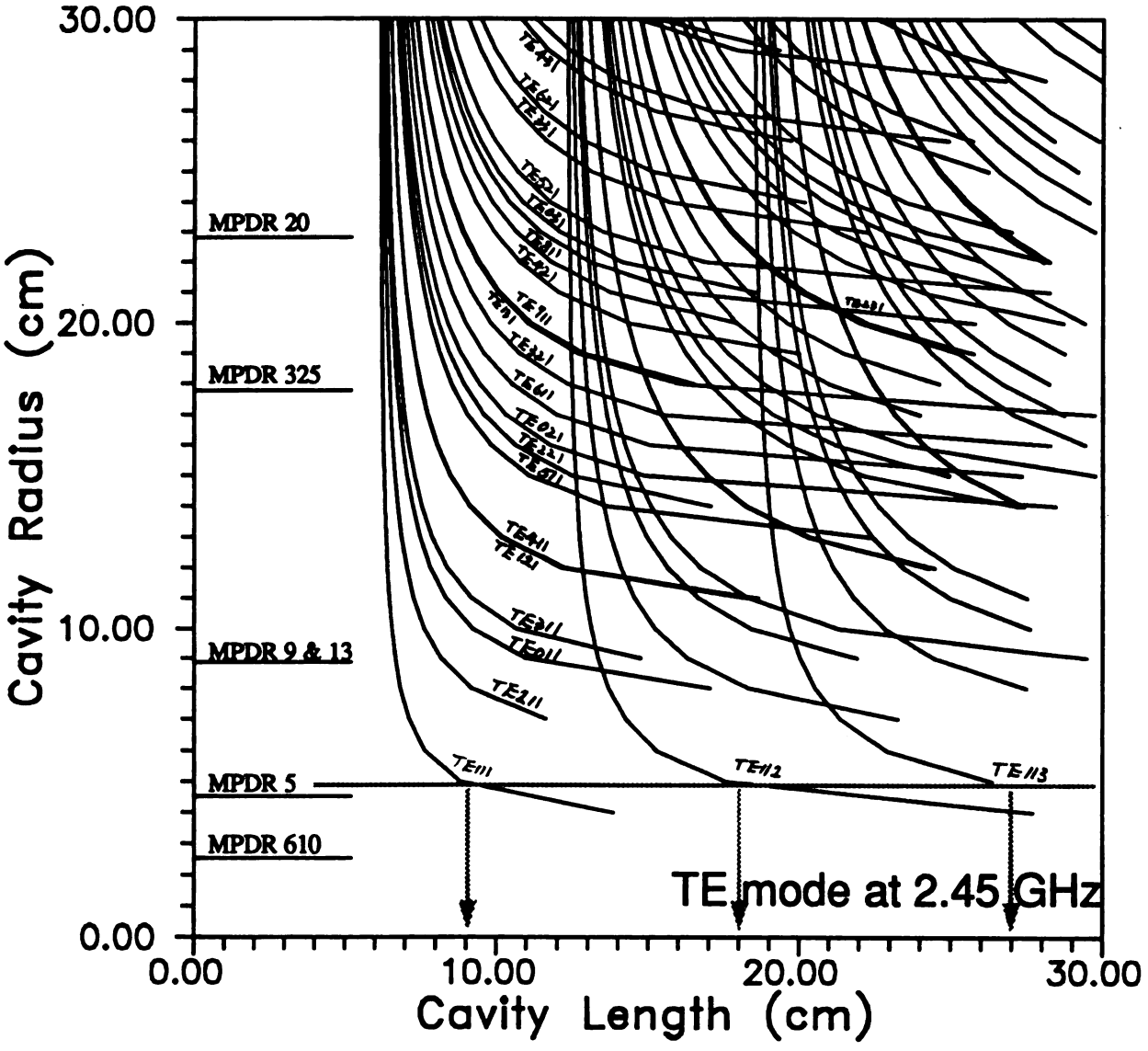

Figure 4.5 TE mode at 2.45 GHz

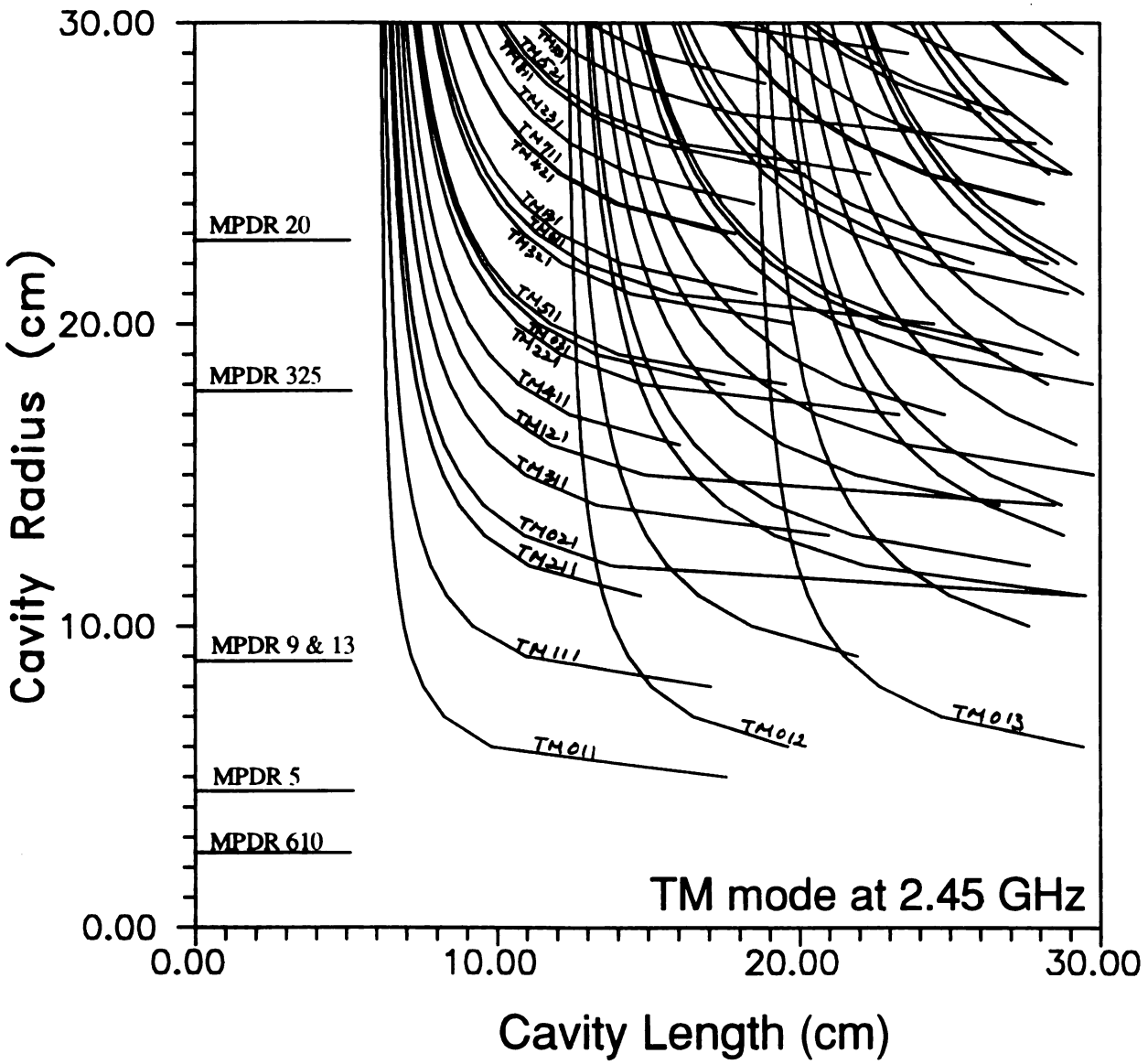
30.00
20.00
10.00
0.00
Cavity Radius (cm)
MPDR 20
MPDR 325
MPDR 9 & 13
MPDR 5
MPDR 610
TM011
TM012
TM013
TM111
TM021
TM211
TM311
TM121
TM411
TM221
TM511
TM321
TM611
TM421
TM711
TM331
TM431
TM531
TM631
TM731
TM831
TM931
TM041
TM541
TM641
TM741
TM841
TM941
TM051
TM151
TM251
TM351
TM451
TM551
TM651
TM751
TM851
TM951
TM061
TM161
TM261
TM361
TM461
TM561
TM661
TM761
TM861
TM961
TM071
TM171
TM271
TM371
TM471
TM571
TM671
TM771
TM871
TM971
TM081
TM181
TM281
TM381
TM481
TM581
TM681
TM781
TM881
TM981
TM091
TM191
TM291
TM391
TM491
TM591
TM691
TM791
TM891
TM991
TM0101
TM1101
TM2101
TM3101
TM4101
TM5101
TM6101
TM7101
TM8101
TM9101
TM0111
TM1111
TM2111
TM3111
TM4111
TM5111
TM6111
TM7111
TM8111
TM9111
TM0121
TM1121
TM2121
TM3121
TM4121
TM5121
TM6121
TM7121
TM8121
TM9121
TM0131
TM1131
TM2131
TM3131
TM4131
TM5131
TM6131
TM7131
TM8131
TM9131
TM0141
TM1141
TM2141
TM3141
TM4141
TM5141
TM6141
TM7141
TM8141
TM9141
TM0151
TM1151
TM2151
TM3151
TM4151
TM5151
TM6151
TM7151
TM8151
TM9151
TM0161
TM1161
TM2161
TM3161
TM4161
TM5161
TM6161
TM7161
TM8161
TM9161
TM0171
TM1171
TM2171
TM3171
TM4171
TM5171
TM6171
TM7171
TM8171
TM9171
TM0181
TM1181
TM2181
TM3181
TM4181
TM5181
TM6181
TM7181
TM8181
TM9181
TM0191
TM1191
TM2191
TM3191
TM4191
TM5191
TM6191
TM7191
TM8191
TM9191
TM0201
TM1201
TM2201
TM3201
TM4201
TM5201
TM6201
TM7201
TM8201
TM9201
TM0211
TM1211
TM2211
TM3211
TM4211
TM5211
TM6211
TM7211
TM8211
TM9211
TM0221
TM1221
TM2221
TM3221
TM4221
TM5221
TM6221
TM7221
TM8221
TM9221
TM0231
TM1231
TM2231
TM3231
TM4231
TM5231
TM6231
TM7231
TM8231
TM9231
TM0241
TM1241
TM2241
TM3241
TM4241
TM5241
TM6241
TM7241
TM8241
TM9241
TM0251
TM1251
TM2251
TM3251
TM4251
TM5251
TM6251
TM7251
TM8251
TM9251
TM0261
TM1261
TM2261
TM3261
TM4261
TM5261
TM6261
TM7261
TM8261
TM9261
TM0271
TM1271
TM2271
TM3271
TM4271
TM5271
TM6271
TM7271
TM8271
TM9271
TM0281
TM1281
TM2281
TM3281
TM4281
TM5281
TM6281
TM7281
TM8281
TM9281
TM0291
TM1291
TM2291
TM3291
TM4291
TM5291
TM6291
TM7291
TM8291
TM9291
TM0301
TM1301
TM2301
TM3301
TM4301
TM5301
TM6301
TM7301
TM8301
TM9301
TM0311
TM1311
TM2311
TM3311
TM4311
TM5311
TM6311
TM7311
TM8311
TM9311
TM0321
TM1321
TM2321
TM3321
TM4321
TM5321
TM6321
TM7321
TM8321
TM9321
TM0331
TM1331
TM2331
TM3331
TM4331
TM5331
TM6331
TM7331
TM8331
TM9331
TM0341
TM1341
TM2341
TM3341
TM4341
TM5341
TM6341
TM7341
TM8341
TM9341
TM0351
TM1351
TM2351
TM3351
TM4351
TM5351
TM6351
TM7351
TM8351
TM9351
TM0361
TM1361
TM2361
TM3361
TM4361
TM5361
TM6361
TM7361
TM8361
TM9361
TM0371
TM1371
TM2371
TM3371
TM4371
TM5371
TM6371
TM7371
TM8371
TM9371
TM0381
TM1381
TM2381
TM3381
TM4381
TM5381
TM6381
TM7381
TM8381
TM9381
TM0391
TM1391
TM2391
TM3391
TM4391
TM5391
TM6391
TM7391
TM8391
TM9391
TM0401
TM1401
TM2401
TM3401
TM4401
TM5401
TM6401
TM7401
TM8401
TM9401
TM0411
TM1411
TM2411
TM3411
TM4411
TM5411
TM6411
TM7411
TM8411
TM9411
TM0421
TM1421
TM2421
TM3421
TM4421
TM5421
TM6421
TM7421
TM8421
TM9421
TM0431
TM1431
TM2431
TM3431
TM4431
TM5431
TM6431
TM7431
TM8431
TM9431
TM0441
TM1441
TM2441
TM3441
TM4441
TM5441
TM6441
TM7441
TM8441
TM9441
TM0451
TM1451
TM2451
TM3451
TM4451
TM5451
TM6451
TM7451
TM8451
TM9451
TM0461
TM1461
TM2461
TM3461
TM4461
TM5461
TM6461
TM7461
TM8461
TM9461
TM0471
TM1471
TM2471
TM3471
TM4471
TM5471
TM6471
TM7471
TM8471
TM9471
TM0481
TM1481
TM2481
TM3481
TM4481
TM5481
TM6481
TM7481
TM8481
TM9481
TM0491
TM1491
TM2491
TM3491
TM4491
TM5491
TM6491
TM7491
TM8491
TM9491
TM0501
TM1501
TM2501
TM3501
TM4501
TM5501
TM6501
TM7501
TM8501
TM9501
TM0511
TM1511
TM2511
TM3511
TM4511
TM5511
TM6511
TM7511
TM8511
TM9511
TM0521
TM1521
TM2521
TM3521
TM4521
TM5521
TM6521
TM7521
TM8521
TM9521
TM0531
TM1531
TM2531
TM3531
TM4531
TM5531
TM6531
TM7531
TM8531
TM9531
TM0541
TM1541
TM2541
TM3541
TM4541
TM5541
TM6541
TM7541
TM8541
TM9541
TM0551
TM1551
TM2551
TM3551
TM4551
TM5551
TM6551
TM7551
TM8551
TM9551
TM0561
TM1561
TM2561
TM3561
TM4561
TM5561
TM6561
TM7561
TM8561
TM9561
TM0571
TM1571
TM2571
TM3571
TM4571
TM5571
TM6571
TM7571
TM8571
TM9571
TM0581
TM1581
TM2581
TM3581
TM4581
TM5581
TM6581
TM7581
TM8581
TM9581
TM0591
TM1591
TM2591
TM3591
TM4591
TM5591
TM6591
TM7591
TM8591
TM9591
TM0601
TM1601
TM2601
TM3601
TM4601
TM5601
TM6601
TM7601
TM8601
TM9601
TM0611
TM1611
TM2611
TM3611
TM4611
TM5611
TM6611
TM7611
TM8611
TM9611
TM0621
TM1621
TM2621
TM3621
TM4621
TM5621
TM6621
TM7621
TM8621
TM9621
TM0631
TM1631
TM2631
TM3631
TM4631
TM5631
TM6631
TM7631
TM8631
TM9631
TM0641
TM1641
TM2641
TM3641
TM4641
TM5641
TM6641
TM7641
TM8641
TM9641
TM0651
TM1651
TM2651
TM3651
TM4651
TM5651
TM6651
TM7651
TM8651
TM9651
TM0661
TM1661
TM2661
TM3661
TM4661
TM5661
TM6661
TM7661
TM8661
TM9661
TM0671
TM1671
TM2671
TM3671
TM4671
TM5671
TM6671
TM7671
TM8671
TM9671
TM0681
TM1681
TM2681
TM3681
TM4681
TM5681
TM6681
TM7681
TM8681
TM9681
TM0691
TM1691
TM2691
TM3691
TM4691
TM5691
TM6691
TM7691
TM8691
TM9691
TM0701
TM1701
TM2701
TM3701
TM4701
TM5701
TM6701
TM7701
TM8701
TM9701
TM0711
TM1711
TM2711
TM3711
TM4711
TM5711
TM6711
TM7711
TM8711
TM9711
TM0721
TM1721
TM2721
TM3721
TM4721
TM5721
TM6721
TM7721
TM8721
TM9721
TM0731
TM1731
TM2731
TM3731
TM4731
TM5731
TM6731
TM7731
TM8731
TM9731
TM0741
TM1741
TM2741
TM3741
TM4741
TM5741
TM6741
TM7741
TM8741
TM9741
TM0751
TM1751
TM2751
TM3751
TM4751
TM5751
TM6751
TM7751
TM8751
TM9751
TM0761
TM1761
TM2761
TM3761
TM4761
TM5761
TM6761
TM7761
TM8761
TM9761
TM0771
TM1771
TM2771
TM3771
TM4771
TM5771
TM6771
TM7771
TM8771
TM9771
TM0781
TM1781
TM2781
TM3781
TM4781
TM5781
TM6781
TM7781
TM8781
TM9781
TM0791
TM1791
TM2791
TM3791
TM4791
TM5791
TM6791
TM7791
TM8791
TM9791
TM0801
TM1801
TM2801
TM3801
TM4801
TM5801
TM6801
TM7801
TM8801
TM9801
TM0811
TM1811
TM2811
TM3811
TM4811
TM5811
TM6811
TM7811
TM8811
TM9811
TM0821
TM1821
TM2821
TM3821
TM4821
TM5821
TM6821
TM7821
TM8821
TM9821
TM0831
TM1831
TM2831
TM3831
TM4831
TM5831
TM6831
TM7831
TM8831
TM9831
TM0841
TM1841
TM2841
TM3841
TM4841
TM5841
TM6841
TM7841
TM8841
TM9841
TM0851
TM1851
TM2851
TM3851
TM4851
TM5851
TM6851
TM7851
TM8851
TM9851
TM0861
TM1861
TM2861
TM3861
TM4861
TM5861
TM6861
TM7861
TM8861
TM9861
TM0871
TM1871
TM2871
TM3871
TM4871
TM5871
TM6871
TM7871
TM8871
TM9871
TM0881
TM1881
TM2881
TM3881
TM4881
TM5881
TM6881
TM7881
TM8881
TM9881
TM0891
TM1891
TM2891
TM3891
TM4891
TM5891
TM6891
TM7891
TM8891
TM9891
TM0901
TM1901
TM2901
TM3901
TM4901
TM5901
TM6901
TM7901
TM8901
TM9901
TM0911
TM1911
TM2911
TM3911
TM4911
TM5911
TM6911
TM7911
TM8911
TM9911
TM0921
TM1921
TM2921
TM3921
TM4921
TM5921
TM6921
TM7921
TM8921
TM9921
TM0931
TM1931
TM2931
TM3931
TM4931
TM5931
TM6931
TM7931
TM8931
TM9931
TM0941
TM1941
TM2941
TM3941
TM4941
TM5941
TM6941
TM7941
TM8941
TM9941
TM0951
TM1951
TM2951
TM3951
TM4951
TM5951
TM6951
TM7951
TM8951
TM9951
TM0961
TM1961
TM2961
TM3961
TM4961
TM5961
TM6961
TM7961
TM8961
TM9961
TM0971
TM1971
TM2971
TM3971
TM4971
TM5971
TM6971
TM7971
TM8971
TM9971
TM0981
TM1981
TM2981
TM3981
TM4981
TM5981
TM6981
TM7981
TM8981
TM9981
TM0991
TM1991
TM2991
TM3991
TM4991
TM5991
TM6991
TM7991
TM8991
TM9991
TM01001
TM11001
TM21001
TM31001
TM41001
TM51001
TM61001
TM71001
TM81001
TM91001
TM01011
TM11011
TM21011
TM31011
TM41011
TM51011
TM61011
TM71011
TM81011
TM91011
TM01021
TM11021
TM21021
TM31021
TM41021
TM51021
TM61021
TM71021
TM81021
TM91021
TM01031
TM11031
TM21031
TM31031
TM41031
TM51031
TM61031
TM71031
TM81031
TM91031

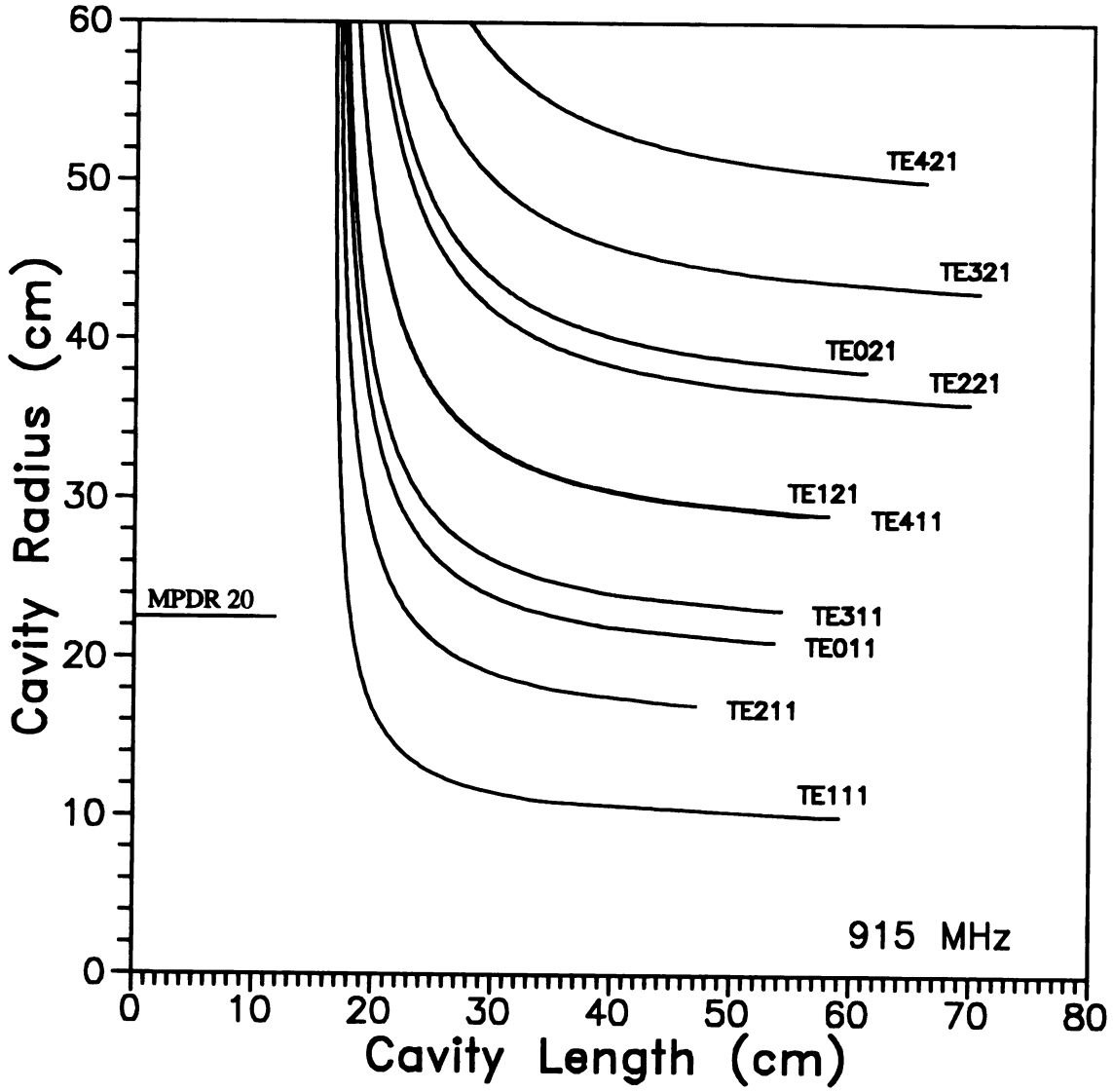

Figure 4.7 TE mode at 915 MHz

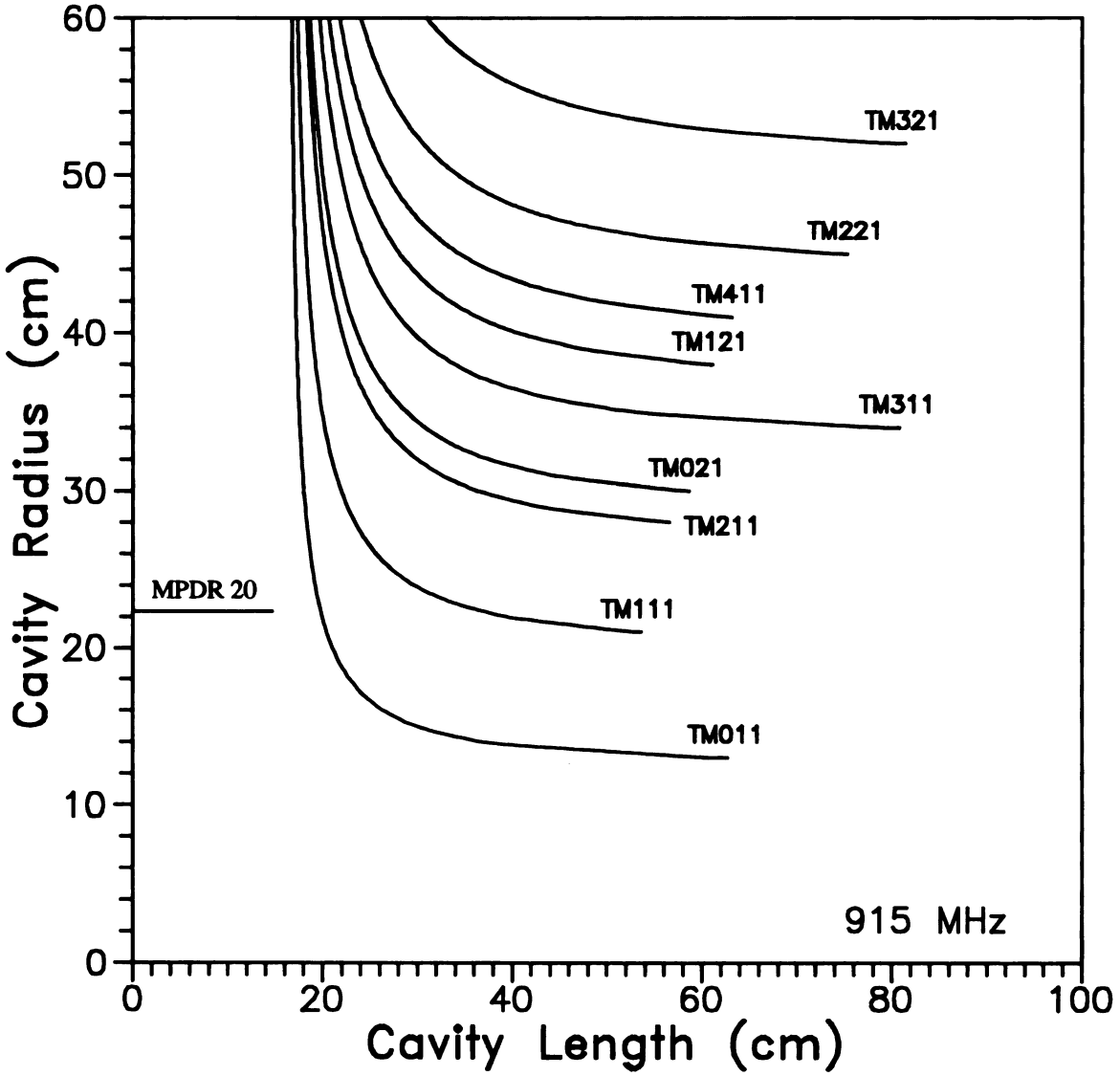

Figure 4.8 TM mode at 915 MHz

cavity. When the cavity diameter is large such as the MPDR 325, the resonant modes are close to each other. As a result, more than one resonant mode can be excited.

In general, orientation of the microwave excitation probe has to match with the electric field pattern of the mode which is excited. This can be explained by the electric field distribution in each mode diagram described below.

MODE DIAGRAM

Consider a cylindrical cavity with its axis on the z-axis. The electric field for the TE_{np} mode can then be obtained by following relations [66]:

$$E_r = -\frac{\partial \Psi}{r\,\partial \phi} \tag{4.5a}$$

$$E_\phi = \frac{\partial \Psi}{\partial r} \tag{4.5b}$$

$$E_z = 0 \tag{4.5c}$$

The magnetic field is perpendicular to the electric field with a non-zero z-component:

$$H_r = \frac{\partial^2 \Psi}{\partial r\,\partial z} \tag{4.6a}$$

$$H_\phi = \frac{\partial^2 \Psi}{\partial \phi \, \partial z} \tag{4.6b}$$

$$H_z = (x'_{np}/a)^2 \Psi \tag{4.6c}$$

For TM mode:

$$H_r = \frac{\partial \Psi}{r \, \partial \phi} \tag{4.7a}$$

$$H_\phi = -\frac{\partial \Psi}{\partial r} \tag{4.7b}$$

$$H_z = 0 \tag{4.7c}$$

$$E_r = \frac{\partial^2 \Psi}{\partial r \, \partial z} \tag{4.8a}$$

$$E_\phi = \frac{\partial^2 \Psi}{\partial \phi \, \partial z} \tag{4.8b}$$

$$E_z = (x_{np}/a)^2 \Psi \tag{4.8c}$$

Figure 4.9 to Figure 4.10 are the graphic displays of TM_{11} and TE_{01} resonant modes in a cylindrical cavity. Each figure consists of a two-dimensional plot of the electric field strength and the orientation of the

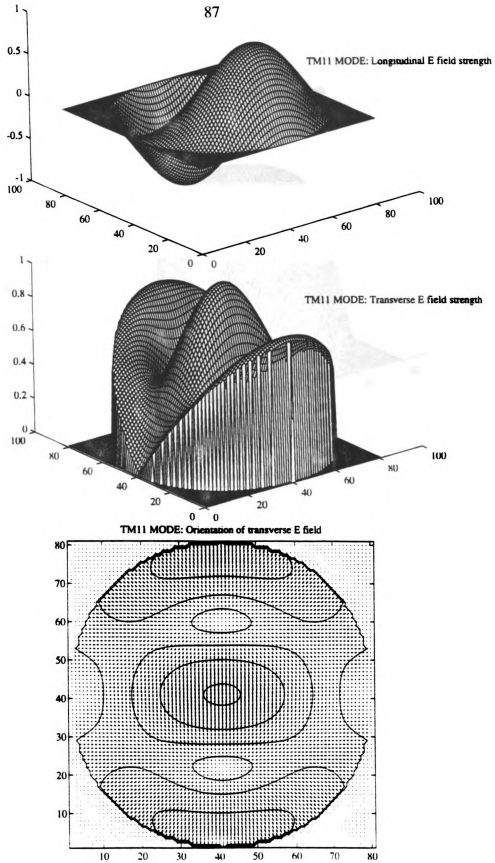

Figure 4.9 Distribution of E-field at TM_{11} mode

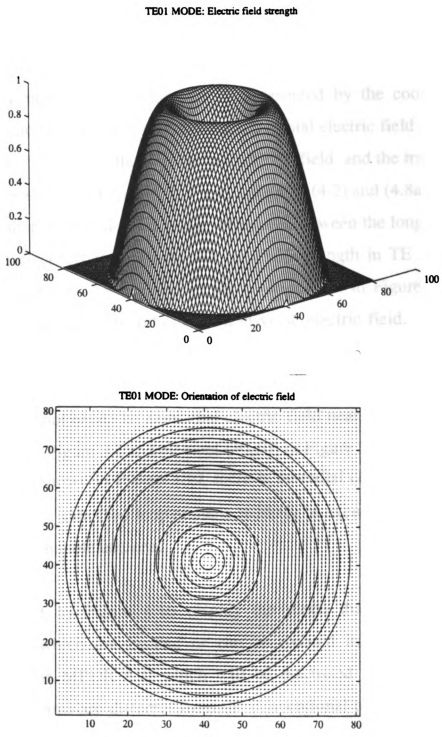

Figure 4.10 Distribution of E-field at TE_{01} mode

transverse electric field. A polar coordinate system is used even thought a square matrix is displayed. The numerical model uses 80 x 80 elements that gives sufficient resolution for the vector presentation. The radius of the cylindrical cavity is represented by 40 elements. The axis of the cylindrical cavity or the center of each polar plot is represented by the coordinates (41,41). It should be noted that in TM modes, the total electric field strength is not a direct vector sum of the longitudinal electric field and the transverse electric field as shown in Figure 4.9. From equations (4.2) and (4.8a-c), it is indicated that there is a 90 degrees phase difference between the longitudinal and transverse electric field. All the electric field strength in TE and TM modes are normalized. The quivers in the contour plots in Figures 4.9 to Figure 4.16 represent the direction of the transverse electric field. Because of using a side-feed antenna, TE_{12}, TE_{13} and TE_{01} modes are not likely to be excited in the MPDR. In the case of TE_{12} and TE_{13} modes, a side-feed probe antenna cannot excite an azimuthal electric field near to the wall (see element (40,15) in Figure 3.2 and element (40,10) in Figure 3.2). In the case of TE_{01} mode as shown in Figure 3.10, there is no radial component of the electric field, thus a side-feed loop antenna is likely to excite this mode, but not a side-feed monopole antenna.

Figure 4.11 to Figure 4.16 display the mode diagrams of those resonant modes which are excited or can be excited in MPDR plasma sources except the MPDR 610 which will be discussed in later section. These mode diagrams are different from the conventional plots in most text books which only indicate the orientation of the transverse electric field, but no information about the field strength.

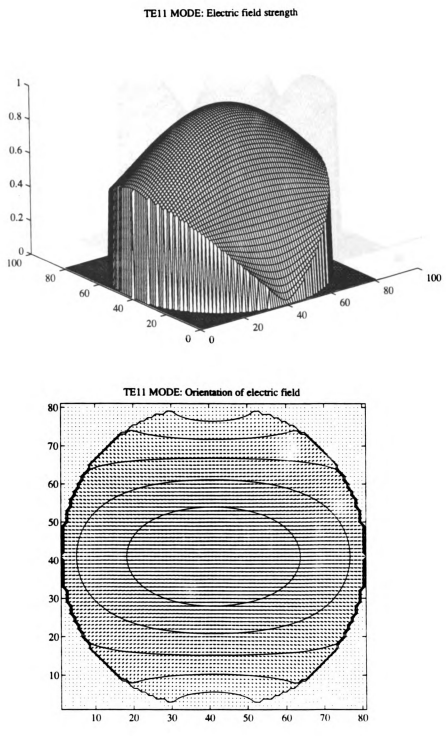

Figure 4.11 Distribution of E-field at TE_{11} mode

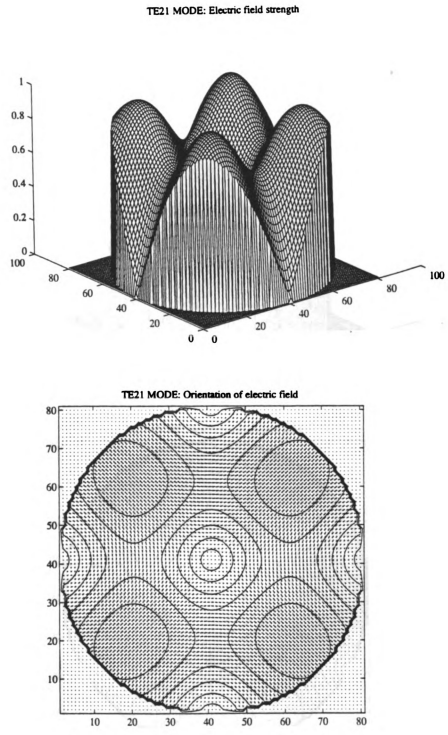

Figure 4.12 Distribution of E-field at TE_{21} mode

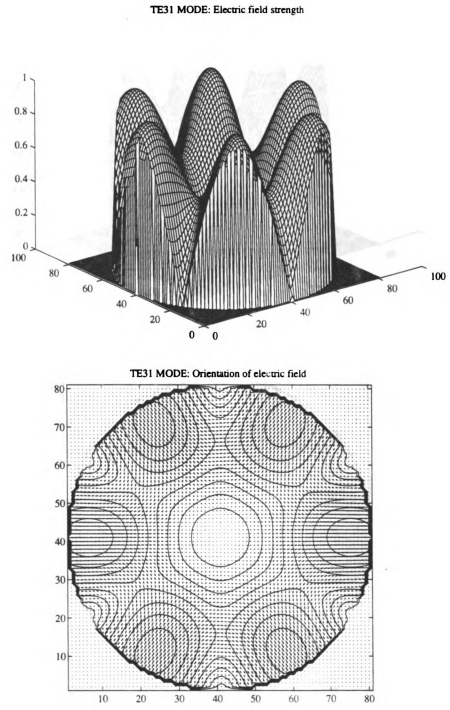

Figure 4.13 Distribution of E-field at TE_{31} mode

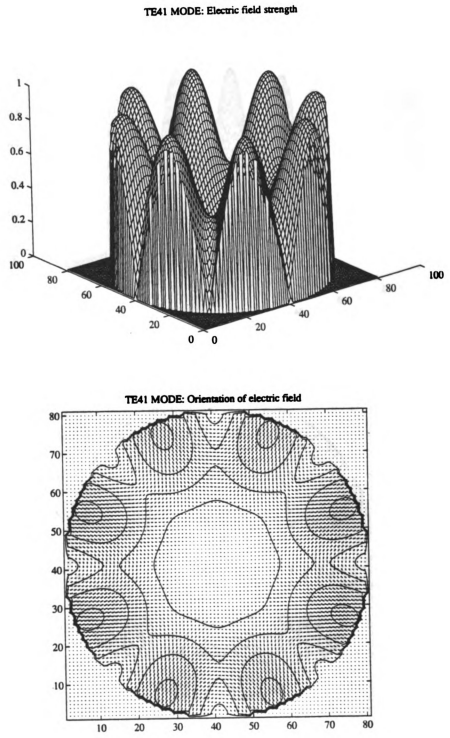

Figure 4.14 Distribution of E-field at TE_{41} mode

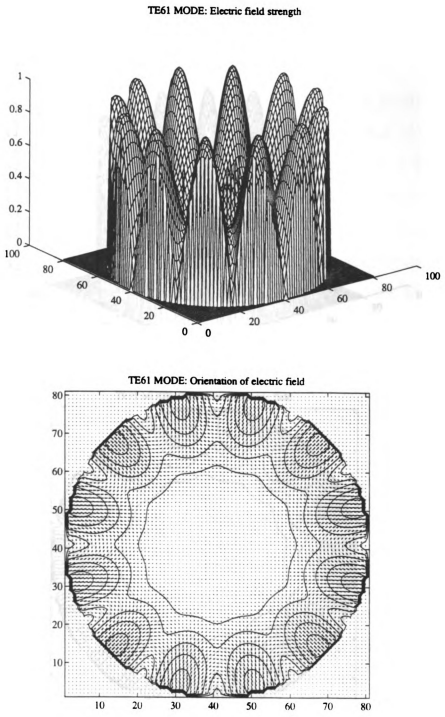

Figure 4.15 Distribution of E-field at TE_{61} mode

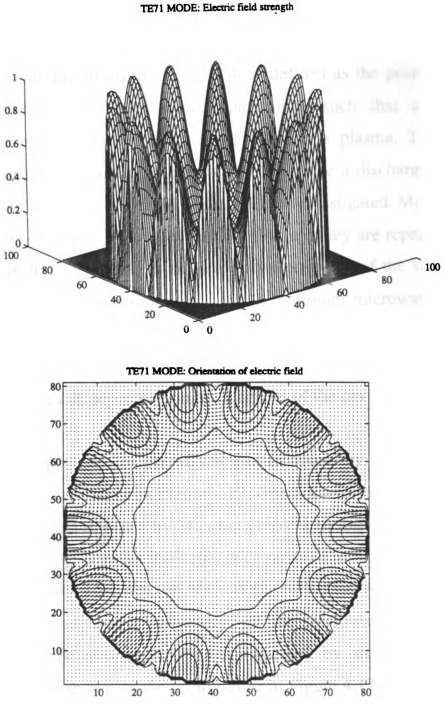

Figure 4.16 Distribution of E-field at TE_{71} mode

4.3.2 Ignition and tuned positions in MPDRs

Every MPDR has two degrees of freedom in tuning. The input microwave probe and the sliding short allow tuning and tracking of an operation mode. The **starting position** of a MPDR is defined as the positions of the sliding short and the microwave input probe such that a minimum microwave reflected power is observed *without* a plasma. The **ignition positions** are those **starting positions** that can ignite a discharge. It should be noted that no grid was used in all the MPDRs investigated. More than one ignition position may be found in each MPDR and they are repeatable. The **tuned position** of a MPDR is defined as the positions of the sliding short and the microwave input probe such that a minimum microwave reflected power is observed *with* a discharge. Each starting position, ignition position or tuned position represents either a single resonant mode or several resonant modes in the MPDR depending on the diameter of the cavity.

Starting positions of the MPDR can be found by using a frequency sweeping circuit as shown in Figure 4.17. Operation of the sweeping circuit has been described in detail by Manring [166], therefore not repeated here. In brief, the MPDR is swept through a wide range of microwave frequencies. When the resonant frequency of the cavity, such as f_0=2.45GHz, matches with the input microwave frequency, all the microwave energy at that frequency will be absorbed. This is indicated by an "inverted" power absorption curve shown on the oscilloscope in Figure 4.17. By adjusting the positions of the sliding short and the microwave input probe, the sweeping circuit can determine all the starting positions in each MPDR.

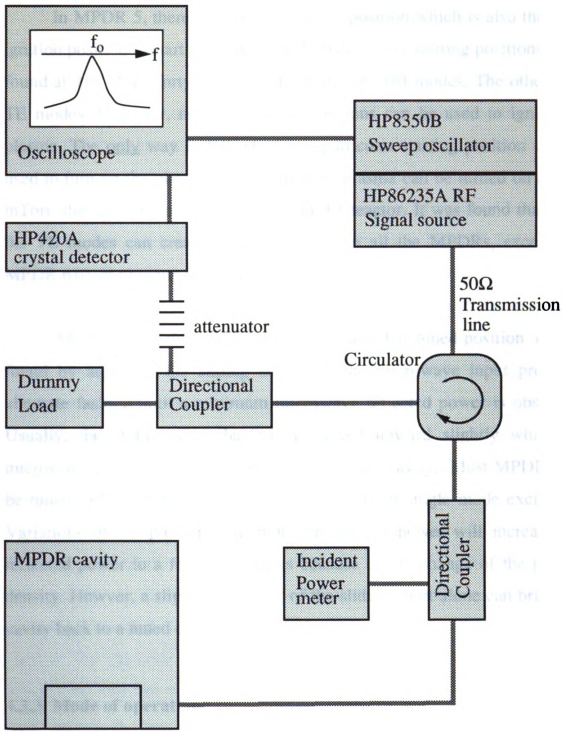

Figure 4.17 Schematic setup of sweeping circuit

In

ignition p

found at

TE mode

plasma. T

used to tu

mTorr, th

the TE m

MPDR 61

Afte

found by

alternate f

Usually, t

microwave

be tuned t

Variations

reflected p

density. H

cavity back

4.3.3 Mod

The

explained H

modes of op

In MPDR 5, there is only one starting position which is also the only ignition position to start the plasma. In MPDR 20, six starting positions were found at 915 MHz, forty at 2.45 GHz. Some are TM modes. The others are TE modes. However, not all of these positions can be used to ignite the plasma. The only way to tell whether a particular starting position can be used to turn on the plasma is to try it. If no plasma can be turned on at 100 mTorr, the starting position is useless in the reactor. It was found that only the TE modes can create a stable plasma in all the MPDRs, except the MPDR 610, at pressure below 100 mTorr.

After ignition, the resonant position shifts. The tuned position can be found by adjusting the sliding short and the microwave input probe in alternate fashion until a minimum microwave reflected power is observed. Usually, the sliding short has to be moved upward slightly while the microwave excitation probe is moved towards the cavity. Most MPDRs can be tuned to less than 1% reflected power while in single mode excitation. Variations of the pressure and input microwave power will increase the reflected power to a few percentages because of the change of the plasma density. Howver, a slight adjustment of the sliding short alone can bring the cavity back to a tuned condition.

4.3.3 Mode of operation

The mode of operation of each MPDR plasma source can best be explained by using mode charts as shown in Figure 4.5 to Figure 4.8. The modes of operation in different diameters of MPDR are discussed separately.

MPDR

M

MPDR

Figure

Figure

that allo

radius fo

radius fo

cavity di

cavity re

and mag

has been

MPDR 5

All

probe ante

to be exci

excited. T

This mean

order mod

reactor wa

Table 4.1.

from the fi

has to be

MPDR 610

MPDR 610 is different from the rest of the plasma source in the MPDR family in two aspects. First, it uses an end-feed antenna as shown in Figure 4.3. Second, its radius is less than the cutoff radius as shown in Figure 4.5. The cutoff radius is the smallest radius of a cylindrical cavity that allows a resonant mode to be excited. As shown in Figure 4.5, the cutoff radius for TE mode at 2.45 GHz is about 3 cm. In Figure 4.6, the cutoff radius for TM mode at 2.45 GHz is about 4.5 cm. The MPDR 610 has a cavity diameter of 5 cm. Therefore it is not possible to excite a cylindrical cavity resonant mode. Instead a TEM mode, whose time-varying electric and magnetic fields are perpendicular to the cylindrical axis, is excited and has been reported earlier by Asmussen et al. [40].

MPDR 5

All MPDR plasma sources, except the MPDR 610, use a side-feed probe antenna similar to that shown in Figure 4.1. TE modes are more likely to be excited with this kind of configuration although TM modes can also be excited. The diameter of the cylindrical cavity of the MPDR 5 is 8.9 cm. This means that this reactor can only be operated at TE_{111} mode or its high order modes as shown in Figure 4.5. This was the original idea when the reactor was designed [61]. The ignition position of the source is shown in Table 4.1. The initial position of the sliding short is about two centimeters from the final tuned position. Once the plasma is turned on, the sliding short has to be moved up to keep the cavity in a resonant mode so that all

TABLE 4.1 OPERATION POSITIONS OF MPDR 5 WITHOUT A GRID

Experimental conditions:

Gas: Argon
Flow: 50.2 sccm
Pressure: 1.5 mTorr
Power: 100 watts

	Cavity Height (cm): Ls	Probe Length (cm): Lp
Theoretical position[1]	10.5	-
Ignition	8.6	1.1
Tuned position[2]	10.6	1.8

[1] For a perfect empty cylindrical cavity

[2] In MPDR with plasma

microwave energy is coupled into the plasma. Compared with previous report by Leonard Mahoney who attached a grid to the baseplate for his ion beam experiments [61], the main differences are the initial and final positions of the microwave input probe.

MPDR 9 and MPDR 13

The diameter of the cylindrical cavity in MPDR 9 and MPDR 13 is 17.8 cm. Figure 4.5 and Figure 4.6 indicate that four single TE modes, TE_{111}, TE_{211}, TE_{011} and TE_{311}, and two TM modes, TM_{011} and TM_{111}, can be excited in these cavities with 2.45 GHz microwave energy. The TE_{211} mode is used in most of the ECR applications and diagnostics in these two plasma sources. The change of the size of the quartz disk did not have major influence on the excitation modes. The choice of which mode to be used was based on the uniformity, stability and density of the plasma. The difference in performance in the MPDR versus mode excitation is under investigation by Mak [47].

MPDR 20

MPDR 20 was designed to be excited with 915 MHz microwave energy. The cavity has a diameter of 45.7 cm. At 915 MHz, the resonant modes are wider apart as shown in Figure 4.7 and Figure 4.8. Six possible resonant modes were detected in this reactor by using the frequency sweeping circuit. They are listed in Table 4.2. Two modes have been used to create a discharge in this reactor. The first one is the TE_{111}. The other is the TE_{211} mode which was used in most of the diagnostics experiments. TE_{112},

TABLE 4.2 RESONANT MODES IN EMPTY MPDR 20

Cavity Height[2] (Ls)	Probe Length (Lp)	Theoretical Height[1]	Mode
18.78 cm	3.90 cm	18.06 cm	TE_{111}
20.34 cm	4.35 cm	19.61 cm	TM_{011}
23.54 cm	3.44 cm	22.86 cm	TE_{211}
34.24 cm	5.67 cm	33.82 cm	TM_{111}
36.79 cm	3.66 cm	36.13 cm	TE_{112}
39.89 cm	4.09 cm	39.22 cm	TM_{012}

[1] For a perfect empty cylindrical cavity

[2] In MPDR without plasma

which has similar field distribution as the TE_{111}, was not used. The other modes, TM_{011}, TM_{111} and TM_{012}, could not ignite the plasma.

Verification of the mode was done by direct measurement of the electric field pattern along the cavity wall with a 2 mm diameter microcoaxial probe [33] shown in Figure 5.2. The theoretical distribution of electric field of TE_{npq} mode on the cavity wall is given by the equation:

$$E_r(r,\phi,z) = (n/r)E_o J_n(x'_{np}r/a)[b\cos(n\phi) + c\sin(n\phi)]\sin(q\pi z/d) \qquad (4.9)$$

where J_n is the Bessel function of order n, x'_{np} is the p^{th} zero of J'_n, **a** is the radius of the cavity and **d** is the cavity length. Figure 4.18 and Figure 4.19 show the experimental data and the theoretical distributions of the electric field strength in TE_{111} and TE_{211} respectively. As shown in the figures, the experimental results match very well with the theoretical distribution although there are some deviations of the electric field strength near the peak, which are caused by the variations of the inserted length of the micro-coaxial probe inside the cavity.

Table 4.3 and 4.4 shows the operation positions at these two modes. The tuned position of the sliding short with the presence of a discharge is very close to the theoretical value for a perfect empty cylindrical cavity at TE_{211} mode. A slightly bigger deviation between the theoretical cavity length and the height of the sliding short at tuned condition was found in the TE_{111} mode. This is because the distortion caused by the dome shaped plasma becomes significant.

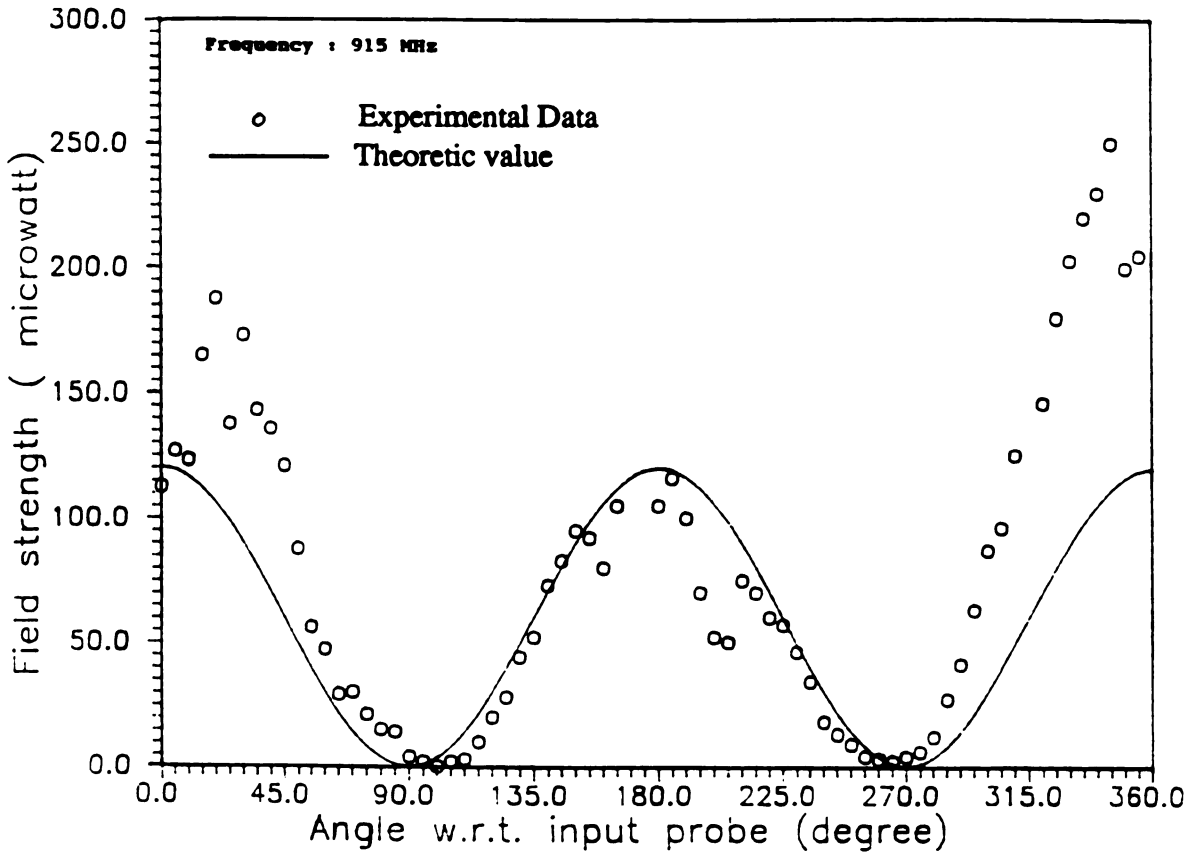

Figure 4.18 Experimental measurement of E-field at TE_{111} mode

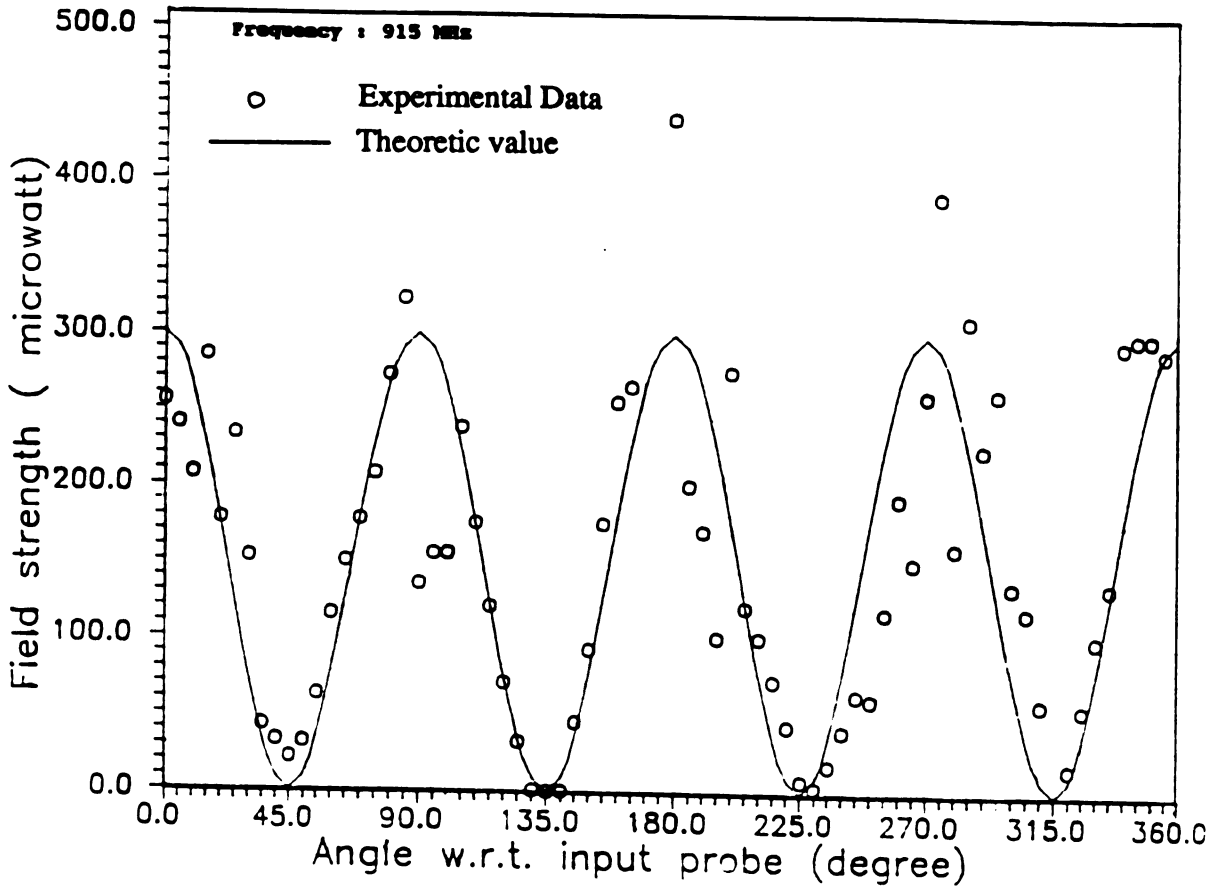

Figure 4.19 Experimental measurement of E-field at TE_{211} mode

TABL

Experimental	
Gas:	
Flow:	
Pressure:	
Power:	
Theoretical po	
Ignition	
Tuned position	

[1] For a perfect

[2] In MPDR wi

TABLE 4.3 OPERATION POSITIONS OF MPDR 20 AT TE_{211} MODE

Experimental conditions:

Gas: Argon
Flow: 30.4 sccm
Pressure: 0.8 mTorr
Power: 200 watts

	Cavity Height (cm): Ls	Probe Length (cm): Lp
Theoretical position[1]	22.86	-
Ignition	22.6	5.3
Tuned position[2]	22.8	9.5

[1] For a perfect empty cylindrical cavity

[2] In MPDR with plasma

TABLE 4.4 OPERATION POSITIONS OF MPDR 20 AT TE_{111} MODE

Experimental conditions:

Gas: Argon
Flow: 25.7 sccm
Pressure: 0.6 mTorr
Power: 200 watts

	Cavity Height (cm): Ls	Probe Length (cm): Lp
Theoretical position[1]	18.06	-
Ignition	18.8	5.8
Tuned position[2]	18.95	9.9

[1] For a perfect empty cylindrical cavity

[2] In MPDR with plasma

A

from th

17.78 c

is well

Figure

about 6

and ign

strength

electric

is discu

pressure

The igni

as shown

M

resonant

From Fig

cavity le

TE_{313} an

experimen

more than

tuned to a

power. In

input of 5

MPDR 325

A large diameter reactor at 2.45 GHz has some difference properties from those reactors with small radii. The MPDR 325 has a cavity radius of 17.78 cm. The inner diameter of the plasma disk is 24 cm in diameter which is well above the cutoff radii of many modes as shown in Figure 4.5 and Figure 4.6. For example, at 2.45 GHz, the cutoff radius of TE_{211} mode is about 6 cm. Microwave energy thus propagates through the quartz vessel and ignites the plasma. Once a plasma is formed, the microwave field strength will decay as it moves through the discharge. The decay of the electric field in the plasma depends on the conductivity of the plasma, which is discussed in Chapter Two. In MPDR 325, plasma can be started at pressure as low as 1.5 mTorr. This makes the reactor very easy to operate. The ignition position and the final tuned position are very close to each other as shown in Table 4.5. Therefore only a small adjustment is needed.

MPDR 325 is operated in a controlled multimode [42] in which resonant modes are close to each other for a cavity radius of 17.78 cm. From Figure 4.5, four TE resonant modes, which are close to the tuned cavity length shown in Table 4.5, can be identified. They are TE_{131}, TE_{711}, TE_{313} and TE_{612}. For TM modes, TM_{031} and TM_{221} are close to the experimental positions (see Figure 4.6). In controlled multimode mode, more than one resonant mode are excited. However, the MPDR can still be tuned to a position such that the plasma is stable and has minimum reflected power. In MPDR 325, typical reflected power is less than 7 watts for an input of 500 watts microwave energy at 0.6 mTorr argon plasma.

Experimental

Gas:
Flow:
Pressure:
Power:

Theoretical po

Ignition

Tuned position

[1] For a perfect

[2] In MPDR wit

TABLE 4.5 OPERATION POSITIONS OF MPDR 325

Experimental conditions:

Gas:	Argon
Flow:	20 sccm
Pressure:	0.6 mTorr
Power:	500 watts

	Cavity Height (cm): Ls	Probe Length (cm): Lp
Theoretical position[1]	-	-
Ignition	21.5	1.5
Tuned position[2]	21.1	1.4

[1] For a perfect empty cylindrical cavity

[2] In MPDR with plasma

4.3.4 C

I

magnitu

static m

static m

of the t

This is

transver

Fo

configur

center ar

creates th

pole mag

configura

configura

Th

excitation

maximum

ECR surf

MPDR g

magnets

any two

somewhe

broken E

4.3.4 Optimal magnetic configuration

If the energy coupling efficiency is directly proportional to the magnitude of the cross product of the microwave electric field, **E**(t), and the static magnetic field, **B**, created by the permanent magnets, then the optimal static magnetic configuration will be the one which has the same distribution of the transverse H-field of the microwave in the excited resonant mode. This is because the transverse H-field is always perpendicular to the transverse E-field in each resonant mode.

For example, if TE_{111} mode is being excited, the optimal magnetic configuration will be a dipole magnetic field which has a maximum at the center and runs perpendicular to the E-field as shown in Figure 4.11. This creates the maximum value of $\mathbf{E}(t) \times \mathbf{B}$. If TE_{211} mode is excited, then a 4-pole magnetic configuration should be used. Similarly, the optimal magnetic configuration for a TE_{n1} mode excitation would be a 2n-cusp magnetic configuration.

The MPDR plasma source is intrinsically ideal for TE_{n1} mode excitation where n can be any non-zero integer. This assumption for maximum efficient energy coupling holds as long as there is a continuous ECR surface within the plasma disk. For illustration, TE_{211} mode is used in MPDR 9. A 4-pole magnetic configuration should be used. If only four magnets are used to form the four magnetic cusps, then the distance between any two neighboring magnets is too far apart. The ECR surface is broken somewhere in between the two magnets as shown in Figure 4.20. This broken ECR surface, if used, creates an unstable plasma. Jeff Hopwood

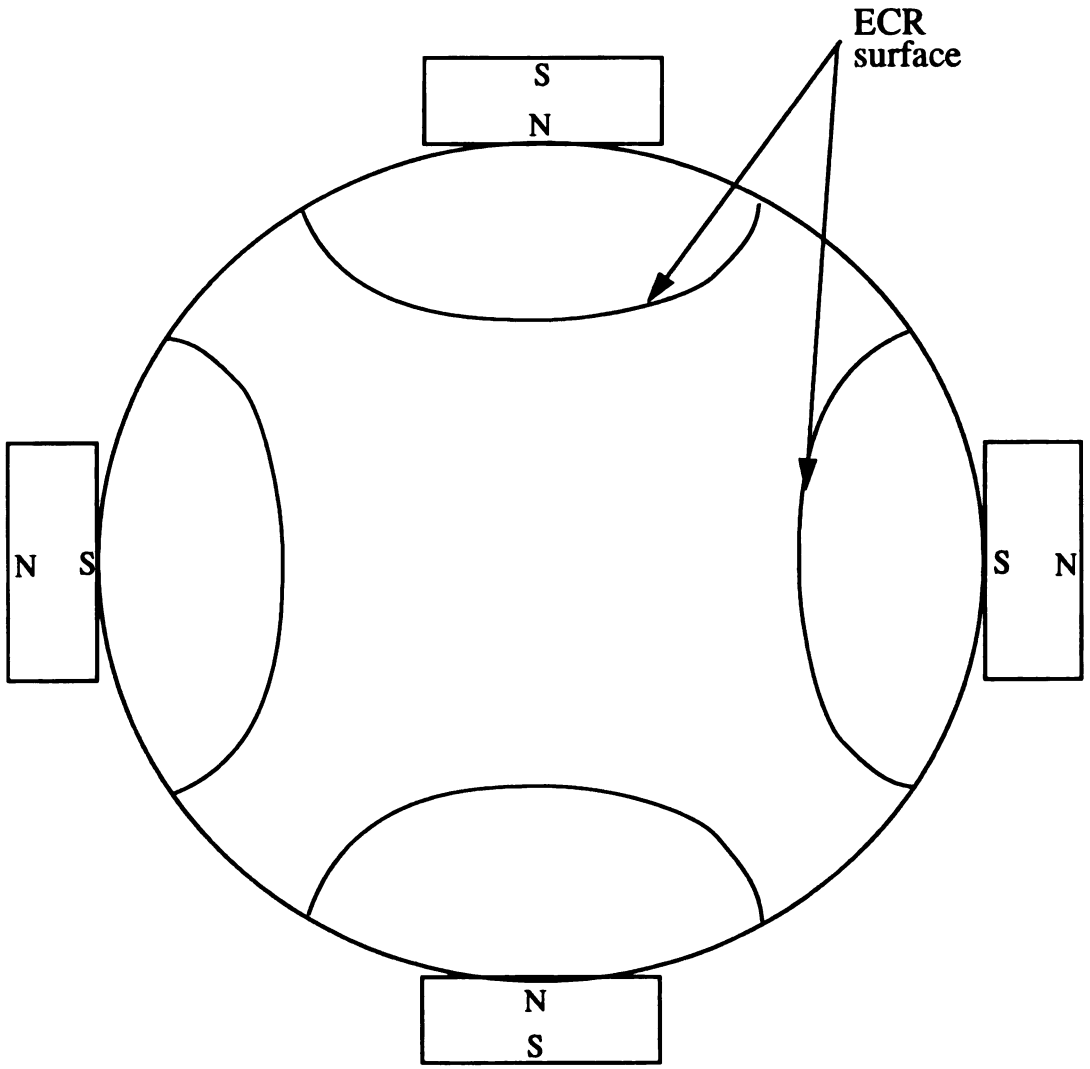

Figure 4.20 Distribution of ECR surface using 4 magnets in MPDR 13

Figu

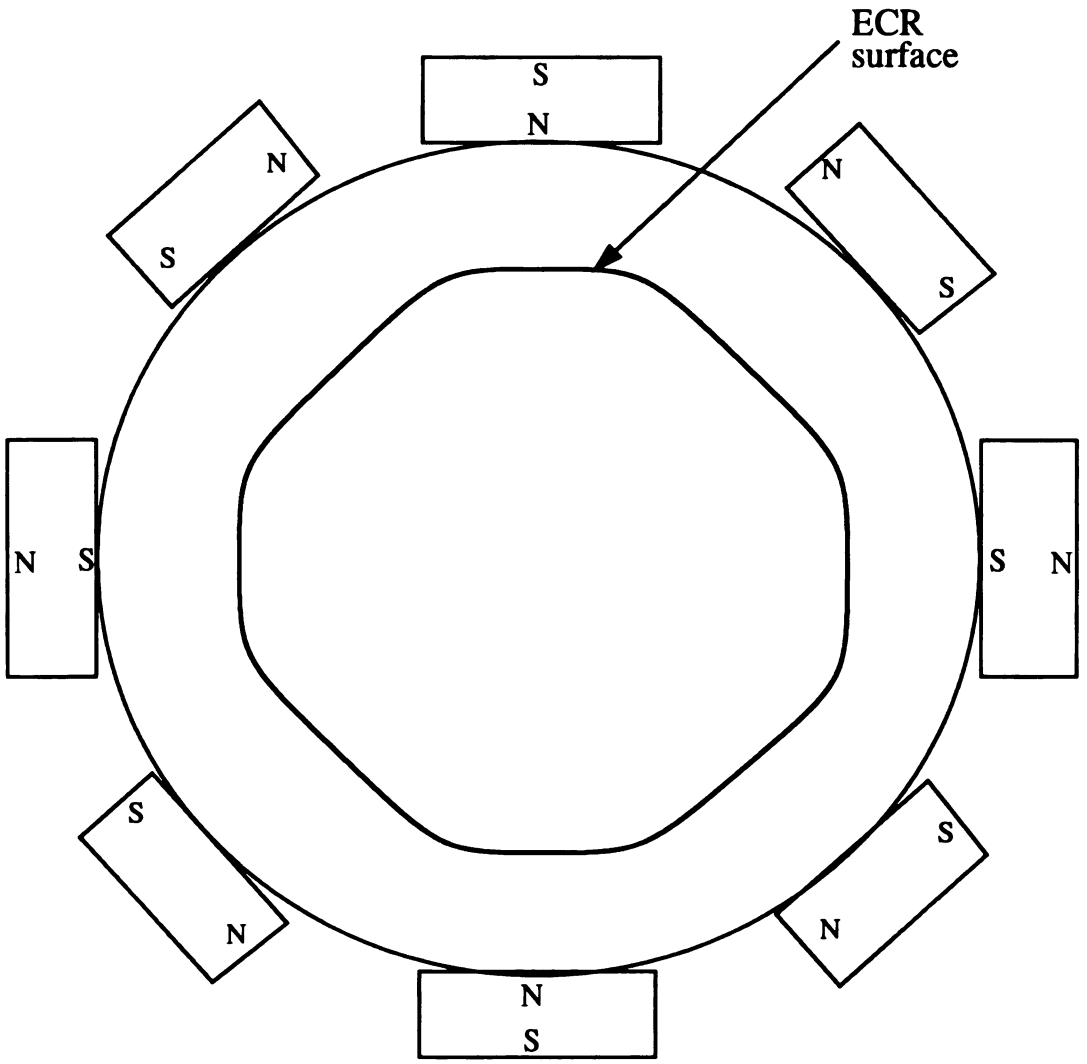

Figure 4.21 Tetrapole magnetic configuration using 8 magnets

indicated in his thesis that an octapole magnetic configuration should be used to keep a stable plasma in MPDR 9 using TE_{211} mode. However, a better solution has been proposed by Mak [47] in his 4-pole/8-magnet configuration. Figure 4.21 illustrates the formation of a tetra-pole magnetic configuration using eight magnets. By using two different sets of magnets, a continuous ECR surface is created. This technique is useful to maintain an unbroken ECR surface inside a large diameter plasma disk such that the number of static magnetic pole matches with the electric field pattern of the resonant mode.

CHAPTER FIVE

DIAGNOSTICS OF MPDR

§ 5.1 INTRODUCTION

Characterization of three MPDRs is the main topic in this chapter. They are the MPDR 5, MPDR 20 and MPDR 325. The MPDR 9 has been studied by Jeff Hopwood in his graduate research and MPDR 13 is currently under the investigation by Mak and King [46,47] while the MPDR 610 is the subject of Aseem Srivastava's thesis research [48,165]. Although MPDR 5 was studied by L. Mahoney, yet the source has not been characterized without using a grid. It is included in this dissertation because it has some properties that have not been observed in other MPDRs.

The MPDR 5 and MPDR 325 were characterized at 2.45 GHz microwave energy while the MPDR 20 was characterized at 915 MHz microwave energy. A schematic diagram of the microwave circuit for the characterization is shown in Figure 5.1. The diagram shows the essential elements for the operation of a MPDR. Microwave input power to the MPDR was monitored by the incident and reflected power meters. In the cases of characterizing MPDR 5 and MPDR 20, 50 Ω coaxial cables were used to connect the components together. However, experiments carried out with the MPDR 325 used rectangular waveguides instead of coaxial cables.

Figure 5.2 shows the experimental setup of the MPDR 325 in a vacuum system for plasma diagnostic experiments. A similar experimental setup was used for the MPDR 5 and MPDR 20. A downstream plasma confinement structure, which has been described in Chapter Four, was mounted below each reactor as shown in Figure 5.2. Because MPDR 5 has a smaller diameter than the confinement structure, downstream confinement

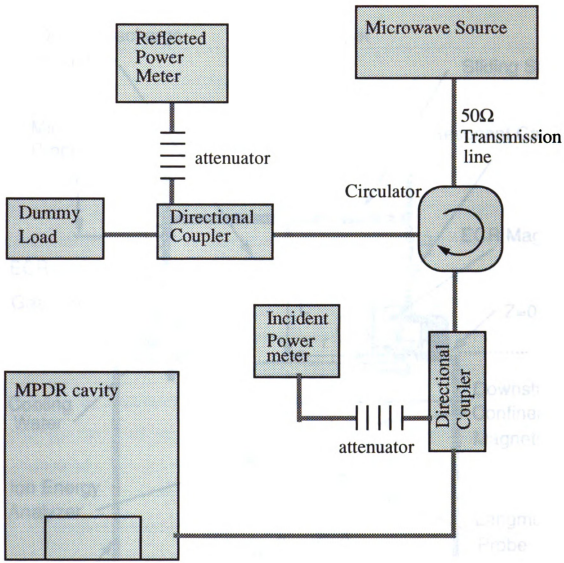

Figure 5.1 Schematic diagram of microwave circuit

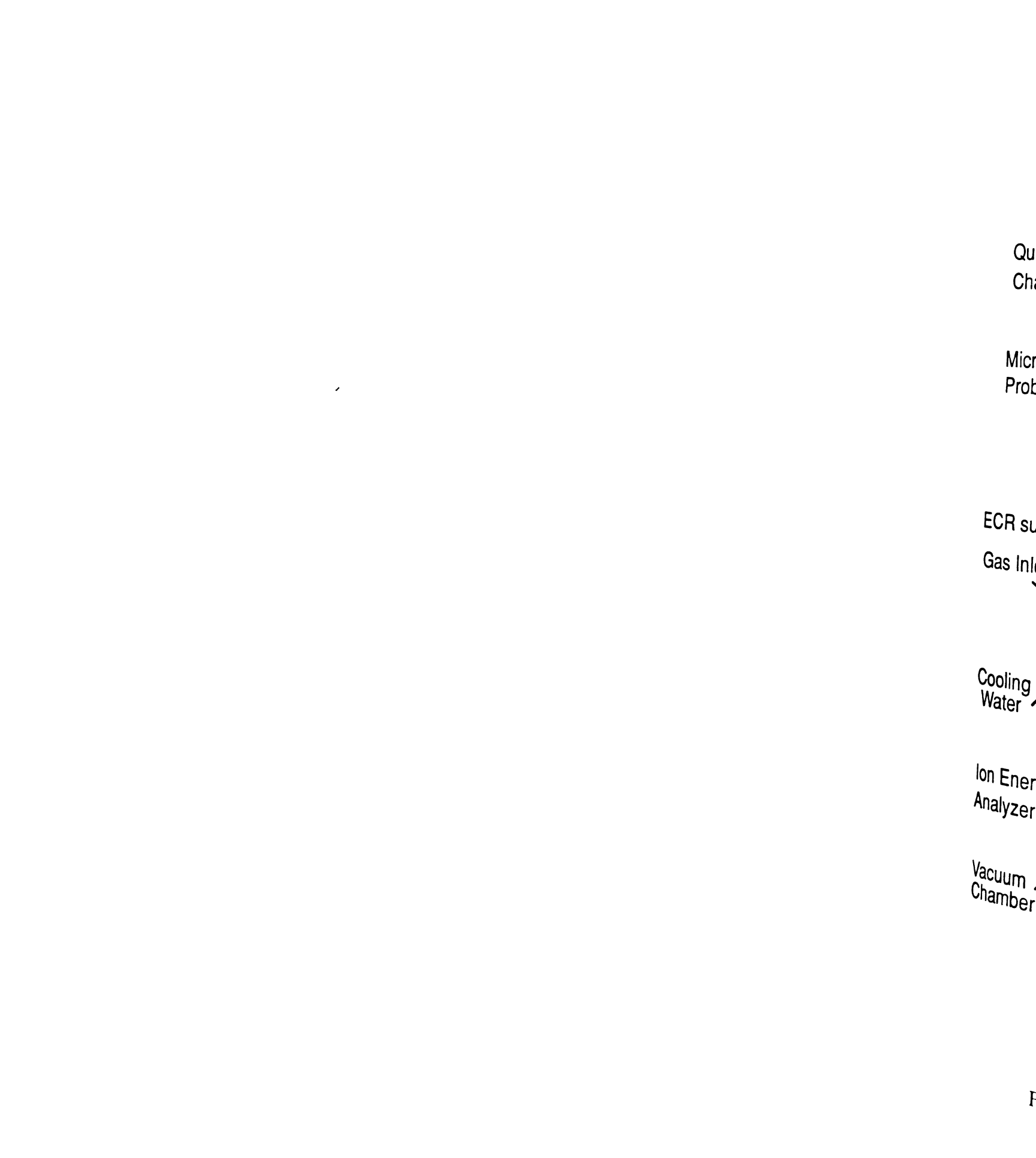
Qu
Cha
Micr
Prob
ECR su
Gas Inl
Cooling
Water
Ion Ener
Analyzer
Vacuum
Chamber

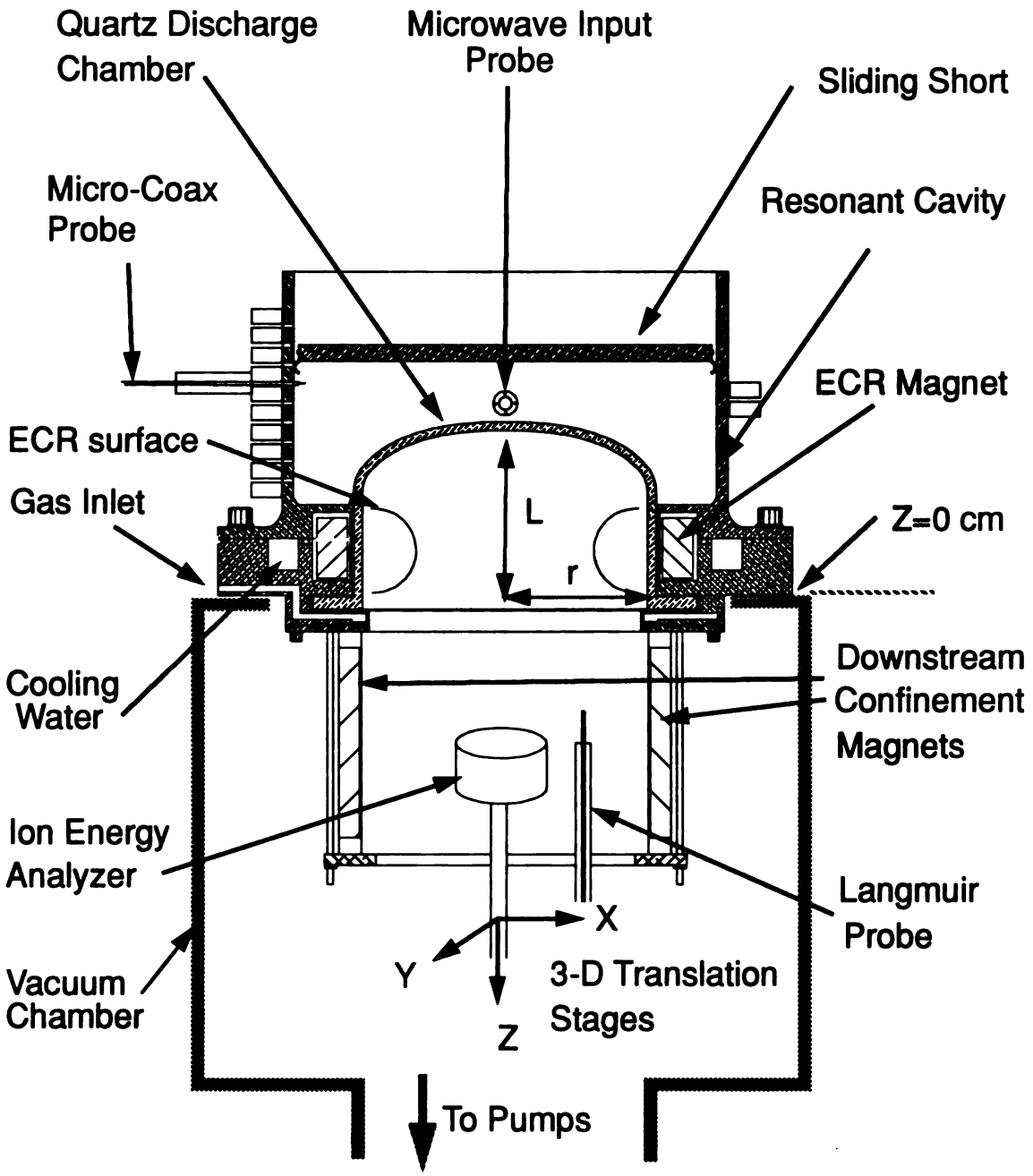

Figure 5.2 Experimental setup for plasma diagnostics

magnets
MPDR
defined a

Pla
analyzer
the meas
function
plasma de
by a mult
Langmuir
help of th
probe was
measureme
measureme
chapter. B
near to th
determined.

§ 5.2 Expe

5.2.1 Doub

Double
Malter [56].
density in a d
were made wi

magnets were mounted underneath a stainless steel plate on which the MPDR 5 was placed. The bottom of the baseplate in each MPDR was defined as the zero downstream position, Z=0, as shown in the figure.

Plasma diagnostic tools used included Langmuir probes, an ion energy analyzer and a micro-coaxial probe. A single Langmuir probe was used for the measurements of plasma potential and electron energy distribution function (EEDF) while double Langmuir probes were used to measure plasma density. The ion energy distribution function (IEDF) was measured by a multi-grid ion energy analyzer. Both the ion energy analyzer and the Langmuir probe could be moved at different downstream locations with the help of three remotely controlled translation stages. The micro-coaxial probe was a 50 Ω 2-mm diameter coaxial cable. It was used both for the measurement of electric field strength inside the resonant cavity and the measurement of microwave coupling efficiency, which is described in next chapter. By measuring the circumferential and axial electric field strength near to the wall inside the cavity, the mode of excitation could be determined.

§ 5.2 Experimental techniques

5.2.1 Double Langmuir probes

Double Langmuir probes technique was first proposed by Johnson and Malter [56]. This technique has widely been used to measure the plasma density in a discharge because of its simple structure. The two probes used were made with a 0.9 mm diameter tungsten wire. Part of the wire, 8 mm in

length.
glass tu
shows
characte
the prob
Digital)
current
There w
did not f
when the

Fi
measurer
two regio
figure, a
surface a
variation
curve sho
is that w
probes.
unevenly
left or to
conductiv

Figu
measureme
surface at

length, was exposed to the plasma. The rest of the wire was sealed inside a glass tube. The distance between the two probes was 6 mm. Figure 5.3(a) shows the circuit diagram for the measurement of current-voltage characteristics. Both the current through the probes and the voltage across the probes were sampled and taken by a computer through A/D (Analog to Digital) converters as shown in the figure. As shown in the figure, the current sampled by the computer was the total current flow in the circuit. There was current loss in the parallel resistor and the voltmeter. This current did not flow through the probes. It was deducted by the computer at the time when the I-V data was taken.

Figure 5.3 (b) shows an actual current-voltage plot of a double-probe measurement taken in one of the MPDRs. The curve can be distinguished by two regions. A nearly linear region, which is indicated by segment OA in the figure, and a saturated region, which is indicated by segment AB. If the surface areas of the two probes are made the same and if there is no spatial variation of the plasma potential around the two probes, a symmetric I-V curve should be obtained as the one shown in Figure 5.3(b). What it means is that when V_d is zero, there is no net current flowing between the two probes. The I-V curve should pass through the origin. If the probes are unevenly coated with an insulated layer, the I-V curve will shift either to the left or to the right. If the probes are shorted due to the deposition of conductive film, a nearly straight I-V curve will be observed.

Figure 5.4 is an illustration of the I-V characteristics in double probes measurements. When V_d is zero, both electrons and ions reached the probe surface at the same rate. When V_d is equal to a small negative voltage, the

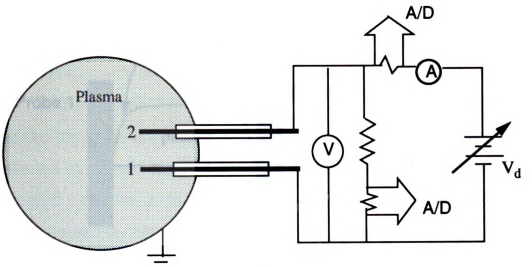

(a)

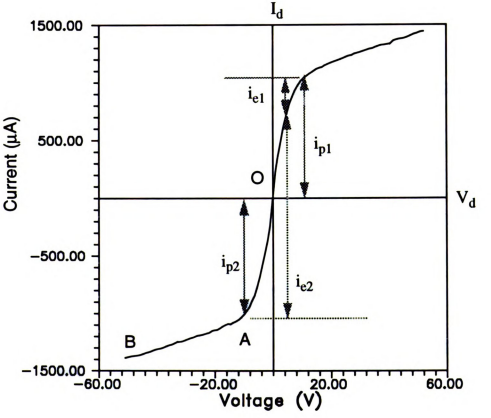

(b)

Figure 5.3 Double Langmuir probes technique: (a) schematic circuit and (b) I-V characteristics

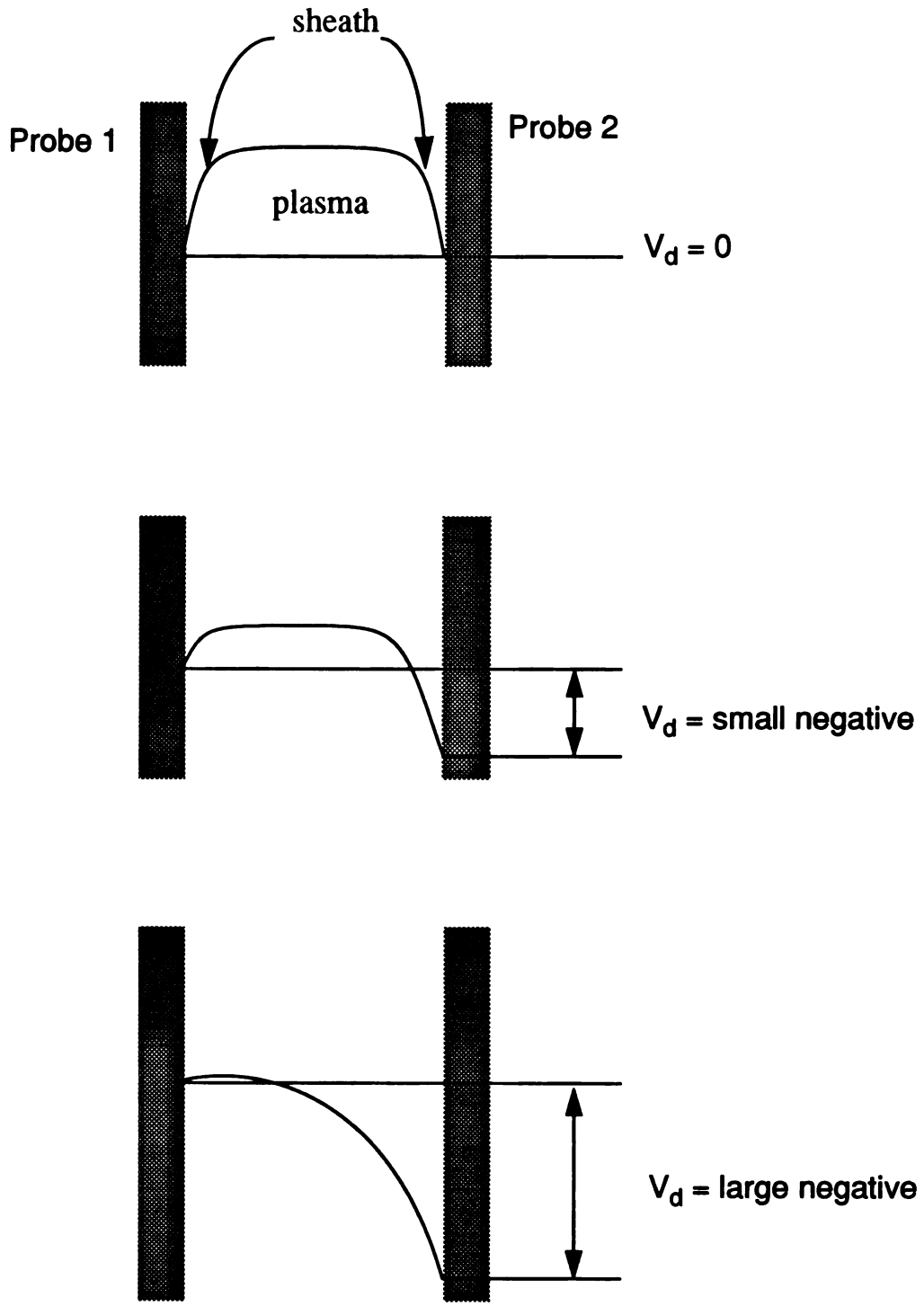

Figure 5.4 Variation of sheath potential with applied voltage

potential of probe 1 is raised. More electrons are collected in probe 1 because of the decrease in sheath potential between probe 1 and the plasma. A negative current flows through the external circuit to neutralize some the ions collected by probe 2. When V_d equals to the space potential of the plasma, the electrons collected by probe 1 are nearly the sum of the ions collected by probe 1 and probe 2. Probe 2 is at a state of saturation and is indicated by point A in Figure 5.3 (b). Further decrease of the applied voltage causes an expansion of the sheath between probe 2 and the plasma, which explains why segment AB is not flat. The knee point, such as point A, is the most critical point in double probe analysis to obtain the correct saturation current.

The ion density, n_i, is related to the ion saturation current, i_p, according to following equation [55]:

$$n_i = (5/3eA_p)\, i_p\, (M_i / k_b T_e)^{1/2} \qquad (5.1)$$

where A_p is the probe area, M_i is the mass of the ions, k_b is the Boltzmann constant, e is the electron charge and T_e is the electron temperature.

In order to find the electron temperature, two assumptions are made. First, the total ion current collected by the two probes is independent of the applied external circuit. Second, a Maxwellian distribution of electron energy is assumed. Let i_e and i_p be the electron current and ion current collected by each probe. According to Kirchhoff's law of current, following relation is established:

Let V
potent

The el
potenti

where
current
have:

=
=

Therefor
voltage v

Al
which bo
good for

$$i_{p1} - i_{e1} = i_{e2} - i_{p2} \tag{5.2}$$

$$\Rightarrow \quad I_p = i_{p1} + i_{p2} = i_{e1} + i_{e2} = \text{constant} \tag{5.3}$$

Let V_{probe} be the potential of each probe with respect to the plasma potential. Then the applied voltage, V_d would be:

$$V_d = V_{probe1} - V_{probe2} \tag{5.4}$$

The electron current reaching the probe is governed by the retardation potential of the sheath [55]:

$$i_{e1} = I_{eo1}\exp(-eV_{probe1}/k_bT_e) \tag{5.5}$$

where i_{e1} is the electron current collected by probe 1, I_{eo} is the electron current when V_{probe1} is zero. Therefore using equations (5.4) and (5.5), we have:

$$(i_{e1}/i_{e2}) = (A_1/A_2)\exp(-eV_d/k_bT_e) \tag{5.6}$$

$$\Rightarrow \quad (I_p/i_{e2} - 1) = (A_1/A_2)\exp(-eV_d/k_bT_e) \tag{5.7}$$

$$\Rightarrow \quad \ln(I_p/i_{e2} - 1) = \ln(A_1/A_2) - eV_d/k_bT_e \tag{5.8}$$

Therefore the slope of a semi-logarithmic plot of $(I_p/i_{e2} - 1)$ versus applied voltage V_d can be used to find the electron temperature.

All plasma density measurements were carried out in argon plasma in which both the charge and mass of the ions were known. The analysis is not good for gas with large molecular structure in which different charged

species
quite di
microwa
concentr
density
and the
optical
inside th

5.2.2 S

measur
functio
taken b

where
to V_p-
electro
defined
derivati

current

species may exist. This is because the composition of the discharge can be quite different at different operation conditions such as pressure and microwave power. For example, in an oxygen plasma, the O^+ and O_2^+ concentrations vary with operation conditions [28]. In this case, the plasma density should fall between two values, one assuming that all the ions are O^+ and the other assuming that all the ions are O_2^+. A better way is to use optical methods to measure the concentrations of different charged species inside the plasma [167,168].

5.2.2 Single Langmuir probe

Plasma potential and electron energy distribution function can be measured by a single Langmuir probe. The electron energy distribution function, f(E), is related to the second derivative of the I-V characteristics taken by a single Langmuir probe [57-60]:

$$f(E) \propto (V_p - V)^{1/2} \frac{d^2 I}{dV^2} \qquad (5.9)$$

where V_p is the plasma potential, I is the current through the probe, E equals to V_p-V, and V is the applied d.c. voltage. Once f(E) is found, the average electron energy can be determined numerically. The plasma potential is defined as the voltage which gives the maximum value of the second derivative of the current with respect to the voltage [59].

There are two possible methods to find the second derivative of the current with respect to the voltage. One method is to take the I-V data using

a single

twice to

accuracy

attempt

the smal

techniqu

Th

with resp

across a

Th

applied v

where V

expanding

a single Langmuir probe and then a numerical differentiation is carried out twice to find the second derivative. The problem of this method is that the accuracy is very poor unless the original data is free from noise. Any attempt to remove the noise by numerical technique will also screen away the small population of the high energy electrons. As a result, numerical technique is not recommended.

The other method is to measure the second derivative of the current with respect to the voltage directly. A small sinusoidal signal is applied across a single Langmuir probe with a d.c. bias as shown in Figure 5.5.

The current flowing through the probe can be treated as a function of applied voltages:

$$I = I(V+v\sin\omega t) \tag{5.10}$$

where V is the d.c. voltage and v is the small a.c. signal voltage. By expanding equation (5.10) into a Taylor series, it can be shown that:

$$I = I(V) + \frac{v^2}{4} * \frac{d^2I(V)}{dV^2} + \frac{v^4}{64} * \frac{d^4I(V)}{dV^4} + \ldots$$

$$\ldots + \left[v * \frac{dI(V)}{dV} + \frac{v^3}{8} * \frac{d^3I(V)}{dV^3} + \ldots \right] \sin\omega t$$

$$- \left[\frac{v^2}{4} * \frac{d^2I(V)}{dV^2} + \frac{v^4}{48} * \frac{d^4I(V)}{dV^4} + \ldots \right] \cos 2\omega t + \ldots \tag{5.11}$$

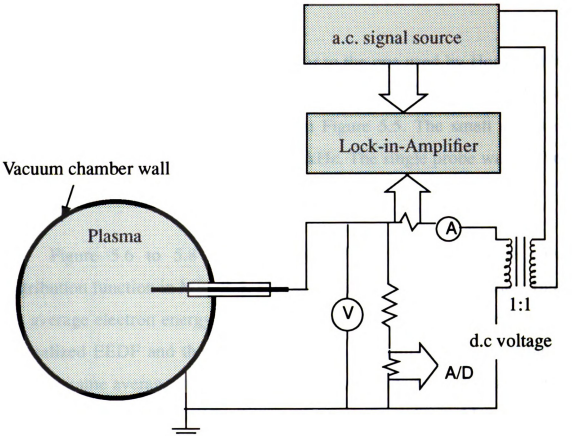

Figure 5.5 Schematic circuit of single probe measurement

When th
higher c
second
frequenc

T
except t
used. Th
chosen t
long and

F
distribut
the aver
normali
with the
figures,
Druyves
energy e

5.2.3 Io

Io
plasma p
used to f

When the small signal, v, is smaller than one volt, the coefficient of the higher orders terms can be neglected. As a result the magnitude of the second derivative can be picked up by setting the lock-in-amplifier to a frequency which is twice the frequency of the small a.c. signal.

The experimental setup was similar to the one used by Hopwood [60] except that an audio transformer with frequency response up to 3kHz was used. The schematic circuit is shown in Figure 5.5. The small signal was chosen to be 0.35 volt peak to peak at 1 kHz. The single probe was a 10 mm long and 0.9 mm in diameter tungsten wire.

Figure 5.6 to 5.8 show the typical normalized electron energy distribution function in MPDR 5, MPDR 20 and MPDR 325. In each figure, the average electron energy of the experiment data was calculated from the normalized EEDF and then the Maxwellian and Druyvesteyn distributions with the same average energy were plotted for comparison. As shown in the figures, the EEDF in MPDR plasma sources was neither a Maxwellian nor Druyvesteyn type distribution. In all these cases, the population of the high energy electrons in each EEDF is less than that in Maxwellian distribution.

5.2.3 Ion energy analyzer

Ion energy distribution function (IEDF) is probably the most important plasma parameter in ECR plasma sources. A multi-grid energy analyzer is used to find the ion energy distribution in a discharge.

0.10
0.08
0.06
0.04
0.02
0.00
f(E) (Normalized)

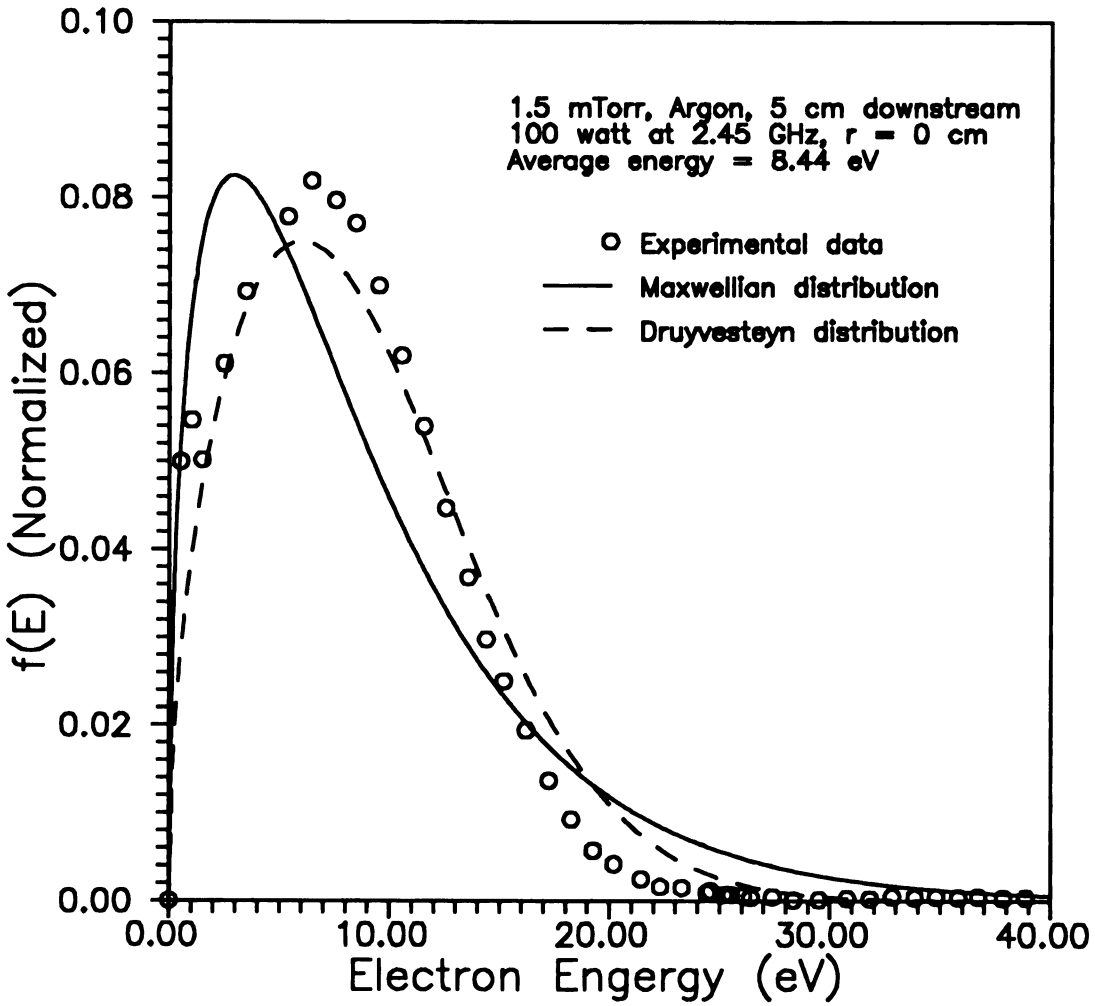

Figure 5.6 EEDF in MPDR 5

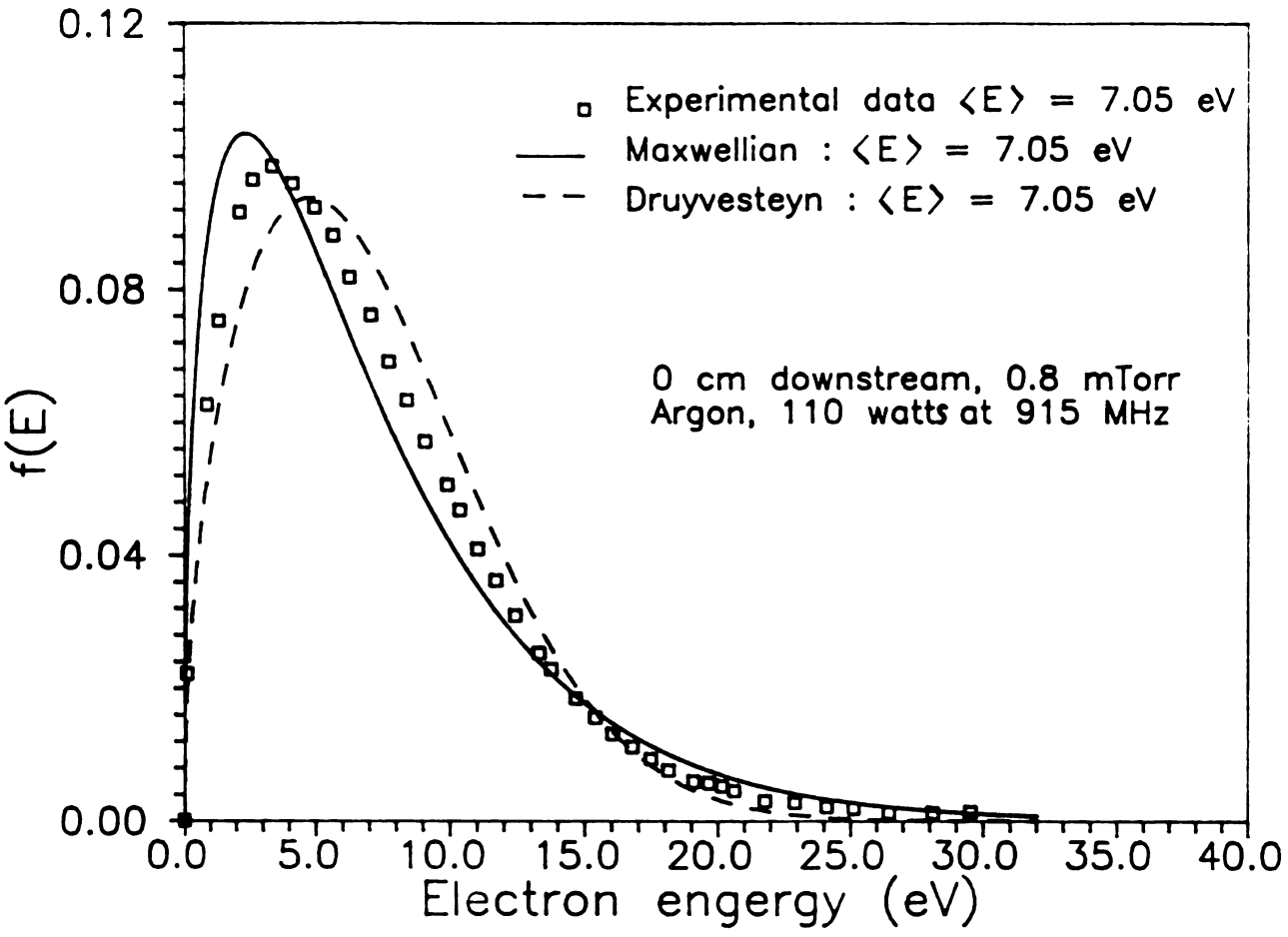

Figure 5.7 EEDF in MPDR 20

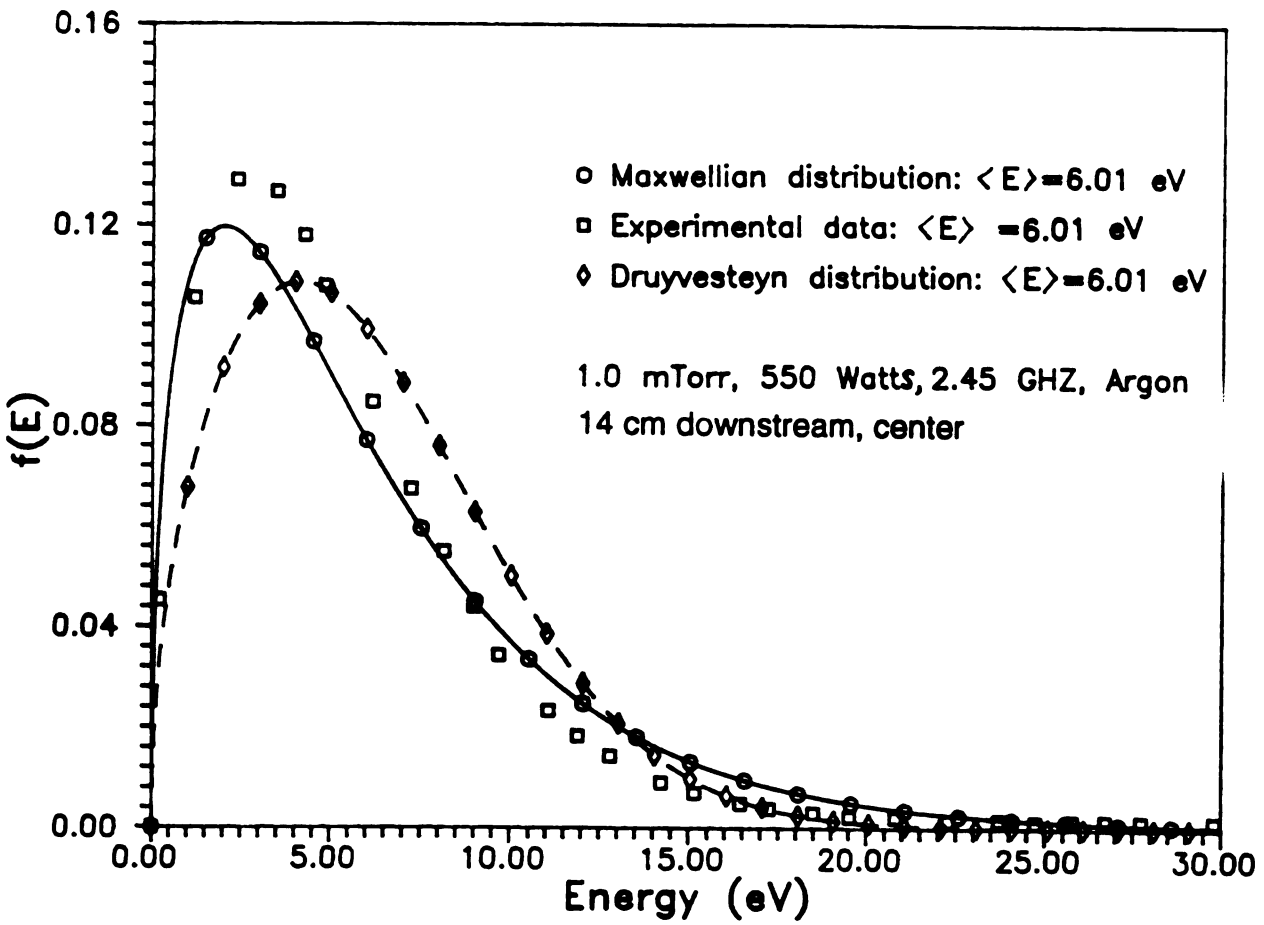

Figure 5.8 EEDF in MPDR 325

F

Th ion e

which h

has to b

collecte

analyzer

electron

retardati

retardati

collectin

during th

The

where I_{ic} i

the potenti

equal to q

was added

the same f

Hz. The ma

peak throug

few houndr

relative to t

to 60 volts a

Figure 5.9 shows a schematic circuit for the ion energy measurement. Th ion energy analyzer consists of a 50 μm thick stainless steel membrane which has a center hole with 100 μm in diameter. The diameter of the hole has to be smaller than the thickness of the sheath so that only the ions are collected. There are two grids and a collecting plate inside the energy analyzer. The first grid is an electron repulsion grid, which repels away any electrons that diffuse through the center hole. The second grid is an ion retardation grid. Only those ions that have energies greater than the retardation potential can pass through the second grid and reach the collecting plate. A picoammeter was used to monitor the ion current, I_{ic}, during the experiment.

The ion energy distribution function is given as [60]:

$$f_i(E) \propto \frac{d\, I_{ic}}{d\, V_{ir}} * (V_{ir}-V_{ic})^{-1/2} \qquad (5.12)$$

where I_{ic} is the ion current, V_{ir} is the potential of ion retardation grid, V_{ic} is the potential of the collecting plate and E is the energy of the ion which is equal to qV_{ir}. Similar to the single probe measurement, a small a.c. signal was added to the retardation potential, V_{ir}. The lock-in-amplifier was set to the same frequency of the a.c. signal, which was chosen between 40 to 45 Hz. The magnitude of the small signal was maintained at 0.35 volt peak to peak throughout the experiment. A typical ion current was in the range of a few houndreds nanoammperes. The ion energy analyzer can also be biased relative to the grounded chamber wall. During the experiments, V_{er} was set to 60 volts and V_{ic} was set to 13.8 volts.

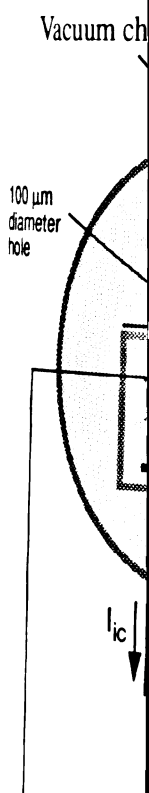

Figu

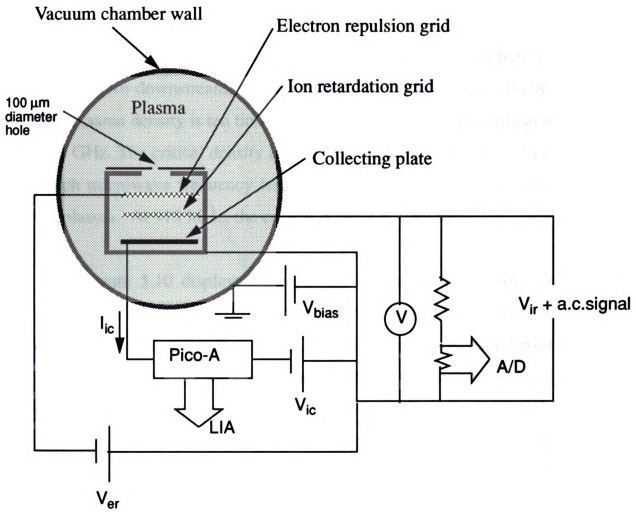

Figure 5.9 Schematic circuit for ion energy measurement

§ 5.3

5.5.1

cm^{-3} a

This pl

2.45 G

which

the plas

F

downstr

constant

At const

plasma

drastical

generate

ionic sp

confinem

diameter

distribute

shows the

and micro

§ 5.3 Experimental Results

5.5.1 MPDR 5

The plasma densities obtained in the MPDR 5 were as high as $7x10^{11}$ cm^{-3} at zero downstream, which was the highest of all the MPDR sources. This plasma density is ten times the theoretical value of the critical density at 2.45 GHz. The critical density at 2.45 GHz is the density of a cold plasma in which microwave frequency less than 2.45 GHz cannot propagate through the plasma. At 915 MHz, the critical density is 10^{10} cm^{-3}.

Figure 5.10 displays the variation of the plasma density versus the downstream position for different pressures and input microwave power. At constant 1.5 mTorr pressure, a higher input power produces a denser plasma. At constant 160 watts microwave power, there is no significant difference in plasma densities at 1 mTorr and 1.5 mTorr. The plasma densities drop drastically as the plasma diffuses downstream. This is because plasma is generated in a 5 cm diameter region. Once coming out of the MPDR, the ionic species diffuse freely inside the downstream chamber. A plasma confinement structure is situated right under the MPDR 5 source. It has a diameter of 20 cm. As a result, plasma distribution is more uniformly distributed in the downstream locations as shown in Figure 5.11. Figure 5.12 shows the variations of radial distribution of plasma at different pressures and microwave input power.

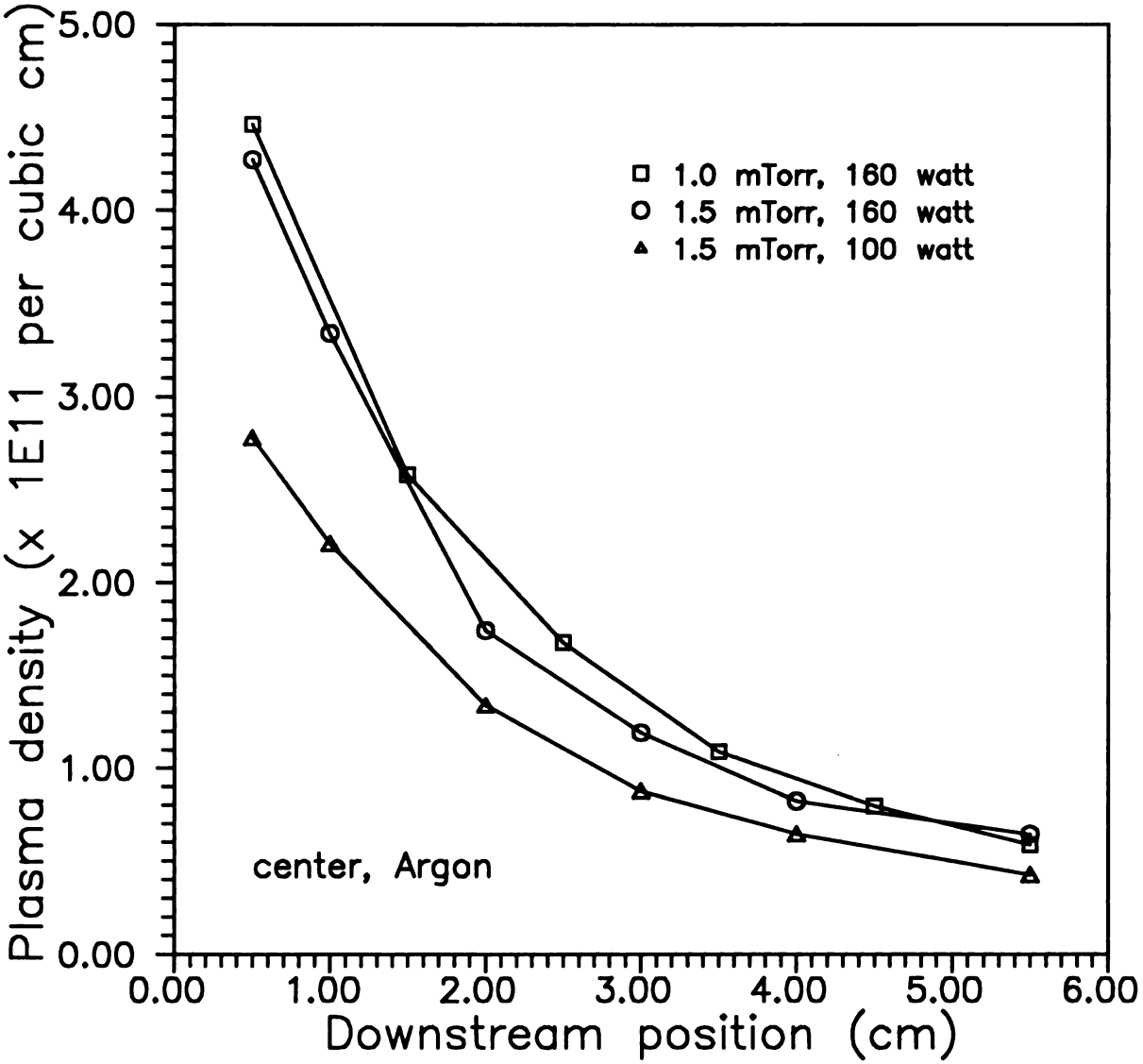

Figure 5.10 Variations of plasma density with downstream positions in MPDR 5

Fi

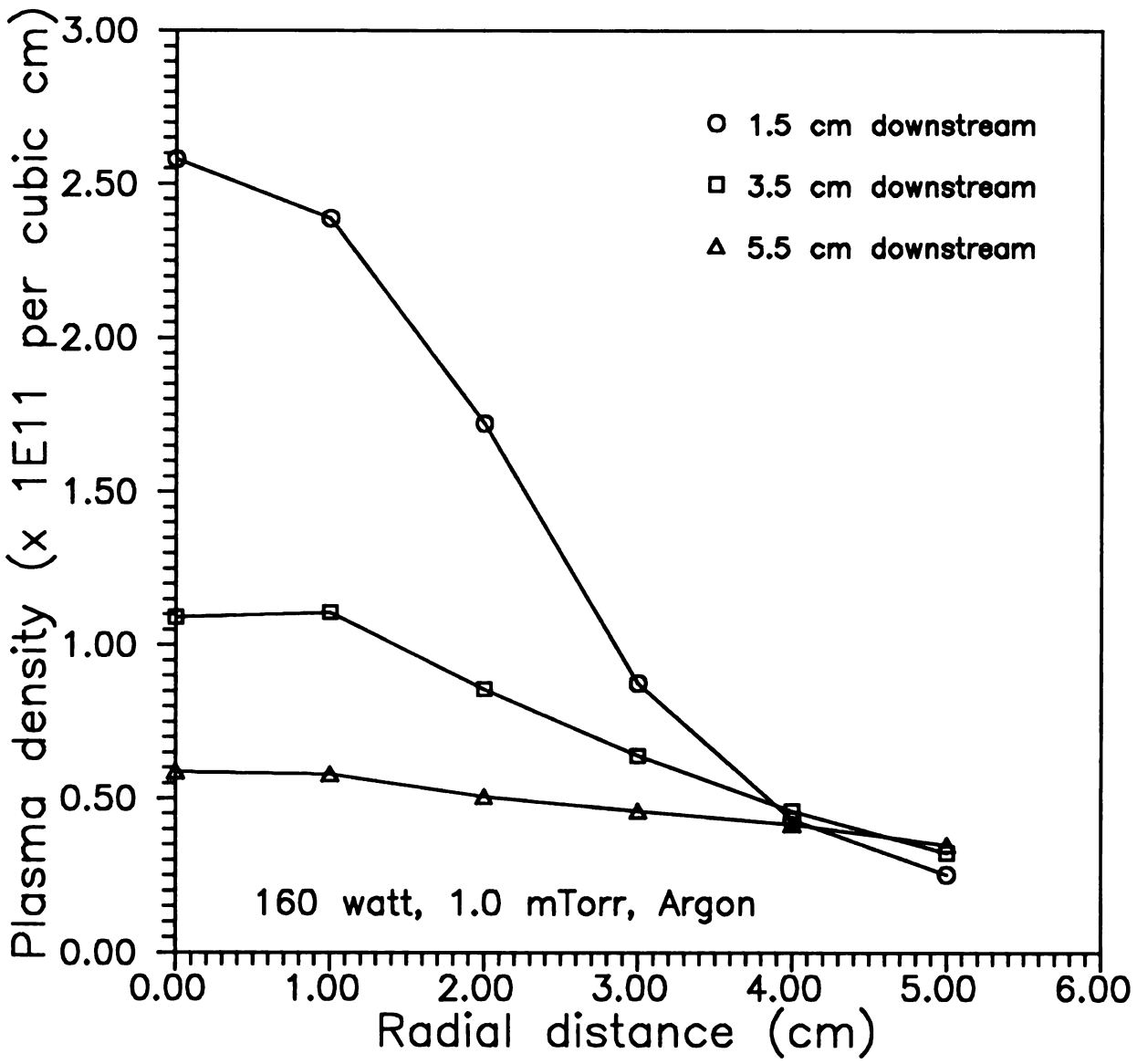

Figure 5.11 Radial distributions of plasma density at different downstream positions in MPDR 5

Figure

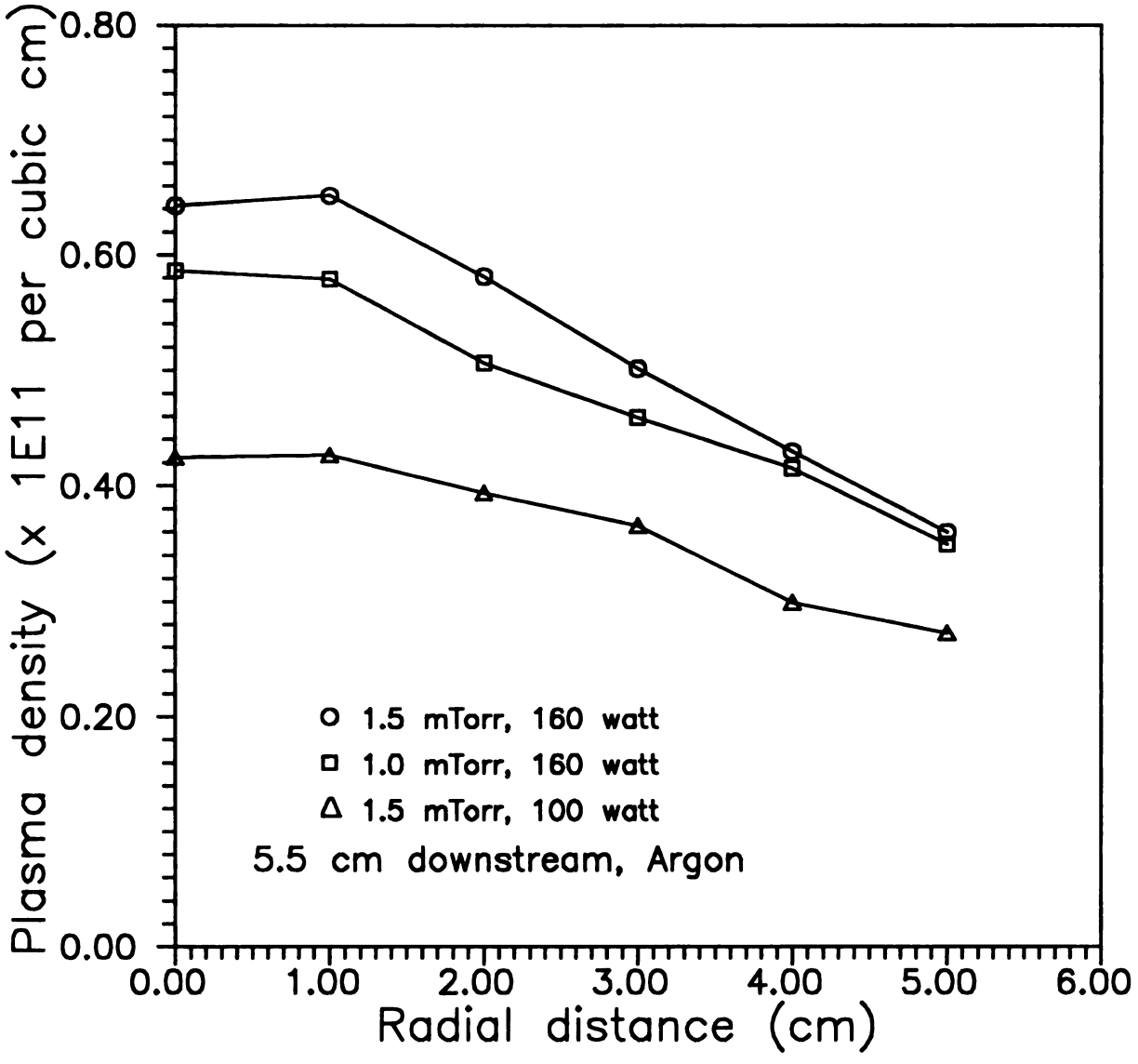

Figure 5.12 Radial distributions of plasma density at different pressures and microwave power in MPDR 5

Varia

shown in

direction ar

cm downstr

downstrean

dropped fro

downstrean

the ion ener

One

sources is i

plot in Figu

the radial d

is the dowr

Maximum

distribution

As in

Gaussian ty

downstrean

microwave

downstrean

energy pea

radial distri

5.17.

Variations of plasma potential in radial and downstream directions are shown in Figure 5.13. Plasma potential decreases in the downstream direction and radial distribution of the plasma potential is very uniform at 5 cm downstream. Figure 5.14 shows the average ion energies as a function of downstream position at different power and pressure. The energy of the ions dropped from nearly 30 eV at 2 cm downstream to half of its value at 5 cm downstream. Such a big drop in ion energy can be explained by examining the ion energy distribution functions.

One important difference in MPDR 5 from other MPDR plasma sources is its ion energy distribution function shown in Figure 5.15. Each plot in Figure 5.15 represents a normalized IEDF at different locations. ***r*** is the radial distance in centimeter from the central axis of the system while ***d*** is the downstream position, also measured in centimeter. Full Width Half Maximum (FWHM) of the ion energy distribution is given only when the distribution is Gaussian type, i.e., single peak distribution.

As indicated in Figure 5.15, there was a gradual change of IEDF from Gaussian type distribution to a bimodal distribution as the plasma diffused downstream. This phenomenon was also observed at a different pressure and microwave power as shown in Figure 5.16. As the plasma diffused downstream, the population of the high energy ions dropped and a low energy peak emerged. However, there was no significant change in the radial distributions of the IEDF at 4 cm downstream as shown in Figure 5.17.

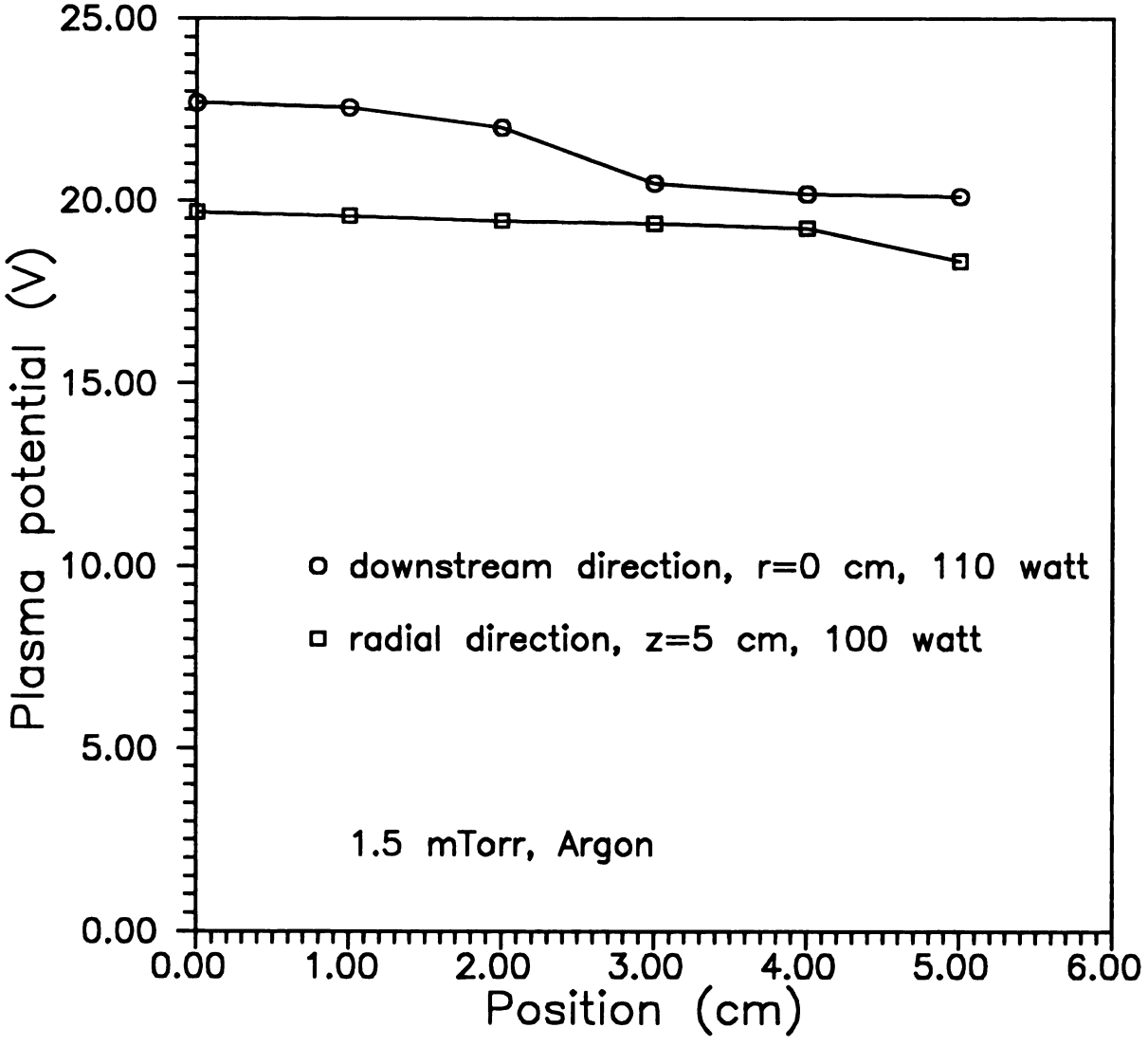

Figure 5.13 Variations of plasma potential in MPDR 5


Ion energy (eV)

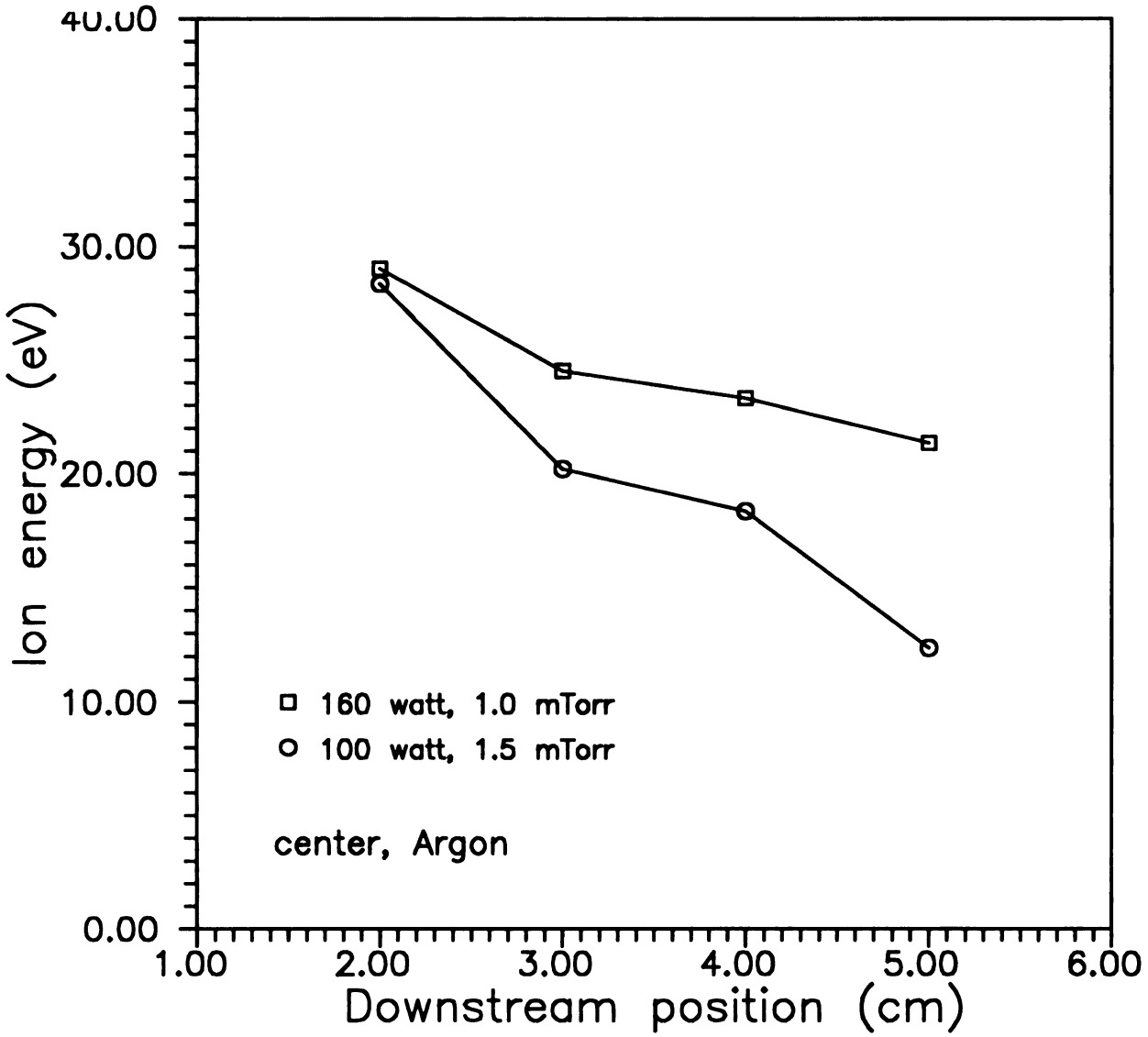

Figure 5.14 Variations of ion energy with downstream positions in MPDR 5

0.10
0.08
0.06
0.04
0.02
0.00
f(E) (Normalized)
0.00

0.10
0.08
0.06
0.04
0.02
0.00
f(E) (Normalized)
0.00

Fi

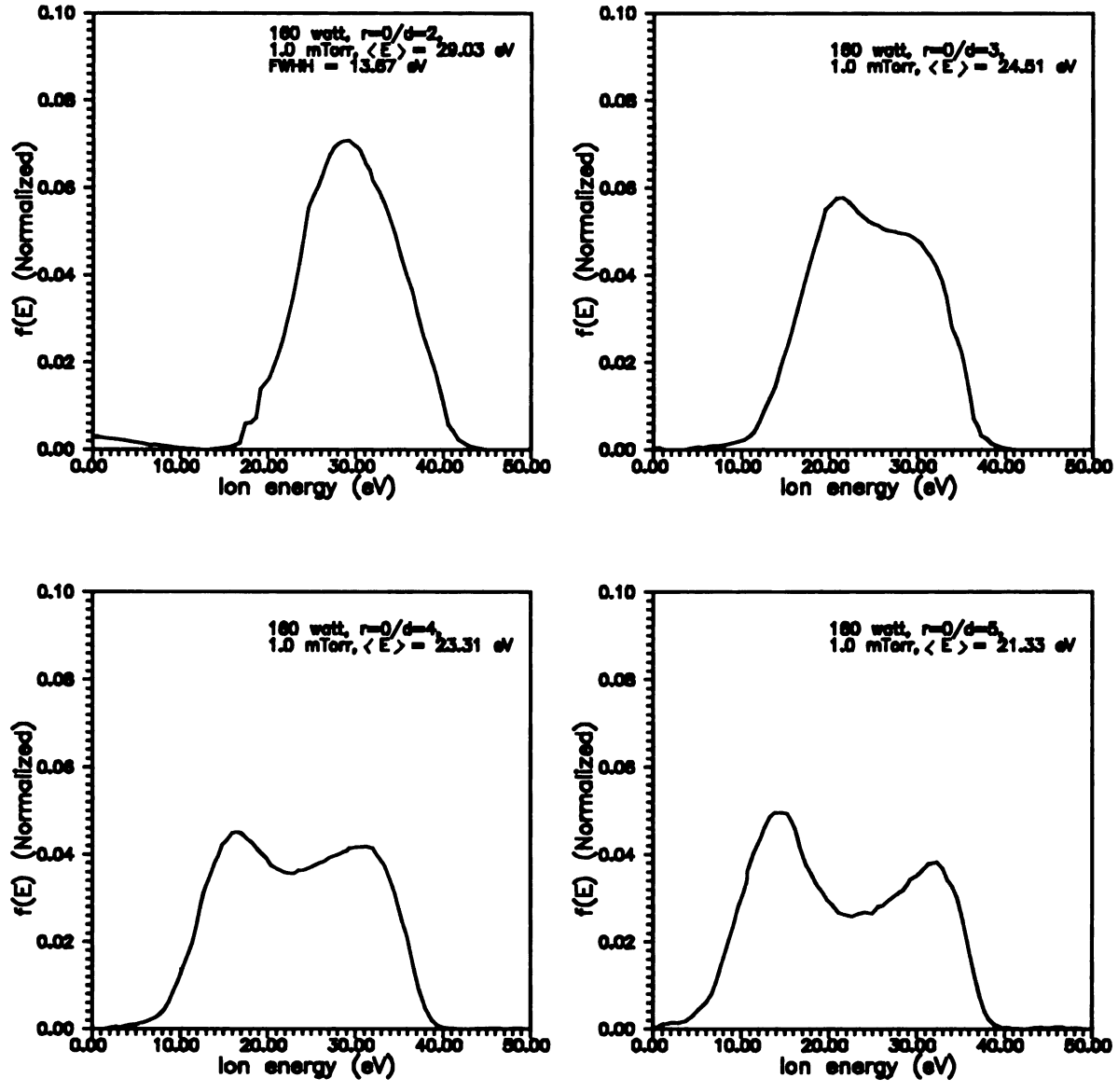

Figure 5.15 Variations of IEDF with downstream positions at 1 mTorr, 160 watts micrwave power in MPDR 5

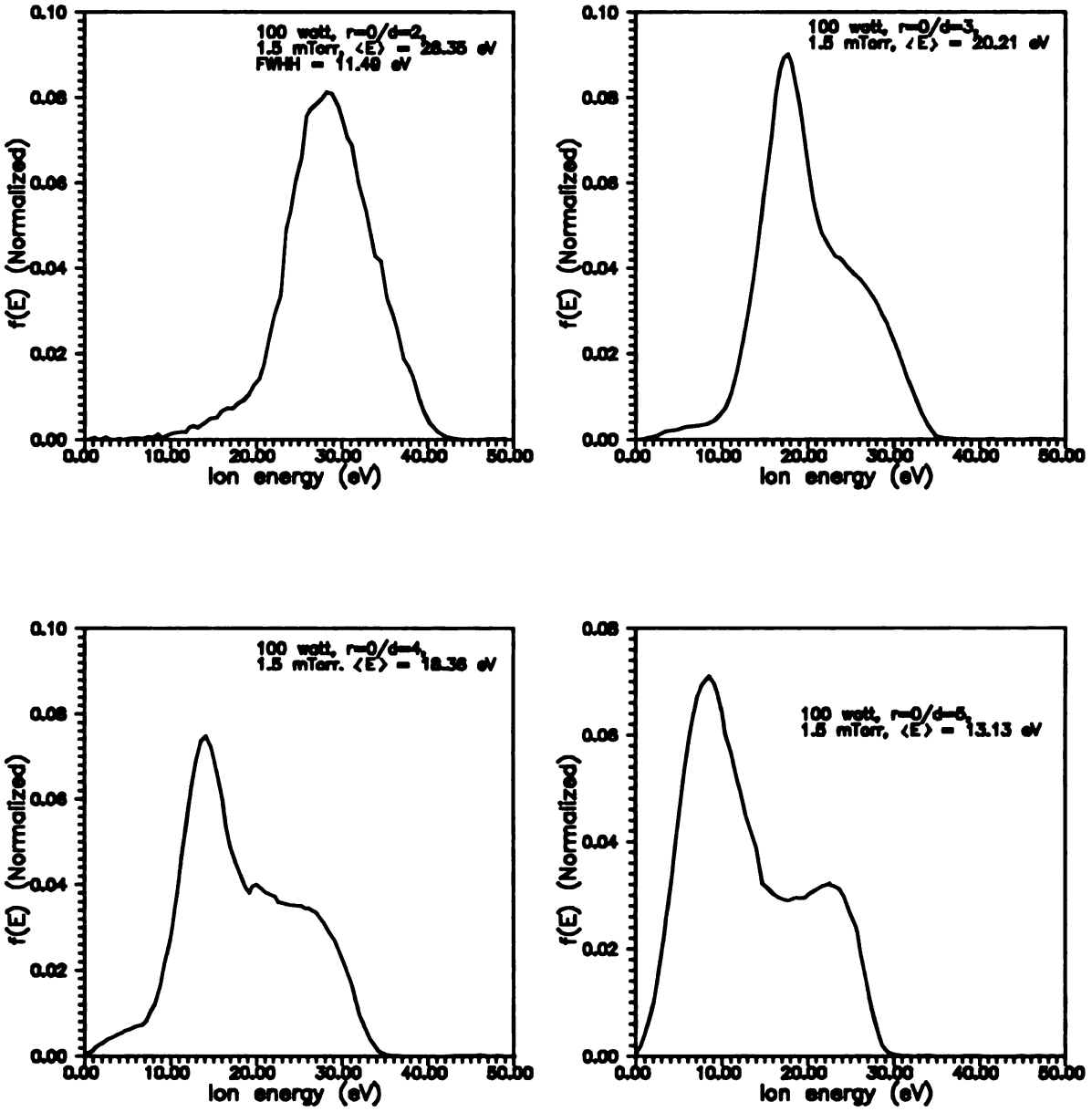

Figure 5.16 Variations of IEDF with downstream positions at 1.5 mTorr and 100 watts microwave power in MPDR 5

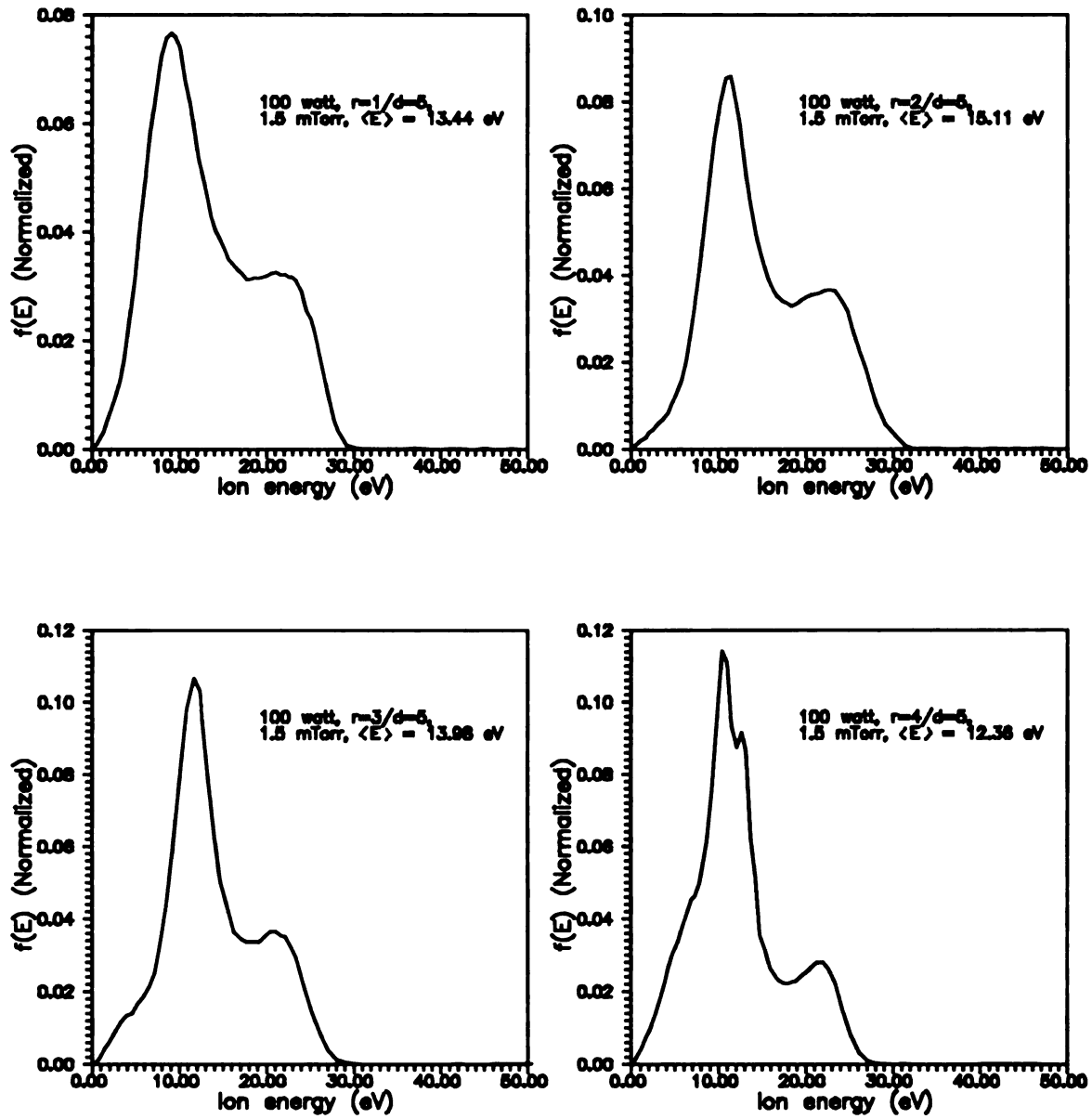

Figure 5.17 Variations of IEDF with radial positions in MPDR 5

To explain the formation of the bimodal distribution, there are two possibilities. The first possibility is downstream ionization, in which ions are generated and forming the second low energy peak shown in the figures. However, this cannot explain the rapid disappearance of the high energy ions. If downstream ionization takes place, the plasma density will increase as reported by Meyer et al. [170] in divergent ECR plasma source. If only a few energetic electrons exist in the downstream and thus downstream ionization rate is insignificant, then the effect on the IEDF is insignificant.

Another possible reason to explain the formation of the bimodal distribution is resonant charge exchange [63]. This process takes place when energetic ions, for example Ar^+, pass through thermal-velocity neutral argon molecules. Electrons are dissociated from the low energy neutral atoms and neutralize the energetic argon ions. As a result, a low energy ion and high energy neutral are produced. As pointed out by Kaufman [63], this exchange process slows down when the ion energy or pressure decreases. In Figure 5.15, the pressure was at 1.0 mTorr while Figure 5.16 was at 1.5 mTorr. Both figures have about the same average ion energy in IEDF at 2 cm downstream. One is 29 eV and the other is 28.4 eV. If Kaufman is right, the ion exchange process should be faster at higher pressure, i.e., at 1.5 mTorr. This is exactly shown in Figure 5.16 in which a prominent low energy peak appears in 3 cm downstream. This suggests that an ion exchange process has taken place in the MPDR 5. No such phenomenon was observed in the MPDR 9, MPDR 13, MPDR 20 and MPDR 325.

5.5.2

laborat
Most o
MHz r

density
500 wa
density,
240 wa
cannot b
will burn
MHz mi
biggest
magnets,
downstre
distributi
(1σ) unif
plasma is
plasma d
5.20. At
power wh

Mos
the downs

5.5.2 MPDR 20

MPDR 20 was the first large diameter plasma source built in the laboratory. The source was designed for large diameter substrate processing. Most of the experiments were carried out with TE_{211} mode excitation at 915 MHz microwave energy.

Figure 5.18 shows the distributions of the electron density or plasma density at zero downstream at different microwave input power. At about 500 watts input power, the plasma density was ten times of the critical density, which is 10^{10} cm^{-3} at 915 MHz. Doubling the input power from 240 watts to 480 watts nearly doubled the plasma density. This source cannot be driven hard because of two reasons. First, the L-shaped gasket will burn at high power and second the maximum power available in the 915 MHz microwave source is 500 watts. Radial variation of the plasma was the biggest concern in this plasma source. With downstream confinement magnets, the plasma density became uniformly distributed as it diffused downstream. Shown in Figure 5.19 are the variations of the radial distribution at different downstream locations. At 13 cm downstream, a 2.6% (1σ) uniformity over 18 cm in diameter was obtained. This highly uniform plasma is ideal for large diameter wafer processing. The variations of plasma density with pressure and microwave energy are shown in Figure 5.20. At constant pressure, the plasma density increased with the input power while at constant power, it went down with the pressure.

Most of the plasma diagnostic experiments were done at locations in the downstream chamber where wafers were being processed. The radial

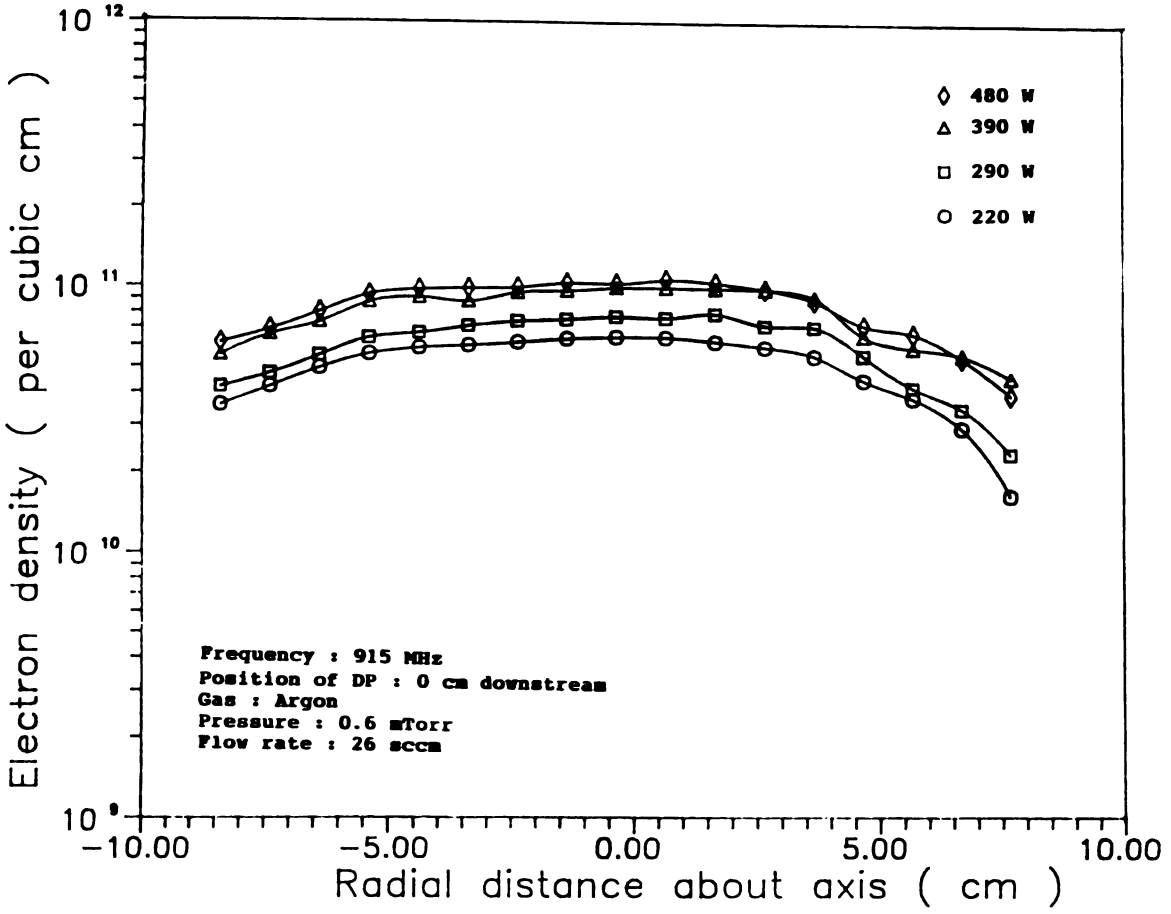

Figure 5.18 Radial variations of electron density at different microwave power in MPDR 20

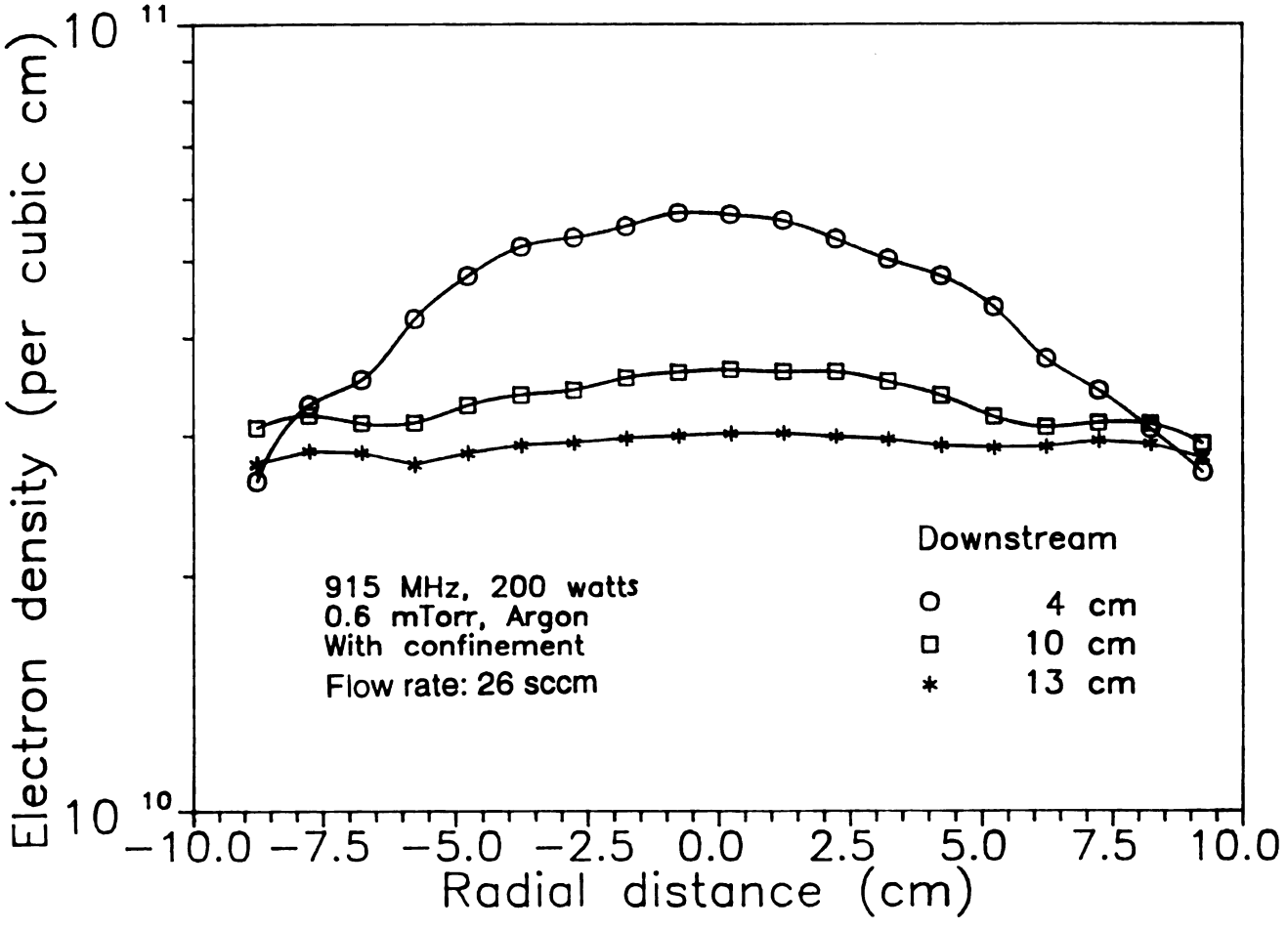

Figure 5.19 **Radial distributions of plasma density at different downstream positons in MPDR 20**

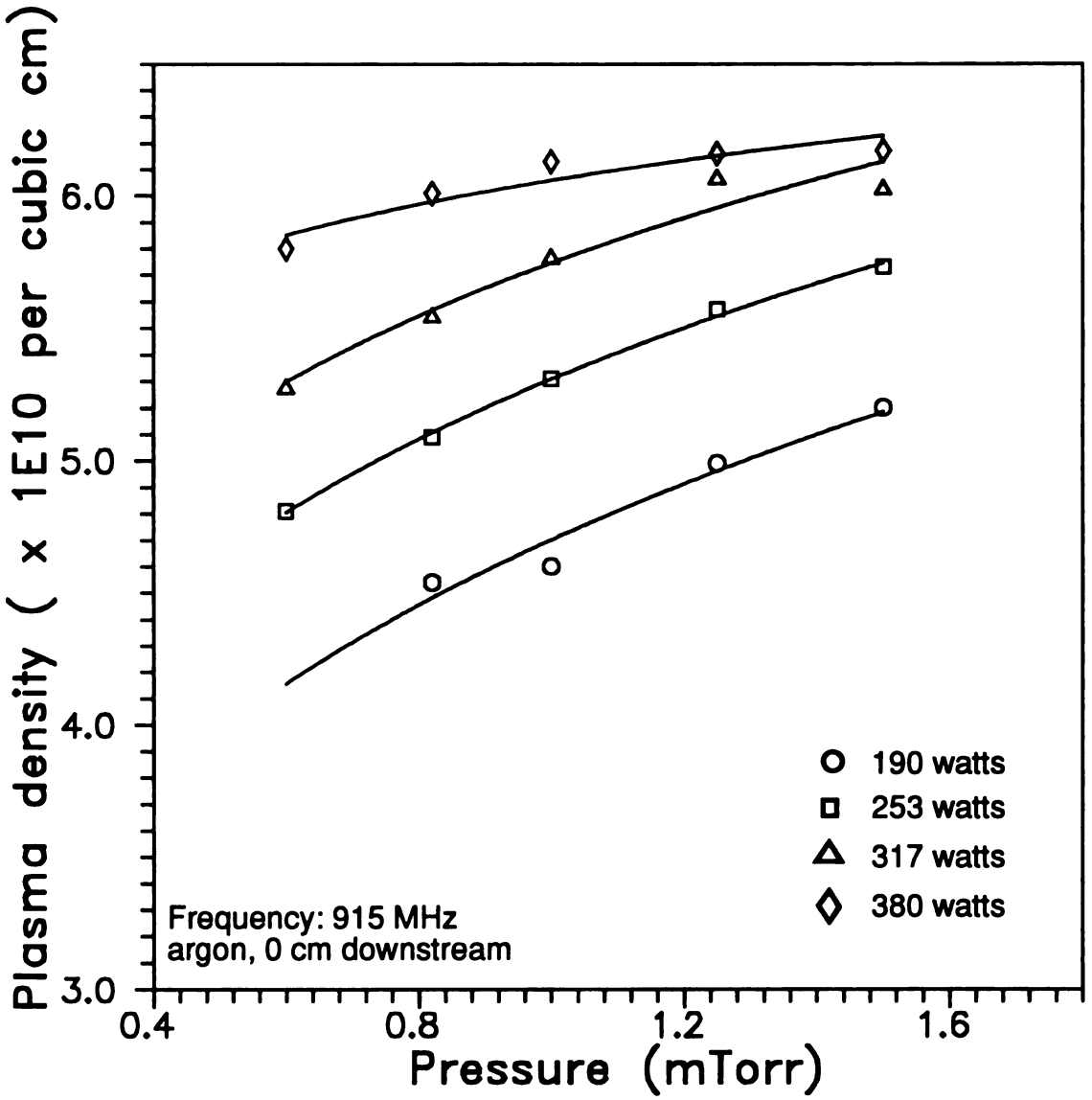

Figure 5.20 Variations of plasma density with pressure at 0 cm downstream and different microwave power in MPDR 20

distributions of the plasma potential at different pressures and microwave power are shown in Figure 5.21 and 5.22 respectively. Plasma potential is related to the population of high energy electrons in the EEDF. When pressure increases, the collision frequency increases. Therefore the energetic electrons are more likely to loss part of their energies as a result of the collision processes. At constant microwave input power, plasma potential will drop as the pressure increases. An increase in microwave input power also increased the plasma potential as shown in Figure 5.22. The distributions were very uniform at 12 cm downstream over 9 cm in radius. Variation of plasma potential with downstream location is shown in Figure 5.23. The plasma potential decreased from about 10 volts at zero downstream to about 7 volts at 14 cm downstream.

The radial distribution of the electron energy is shown in Figure 5.24. As expected, the distribution was similar to the radial distribution of the plasma potential. Figure 5.24 shows the variation of the electron energy with downstream positions. The electron energy dropped very slightly because of the downstream magnetic confinement.

Plasma potential in the MPDR 20 is much lower than the plasma potential in the MPDR 5. The low plasma potential in MPDR 20 has a direct impact on the ion energy distribution. A high plasma potential means a thick sheath between the plasma and the substrate surface, in which ions are accelerated. Figure 5.26 shows the IEDF in MPDR 20 without any d.c. bias to the ion energy analyzer. The figure shows a decrease of average ion energy from 12.8 eV at 4 cm downstream to 8.8 eV at 14 cm downstream without any broadening. Such decrease in ion energy was the result of a

12.00
10.00
8.00
6.00
Plasma potential (eV)
0.0

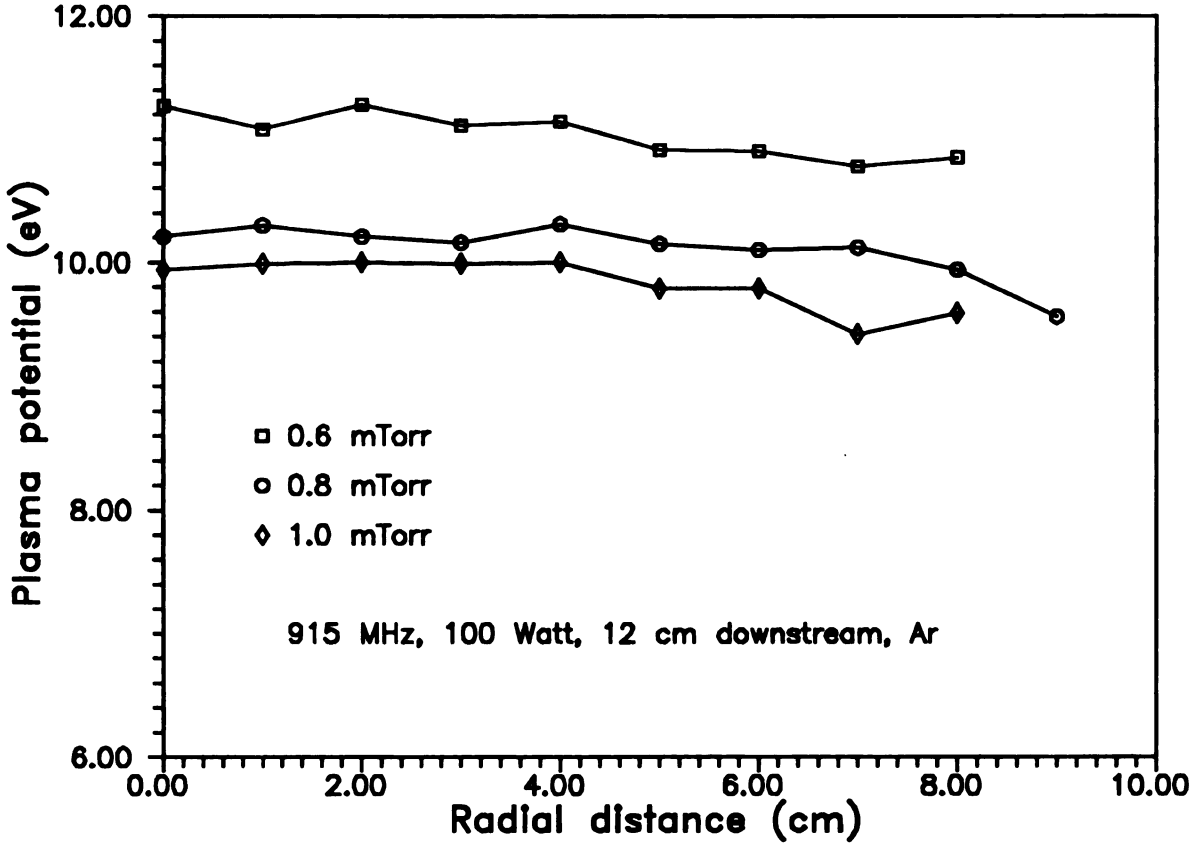

Figure 5.21 Radial distributions of plasma potential at different pressures in MPDR 20

12.00
11.00
10.00
9.00
8.00
7.00
6.00
Plasma potential (eV)

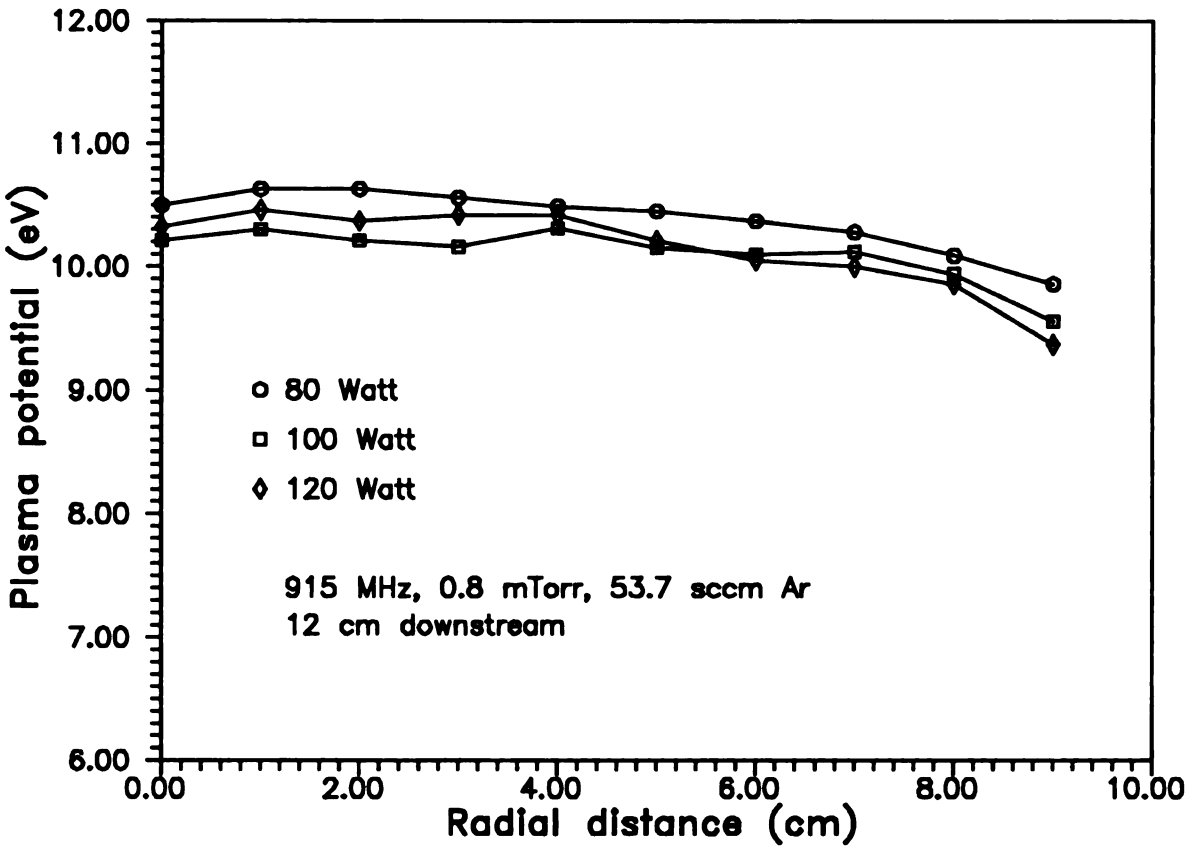

Figure 5.22 Radial distributions of plasma potential at different microwave power in MPDR 20

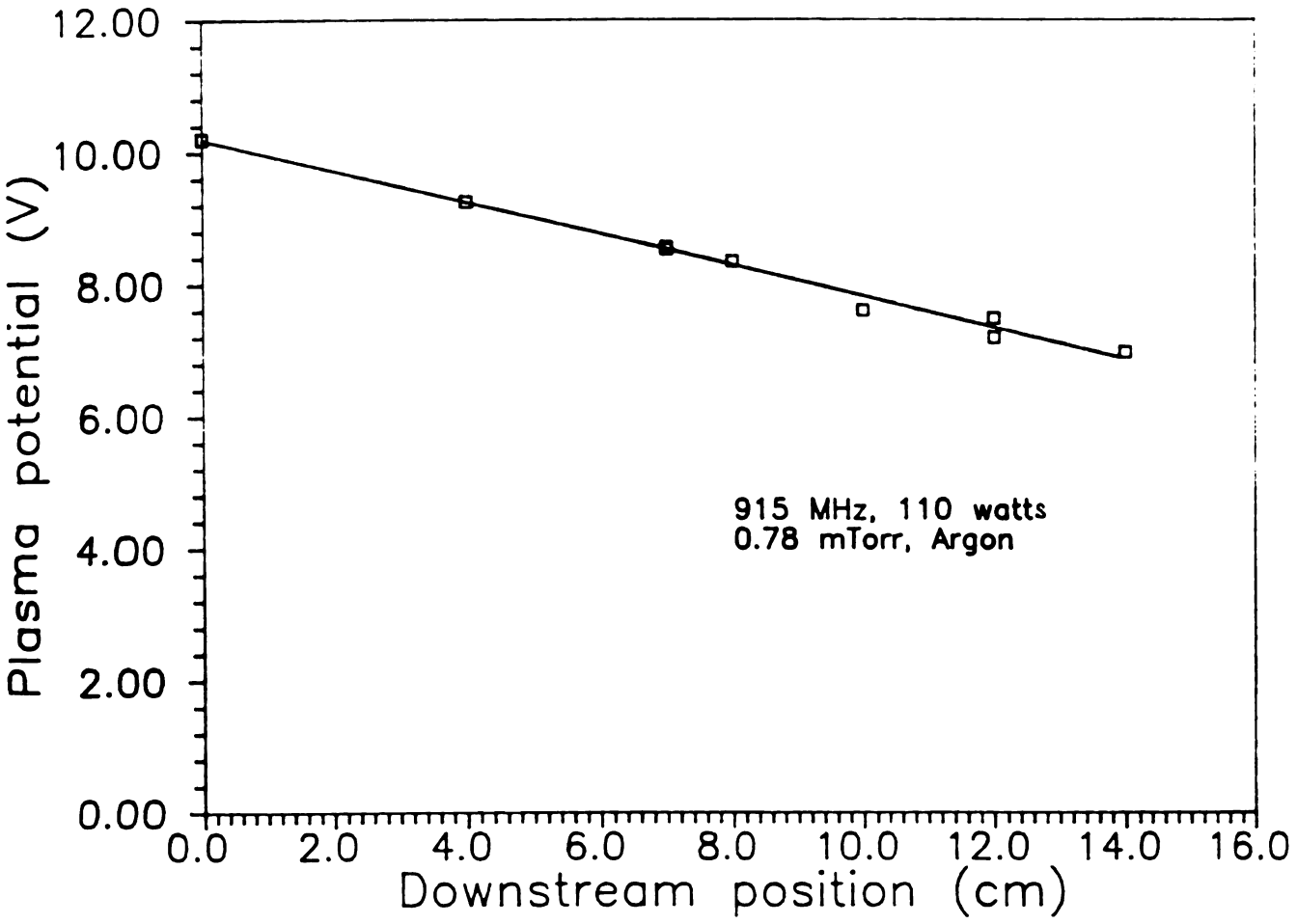

Figure 5.23 Variation of plasma potential with downstream positions in MPDR 20

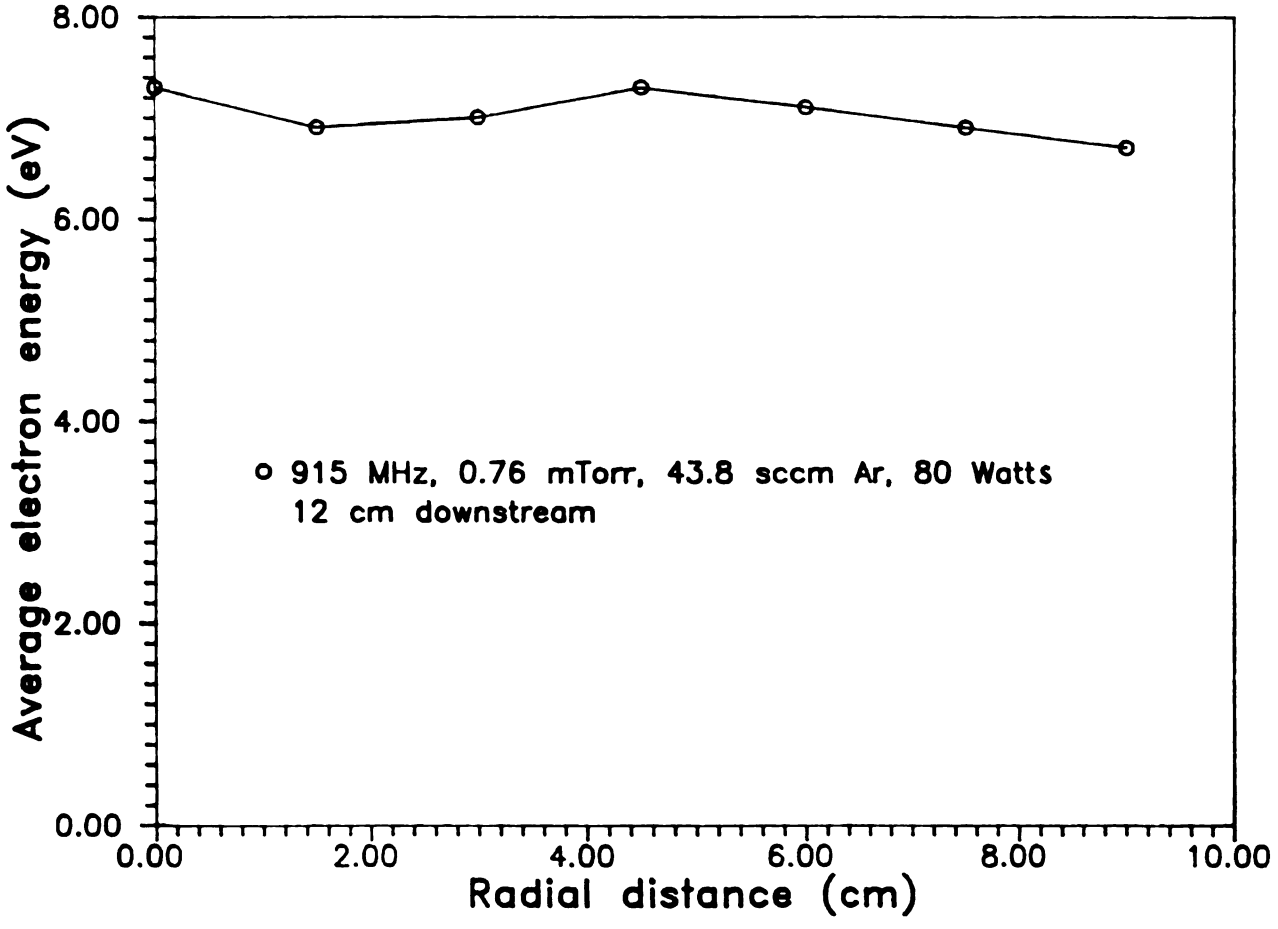

Figure 5.24 Radial variation of electron energy at 0.76 mTorr and 80 watts microwave power in MPDR 20

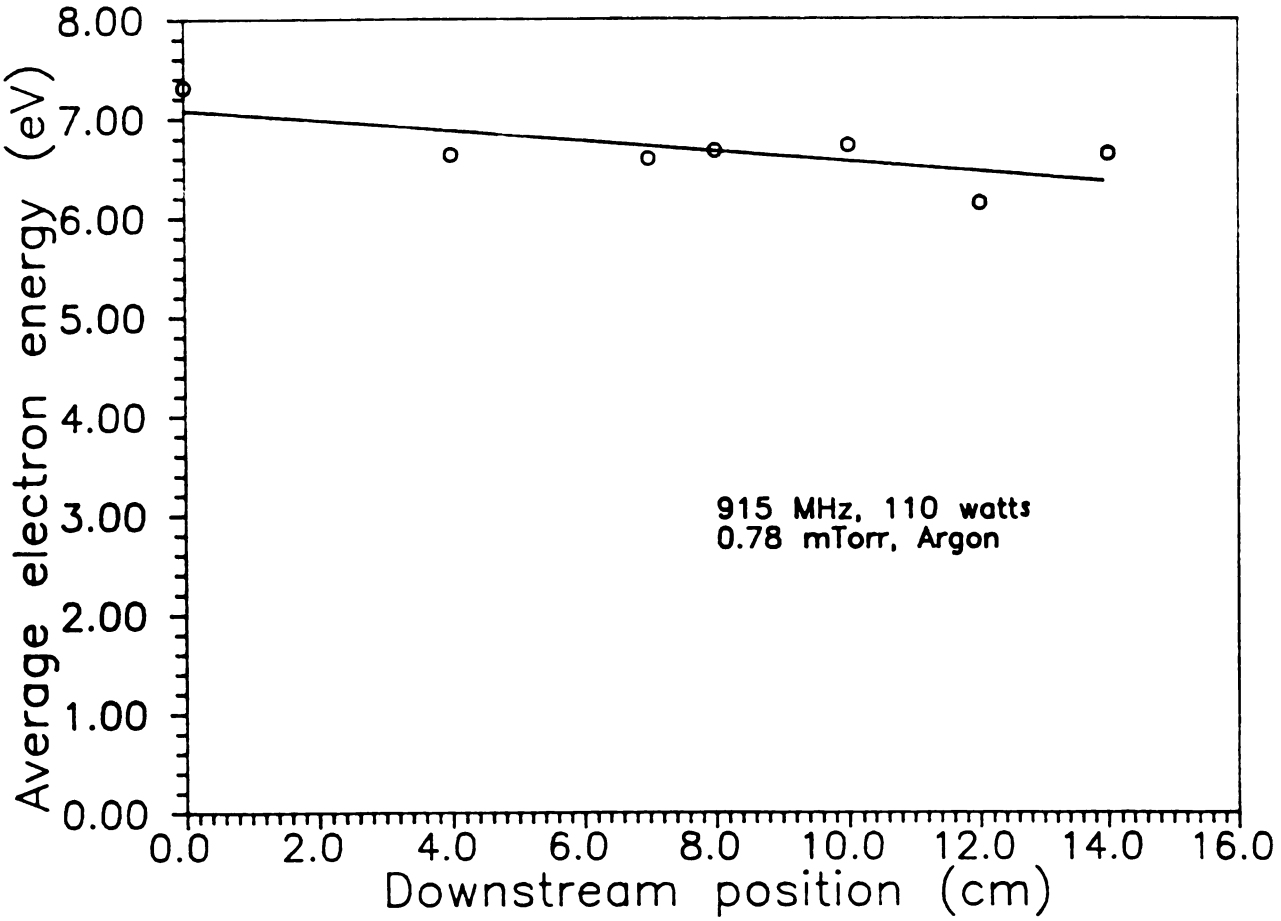

Figure 5.25 Variation of electron energy with downstream position at 0.78 mTorr in MPDR 20

0.15
0.10
f(E)
0.05
0.00
0.0

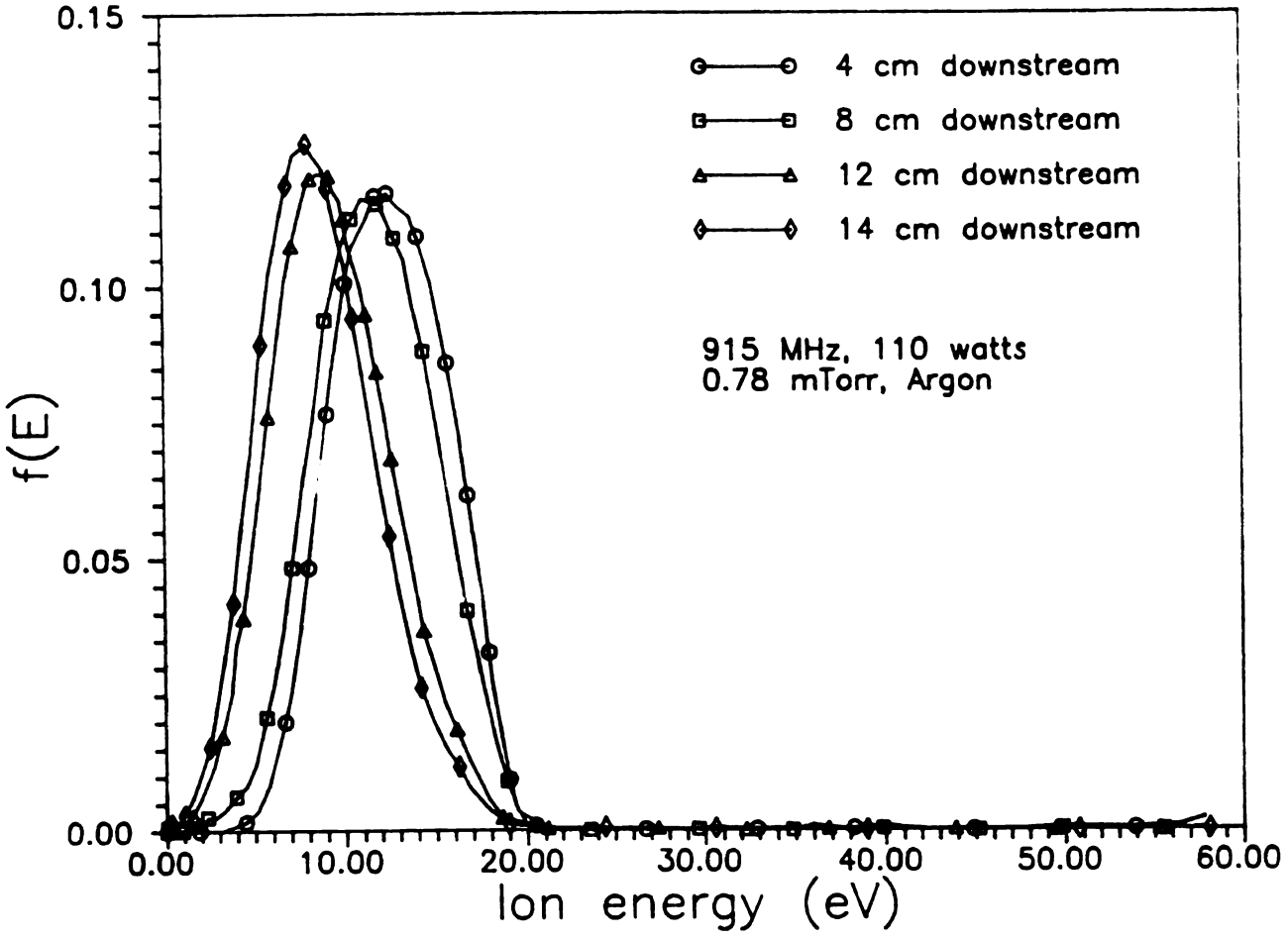

Figure 5.26 Variations of IEDF at different downstream positions in MPDR 20

decrease in plasma potential. The full width at half maximum (FWHM) of each IEDFs in Figure 5.25 was about 8 eV, which was smaller than those results obtained in MPDR 9 by Jeff Hopwood and the FWHM shown in the MPDR 5. When a d.c. bias voltage was applied to the ion energy analyzer, the ion energy distribution shifted by about the same amount without broadening as shown in Figure 5.27. As a result, the energy of the ions impinging on a substrate surface can be controlled by the use of an external bias. One application is to increase the selectivity in the etching of silicon using silicon dioxide etch mask in chlorine plasma. Silicon dioxide can be sputtered off by an ion with energy of 20 eV or above. Therefore, by controlling the bias to the substrate, selective etching can be achieved.

Radial variations of the average ion energy with power and pressure are shown in Figure 5.28 and Figure 5.29. The ion energies were higher at 0.6 mTorr than at 1.0 mTorr. This was primarily caused by the variation of the sheath potential at different pressure. Radial uniformity of the ion energy was very good at 12 cm downstream as shown in Figure 5.28. Variation of the average ion energy is shown in Figure 5.30. The ion energy decreased from about 13 eV at 4 cm downstream to 8 eV at 14 cm downstream.

The most significant features in MPDR 20 are its low ion energy and high uniformity in the downstream position at about 12-14 cm below the baseplate. A low ion energy plasma is essential for anisotropic etching of semiconductor with minimum substrate bias. This is critically important because the etching process is controllable by an external bias and the damage to the substrate material is minimal. A uniform plasma over a large

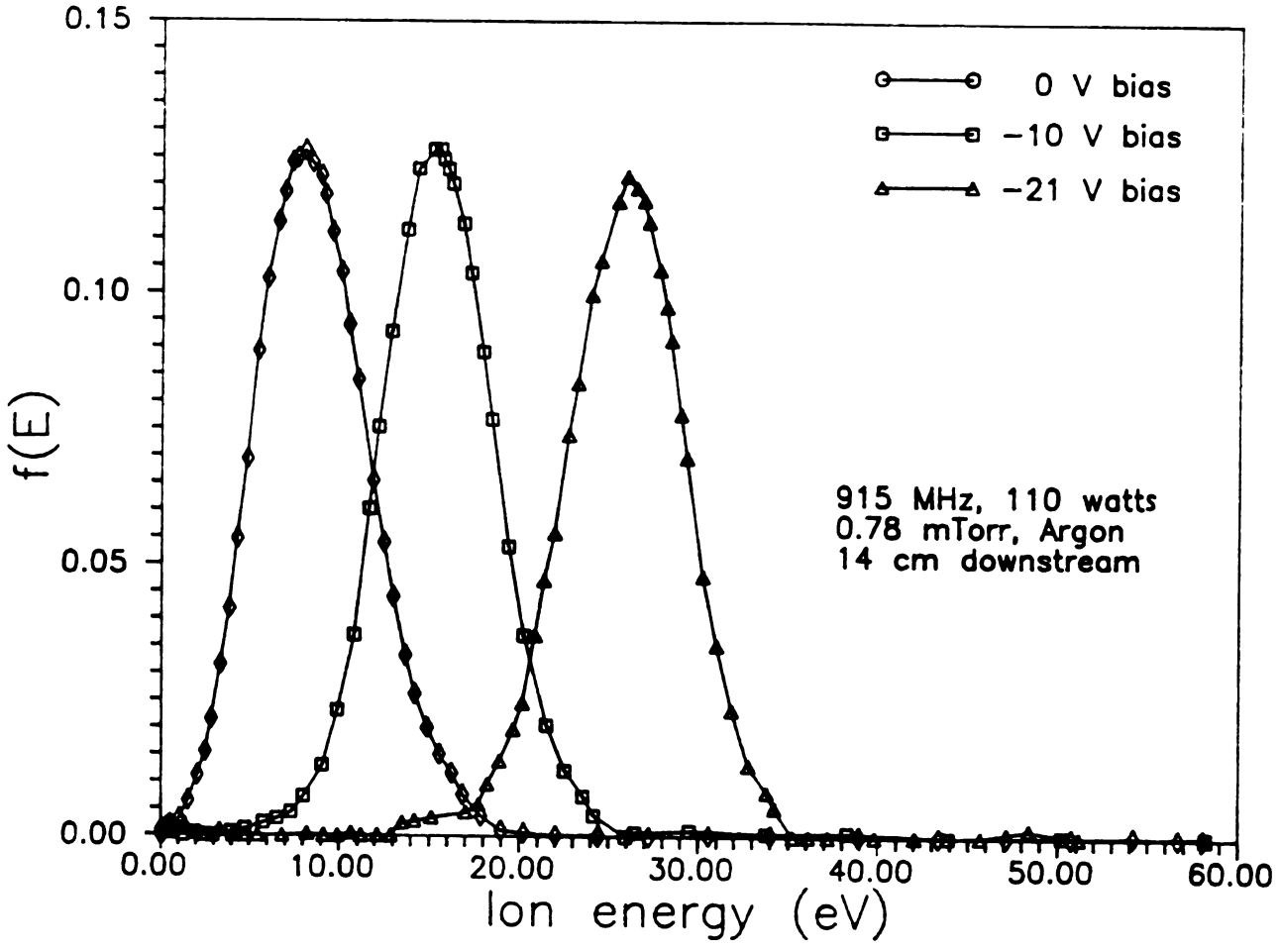

Figure 5.27 Variations of IEDF with external d.c. bias in MPDR 20

15.00
10.00
5.00
0.00
0.00
Average ion energy (eV)

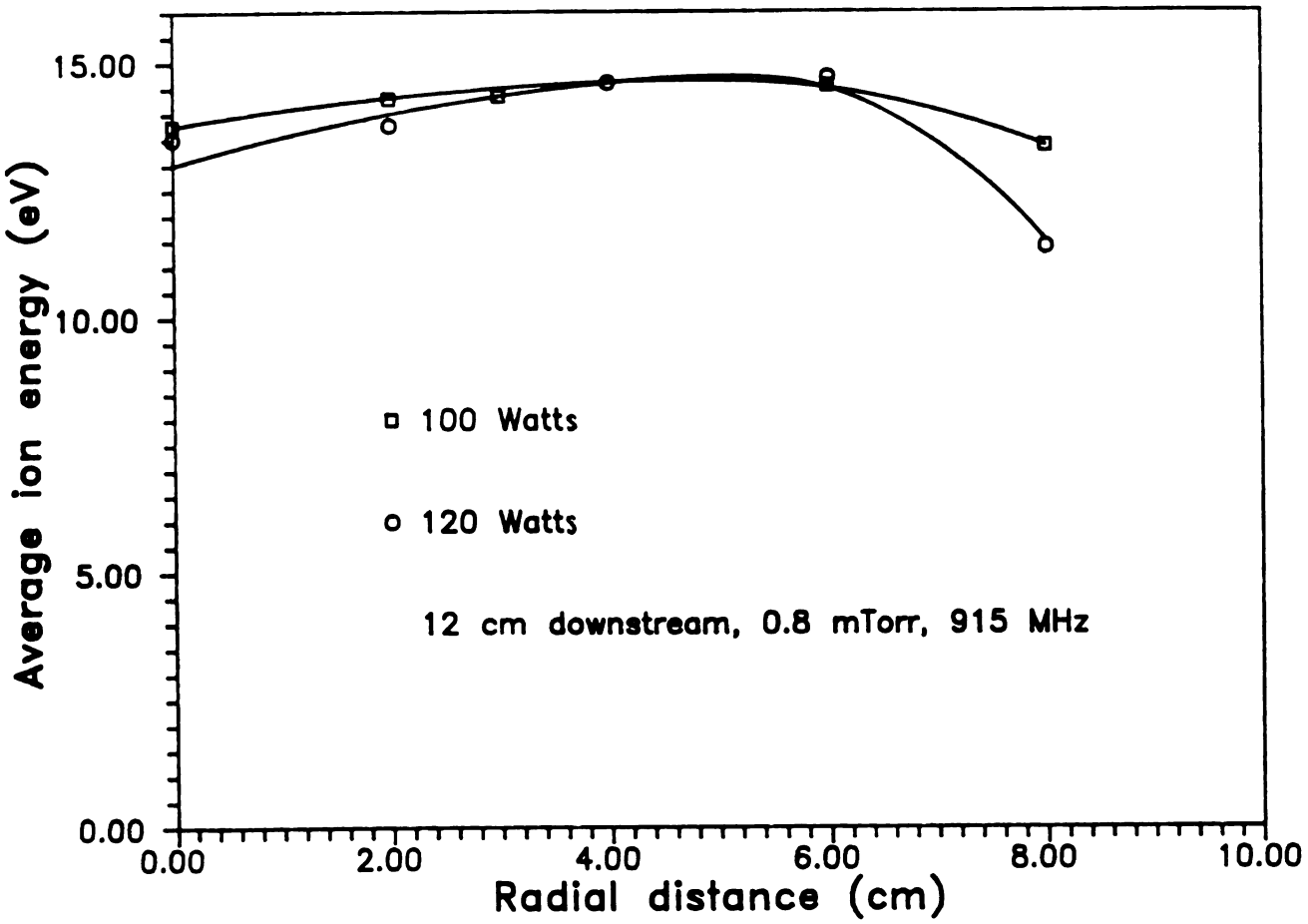

Figure 5.28 Radial variations of average ion energy with microwave power in MPDR 20

20.00
15.00
10.00
5.00
0.00
0.00
Average ion energy (eV)

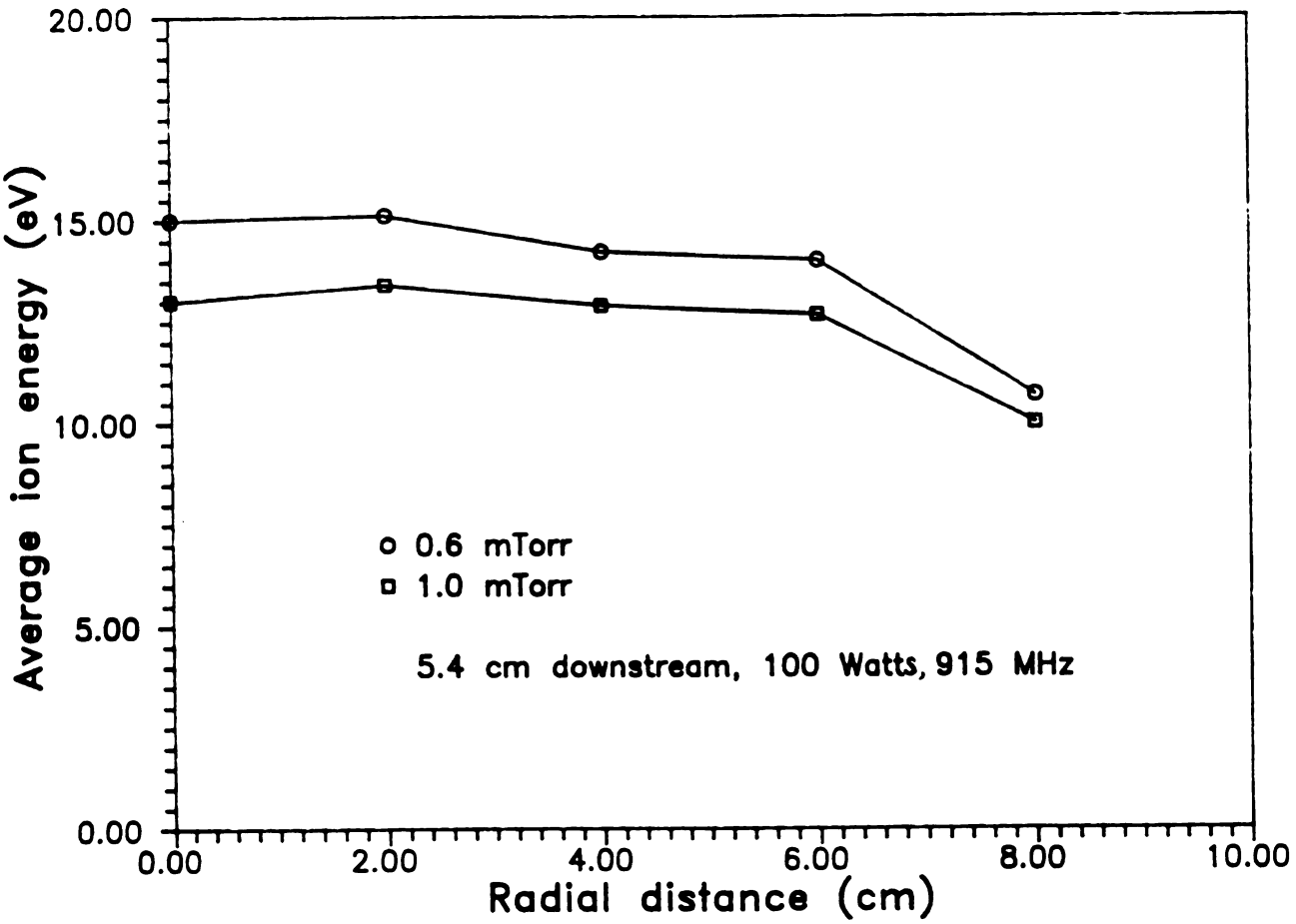

Figure 5.29 Radial variations of average ion energy with pressure in MPDR 20

Average ion energy (eV)
16.0
12.00
8.00
4.00
0.00

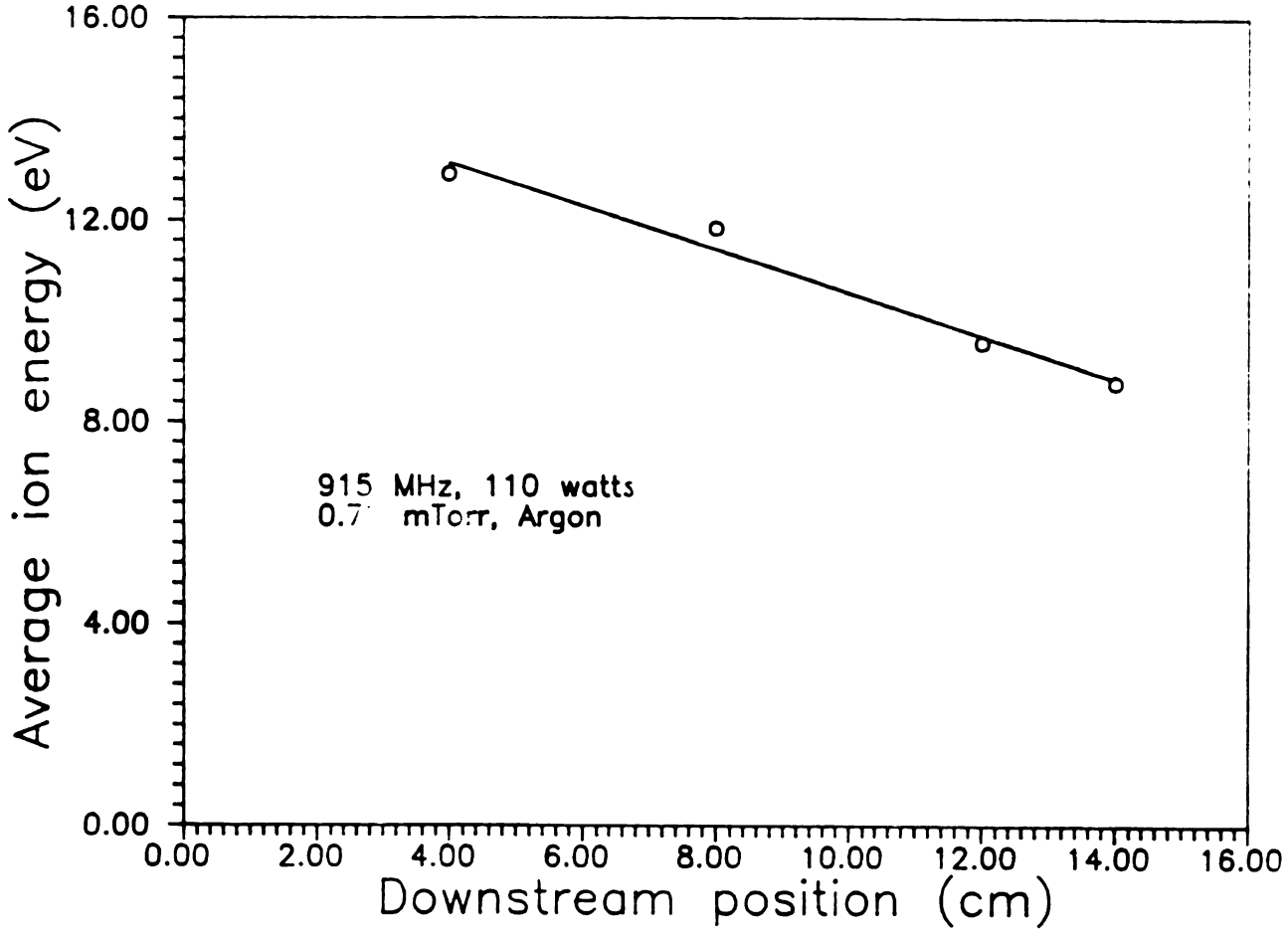

Figure 5.30 Variation of average ion energy with down-stream position in MPDR 20

area is important for the processing of large diameter wafer. Currently, up to eight inches in diameter wafer are being used for production. Thus a uniform plasma is necessary to achieve uniform processing and high production yield.

The MPDR 20 was also tested at 2.45 GHz. It was the first MPDR source that had a discharge diameter larger than the cutoff radii of the cavity resonant modes. However, most of the characterization experiments at 2.45 GHz were performed in another large diameter MPDR, the MPDR 325. It is reported in next section.

5.5.3 MPDR 325

The discharge diameter of the MPDR 325 was 10 inches, the largest among all the MPDRs. This reactor is a commercial plasma source which was used in the etching application in this dissertation [43,45]. Figure 5.31 shows the variation of plasma density with pressure and microwave power in this source. The plasma densities increased with both power and pressure. Although the plasma density is not as high as in the MPDR 5, the ion production efficiency in the MPDR 325 is the highest among all the MPDRs. More discussions about the production efficiency are given in next chapter.

Uniformity was again one of the major concerns in this reactor. Most of the characterization experiments were conducted at downstream positions where etching experiments were conducted [43,44]. The radial distribution of the plasma density is shown in Figure 5.32. At 14 cm downstream, the variation of the plasma density was 8.1 % over 18 cm. At 18 cm

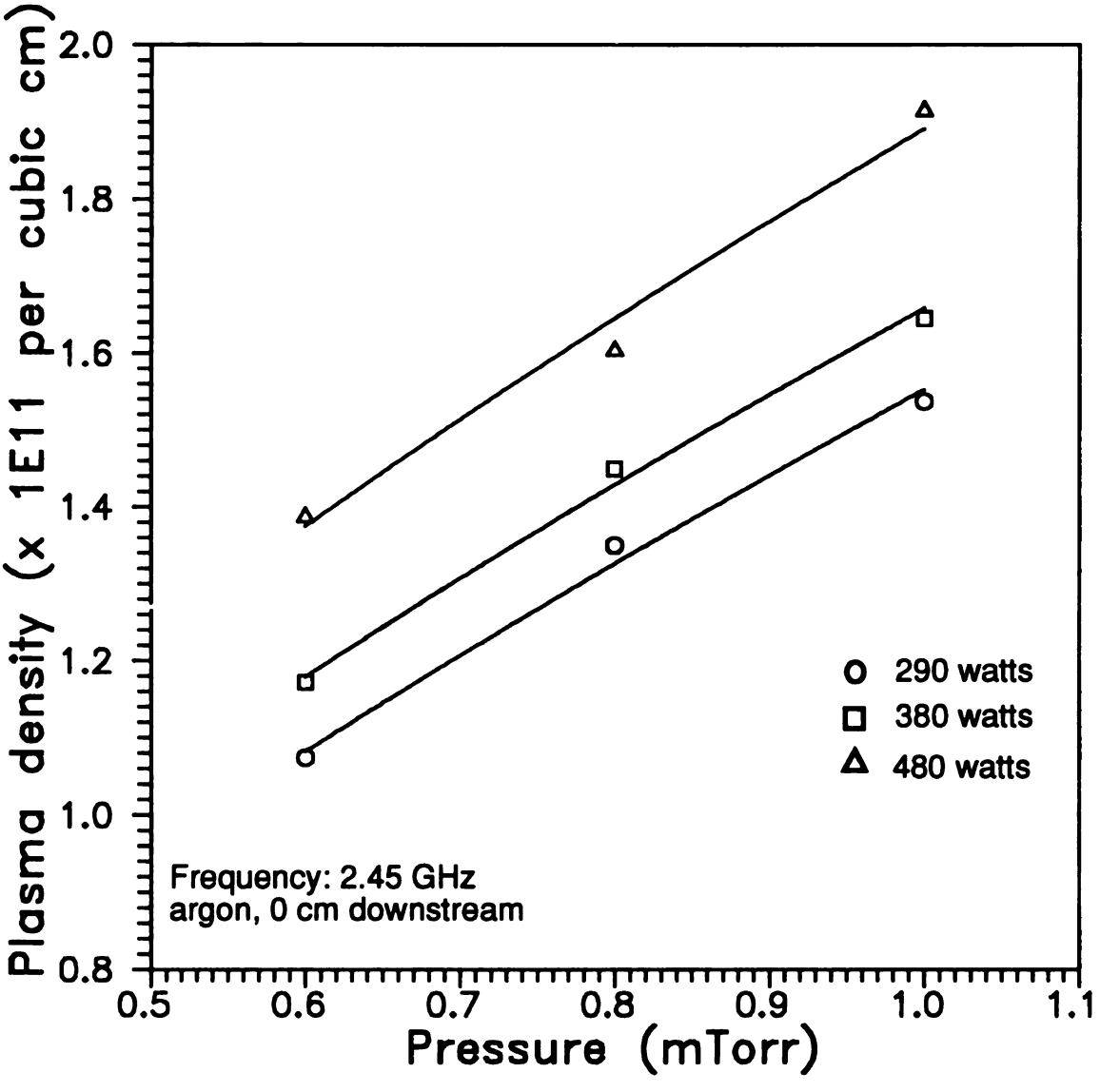

Figure 5.31 Variations of plasma density with pressure at 0 cm downstream and different microwave powers in MPDR 325

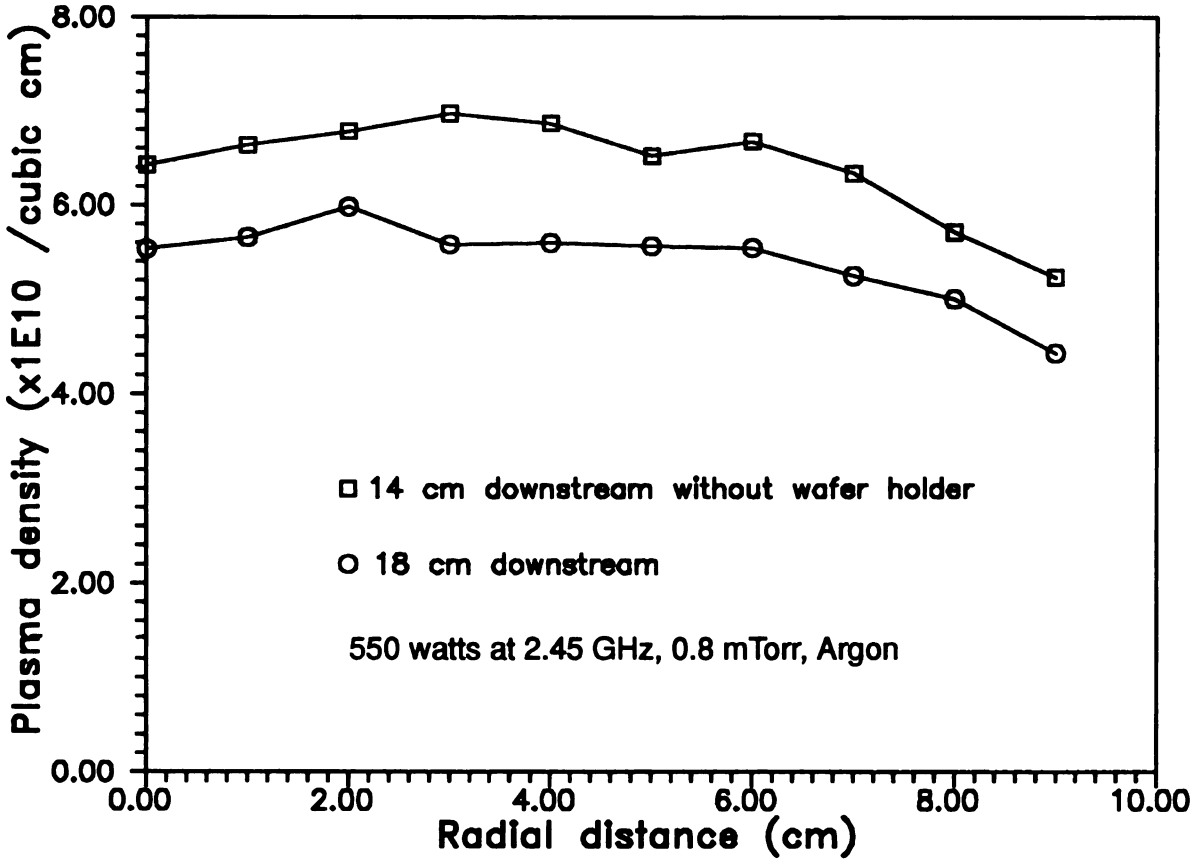

Figure 5.32 Radial distributions of plasma density at different downstream positions in MPDR325

downstream, the variation was 7.5% over 18 cm. Uniformity of the plasma within the downstream confinement structure was further improved by the presence of a 18 cm diameter wafer holder as shown in Figure 5.33 and 5.34. At 14 cm downstream the uniformity of the plasma right above the wafer holder was 3.8 % over 16 cm in diameter. Without the wafer holder, it was 5.4% over 16 cm in diameter. At 18 cm downstream, the uniformity was 3.1% over 16 cm in diameter above the wafer holder. Without the wafer holder, it was 4.7% over the same diameter. This shows that current configuration of the MPDR 325 is capable to process substrate up to seven inches in diameter. Further increase of the substrate diameter require a larger downstream confinement structure. The one used has a 24 cm inner diameter which is too small for the processing of wafers with diameter of eight-inch or above.

Radial distributions of the plasma potential at two different downstream positions and pressures are shown in Figure 5.35. When a wafer holder was placed in the downstream chamber, the plasma potential right above the wafer holder was more uniform than the distribution of plasma potential without the wafer holder. This is shown in Figure 5.36. Without the wafer holder, the uniformity was 2.9% over 16 cm in diameter. With the wafer holder it was 1.9% over the same diameter. The results agreed with the results of the plasma density distribution with wafer holder shown earlier. The variations of average electron energy with pressure and microwave power are shown in Figure 5.37. Without exception, the electron energy went up when the pressure was decreased. At constant pressure, the electron energy increased with the input microwave power.

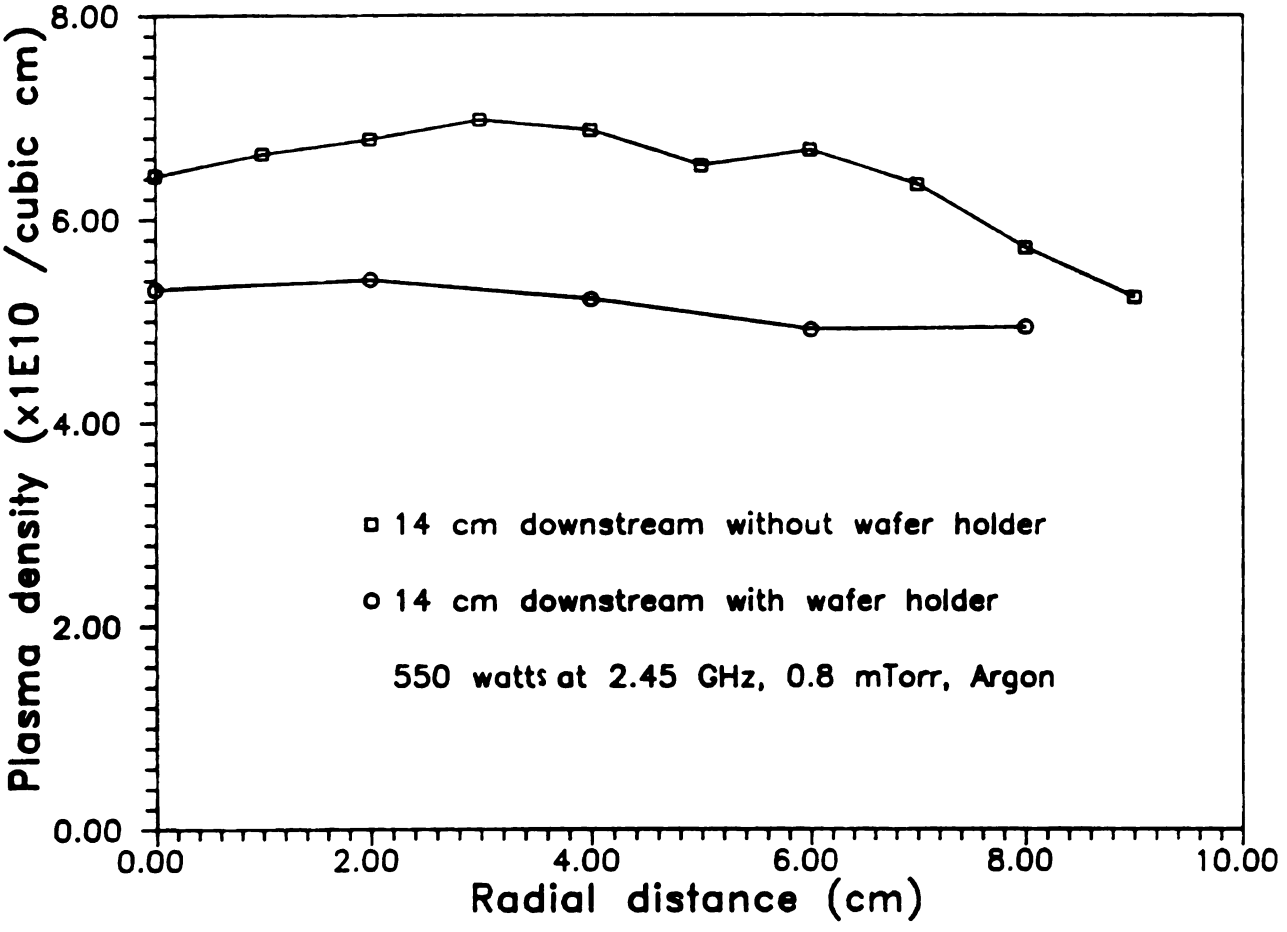

Figure 5.33 Radial distribution of plasma density with and without wafer holder at 14 cm downstream in MPDR 325

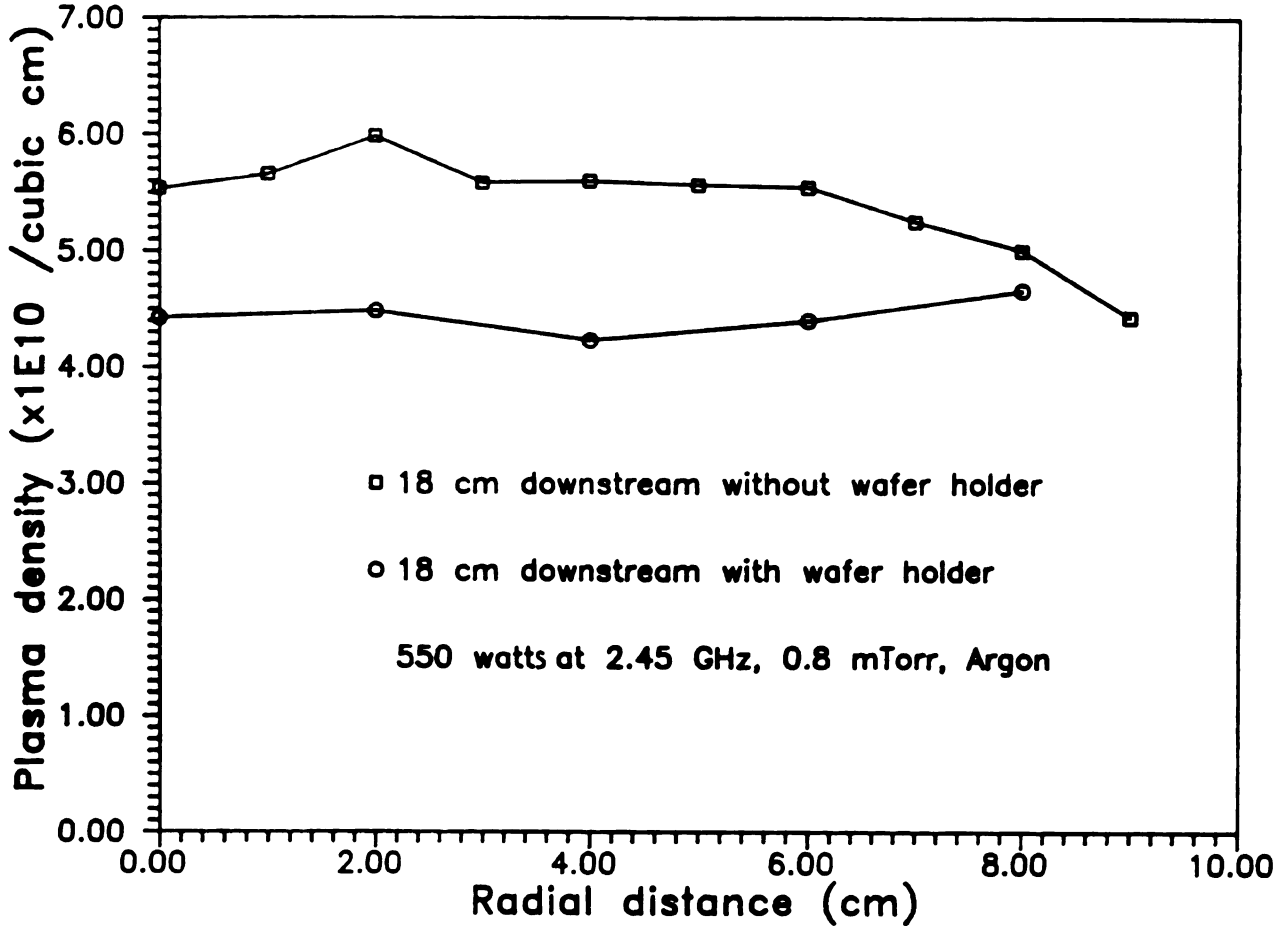

Figure 5.34 Radial distribution of plasma density with and without wafer holder at 18 cm downstream in MPDR 325

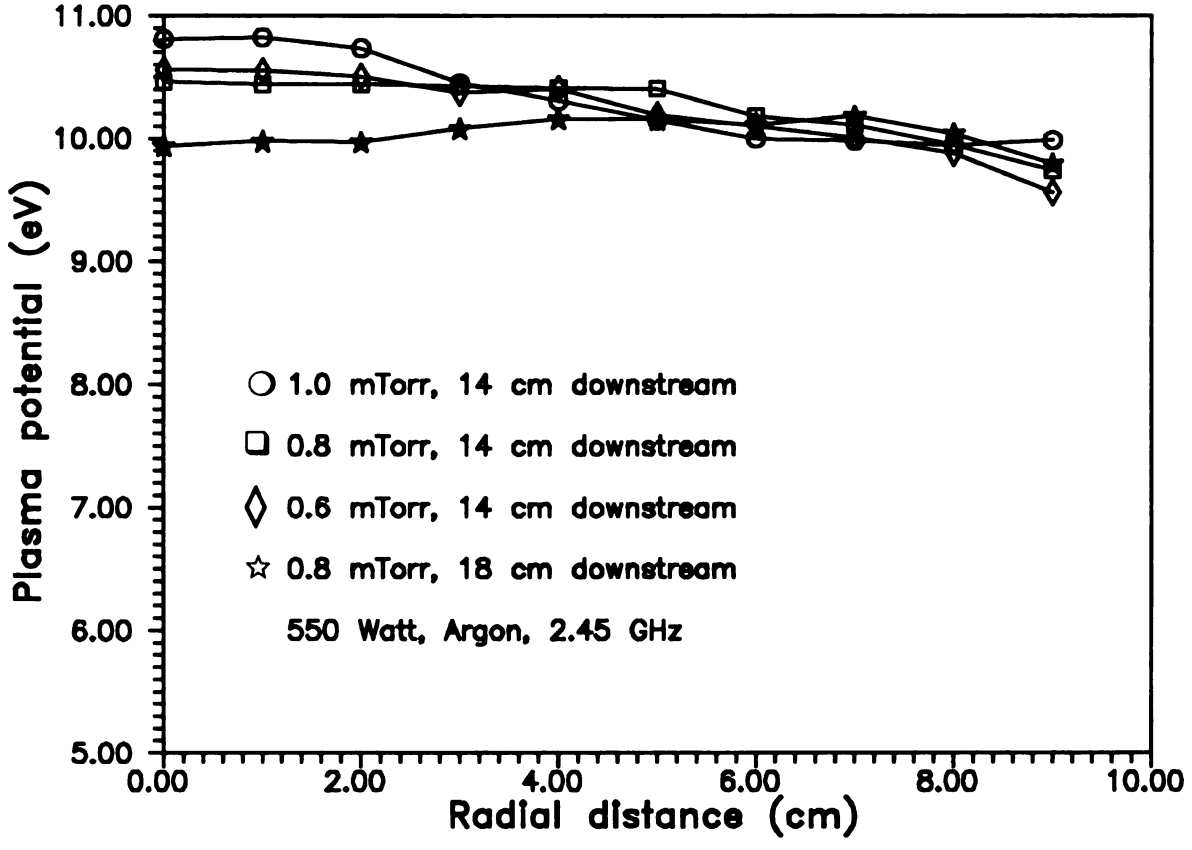

Figure 5.35 Radial distributions of plasma potential at different pressures and positions in MPDR325

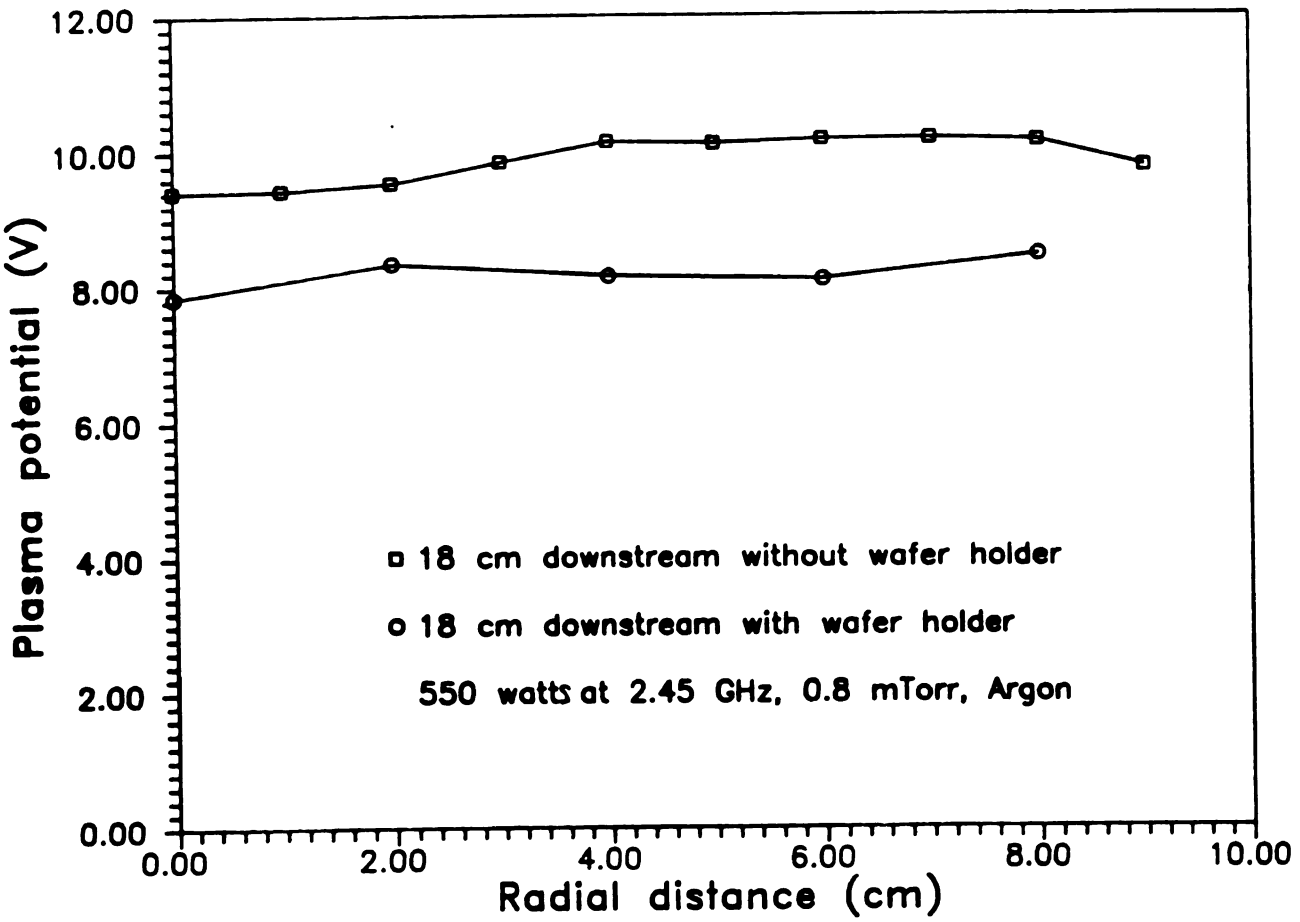

Figure 5.36 Radial distribution of plasma potential with and without wafer holder at 18 cm downstream in MPDR 325

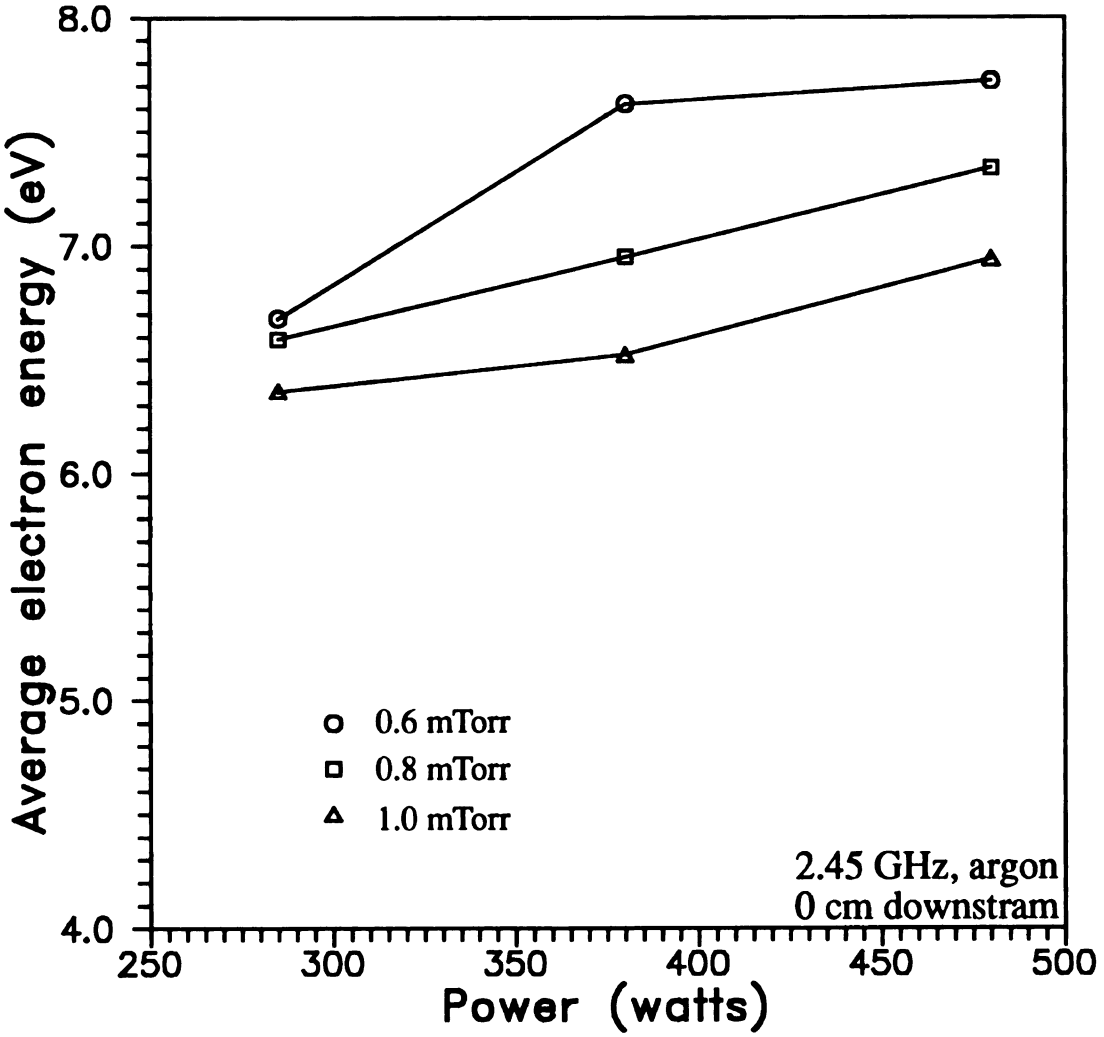

Figure 5.37 Variations of average electron energy with microwave power at 0 cm downstream and different pressrues in MPDR 325

The ion energy distribution functions (IEDFs) of the MPDR 325 are shown in Figure 5.38 and 5.39. Figure 5.38 shows the IEDFs at different pressure 14 cm down below the reactor. As the pressure was decreased, the average ion energy increased from 11.5 eV at 1 mTorr to about 12.8 eV at 0.6 mTorr. FWHM of the IEDFs varied from 7 eV to 9 eV, which were about the same observed in the MPDR 20. Figure 5.39 shows the variations of the IEDFs with microwave input power. Only a slight increase in the average ion energy when the input power was increased from 550 watts to 750 watts. This is indicated by a shift of 2 eV to the right in the IEDF in Figure 5.39. At constant power, the IEDFs at 14 cm downstream and 18 cm downstream were essentially the same. This is also observed in the radial distributions of the average ion energy in Figure 5.40. An average ion energy of about 12 eV is distributed over 16 cm in diameter at both downstream locations. Figure 5.41 shows the radial distribution of the average ion energy at different pressure at 14 cm downstream. Similar plots of the average ion energy are shown in Figure 5.42 at different microwave input power. At 550 watts microwave input power, the ion energy distribution has a uniformity of 4% (1σ) over 16 cm in diameter in a location 14 cm below the reactor at 0.8 mTorr.

5.5.4 Summary

In summary, the MPDR 5 plasma source had a bimodal ion energy distribution that was not observed in other MPDR sources. The bimodal distribution was repeatable and consistent both in downstream direction and radial direction indicating a charge exchange process takes place within 5 cm downstream. Downstream ionization may exist but play a minor role for

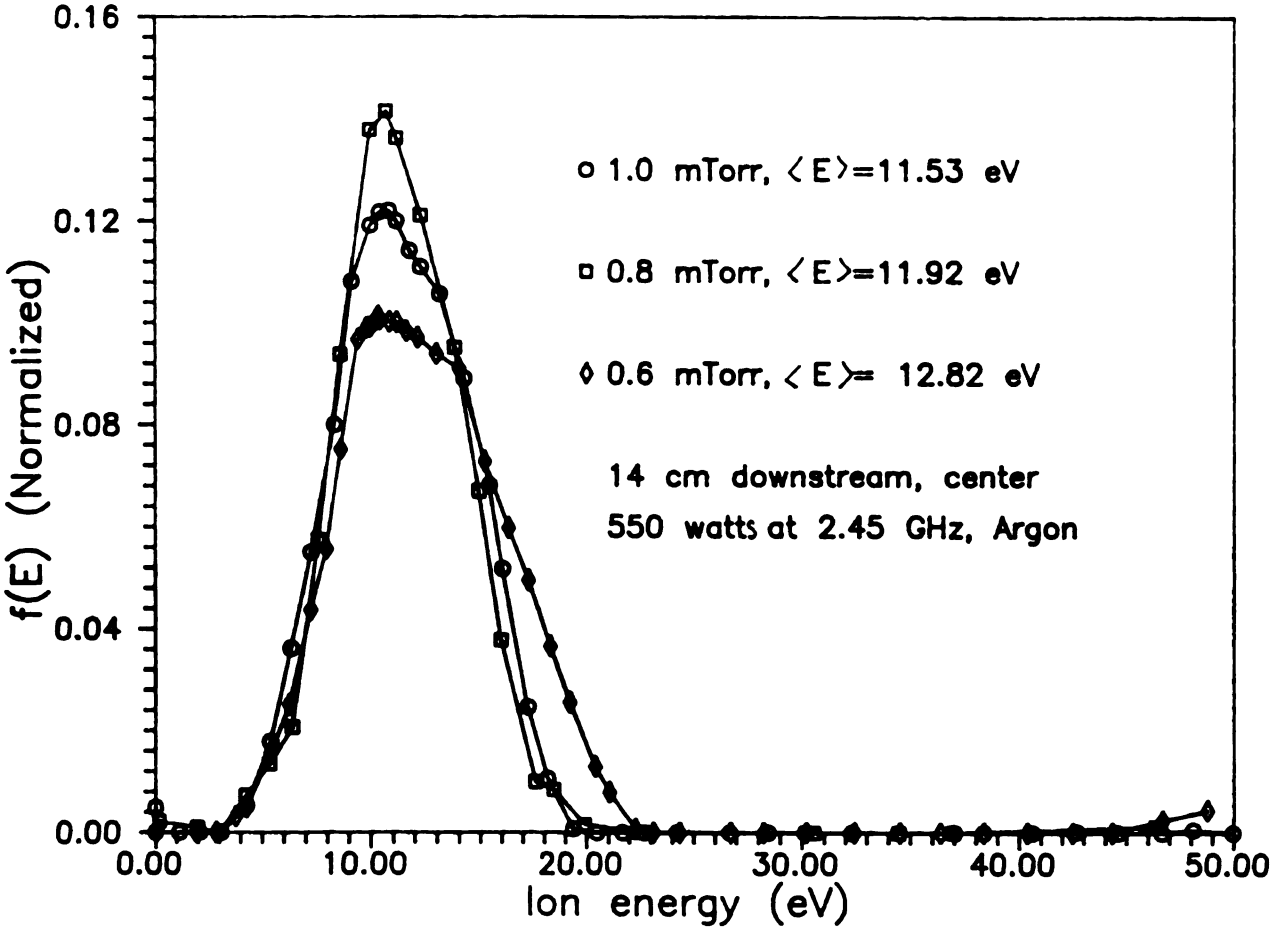

Figure 5.38 IEDF at different pressures in MPDR 325

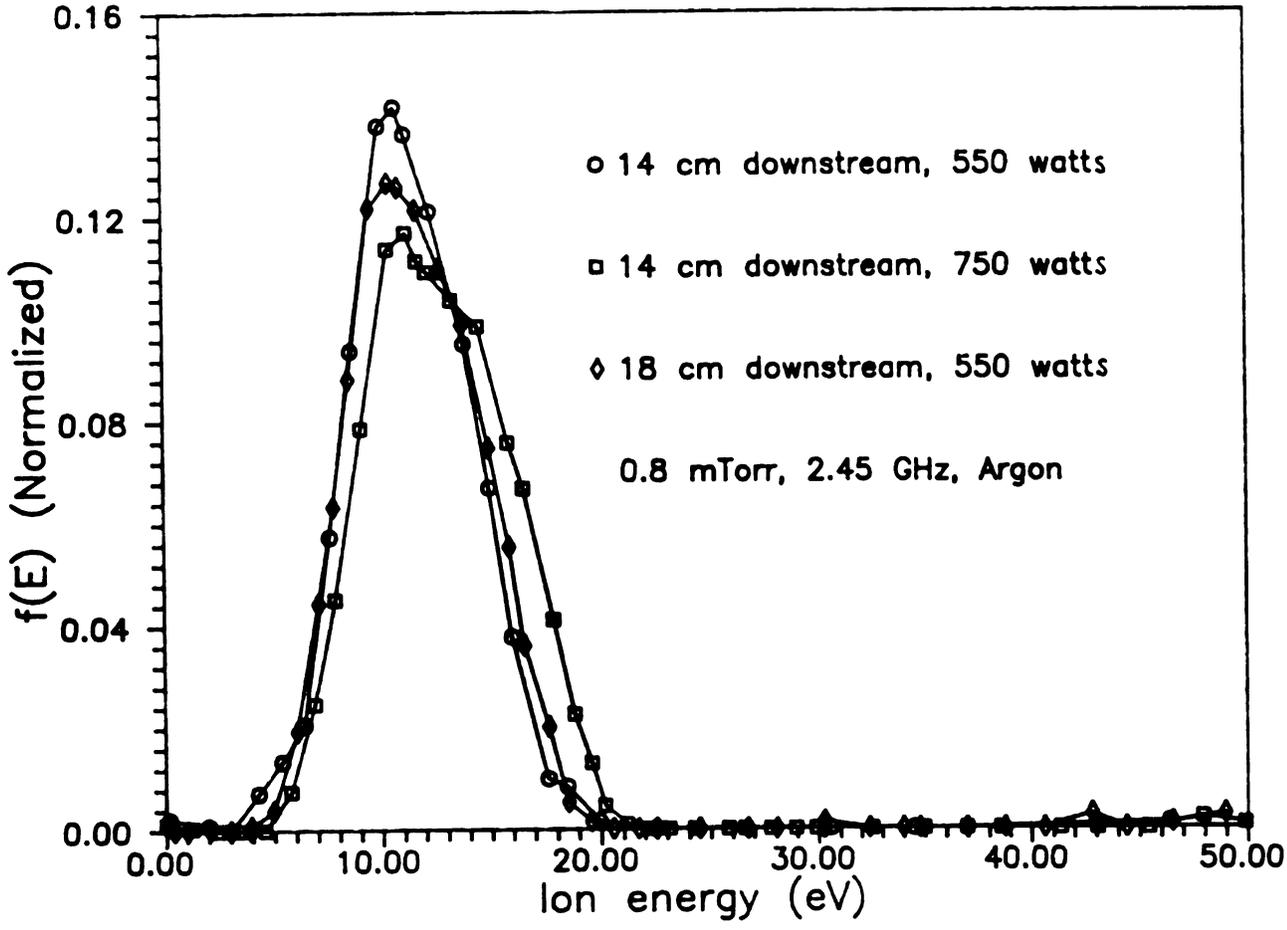

Figure 5.39 IEDF at different microwave power and downstream positions in MPDR 325

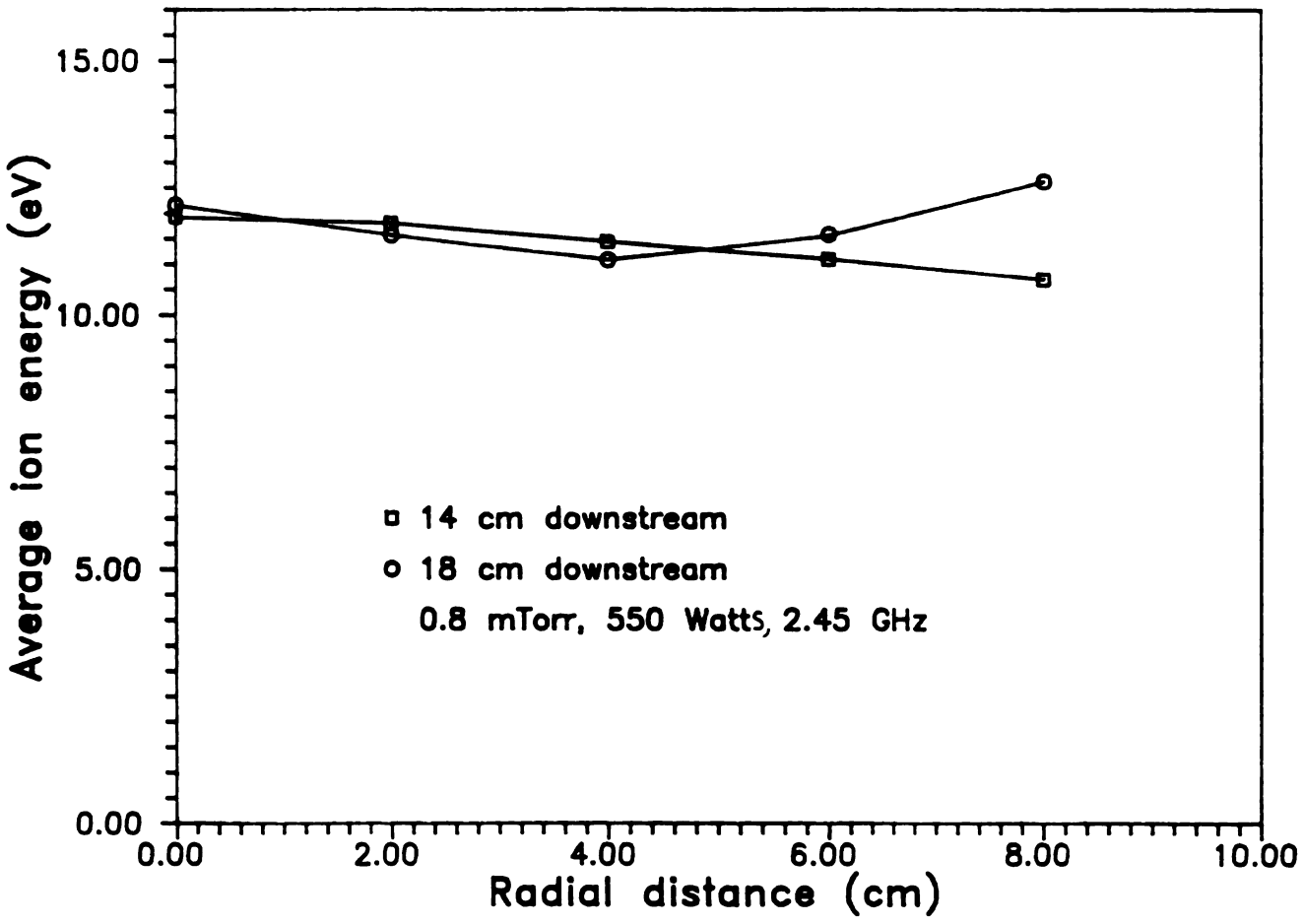

Figure 5.40 Radial distribution of ion energy at different downstream positions in MPDR 325

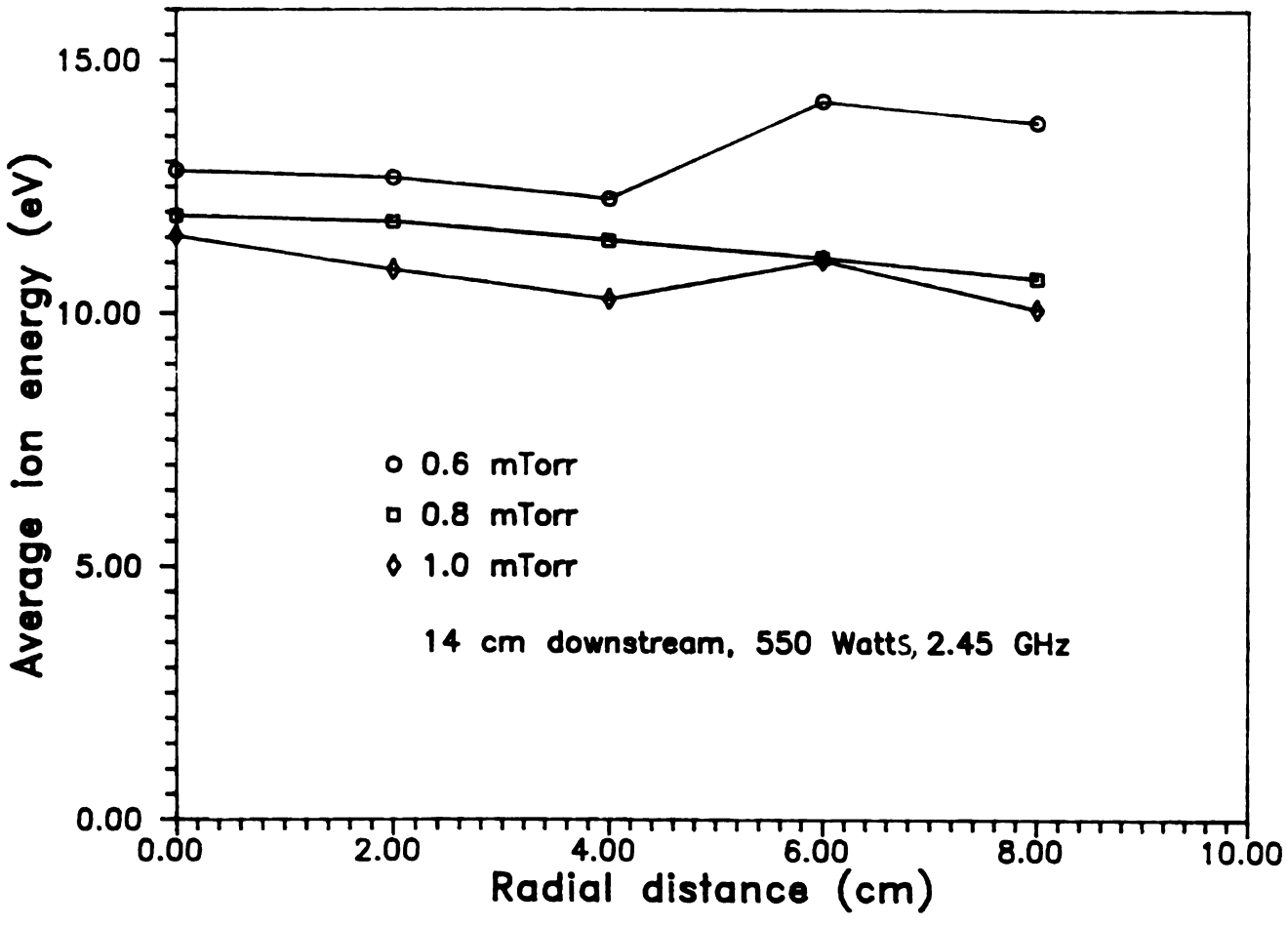

Figure 5.41 Radial distribution of ion energy at different pressures in MPDR 325

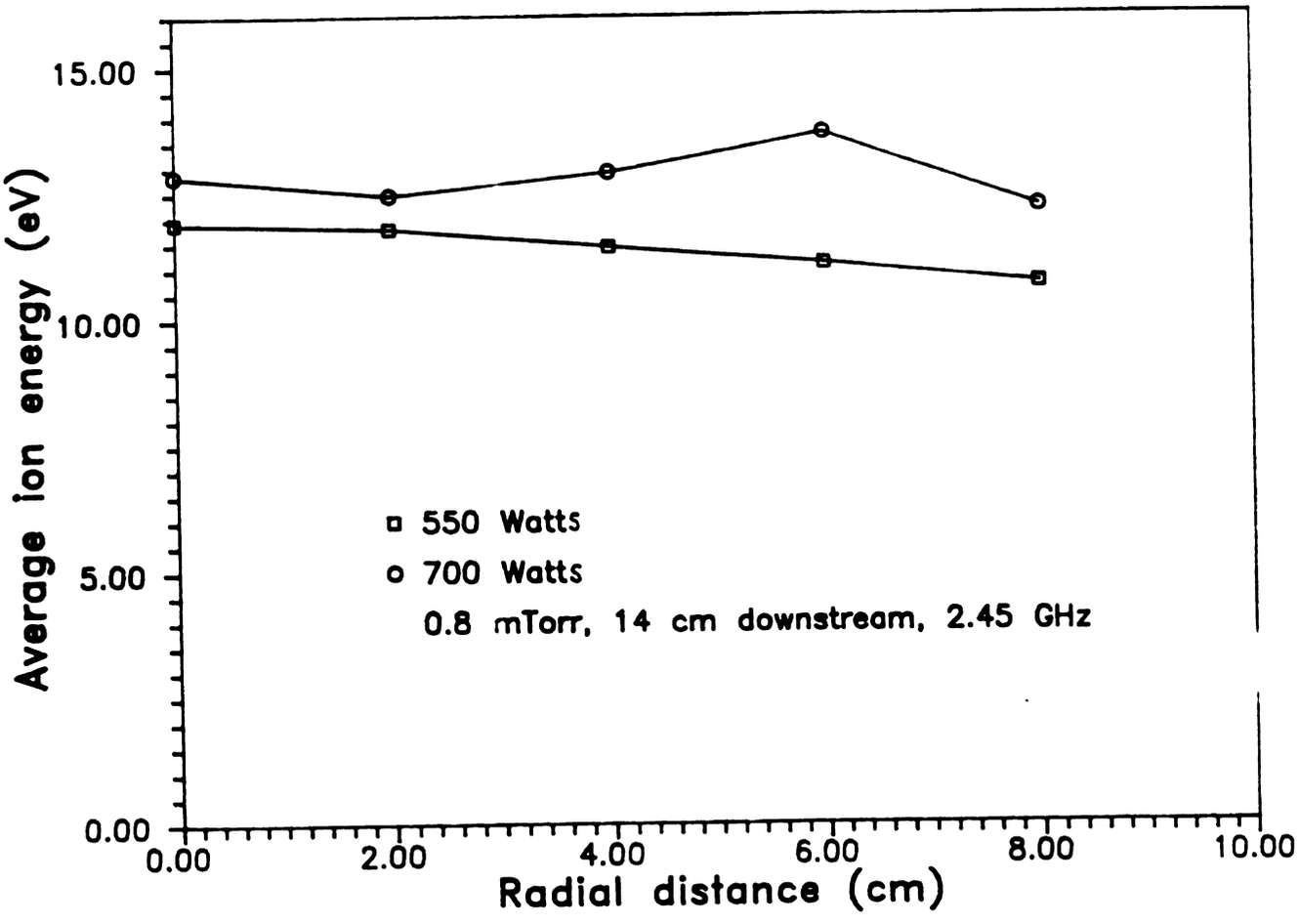

Figure 5.42 Radial distribution of ion energy at different microwave power in MPDR 325

the emergence of the low energy peak in the IEDFs. The source had a high plasma density ($5x10^{11}$ cm^{-3}) at zero downstream position. With an 8-inch in diameter downstream confinement structure, the uniformity of plasma density improved from 92.4% (1σ) at 1.5 cm to 18% (1σ) at 5.5 cm downstream. The average ion energies varied from 12 to 30 eV depending on downstream location. Because of the small size of the discharge volume, the lowest operation pressure is limited to 1.1 mTorr. The microwave power used in this source was limited to 100-190 watts with a power density varied from 2 to 4 watts/cm^3. An increase in microwave power is possible by redesigning the quartz disk. However, a much higher power density is not desirable since the sheath potential will be too high for some applications.

The MPDR 20 plasma source is the only MPDR which was operated with 915 MHz microwave energy. It produced a uniform plasma, 2.6% (1σ) over 18 cm in diameter at 13 cm downstream. It had a low plasma potential, about 10 volts at zero downstream and 7 volts at 14 cm downstream. It has low ion energies, 8 to 10 eV, and a small FWHM (about 8 eV), making the source ideal for etching wafer up to 6 inches in diameter. The reactor was operated at less than 500 watts which was limited by the 915 MHz microwave source.

The MPDR 325 shares all the advantages in MPDR 20. It had a low ion energy plasma (from 10 to 14 eV) and small FWHM (about 8 eV). The plasma was uniform (3.1% over 18 cm at 14 cm downstream) for large diameter wafer processing at downstream location. The MPDR 325 had a high plasma density in the downstream chamber, about $6x10^{10}$ cm^{-3} at 14 cm downstream. The source was operated at about 600 watts microwave.

However, it can be operated at power up to 1500 watts. In addition to those advantages discussed earlier in Chapter Four, the MPDR 325 is the best plasma source in the MPDR family for semiconductor processing.

CHAPTER SIX

PERFORMANCE OF MPDRs VERSUS DISCHARGE SIZE

§6.1 INTRODUCTION

In Chapter Five, the experimental results of three MPDRs are reported. The operation conditions in each MPDR are different from each other. For example, the small MPDR 5 cannot be operated at microwave power greater than 200 watts and the lowest operation pressure is about 1.1 mTorr while microwave power up to 1000 watts can be used in the MPDR 325 and the lowest operation pressure is about 0.4 mTorr.

In the past, many questions concerning specific designs have been solved by intuition or by a "cut and paste" approach. However, important questions remain unanswered. For example, "What is the optimal size for the MPDR ECR plasma source?", "How do the properties of the discharge vary as the input power, discharge pressure and discharge size change?", "How does the microwave coupling efficiency change as the excitation mode or discharge size change?" and "How does the overall ion production cost vary as the design changes?" Answers to these questions will evolve from experimental evaluations and the development of theoretical models of the ECR plasma sources.

This chapter investigates the experimental performance of five different diameter MPDRs using argon plasma. Source performance versus pressure, input power and discharge size are experimentally evaluated using four figures of merit. They are the electron temperature versus pressure-diffusion length product, ion production energy cost, microwave coupling efficiency and discharge power density. The MPDR 5, MPDR 9, MPDR 13 and MPDR 325 are evaluated with 2.45 GHz microwave excitation

frequency while the MPDR 20 is evaluated at 915 MHz. These figures of merit may also be applied to other ECR sources. The definition of each figure of merit is given in section 6.3.

§6.2 Experimental setup

A number of experiments were conducted in each of the MPDRs to evaluate the four figures of merit. Figure 5.2 shows the experimental setup of the experiments. The experimental setup for each MPDR was the same, except that different MPDR was mounted on the top of the vacuum systems. The zero downstream position, z=0cm, was defined as the bottom of the baseplate in each MPDR. Probe measurements of the average electron energy and plasma density were performed at zero downstream position. A 2 mm diameter micro-coaxial probe, as shown in Figure 5.2, was used to measure the electric field strength inside the cavity for the calculation of microwave coupling efficiency. All experiments used downstream plasma confinement structure. As shown in Figure 4.4(b) the MPDR 5, MPDR 9 and MPDR 13 had a 20 cm diameter, eight pole, downstream confinement structure mounted below the stainless steel plate. A 28 cm diameter, twelve pole, downstream confinement structure was used in the evaluation of the MPDR 20 and MPDR 325.

Table 6.1 is a list of information and a collection of plasma data of all the MPDRs. In the table, the cavity inner diameter is listed for each MPDR. The plasma diameter is the inner diameter of the quartz disk. The magnetic configuration represents the number of ECR magnetic cusps arranged in a manner shown in Figure 4.1(b). The discharge volume is defined as the

TABLE 6.1 EXPERIMENTAL DATA FOR MPDRs

Parameters	**MPDR 5** △	**MPDR 9** □	**MPDR 13** ○	**MPDR 325** ☆	**MPDR 20** ✳
Cavity dia. (cm)	8.9	17.8	17.8	35.6	45.7
Plasma dia. (cm)	4.8	9.1	13.1	24.0	19.6
Mag. config.	8 poles	8 poles	8 poles	12 poles	12 poles
Λ (cm)	0.72	1.29	1.81	2.51	2.46
Plasma vol. (cm^3)	54	325	876	3596	2967
Excitation frequency	2.45GHz	2.45GHZ	2.45GHz	2.45GHz	915MHz
Mode	TE_{111}	TE_{211}	TE_{211}	(multimode)	TE_{211}
Input power (watt)	99-184	168-260	247-616	300-500	190-380
Pressure (mTorr)	1.1 - 1.6	0.7-1.3	0.8-1.5	0.6-1.0	0.6-1.5
V_p (V) [a]	18.3-22.6	25.5-36 [c]	17.5-18.5 [d]	9.4-10.8	6.8 -11.8
Ion density (cm^{-3}) [b]	3-5 x1E11	1.3-2 x1E11	1.2-2.5 x1E11	1-2 x1E11	4.6-6 x1E10
$\langle E \rangle_{ion}$ (eV) [a]	12.5 -28.0	19.7 -36.1 [c]	19.5 -21.3 [d]	10.5-14.5	8.4 - 15.0
FWHM (eV) [a]	10.7 -13.6	8.2 -12.5 [c]	10.8 -15.8 [d]	7.0 - 8.7	7.0-8.0

[a] Downstream data ($z \geq 0$ cm)

[b] At $z = 0$ cm

[c] From J. Hopwood [60]

[d] From Mak et al. [46]

Plasma volume = $V = \pi r^2 L$

volume of discharge enclosed by the quartz disk and the boundary at zero downstream position, i.e., z=0 cm, and is equal to $\pi r^2 L$ as shown in Figure 5.2. The parameter, Λ, is the characteristic diffusion length of the discharge volume. The range of input power and pressure listed were the experimental conditions in which the figures of merit were evaluated. The plasma potential (V_p), ion density, ion energy and FWHM were the data either obtained from the experiments or collected from earlier publications [48,60,61,165].

§6.3 Definitions of figures of merit

6.3.1 Electron temperature versus PΛ

One important figure of merit is the discharge electron temperature versus the pressure-characteristic diffusion length product. The electron temperature of the plasma was obtained by single probe measurements taken in the center at z=0 cm downstream position. The characteristic diffusion length, Λ, is defined later by equation (6.7). Two theoretical curves were also generated for reference. One of the two curves was based on Free-Fall Diffusion. The other was based on Schottky or Ambipolar Diffusion.

The mathematical approach used here is similar to Mahoney's work [61]. Details of the derivation in both Free-Fall Diffusion model and Schottky Diffusion model are given. The influence of the neutral temperature on the pressure-characteristic diffusion length curve is also examined.

The starting point of the theoretical analysis is to balance the ionization rate of the neutral molecules with the diffusion loss to the boundary. The ionization rate is represented by $N_o \nu_i V_{eff}$, where N_o is the plasma density, ν_i is the ionization frequency and V_{eff} is the plasma volume.

6.3.1.1 Free-Fall Diffusion

In Free-Fall Diffusion, the Bohm sheath criterion [62] is used to describe the diffusion of the ions towards a wall through a sheath. This model of diffusion through a sheath is only good when the mean free path is much larger than the thickness of the sheath and therefore no collision takes place inside the sheath. A quasi-neutral plasma with Maxwellian distribution outside the sheath is assumed.

Because the electrons move much faster than the ions, they reach a surface and start to accumulate. An electric field is created which repels the incoming low energy electrons but meanwhile attracts the ions towards the surface. At steady state, the flux of the electrons towards the wall is equal to the flux of ions through the sheath. If a planar sheath is assumed, the flux of the ions reaching the surface is [55]:

$$\Gamma_i = \tfrac{1}{2} N_o (k_b T_e / M_i)^{1/2} \qquad (6.1)$$

where N_o is the plasma density, k_b is the Boltzmann constant, T_e is the electron temperature and M_i is the mass of the ions. Assuming a cylindrical

discharge of radius r and length L as shown in Figure 5.2, the volume of the discharge is:

$$V_{eff} = \pi r^2 L \tag{6.2}$$

If ions and electrons cannot diffuse across an azimuthal magnetic field and M is the number of poles in the magnetic configuration, then the effective area for diffusion loss in the plasma volume becomes [171]:

$$A_{eff} = 2\pi r(r + L - \sqrt{A_m}) + MA_m \tag{6.3}$$

where A_m is the pole area of each magnet.

At steady state, the rate of ionization is equal to the rate of diffusion to the wall. Thus:

$$\Gamma_i A_{eff} = N_o \nu_i V_{eff} \tag{6.4}$$

The ionization frequency is given as [61]:

$$\nu_i = N_n \frac{2\sqrt{2}}{(\pi m_e)^{1/2}(k_b T_e)^{3/2}} \int_0^\infty \varepsilon\, \sigma(\varepsilon) \exp(-\varepsilon/k_b T_e)\, d\varepsilon \tag{6.5}$$

where ε is the electron energy, $\sigma(\varepsilon)$ is the ionization cross-section by the electrons and N_n is the neutral density. The neutral density can be expressed in terms of pressure and temperature:

$$N_n = P/T_n k_b \tag{6.6}$$

The characteristic diffusion length is defined as:

$$\Lambda = V_{eff} / A_{eff} \tag{6.7}$$

After substituting equation (6.6) into (6.5) and equations (6.1), (6.2), (6.3) and (6.5) into equation (6.4), following relation can be obtained after rearrangement:

$$P\Lambda = \frac{(k_b T_e)^2}{\int \varepsilon\, \sigma(\varepsilon) \exp(-\varepsilon/k_b T_e)\, d\varepsilon} * \frac{k_b (\pi m_e)^{1/2} T_n}{4(2M_i)^{1/2}} \tag{6.8}$$

where P is the pressure in Pascal and Λ in m. The total cross section, $\sigma(\varepsilon)$, for ionization in argon gas by electron can be found in an earlier publication by Rapp and Englander-Golden [65].

6.3.1.2 Schottky Diffusion

This diffusion model assumes that the mean free path between collision is much smaller than the size of the discharge volume. Since electrons move much faster than the ions, a space electric field is established which accelerates the ions but slows down the electrons. As a result, both ions and electrons diffuse with the same diffusion coefficient, D_a, which is known as Schottky or ambipolar diffusion coefficient.

Considering an infinitesimal volume of discharge with a non-zero space charge field, **E**, the flow of electrons and ions are:

Becau

where

The de

and ele

where

for the

The con

$$\Gamma_e = - N_e\mu_e E - D_e \nabla N_e \tag{6.9}$$

$$\Gamma_i = N_i\mu_i E - D_i \nabla N_i \tag{6.10}$$

Because $N_e=N_i=N$ and $\Gamma_e = \Gamma_i = \Gamma$, it can be shown that:

$$\Gamma = - D_a \nabla N \tag{6.11}$$

where

$$D_a = \frac{\mu_i D_e + \mu_e D_i}{\mu_e + \mu_i} \tag{6.12}$$

The definitions of the mobility, μ, and diffusion coefficient, D, for the ions and electrons are given as below:

$$\mu_i = e / M_i \nu_{im} \quad , \quad \mu_e = e / m_e \nu_{ie}$$

$$D_i = k_b T_i / M_i \nu_{im} \quad , \quad D_e = k_b T_e / m_e \nu_{ie} \tag{6.13}$$

where ν_{im} and ν_{ie} are the collision frequencies of the momentum exchange for the ions and electrons respectively.

The continuity equation is given below:

$$\frac{\partial N}{\partial t} - \nu_i N + \nabla \cdot \Gamma = 0 \tag{6.14}$$

Using equation (6.11), it can be shown that, at steady state, the following relation can be obtained:

$$\nabla^2 N + (\nu_i/D_a)N = 0 \tag{6.15}$$

By the method of separation of variables and using a cylindrical coordinate system, an approximate solution for equation (6.15) is given below:

$$N(r,z)=N_o J_o(2.405r/R)\cos(\pi z/L) \tag{6.16}$$

where R and L is the radius and length of the discharge respectively. The plasma density is zero on the boundary when $z = \pm L/2$ or $r = R$. N_o is the plasma density at the center of the cylindrical discharge volume. The relation of the ν_i and D_a can be obtained using equation (6.15):

$$\nu_i = D_a [(2.405/R)^2 + (\pi/L)^2] \tag{6.17}$$

Since the temperature of electron is much higher than the temperature of ion inside the plasma, D_a can be approximated by $\mu_i k_b T_e/e$ and the mobility is:

$$\mu_i = \tau e / M_i \tag{6.18}$$

$$\tau = \lambda \langle v_i \rangle / \langle v_i^2 \rangle \tag{6.19}$$

where τ is the relaxation time. For a Maxwellian distribution, the mean free path between collision is:

$$\lambda = 1/\sqrt{2} N_n Q_{nn} \tag{6.20}$$

Q_{nn} is the collision cross section of the argon molecules [63] and equals to 4.2×10^{-19} m^2. $\langle v_i \rangle$ and $\langle v_i^2 \rangle$ for Maxwellian distribution are:

$$\langle v_i \rangle = (8k_bT_n/\pi M_i)^{1/2} \tag{6.21}$$

$$\langle v_i^2 \rangle = 3k_bT_n/M_i \tag{6.22}$$

where T_n is the neutral temperature. Using equation (6.5) and substituting all the variables into equation (6.17), following relation can be obtained:

$$(P\alpha)^2 = \frac{(k_bT_e)^2}{\int \varepsilon\, \sigma(\varepsilon) \exp(-\varepsilon/k_bT_e)\, d\varepsilon} * \frac{k_b^2T_n(m_eT_eT_n)^{1/2}}{3\sqrt{2}\, M_i^{1/2}Q_{nn}} \tag{6.23}$$

where P is the pressure and α is the characteristic diffusion length in Ambipolar Diffusion model and is defined as below:

$$\alpha = [(2.405/R)^2 + (\pi/L)^2]^{1/2} \tag{6.24}$$

The values of Λ and α for each reactor are listed in Table 6.2. Figure 6.1 shows the variation of electron temperature with $P\Lambda$ at different neutral temperatures. The unit for the pressure is converted into Torr and Λ into centimeter because they are commonly used in experimental environment. As shown in the figure, at constant pressure, electron temperature has to be high to sustain a plasma in a small discharge volume, which has a small Λ value. On the other hand, at constant Λ, the electron temperature goes up when the pressure goes down. A higher ionization rate, which is related to the electron temperature, is therefore needed to compensate the diffusion loss at low pressure. Figure 6.1 also indicates that an increase of the neutral

TABLE 6.2 CHARACTERISTIC LENGTH FOR MPDR

MPDR	Λ (cm)	α (cm)
5	0.72	.69
9	1.29	1.21
13	1.81	1.64
20	2.46	2.26
325	2.51	2.48

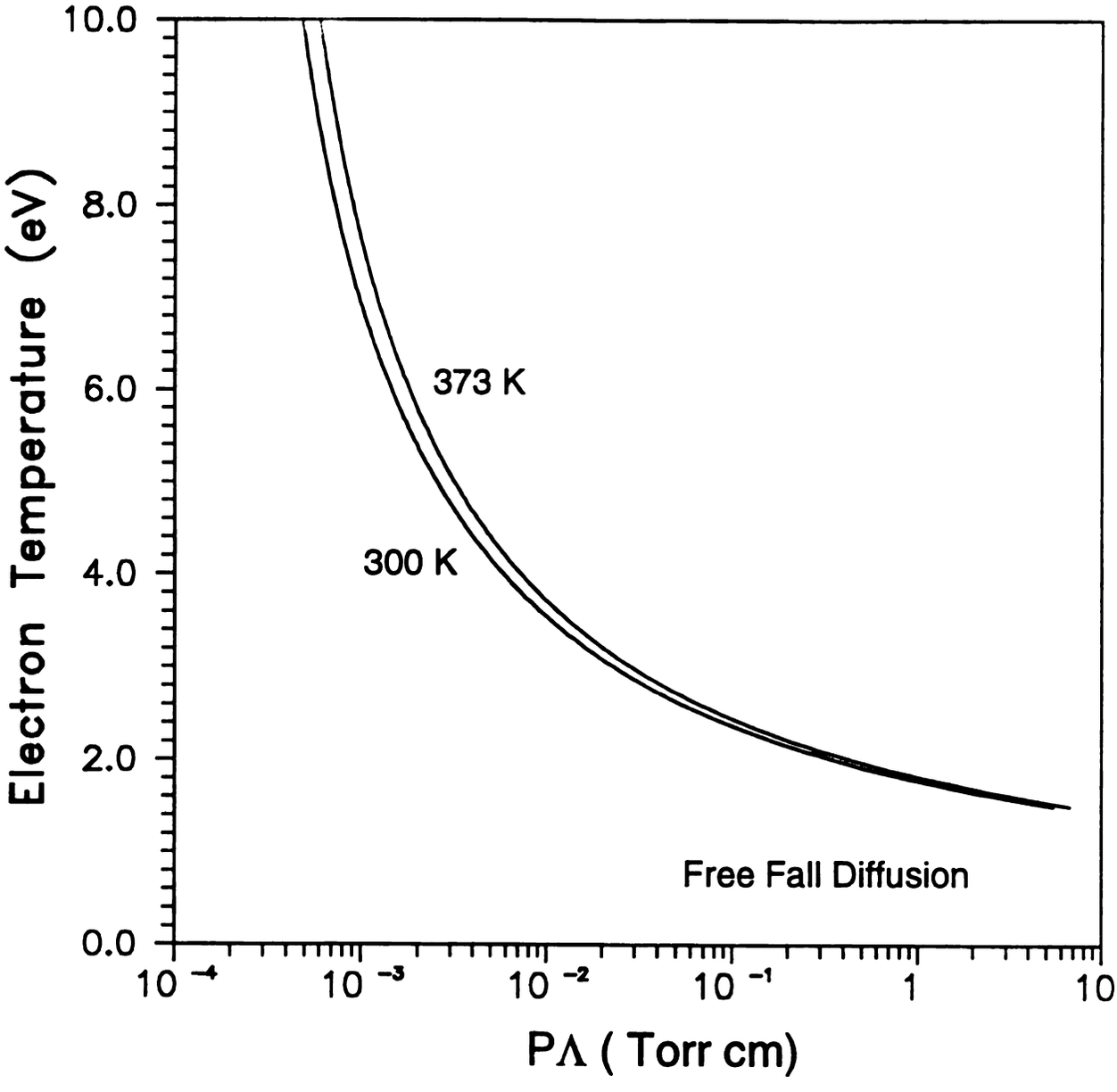

Figure 6.1 Electron Temperature versus CPΛ at different neutral temperatures

temperature from 27 °C to 100 °C shifts the curve to the right. Such shift represents a small increase in the electron temperature when $P\Lambda$ is large, but a big increase electron temperature at small $P\Lambda$. A similar result is also obtained for ambipolar diffusion as shown in Figure 6.2. It is necessary to point out that the values of α and Λ are very close to each other as shown in Table 6.2. Thus the values of $P\alpha$ and $P\Lambda$ are nearly the same in a semilogarithmic plot as shown in Figure 6.1 and 6.2.

6.3.2 Microwave coupling efficiency

The microwave coupling efficiency is another figure of merit to examine the performance of the MPDRs. The technique was developed by Rogers [192] and Manring [166] and is defined as:

$$\text{Coupling efficiency} = 100\ \% \times (1 - Q_u/Q_{uo}) = 100\% \times (P_a/P_t) \tag{6.25}$$

where Q_{uo} is the empty cavity quality factor, Q_u is the (plasma) loaded cavity quality factor, P_a is the power absorbed by the plasma and P_t is the total power input to the cavity. Without repeating Manring's work, the relation of the loaded and empty cavity quality factor is listed below:

$$Q_u = Q_{uo} \frac{P_{to}}{|E_{ro}|^2} \cdot \frac{|E_r|^2}{P_t} \tag{6.26}$$

where P_{to} is the net power to the cavity without the plasma, E_{ro} is the radial electric field at a specific spot of the resonant mode, P_t is the net power to

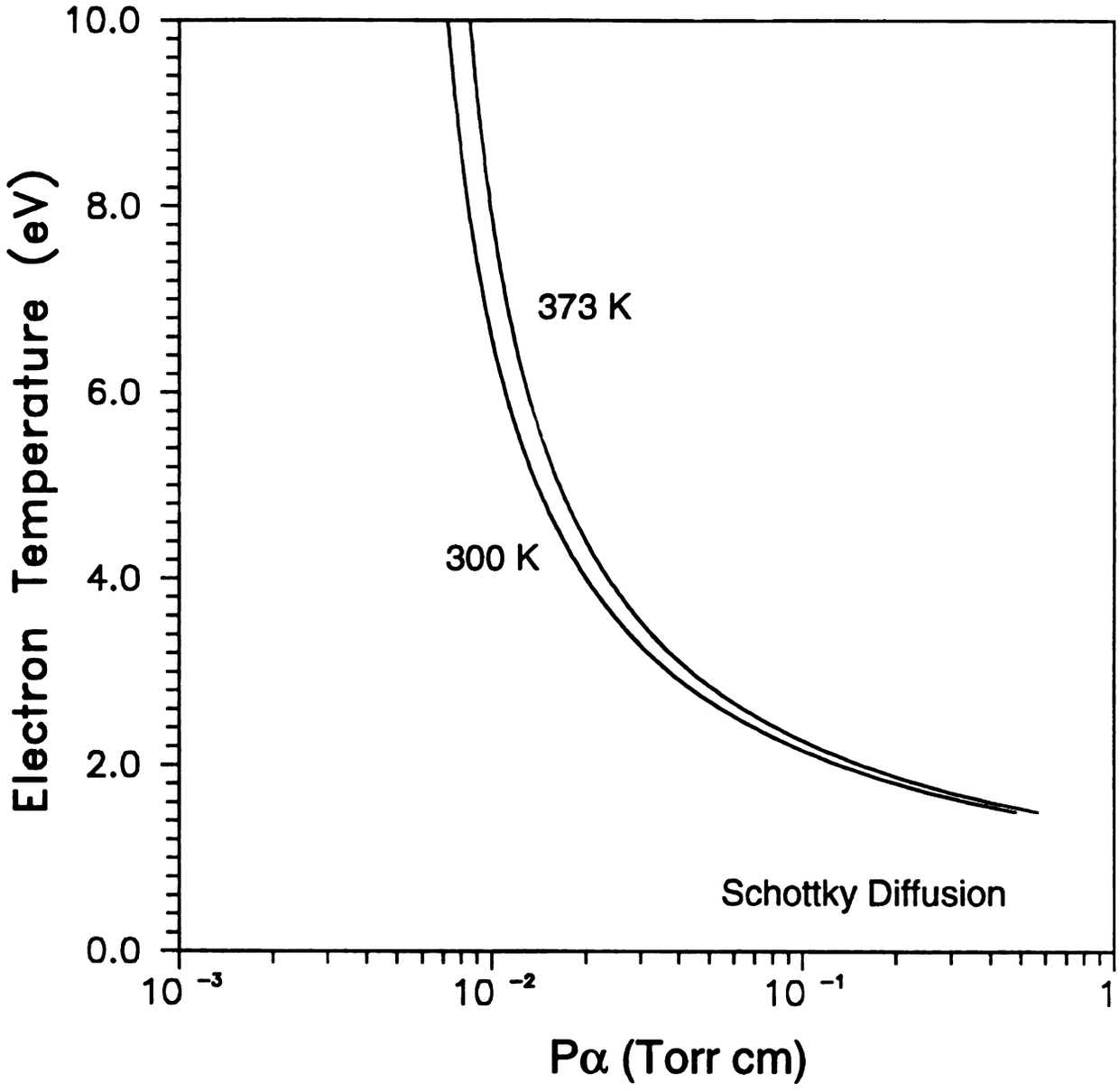

Figure 6.2 Electron Temperature versus CPα at different neutral temperatures

the cavity with plasma and E_r is the radial electric field at the same spot of the resonant mode with plasma. By substituting equation (6.26) into equation (6.25), following relation is obtained:

$$\text{Coupling efficiency} = 100\ \% \times \left(1 - \frac{P_{to}}{|E_{ro}|^2} * \frac{|E_r|^2}{P_t}\right) \qquad (6.27)$$

The radial electric field strengths, $|E_r|$ and $|E_{ro}|$, can be measured by a micro-coaxial probe as shown in Figure 5.2. Two millimeter diameter holes were drilled both vertically on the wall and along the circumference of the cavity in the MPDR 5, MPDR 9, MPDR 13, MPDR 20 and MPDR 325 sources. The mode of excitation was identified before the measurement of the coupling efficiency. This measurement technique is valid only for single mode excitation. The MPDR 5 was operated at TE_{111} mode. The MPDR 9, MPDR 13 and MPDR 20 were operated at TE_{211} mode. A TE_{711} mode, which was the only single mode identified in the reactor, was used in the MPDR 325. The problem of this mode was that it was not a good resonant mode. Without a discharge, more than 20% of the incident power was reflected. All other reactors had less than 2% reflected power. The plasma created by this mode was also weak and microwave propagated down the vacuum chamber. Moreover, the reflected power went up to about 25%. Therefore, this mode is not recommended for normal operation.

A spot that had the strongest electric field strength was chosen to insure the best accuracy of measurement. Calibration of the ratio P_{to}/P_{po} was performed by using a sweeping oscillator (HP8350B) operating in the

cw single frequency mode. The frequency of the signal was adjusted to the same frequency of the microwave source which was used to excite the plasma. P_{to} and P_t, were the net microwave power absorbed by the cavity. They should not include any power loss in the transmission cables.

6.3.3 Ion production energy cost and power densities

The ion production energy cost is defined as [191]:

$$\text{Energy cost} = P_t / \int_{A_s} J_s dA \ \text{(eV/ion)} \tag{6.28}$$

where P_t is the net microwave input power, J_s is the ion saturation current density which can be extracted from the plasma generation region and A_s is the area of the opening at z=0cm for each MPDR through which the ions diffuse downstream for processing. The ion saturation current density, J_s, which flows through a planar sheath is:

$$J_s = 0.5 e N_o (k_b T_e / M_i)^{1/2} \tag{6.29}$$

where N_o is the plasma density, T_e is the electron temperature, M_i is the mass of argon ion and **e** is the electron charge. If the plasma density is uniform inside the plasma volume, then the ion production energy cost is:

$$\text{Energy cost} = P_t / (J_s A_s) \tag{6.30}$$

where A_s is the total cross sectional area of the discharge in each MPDR which opens to the downstream chamber. Since current can be expressed as rate of flow of charged particle, therefore the energy cost can be expressed in units of eV per singly charged ion. Both the plasma density and the electron temperatures were taken at the center of the discharge opening at zero downstream.

The power density is defined as:

$$\text{Power density} = \frac{\text{Total microwave input power}}{\text{plasma volume}} = \frac{P_t}{V_{eff}} \qquad (6.31)$$

When determing the ion production energy cost and the absorbed power density, all MPDRs were operated at their normal operation mode as shown in Table 6.1. In other words, the MPDR 325 was operated at multimode instead of TE_{711} mode, which was used in the evaluation of microwave coupling efficiency.

§6.4 Experimental results

Figure 6.3 shows the distributions of the experimental T_e versus PΛ data as well as the two theoretical diffusion curves at room temperature. Data points from a divergent ECR source [11] are also displayed. Figure 6.3 indicates that electron temperatures in the MPDRs are lower than those predicted by the two simple diffusion models. In general, the electron

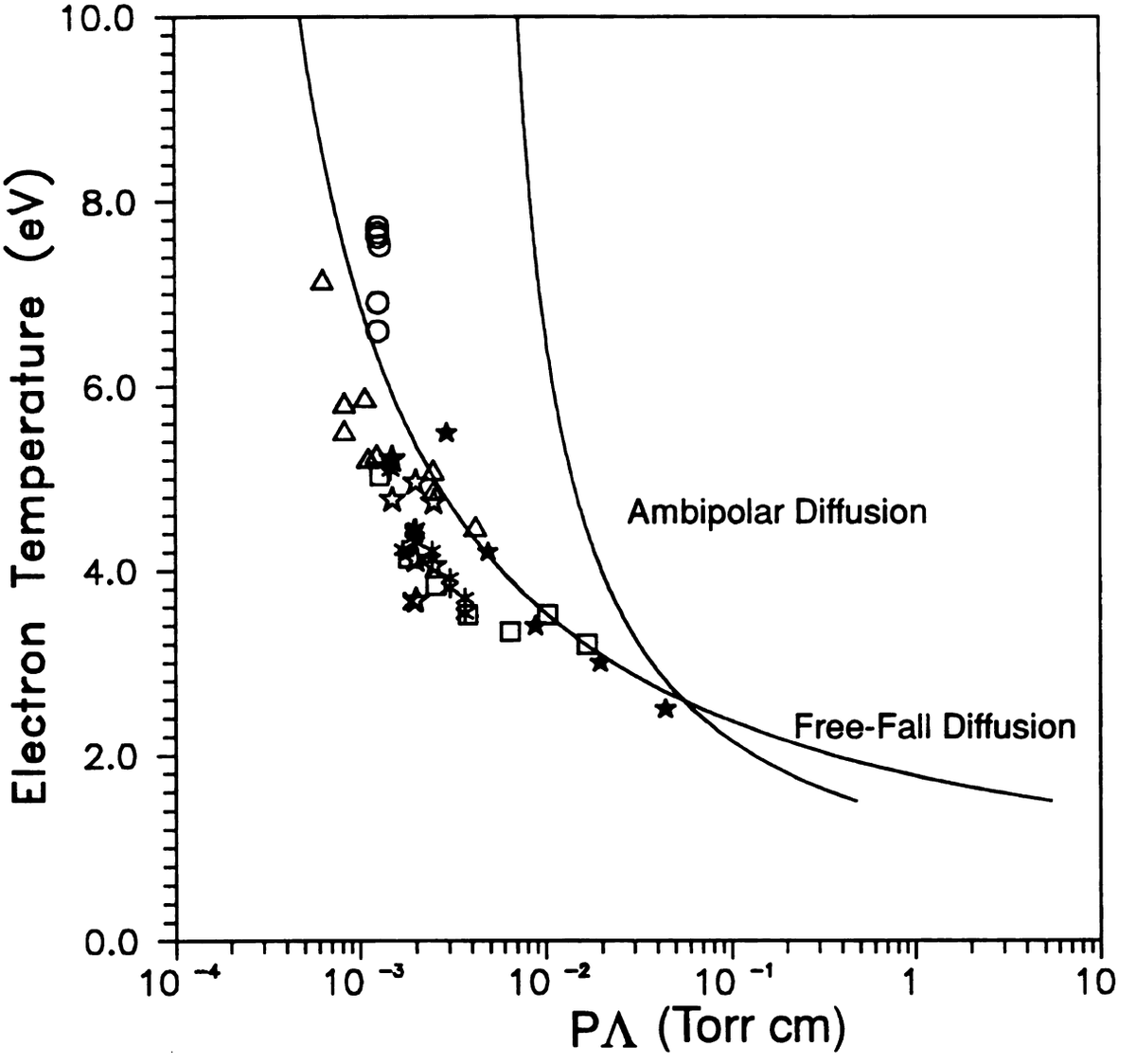

△ MPDR 5

❑ MPDR 9

○ MPDR 13

✶ MPDR 20

☆ MPDR 325

★ Axial Divergent Field ECR source

Figure 6.3 Distributions of the experimental CPΛ data

temperature of the discharge in the MPDRs increases when the PΛ value decreases.

Figure 6.4 shows the microwave coupling efficiency versus the characteristic length of the MPDR. As shown Figure 6.4, within the operation conditions listed in Table 6.1, the microwave coupling efficiencies of all the MPDR sources, except the MPDR 325, were higher than 75%. The coupling efficiencies were above 90% in the MPDR 9 and MPDR 13 while the MPDR 20 had an efficiency between 80-90%. The MPDR 325 has lower coupling efficiencies than the other sources.

Figure 6.5 shows the relation between the coupling efficiency and the discharge pressure. For MPDR 5, the coupling efficiencies were basically the same over the range of pressure in which it was operated. The same was true to the large MPDR 20 source. However, for MPDR 9 and MPDR 13, there was a slight decrease in coupling efficiency as the pressure went up from 0.6 to 1.2 mTorr. For MPDR 325, the coupling efficiency went down as the discharge pressure went up.

Figure 6.6 is another view of the coupling efficiency in each MPDR versus the microwave input power. At constant pressure, the coupling efficiencies were about the same as the power increased in most MPDRs. The only exception was the MPDR 325, which showed an increase in efficiency with the microwave power. Figure 6.5 and Figure 6.6 indicate that the microwave coupling efficiency in each MPDR is not strongly dependent on the pressure and microwave input power within the range of operation conditions investigated in these experiments.

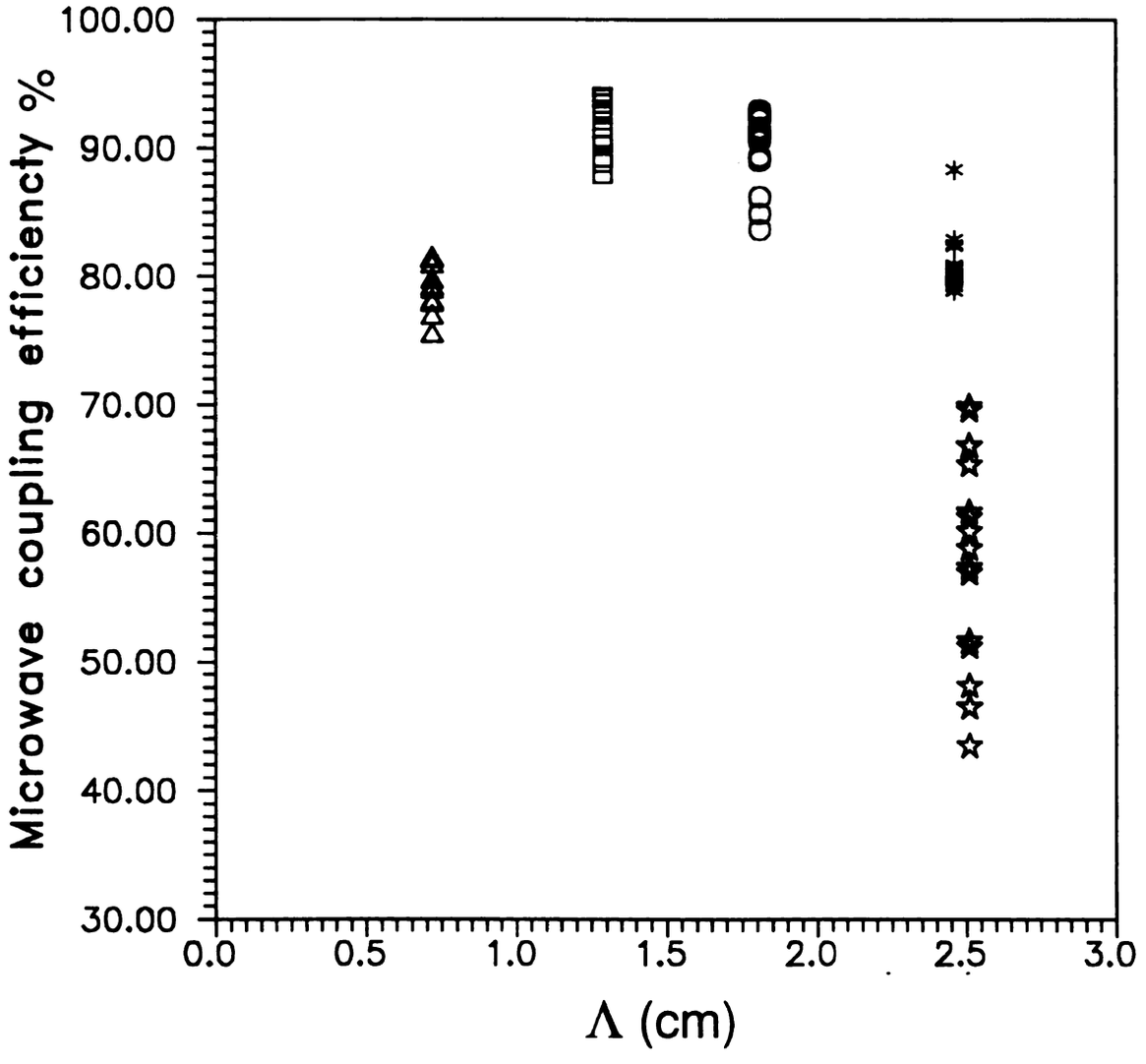

Figure 6.4 Microwave coupling efficiency versus Λ

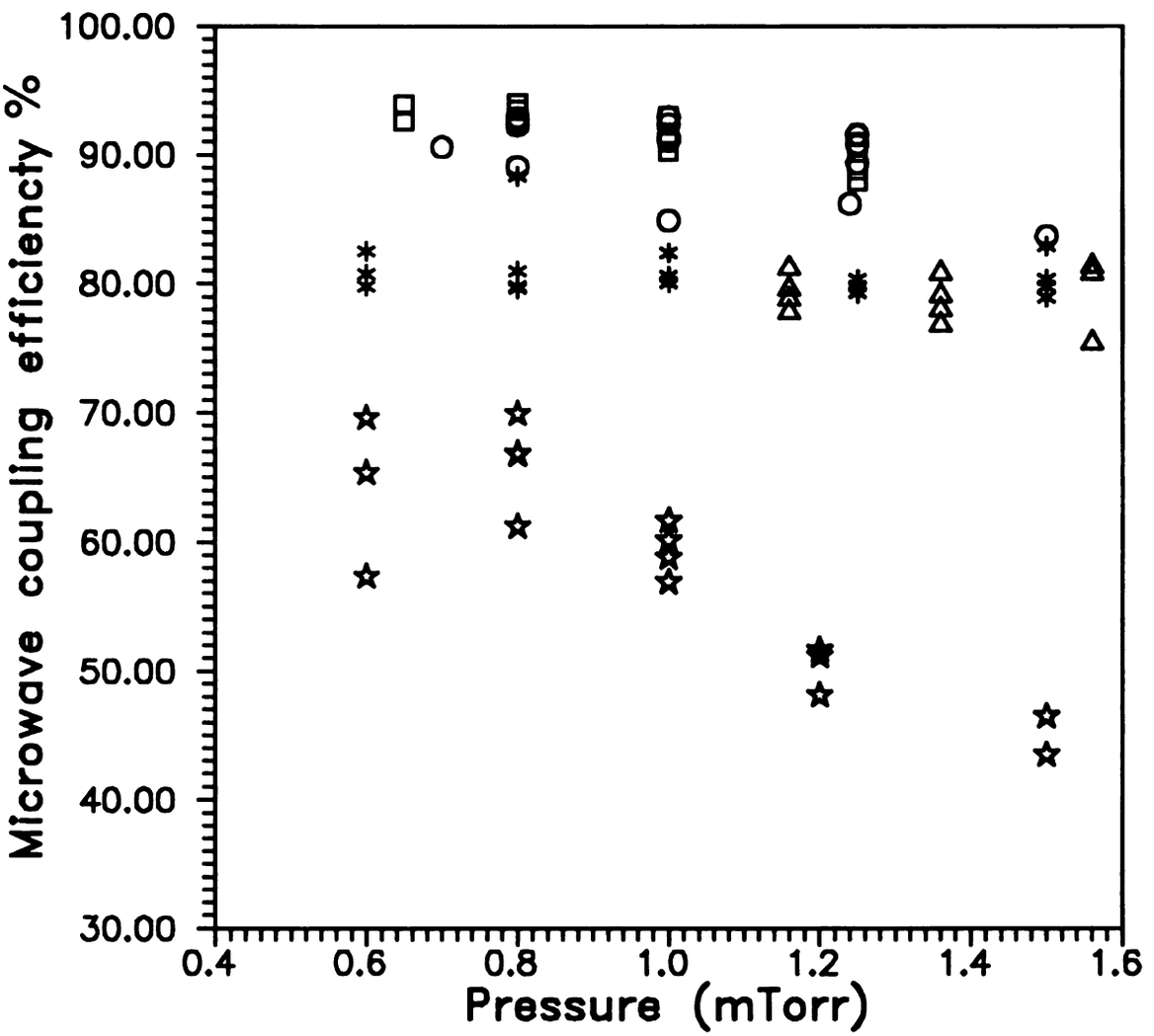

Figure 6.5 Microwave coupling efficiency versus pressure

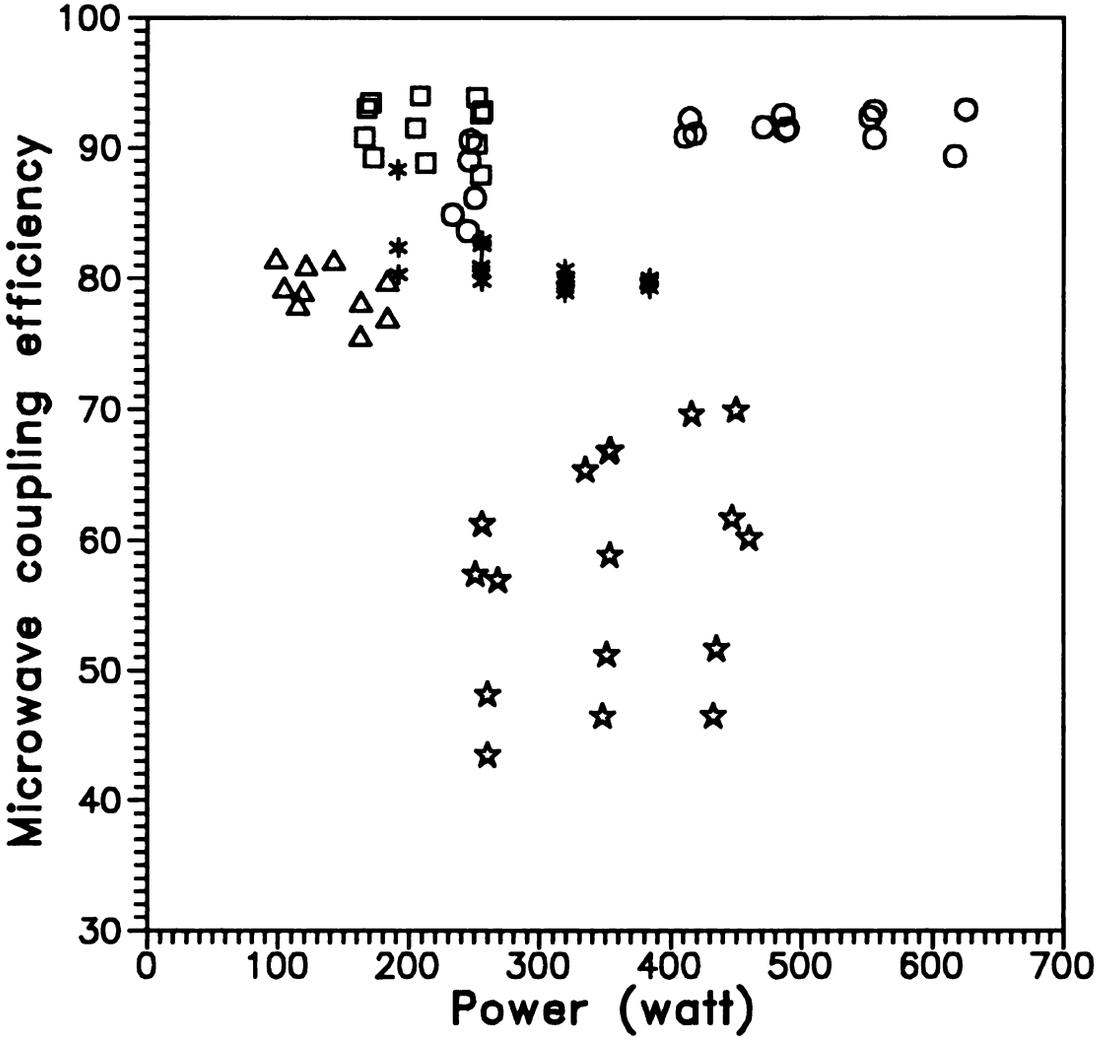

Figure 6.6 Microwave coupling efficiency versus microwave power

The ion production energy cost versus Λ is shown in Figure 6.7. The solid line represents those MPDRs which were operated at approximately the same pressure and power (1.0-1.2 mTorr and 150-260 watts). It shows that the ion production energy cost reaches a maximum in MPDR 9, about 620 eV per ion, and a minimum in the MPDR 325, about 220 eV per ion. This means that the MPDR 325 is the most efficient plasma source among the MPDRs. It should be noted that in this case the MPDR 325 was operated in multimode.

Variation of the ion production energy cost with pressure is shown in Figure 6.8. At constant microwave power, the ion production efficiency goes down as the pressure is decreased. This is because the plasma density decreases when the pressure is decreased as shown in Figure 5.20. Figure 6.9 shows the variation of the ion production energy cost versus microwave input power. Results show that at constant pressure ion production cost increases with input microwave power. In other word, the efficiency goes down as the microwave input power goes up.

Figure 6.10 displays the experimentally measured power densities versus Λ. The MPDR 5 was operated at power densities an order of magnitude higher than the MPDR 325. This is because the surface to volume ratio in a smaller discharge is large. The diffusion loss is high resulting a high power density and a high ionization rate to maintain the discharge. The lowest power density needed to create a discharge in the MPDR 5 was about 2 watts/cm^3. On the other hand, the lowest power density for the large diameter MPDR to sustain a discharge is about 0.06 watt/cm^3 in the MPDR

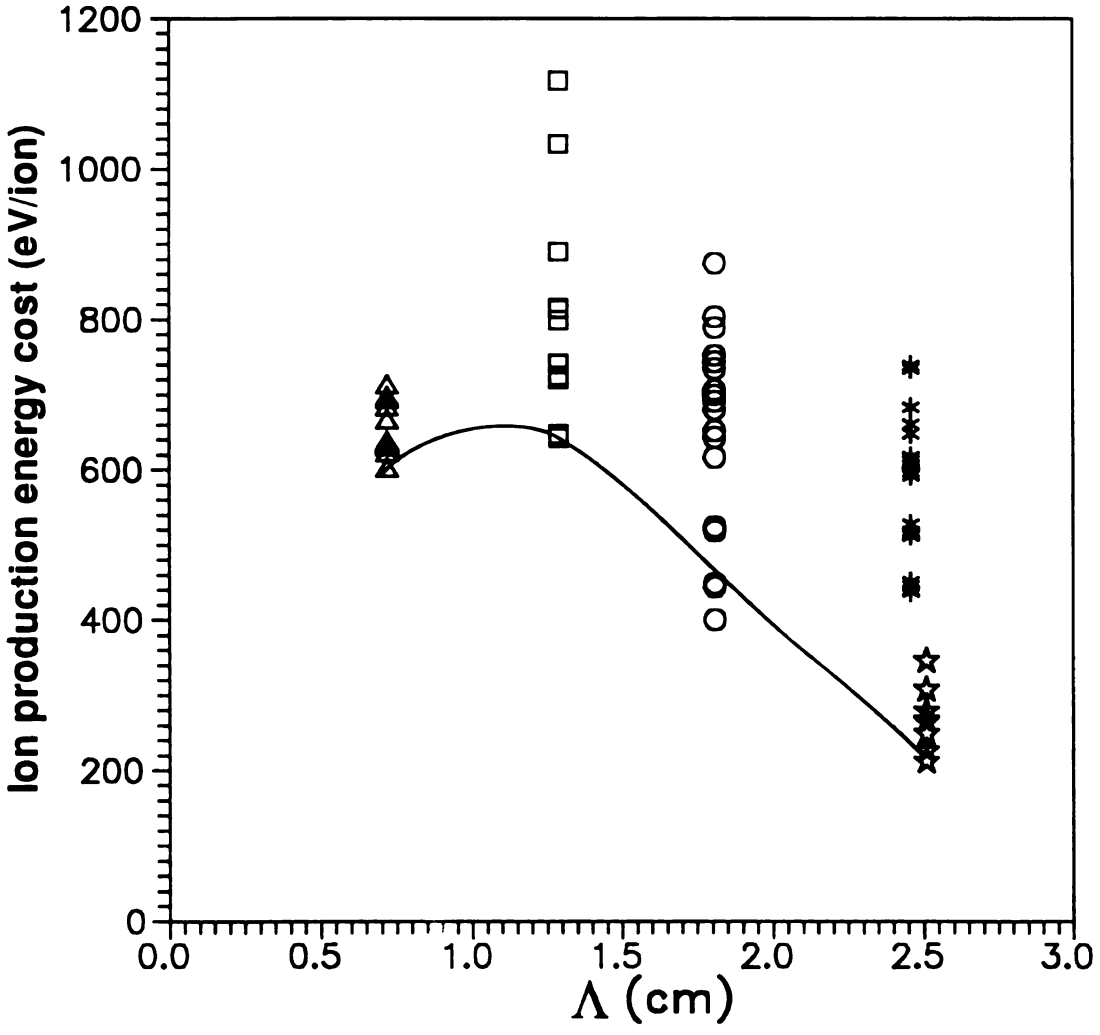

Figure 6.7 Ion production energy cost versus Λ

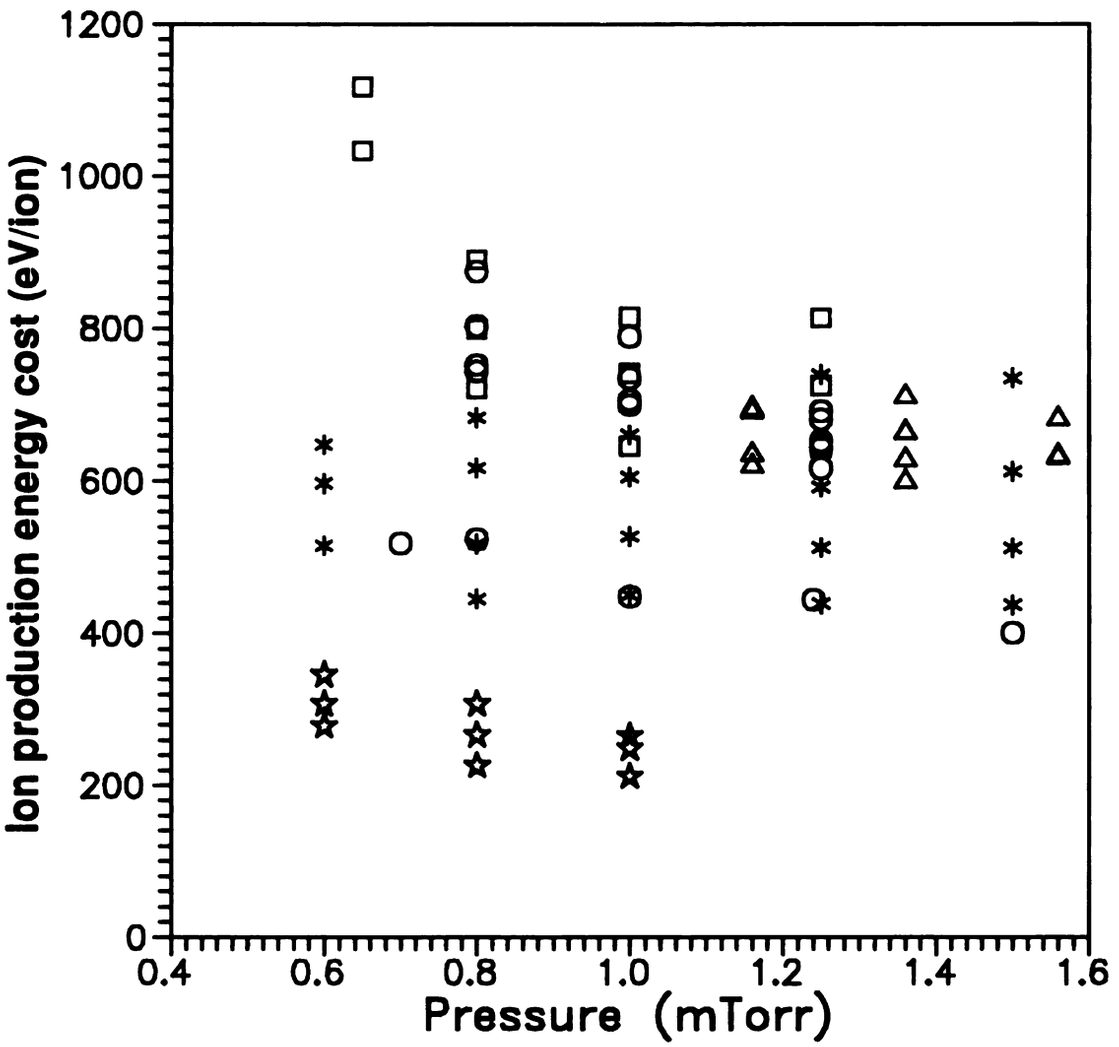

Figure 6.8 Ion production energy cost versus pressure

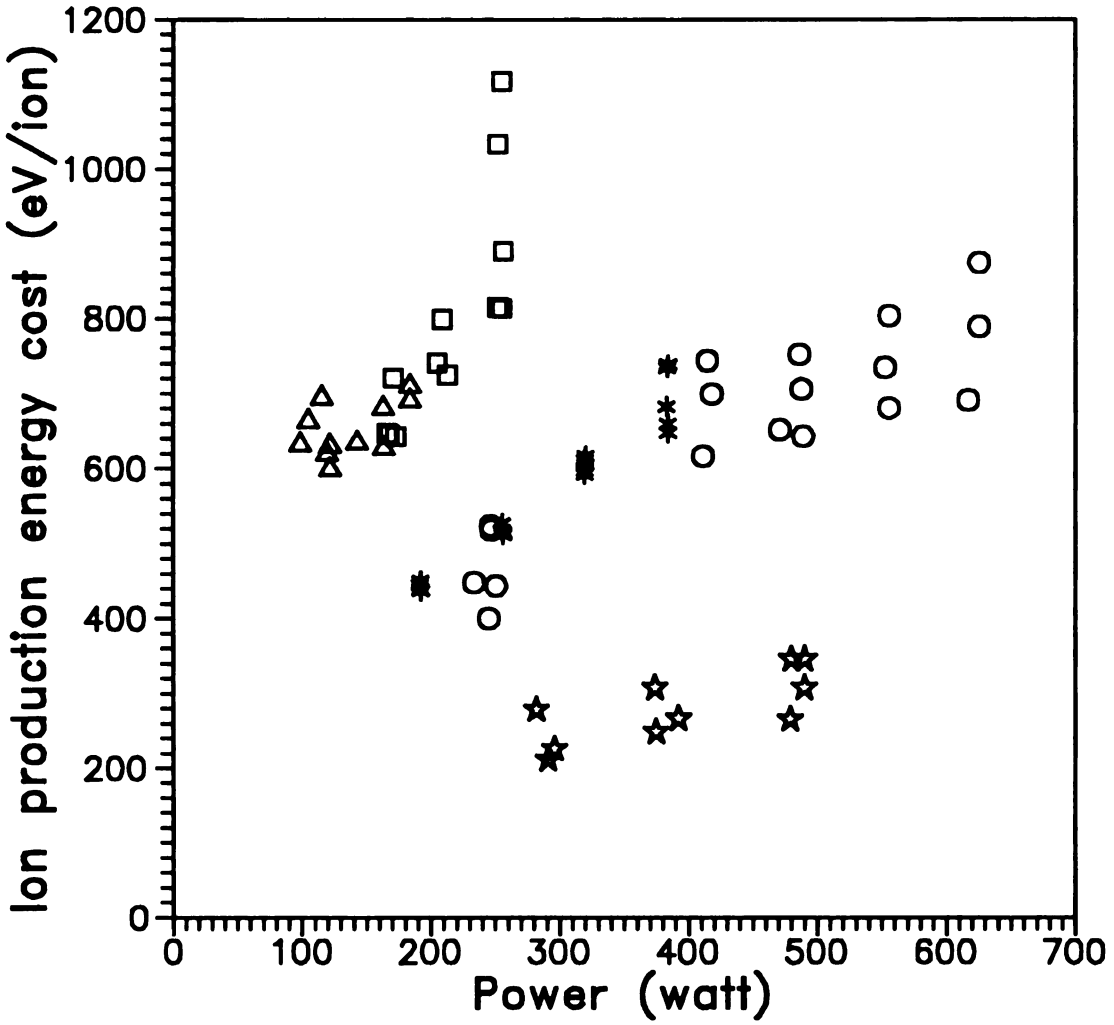

Figure 6.9 Ion production energy cost versus microwave power

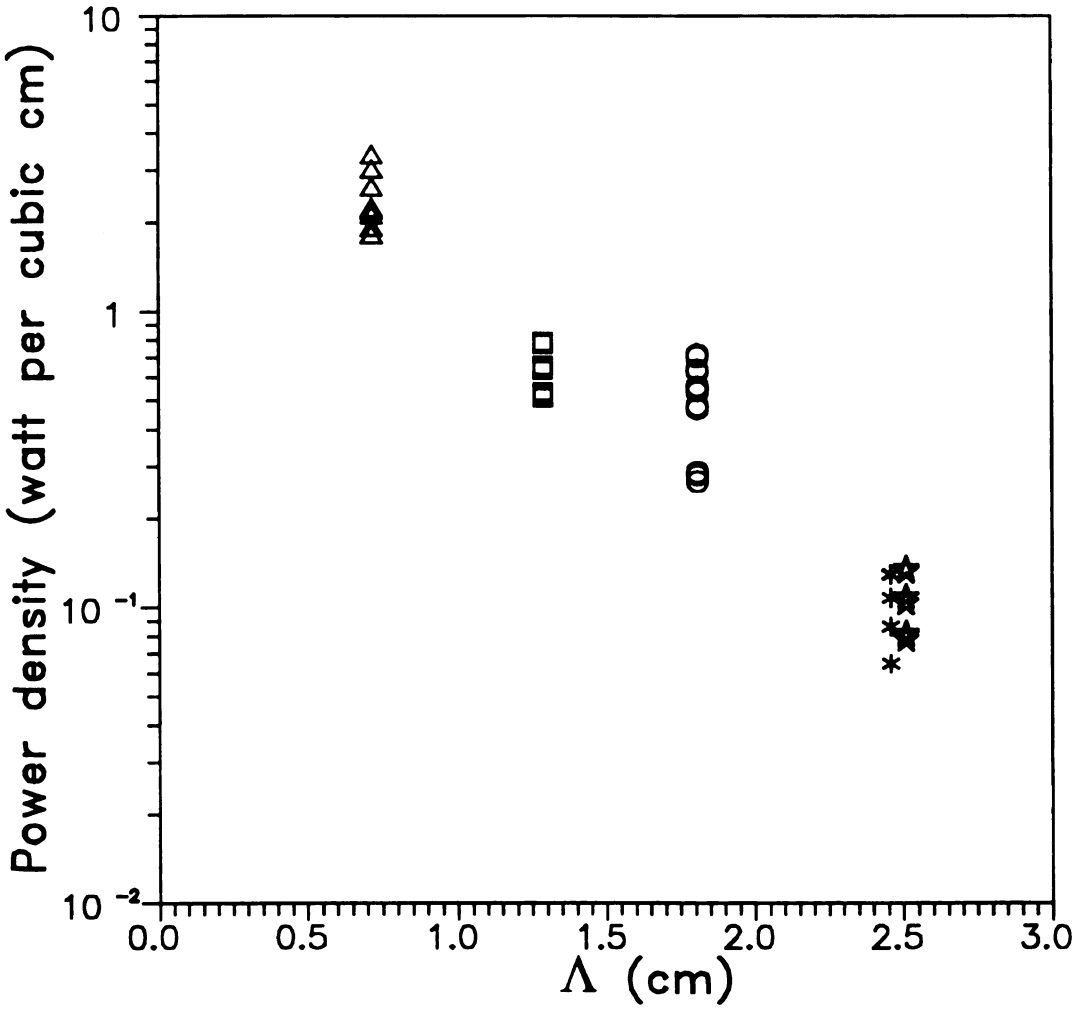

Figure 6.10 Power density versus Λ

20 and 0.1 watt/cm^3 in the MPDR 325. It should be noted that even the MPDR 20 has a slightly smaller power density than the MPDR 325. The discharge density in MPDR 20 is about 30% less than the MPDR 325 at the same microwave input power. Thus the MPDR 325 is more efficient than the MPDR 20.

§6.5 Summary

Discharge temperature in MPDR goes up as PΛ decreases. High microwave coupling efficiencies (80% to 92%) were observed in most of the MPDRs. The coupling efficiency is not strongly dependent on the discharge pressure and microwave power. It is believe that the microwave coupling efficiency is pimarily determined by the design of the MPDR and the ECR magnetic configuration. A variation of the ECR magnetic cusp in MPDR 13 has shown a coupling efficiency of 97% [47] which is a few percentages higher than that observed in this study.

Ion production is more efficient in a large diameter discharge such as the MPDR 325 than in small diameter discharge. As the discharge diameter increases, the minimum power density needed to keep the plasma decreases. The MPDR 325 has the best ion production efficiency among all the MPDRs. As indicated in Chapter Five, it also has a uniform discharge over 7 inches in diameter. The ion energies in the MPDR 325 are low and the IEDF has a small FWHM. It is therefore concluded that the MPDR 325 is the best candidate for large diameter wafer processing.

CHAPTER SEVEN

SUBMICRON ETCHING OF SILICON USING MPDR 325

§ 7.1 Introduction

Plasma etching is one of the important applications of an ECR plasma source [81-121, 123-125, 127-149, 173-175]. The primary objective is to achieve anisotropic submicron etching so that more circuits can be integrated on a small piece of silicon substrate. Since there is a trend of processing single large diameter wafers up to 200 mm [126,147], uniformity of the etching process is an important factor in determining the practical value of a new plasma source in a production line. Other issues such as etch rate and the damage to the substrate are also important. All these issues have to be addressed in all the newly developed ECR and non-ECR plasma sources, including the MPDR.

The damage issue in the MPDR has been investigated by researchers in AT&T [102,108,115-117,176]. III-V compound substrates, which are very sensitive to the etching process, such as GaAs, AlGaAs, InP, InGaAs and AlInAs were etched by the MPDR 9. Results showed that the MPDR source had little damage to these materials. Although silicon substrates are less sensitive compared to the III-V compounds, damage to this substrate still needs to be investigated. Other issues such as oxide charging, hydrogen passivation and so on are also important.

This chapter is concerned with the etching of silicon with feature sizes down to 0.1 micron. A new MPDR 325i was used in the etching experiments. The only difference between MPDR 325 and MPDR 325i is the cavity diameter, which is reduced from 14 inches in MPDR 325 to 12 inches in MPDR 325i. Both MPDRs use the same 24 cm diameter quartz

vessel and the same ECR magnetic configuration. Previous results show that the properties of a discharge are related to the discharge geometry rather than the cavity diameter. Thus properties of the plasma in MPDR 325i should be very similar to the MPDR 325.

§ 7.2 Chemistry of dry etching for silicon

Silicon can be etched by fluorine atom or chlorine atom based plasmas. The most widely used fluorine containing gases are CF_4, SF_6 and NF_3. These gases generate free fluorine radicals which react with silicon to form volatile products. Since SF_6 gas was used in the etching experiments in this dissertation, only its chemistry is described in this section.

The chemistry of the SF_6 with silicon in a plasma is a complicated subject. Table 7.1 shows the reaction set which includes all possible reactions taking place in the discharge [144]. The symbol, M, appeared in some equations represents a third body, such as a surface, required for the reactions to take place. Oxygen appears in some of reactions because it can be released from the quartz vessel or added deliberately.

There are at least two different models to describe the dissociation of SF_6. The first one is d'Agostino and Flamm model [142] which is summarized as below:

$$SF_x + e \rightarrow SF_{x-1} + F + e \qquad (7.1)$$

$$SF_x^- + SF_6 \rightarrow F^- + SF_{x-n} + SF_{6+1-n} \qquad (7.2)$$

TABLE 7.1 REACTION SET FOR SILICON ETCHING USING SF_6

Reaction number	Reaction	Rate coefficient at 1 Torr
*1	$SF_6 \xrightarrow{e} SF_2 + 4F$	28
2	$SF_5 \xrightarrow{e} SF_4 + F$	28
3	$SF_4 \xrightarrow{e} SF_3 + F$	28
4	$SF_3 \xrightarrow{e} SF_2 + F$	28
5	$SF_2 \xrightarrow{e} SF + F$	28
6	$SF \xrightarrow{e} S + F$	28
*7	$SF_5 + F \xrightarrow{M} SF_6$	1.0×10^{-11}
*8	$SF_4 + F \xrightarrow{M} SF_5$	1.7×10^{-12}
*9	$SF_3 + F \xrightarrow{M} SF_4$	1.6×10^{-11}
*10	$SF_2 + F \xrightarrow{M} SF_3$	2.6×10^{-12}
11	$SF + F \xrightarrow{M} SF_2$	2.9×10^{-14}
12	$S + F \xrightarrow{M} SF$	2.0×10^{-16}
13	$SF_5 + SF_5 \rightarrow SF_4 + SF_6$	2.5×10^{-11}
14	$SF_5 + SF_3 \rightarrow SF_3 + SF_4$	2.5×10^{-11}
15	$SF + SF \rightarrow S + SF_2$	2.5×10^{-11}
*16	$O_2 \xrightarrow{e} O + O$	23
*17	$SF_5 + O \rightarrow SOF_4 + F$	2.0×10^{-11}
18	$SF_5 + O \rightarrow SOF_2 + F$	2.0×10^{-11}
*19	$SF_3 + O \rightarrow SOF + F$	1.1×10^{-10}
20	$SF + O \rightarrow SO + F$	1.7×10^{-10}
*21	$SOF + O \rightarrow SO_2 + F$	7.9×10^{-11}
22	$SOF_3 + O \rightarrow SO_2F_2 + F$	5.0×10^{-11}
23	$SOF_4 \xrightarrow{e} SOF_3 + F$	28
24	$SOF_3 \xrightarrow{e} SOF_2 + F$	28
25	$SOF_2 \xrightarrow{e} SOF + F$	28
26	$SOF \xrightarrow{e} SO + F$	28
27	$SO \xrightarrow{e} S + O$	23
28	$SO_2 \xrightarrow{e} SO + O$	23
*29	$SOF_3 + F \xrightarrow{M} SOF_4$	5.0×10^{-11}
*30	$SOF_2 + F \xrightarrow{M} SOF_3$	5.2×10^{-14}
*31	$SOF + F \xrightarrow{M} SOF_2$	1.0×10^{-13}
32	$SO + F \xrightarrow{M} SOF$	1.0×10^{-16}
*33	$SO_2 + F \xrightarrow{M} SO_2F$	2.0×10^{-13}
*34	$SO_2F + F \xrightarrow{M} SO_2F_2$	1.0×10^{-11}
35	$SO + O \xrightarrow{M} SO_2$	1.4×10^{-13}
36	$S + O_2 \rightarrow SO + O$	2.3×10^{-12}
37	$SO + O_2 \rightarrow SO_2 + O$	6.7×10^{-17}
38	$SO + SO \rightarrow SO_2 + S$	8.3×10^{-15}
39	$F + O_2 \xrightarrow{M} FO_2$	5.0×10^{-16}
40	$F + FO_2 \rightarrow F_2 + O_2$	1.0×10^{-13}
41	$O + FO_2 \rightarrow FO + O_2$	5.0×10^{-11}
42	$O + FO \rightarrow F + O_2$	5.0×10^{-11}
43	$F_2 \xrightarrow{e} F + F$	28
*44	$F \xrightarrow{\text{Si}} SiF$	10
*45	$SiF + F \rightarrow SiF_2$	1×10^{-10}
*46	$SiF_2 + F \rightarrow SiF_3$	1×10^{-10}
*47	$SiF_3 + F \rightarrow SiF_4$	1×10^{-10}

where x is a number between 1 to 6 inclusive and n equals to 1 or 2. These reactions dissociate SF_6, producing lighter SF_x radicals and fluorine atoms. Another model is suggested by Ryan and Plumb [144] from IBM. They have argued that the dissociation of SF_6 through electron impact mainly gives SF_2 and four fluorine atoms by the reaction listed as reaction (1) in Table 7.1. Sadeghi et al. [142] also has indicated that with the presence of a fluorine atom-consuming material such as silicon or tungsten, the concentrations of SF and SF_2 molecules drastically increase.

Two different reaction mechanisms between fluorine atoms and silicon have been presented. Figure 7.1 shows the reaction model suggested by Flamm. A layer of fluorinated silicon is formed on the surface of the silicon substrate. Fluorine atoms are adsorbed to form bonding with the silicon atoms on the surface. As described by Flamm, two reaction paths take place in phase **I** as shown in Figure 7.1. The reaction may either proceed in path **a** to form SiF_2 molecule, which leaves the surface as the desorption product [137]. This accounts for about 5% to 30% of the material leaving the silicon surface. The SiF_2 molecules then react in the gas phase with atomic fluorine or fluorine molecule to form SiF_3 with the emission of spectrum peaked around 500 nm [74]. SiF_3 then reacts with atomic fluorine to form the end product SiF_4. According to Flamm, most of the reactions go through path **b** in phase **I** and then phase **II** and **III**. As a result, most of the material leaving the silicon surface is SiF_4.

Another study by Winters and Plumb [135] indicates that the spontaneous etching at room temperature produces stable gases SiF_4, Si_2F_6

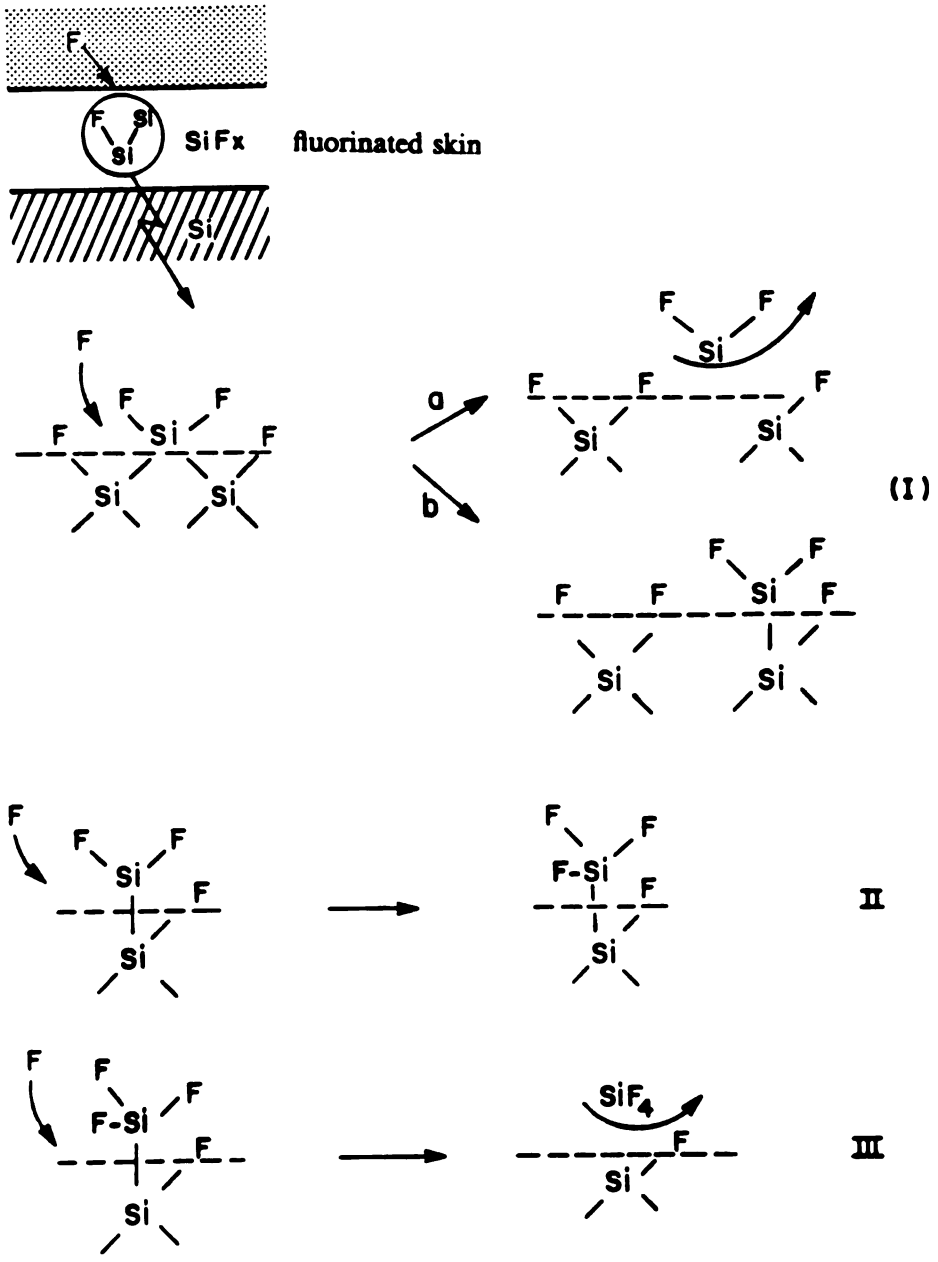

Figure 7.1 Reactions of atomic fluorine with silicon [74]

and Si_3F_8 with SiF_4 being the dominant product. Figure 7.2 shows the mass spectra of the products at various substrate temperatures. Winters and Plumb indicated that the SiF^+ and SiF_2^+ peaks, shown in the mass spectrum analysis, should be assigned to Si_2F_6 and Si_3F_8 rather than SiF_2. However, as the temperature of the substrate increases from room temperature to 1000 ^oC, the relative contributions of the SiF_4, Si_2F_6 and Si_3F_8 etch products decrease while concentration of SiF_2 increases and eventually becomes the major product. Figure 7.3 shows the effect of ion bombardment in an ion assisted etch process. With the help of the argon ions, the etch process is significantly increased.

§ 7.3 Etching methods

According to Flamm [74], there are four basic methods of plasma etching. As shown in Figure 7.4, the first method is sputtering. Etching is achieved by energetic bombardment of ions on the substrate, kicking off the substrate material.

The second method is chemical method. Reactive neutral species react spontaneously with the substrate. The product must be volatile. This process rarely takes place alone in plasma environment because of the formation of sheath.

The third method is ion-enhanced energetic etching. In this case, ions are attracted towards the substrate surface through a sheath, striking the surface where reaction between reactive neutrals and the substrate take place. The ions enhance the etch rate through two possible mechanisms.

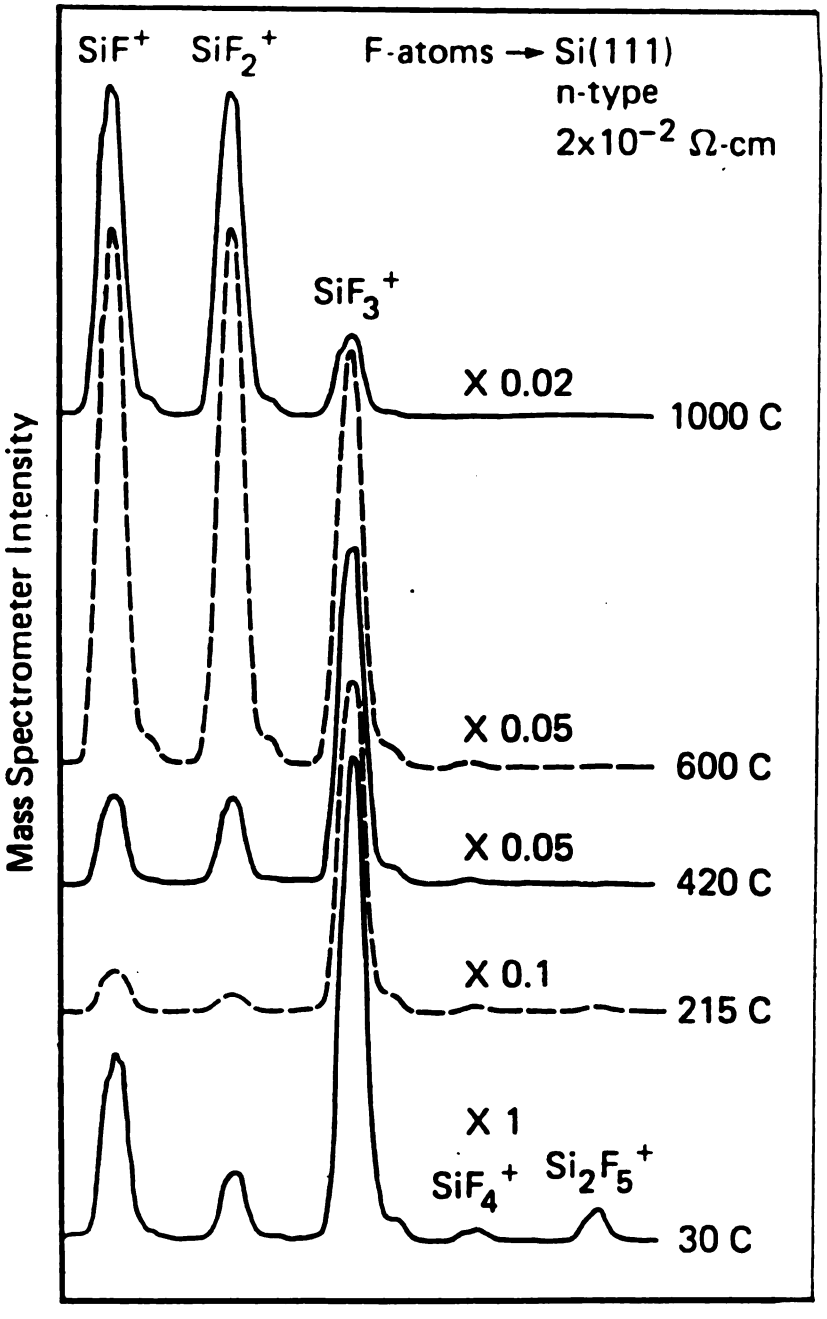

Figure 7.2 Mass spectra of etch products as a function of substrate temperature [135]

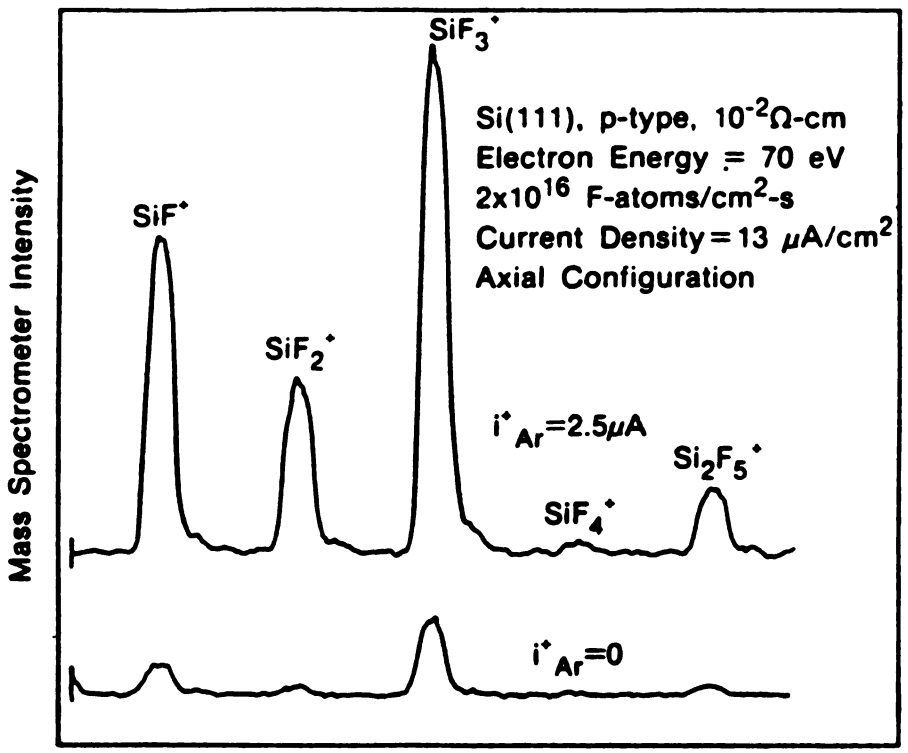

Figure 7.3 Effect of ion bombardment on the mass spectra [135]

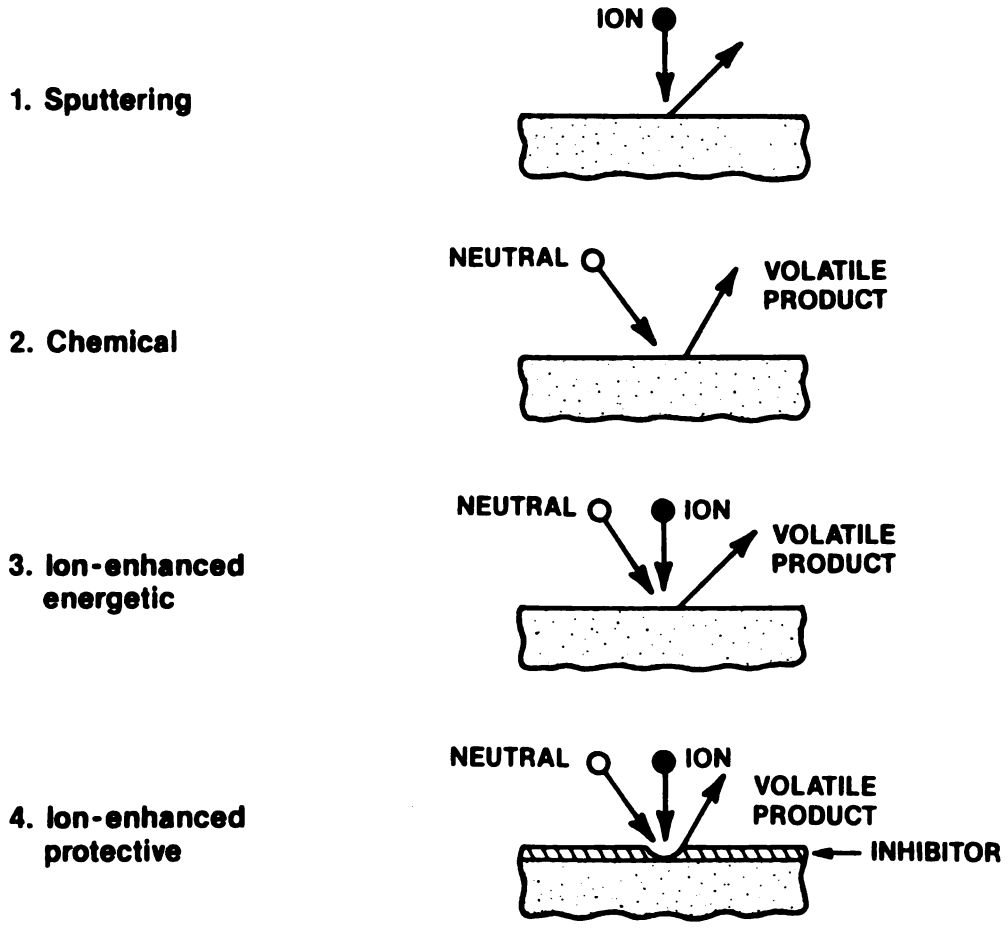

Figure 7.4 Etch methods [74]

They break the surface lattice, opening more reaction sites for the reaction to take place. Furthermore the ions kick off the byproducts or end-products of the etching reaction, thus enhancing the desorption rate. An example is SF_6-argon plasma. Because the paths of the ions are perpendicular to the substrate surface, anisotropic etching can be achieved.

The fourth method is ion-enhanced protective etching. In this process, a protective coating is formed on the surface of the substrate during the reaction. An example is CF_4-argon plasma in silicon etching. After the dissociation of one or more fluorine atoms from CF_4 molecules, the carbon skeletons link themselves together to form a polymer on the silicon surface. The polymer will prohibit the etching reaction to go on. In this case, the ions sputter the polymer away and allow the etch process to proceed. This type of reaction gives a very good vertical etch profile since the side wall is coated with the polymer, prohibiting lateral etching. However, the coating has to be removed. This adds additional step in the fabrication process and therefore this method is not desirable in manufacturing process.

§ 7.4 Etching system

The etching system used for the submicron etching experiments is a customized Plasma Quest model 357-W etching and deposition system. Figure 7.5 shows the cross sectional view of the processing system. It consists of a WAVEMAT model MPDR 325i ECR plasma source, which has a twelve-inch inside diameter cavity and a discharge diameter of 24 cm. The MPDR 325i is similar to MPDR 325. It is equipped with 12 permanent magnets which form the twelve ECR magnetic cusps.

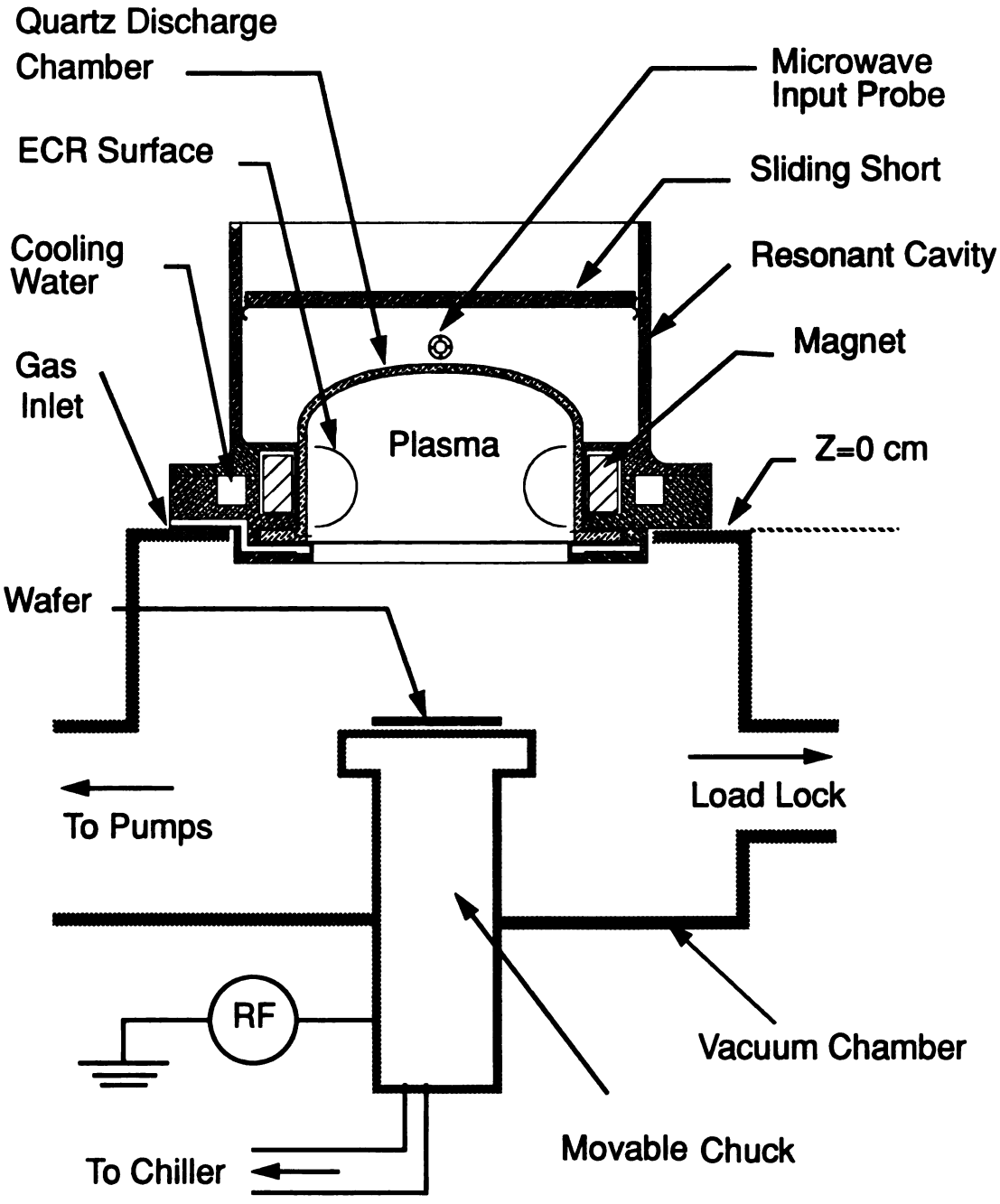

Figure 7.5 Cross sectional view of the processing system

The vacuum system consists of a Leybold TMP 1000C turbomolecular pump, which has a pumping capacity of 1150 liters per second. The system is provided with a rotary vane pump, Stokes V-023-2, placed in line with the turbo pump. The turbo pump can be isolated from the main processing chamber by a VAT series 64 200-mm throttling gate valve. Chamber pressure is monitored by a MKS 390HA capacitance manometer and is controlled by a VAT PM5 adaptive pressure controller. The base pressure of the water jacketed 16-inch diameter main chamber is $6x10^{-8}$ Torr. A single wafer load lock system is equipped in the system. Wafer size up to 6 inches in diameter can be processed.

The circular chuck is made of aluminum and has an anodized outer layer of thickness between 2 to 5 mils. It can be moved to different downstream locations. The chuck temperature was maintained between 20 °C to 22 °C by a recirculating unit during all experiments. As indicated in Figure 7.5, all experiments described in this investigation were performed without downstream confinement magnets. Thus, it is expected that process uniformity can be further improved.

A separate 13.56 MHz rf power supply with an automatic match network is connected to the chuck. Since electrons move much faster than the ions, a self-induced d.c. bias is established on the chuck. Figure 7.6 shows a schematic variation of the potential and current densities for ions and electrons during on rf cycle. The rf voltage, V_{rf}, is shifted downward by a self-induced voltage, V_s. As a result, ion current, J_i, continuously reaches the substrate surface. The ion current is neutralized by a huge electron

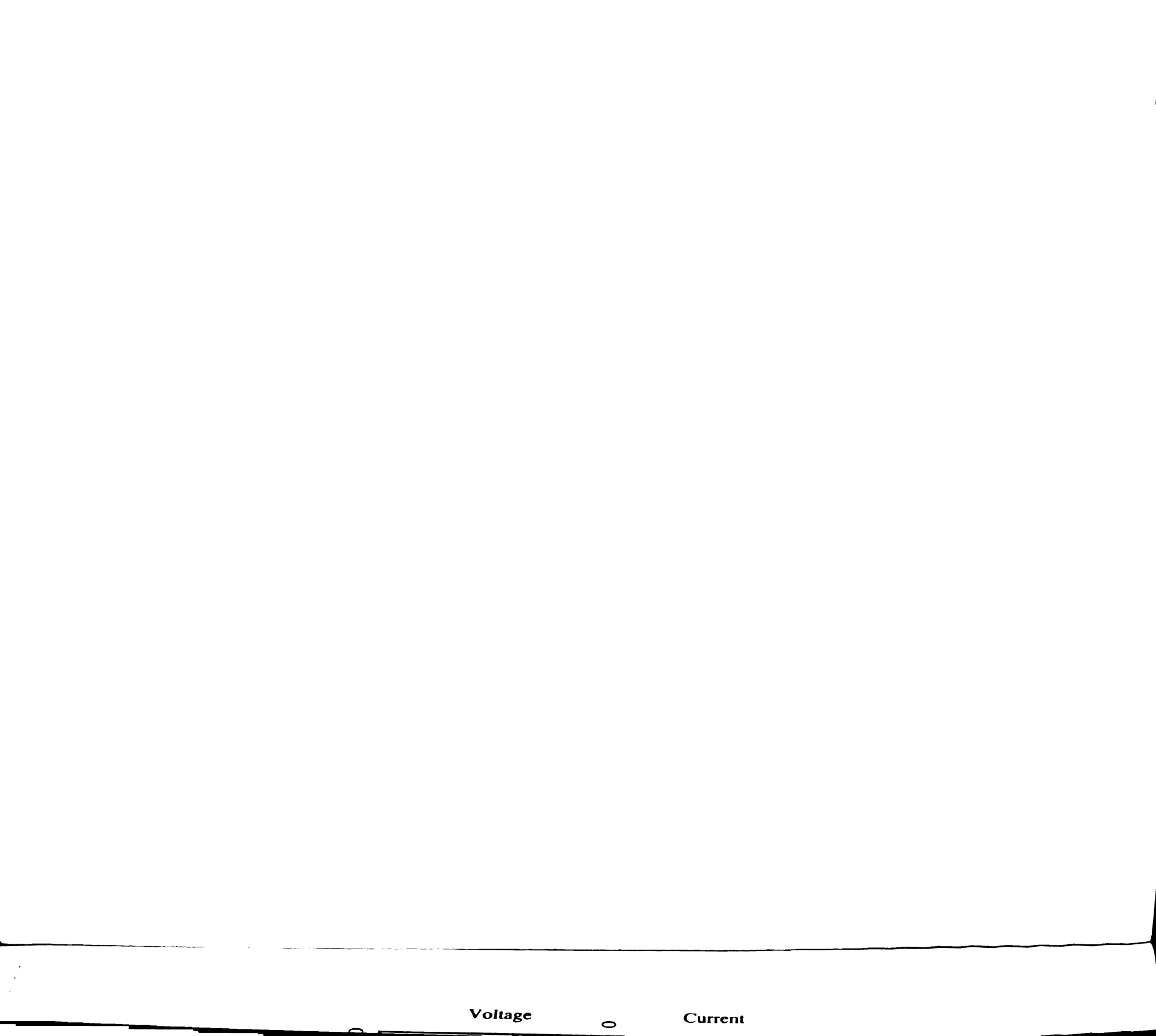
Voltage
Current

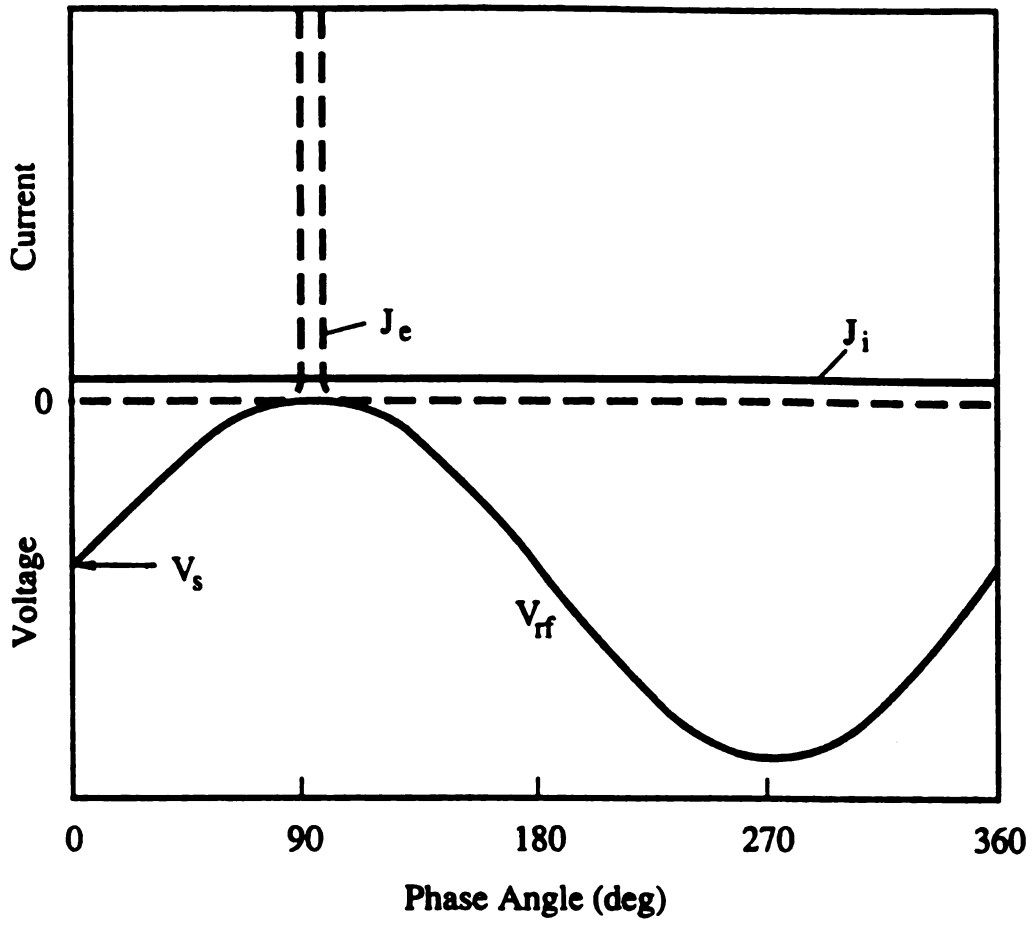

Figure 7.6 Variation of potential and current densities for ions and electrons during on rf cycle

current,

positive

§ 7.5 P

7.5.1 C

prepare

alumin

Prepar

resoluti

feature

The cle

similar

similar

spinnin

baking)

seconds

deioniz

deposit

procedu

current, j_e, which reaches the substrate surface when the rf voltage is positive. This happens at 90 degree phase angle in the Figure 7.6.

§ 7.5 Preparation of the experiments

7.5.1 Optical and electron-beam lithography

Both optical and electron-beam lithographic techniques were used to prepare the submicron features before the inversion of the pattern using an aluminum liftoff procedure.

Preparation of sample using optical lithography

A Suss MJB 3 UV300 mask aligner system, which has an optimal resolution of 0.4 micron in the vacuum contact mode, was used to pattern features sizes down to 0.5 micron using AZ5209 positive photoresist.

The preparation procedures for the samples are shown in Figure 7.7. The cleaning procedures for the three-inch p-type <100> silicon wafers are similar to those given by Reinhard [178]. Preparation of the pattern was similar to those in previous etching experiments [45]. The photoresist spinning for AZ5209 was 4000 rpm for 40 seconds. Soft bake (pre-exposure baking) temperature was 87 ^oC for 30 minutes and the UV exposure was 50 seconds. The wafer was developed in a solution consisting of one part deionized water and one part developer. About 400 nm thick aluminum was deposited by thermal evaporation at about 10^{-6} Torr. Aluminum liftoff procedure was performed by putting the sample wafer in a beaker containing

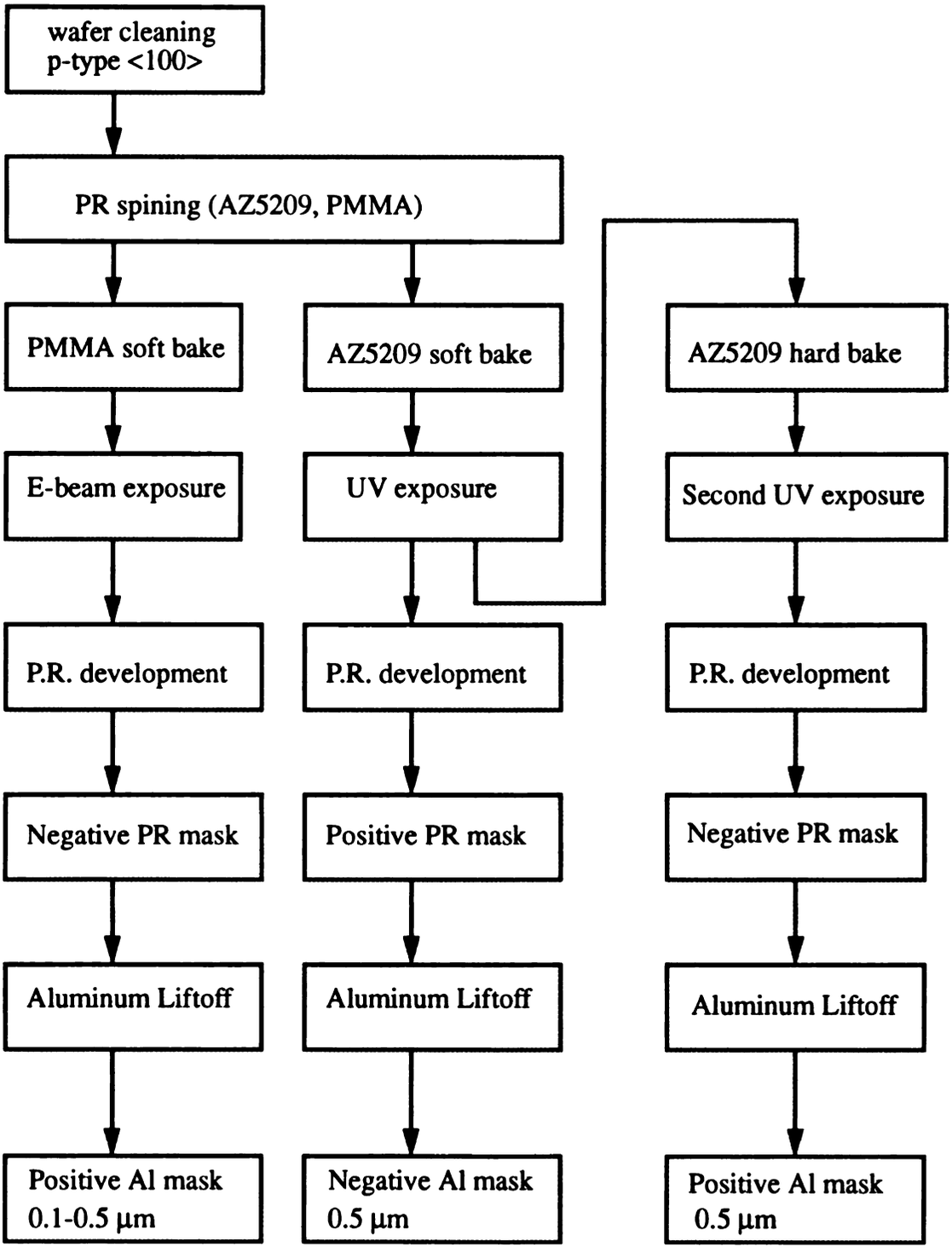

Figure 7.7 Preparation procedure of the etch sample

acetone which can dissolve both AZ5209 and PMMA. An ultrasonic bath was used to assist the liftoff process.

All samples were cut to a size of about 1 cm x 0.5 cm in order to be consistent with the samples prepared by the electron-beam lithography which were restricted to this size. The sample was then mounted with graphite paint on a 3-inch silicon carrier wafer for etching, except during the gas flow experiments and uniformity experiments in which a 6-inch silicon wafer was used.

Preparation of sample using electron-beam lithography

An electron-beam lithographic technique was used for preparation of feature sizes from 0.1 μm to 0.5 μm. The negative resist used was PMMA with a thickness of 250 nm after a spin of 40 seconds at 4000 rpm. The soft bake was 160 ^{o}C for 60 minutes. A JEOL JSM-840A scanning electron microscope with external beam control was used to write the pattern into the PMMA using a beam dosage of 250 nC/cm^2 and accelerating voltage of 35 kV. The PMMA was developed in a solution consisting of one part of methyl isobutyl ketone and three parts of isopropyl alcohol for 60 seconds. A three hundred nanometer thick aluminum film was then deposited by thermal evaporation to define the final etching mask after aluminum liftoff.

7.5.2 Etching conditions

Mixtures of SF_6 and argon were used as the etching gas, which has been used in earlier ion assisted etching of silicon [24,25]. One advantage of

this etch gas composition is no polymer film will form on the substrate surface. The etching performance was investigated under different etching conditions. Gas flow varied from 16 to 32 sccm. Microwave input power was varied from 400 to 800 Watts. Processing pressure was varied from 0.6 mTorr to 9 mTorr, with no change in gas flow, by adjusting the throttle valve. The gas composition was 4% SF_6 which gave highly anisotropic etch profiles as indicated in a previously etching experiment which used d.c. bias [45]. In this study, bias was via rf, with rf power varied from 5 to 50 Watts. An investigation of the etch rate at different downstream locations was also conducted.

§ 7.6 Etching results

Etch depths were measured by Dektak II profilometer after removing the aluminum mask. Microloading and etch profiles of line width less than 500 nm were determined by scanning electron microscopy. Both JEOL T-330 and JEOL JSM-840A SEM machines have been used.

7.6.1 Role of gas flow

The variations of the etch rate versus the gas flow are shown in Figure 7.8 for microwave input power of 500 and 800 Watts. The sample was mounted on a 6-inch wafer. Gas composition was fixed at 4% SF_6 and 96% argon. The rf power was 10 Watts which produced an negative induced d.c. bias of 10 volts. By adjusting the throttle valve, the pressure was kept constant at 1 mTorr while the flow was increased from 16 sccm to 32 sccm. The curves in Figure 7.8 showed that as the flow rate was doubled (from 16

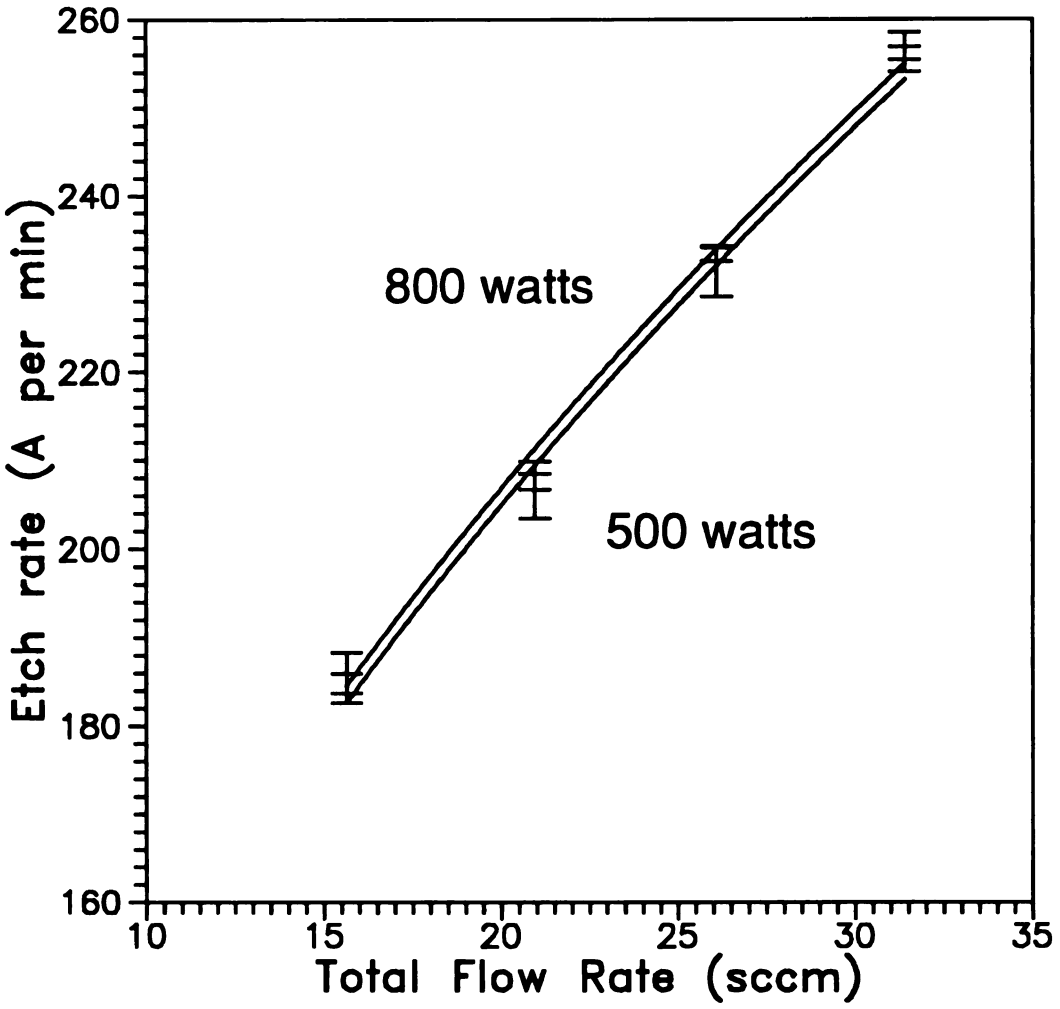

Figure 7.8 Variation of etch rate with flow rate at 1 mTorr 10 cm downstrem, 4%SF_6 and -10 volts bias (10 rf watts)

to 32 sccm), the etch rate increased by about 38%. Increasing the microwave power from 500 Watts to 800 Watts only increases the etch rate by less than 1%.

The etching process was operating under a condition in which fluorine atoms, produced from dissociation of SF_6, are limiting the etch rate. For example, a 16 sccm total flow with 4% SF_6, will produce 1.72×10^{19} fluorine atoms per minute assuming each SF_6 molecule coming into the system is perfectly dissociated and liberates six fluorine atoms. If all fluorine atoms participate in etching and producing SiF_4, these will result in an ideal etch rate of 291 Å/min. The actual etch rate was 182 Å/min. Taking into account that dissociation of each molecule is less than 100%, the etch rate seems to be limited by the supply of fluorine atoms. As the flow increases, more SF_6 molecules are introduced into the plasma. Therefore more fluorine atoms are available for etching as a result of SF_6 dissociation. The etch rate thus increases. The slight increase in etch rate as the microwave power increased can be attributed to a slight increase in dissociation of the remaining SF_6 molecules or associated radicals. Another possible reason is an increase in substrate temperature which increases the reaction rate.

7.6.2 Effect of rf substrate bias

The rf source which is connected to the chuck is autotuned by a match network. The source can be operated in two different modes: a constant rf power mode or a constant bias (self-induced bias) mode. The relation of the rf power and the induced bias is shown in Figure 7.9. Figure 7.9(a) shows the variations of the induced bias versus pressure and power at 10 cm downstream. The discharge consisted of 5% SF_6 and 95% argon. As the rf

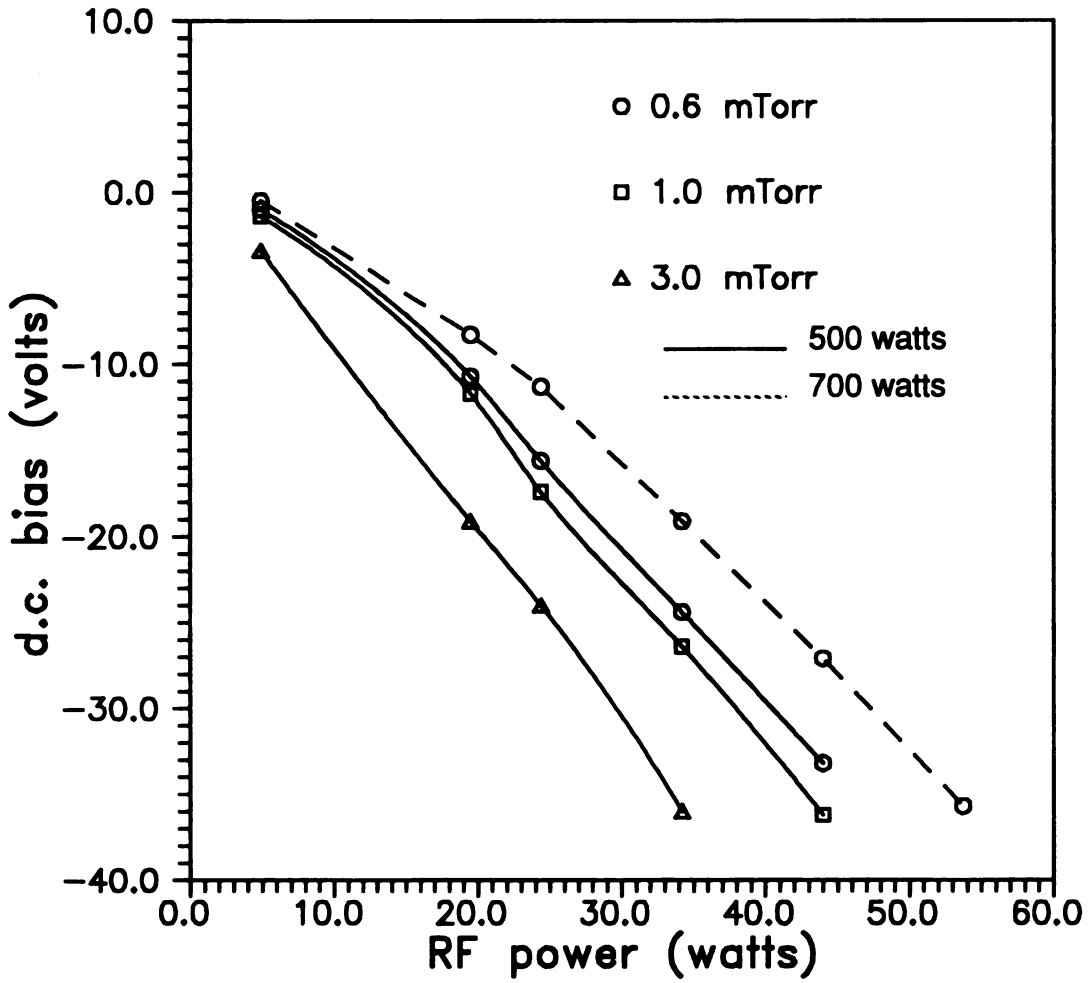

Figure 7.9 (a) Variation of self-induced bias with rf power with 5% SF_6 at 10 cm downstream

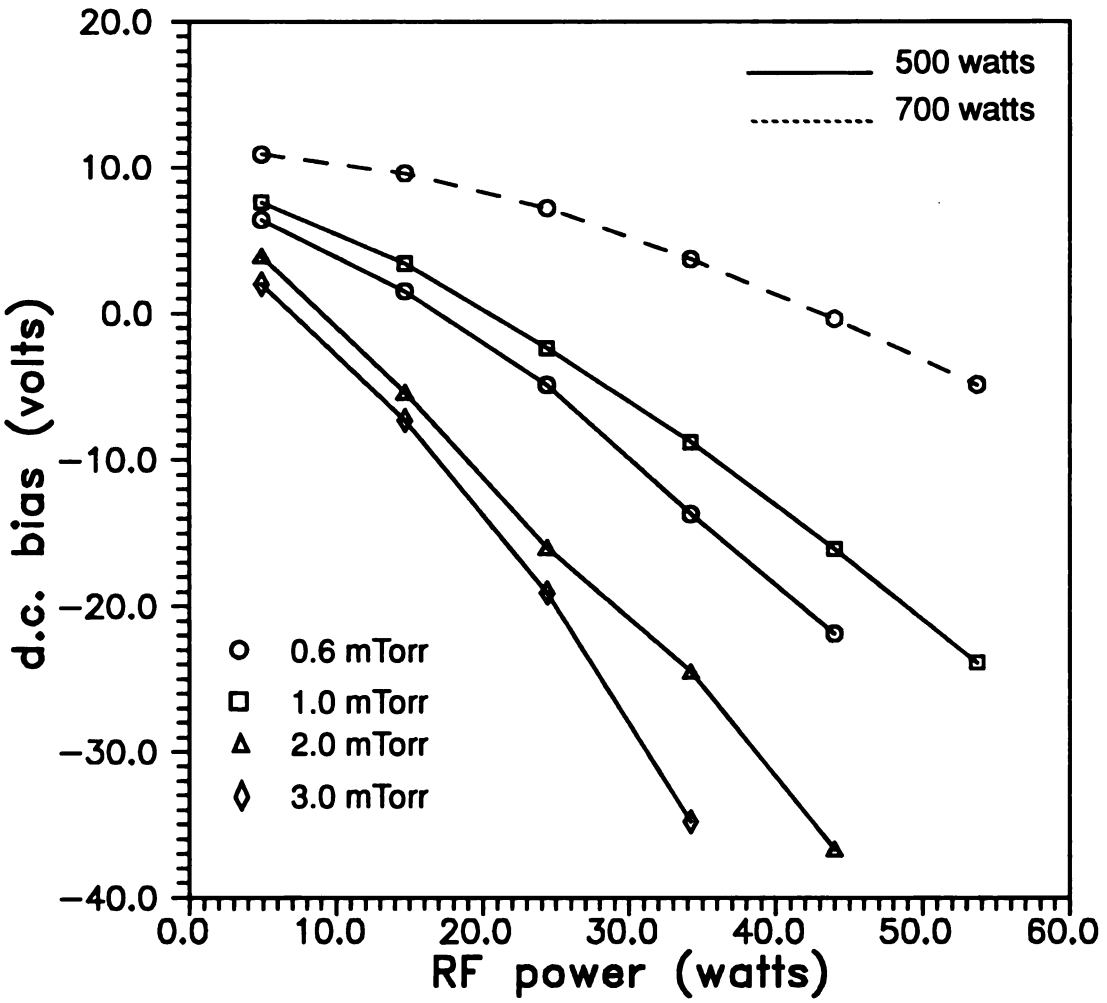

Figure 7.9 (b) Variation of self-induced bias with rf power with 5% SF_6 at 4.5cm downstream

power increases, the induced bias becomes more negative. For a fixed rf power, an increase in pressure will also increase the bias. At 0.6 mTorr an increase in microwave power from 500 Watts to 700 Watts reduced the induced bias. This is because due to an increase in plasma density.

The relation of rf power and induced bias also depends on downstream position as shown in Figure 7.9(b). At 4.5 cm downstream the induced bias voltage is no longer negative at low rf power. A positive induced bias was observed. The appearance of the positive induced bias is due to a change of the ratio of "effective" conductive area between the chuck and the plasma source/chamber. The addition of the rf changes the plasma such that the induced voltage drops as the rf power increases. Another observation is that at constant 500 Watts microwave power, an increase in pressure from 0.6 mTorr to 1 mTorr causes the induced bias to become less negative. Compared with Figure 7.9(a), at 10 cm downstream, the induced bias becomes more negative as pressure increases from 0.6 to 1.0 mTorr. This shows that the plasma density at 1.0 mTorr is higher than that at 0.6 mTorr in the source region. However, the plasma density is lower at 1.0 mTorr than at 0.6 mTorr in lower downstream position. Thus it indicates that the decrease in mean free path between collision due to high pressure results in a larger gradient of plasma density along the z-axis. This suggested that at high pressure, the wafer needs to be placed closer to the source in order to obtain a higher processing rate.

For a given pressure, the higher the bias, the more perpendicular the ions hit the surface. This translates to a better etch profile. However, a high bias can also be deleterious because damage to the etch mask will become

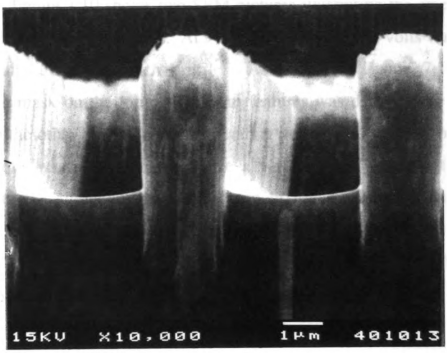

(a) a damaged mask at 9 mTorr, 5% SF_6, -110 volts (50 watts rf)

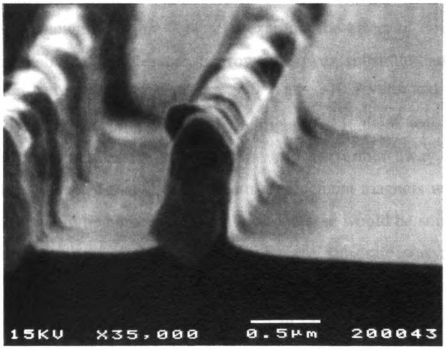

(b) undamage mask at 0.6 mTorr, 4% SF_6, -10 volts bias (11 watts rf)

Figure 7.10 Effect of bias on etch mask. (500 watts microwave power, 10 cm downstream)

an issue. Figure 7.10 shows two SEM pictures illustrating the effect on the etch mask with increasing bias. At 9 mTorr, a bias of -110 volts was needed to maintain anisotropic etch profile. As shown in Figure 7.10(a), the aluminum mask on the top of the 2 μm features was damaged by the high bias. On the other hand, when the operating pressure was 0.6 mTorr, a bias of -10 volts was sufficient to achieve a vertical etch profile without any damage to the aluminum mask as shown in Figure 7.10(b). The feature shown was 0.5 μm line with 1 μm spacing. Compared with the 20 volts d.c. bias used in earlier work [45], a smaller rf bias voltage was sufficient to achieve a vertical etch profile.

7.6.3 Variations of etch rate with other processing parameters

Variations of etch rate with respect to the bias and the downstream positions are shown in Figure 7.11. To examine the effect of downstream position on etch rate, the pressure, microwave power, substrate bias and gas composition were fixed at 0.6 mTorr, 500 Watts, -10.3 volts and 4% SF_6, respectively. As shown in curve (a) in Figure 7.11, there was a steady decrease in etch rate as the substrate was moved further away from the source. It is expected that if downstream confinement magnets were used, the etch rate would be higher and the rate of decrease would be smaller. The lowest etch rate was about 238 Å/min when the substrate was at 17 cm downstream. As shown in the curve (b) in Figure 7.11, the etch rate went up as the bias potential was decreased from -5 to -45 volts. In this case, the substrate was placed at 10 cm downstream while the rf bias voltage was varied.

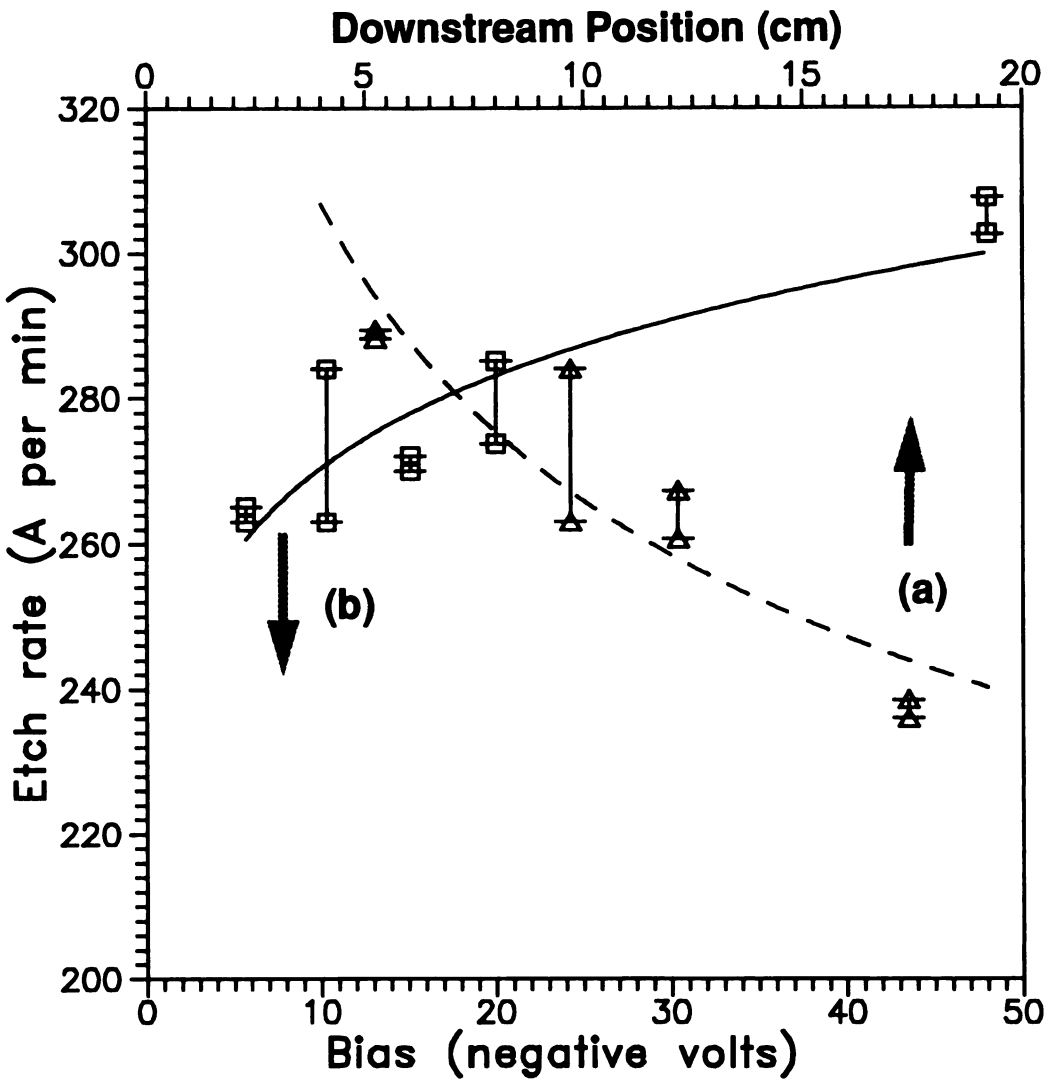

Figure 7.11 Variations of etch rate with (a) downstream position with -10 volts bias (11 watts rf) and (b) bias at 10 cm downstream position (9-40 watts rf). Etching conditions were 4% SF_6, 500 watts microwave power at 0.6 mTorr

Variations of etch rate with the microwave power are shown in Figure 7.12. In this case, the etch sample was mounted on a 3-inch wafer carrier. The pressure was 0.6 mTorr and the rf bias was -10 volts. The increase of the etch rate almost saturated as the power was increased from 400 Watts to 800 Watts. This rate of increase in etch rate was slower than the associated increase in ion density [47]. As discussed earlier, the etch rate was limited by the amount of fluorine atoms, not the ions. Thus the slight increase in etch rate was primarily the result of higher dissociation rate of the SF_6 molecules or associate radicals.

As the pressure increased, the etch rate increased dramatically as shown in Figure 7.13. The gas flow rate was kept constant at 20 sccm (5% SF_6 and 95% argon). A constant 50 Watts rf power was used to maintain a highly anisotropic etched profile. Although Figure 7.3 indicates that ion bombardment significantly changes the chemistry on the substrate surface, the high etch rate at 9 mTorr can not only be the result of a high ion flux. In addition to a possible higher dissociation rate of the SF_6 molecules, it is suspected that the increase in residence time of the fluorine atoms in the chamber from 24 ms at 0.6 mTorr to 355 ms at 9 mTorr may also play a role in the enhancement of the etching process.

7.6.4 Etch uniformity

Previous results using a similar 24 cm discharge reactor and d.c. bias have shown a 2% (1σ) variation over a 6-inch diameter with downstream confinement magnets at 18 cm downstream [45]. This study was performed, without downstream plasma confinement, on a 6-inch silicon wafer on which

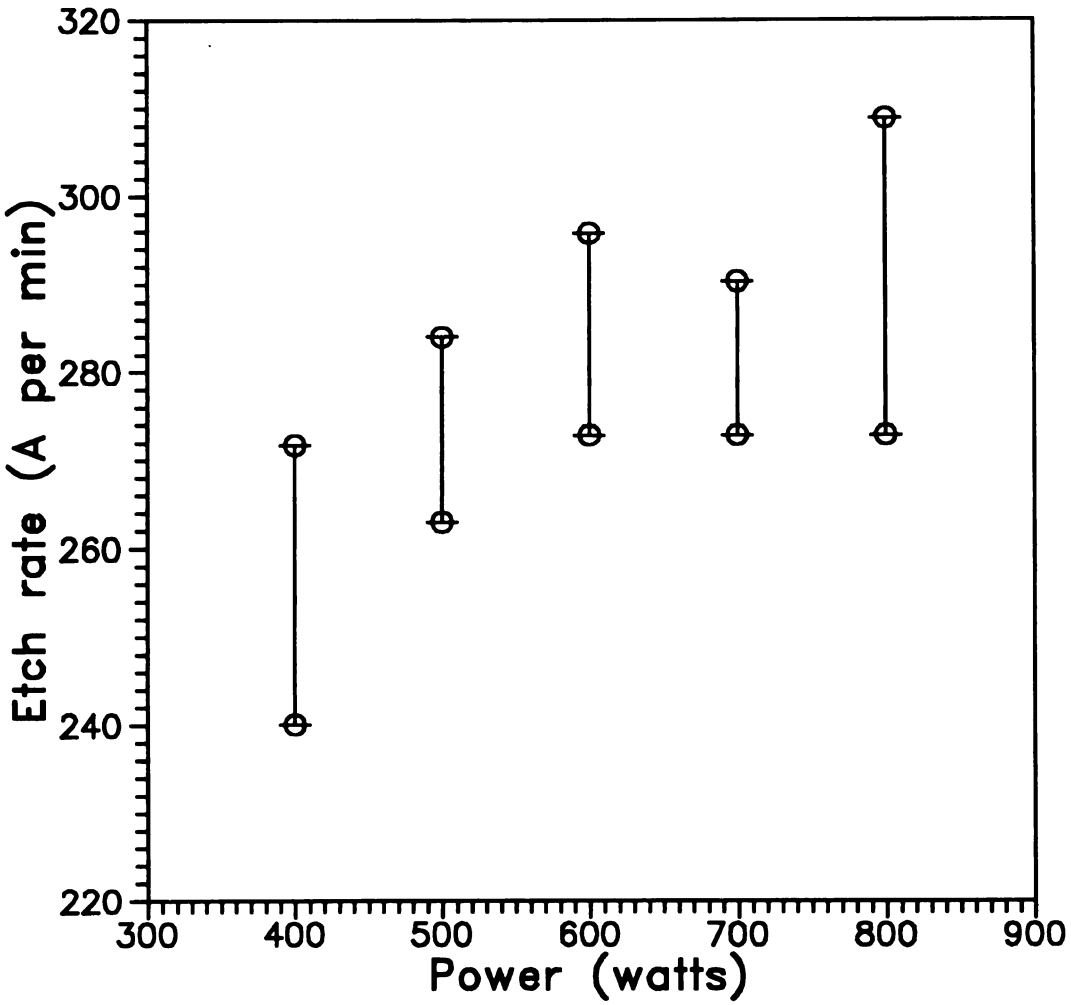

Figure 7.12 Variation of etch rate with microwave power at 0.6 mTorr, 4% SF_6, 10 cm downstream and -10 volts bias (11 watts rf)

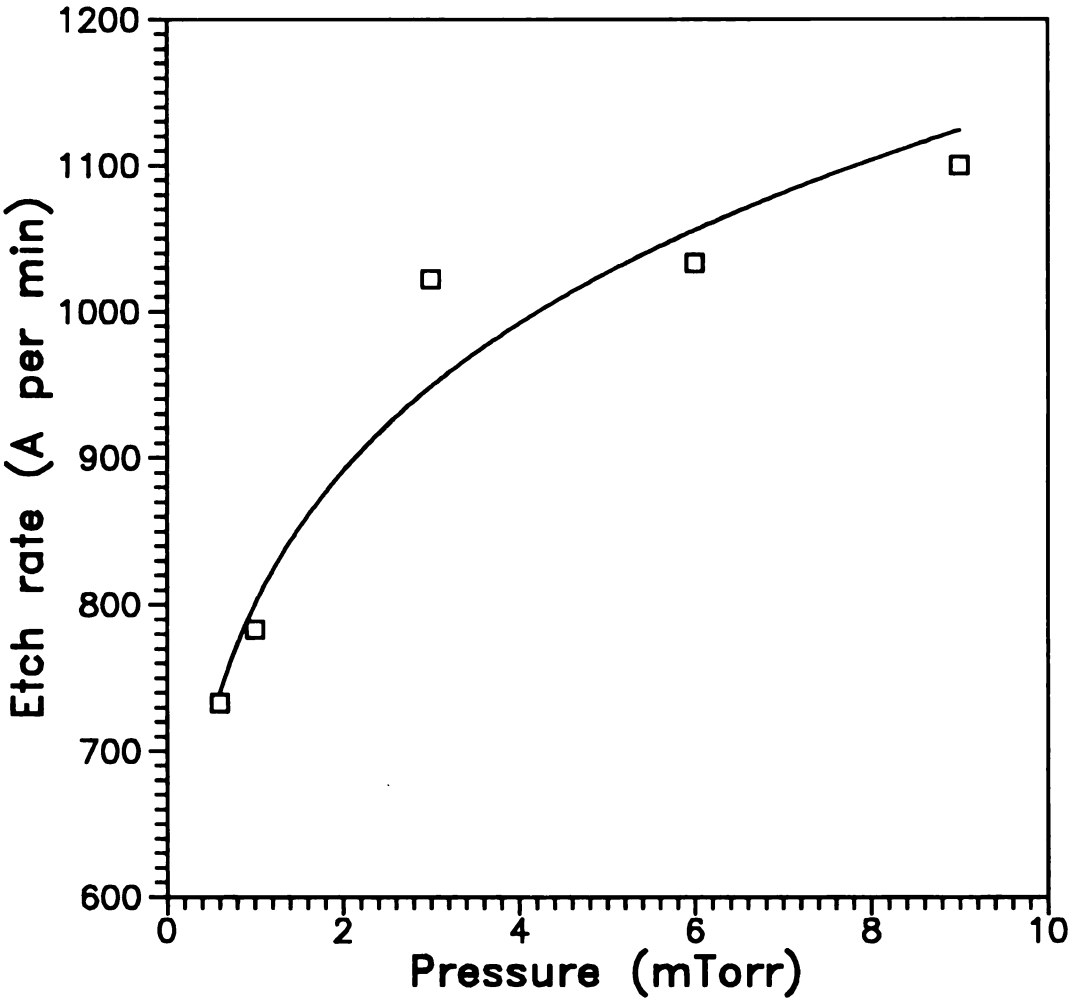

Figure 7.13 Variation of etch rate with pressure in a 5%SF_6 plasma at constant 50 Watts rf and 500 watts microwave power

16 samples were mounted in a cross manner using graphite paint as shown in Figure 7.14(b). A uniformity of 4% (1σ) over 150 mm diameter was obtained at 10 cm downstream position using 500 Watts microwave power. Four percentages of SF_6 and 96% argon gas mixture was used and the pressure was 0.6 mTorr. A single, patterned 3-inch wafer was also etched as shown in Figure 7.14(a), under the same condition and a uniformity of 1.4% (1σ) was obtained.

7.6.5 Loading and Microloading effect

The depletion of the etching species from the gas passing through the wafers is known as the loading effect. Table 7.2 displays the loading effect observed in the etching experiments. When a 6-inch wafer was used to hold a small sample instead of using a 3-inch wafer, the etching rate dropped from 273 Å/min to 200 Å/min. A separate experiment was also conducted. A patterned 3-inch silicon wafer, with about 30% coverage of aluminum mask, was etched and the etch rate was found to be essentially the same as the etch rate of a single small patterned sample which was placed on a blank 3-inch wafer. This is because the probability of fluorine atom loss in silicon is approximately the same in aluminum. Thus the loading effect, in this case, is related to the size of the wafer rather the percentage of mask coverage on the wafer. A mathematical model was given[74] as:

$$R_m/R_0 = 1/(1+ (mA_wK_w)/(A_sK_s)) \qquad (7.3)$$

where R_m is the etch rate, R_0 is a constant under a fixed operating condition, m is the number of wafers, A_w is the wafer area, K_w is the loss factor of

TABLE 7.2 ETCHING RESULTS SHOWING LOADING EFFECT

Experimental conditions: 500 watts microwave power, -10 volts, 4% SF_6, 10 cm downstream at 0.6 mTorr

Diameter	Area	Etch rate	Number of sample
3 inches	45.6 cm^2	273 Å/min	1
6 inches	182.4 cm^2	200 Å/min	16
3 inches	45.6 cm^2	285 Å/min	(patterned wafer)

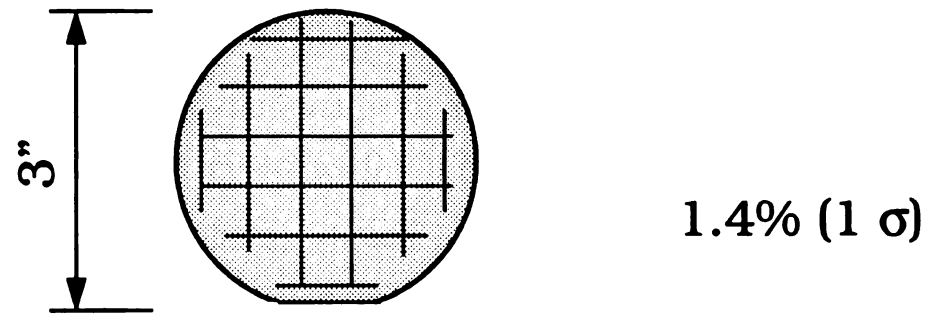

(a)

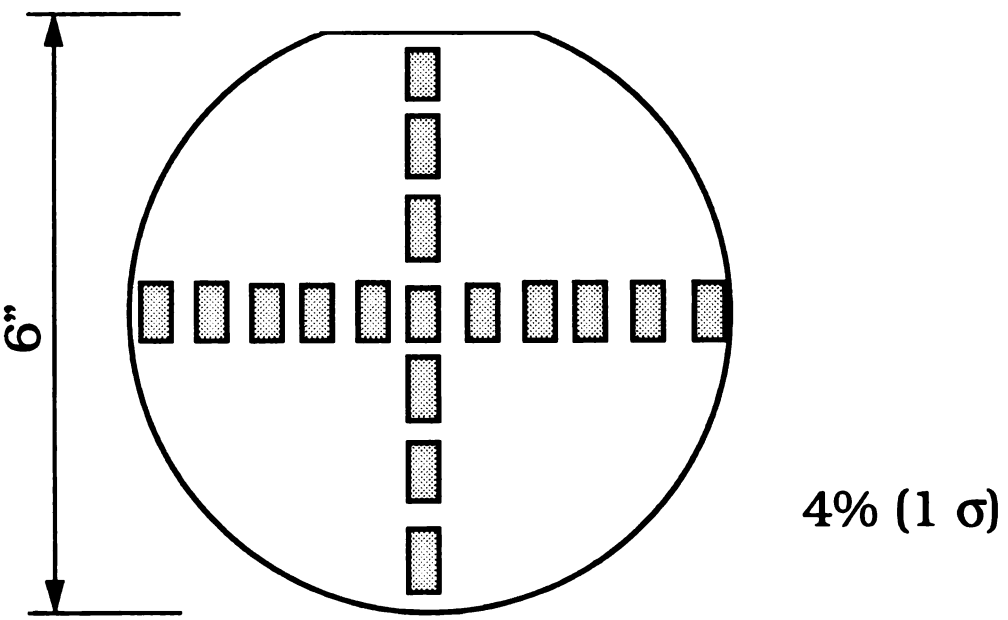

(b)

Figure 7.14 Etching experiment for uniformity measurement

fluorine from etching silicon, A_S is the area of the vessel wall which confines the plasma, and K_S is a combined loss factor accounting for the volume recombination and wall loss of fluorine atoms. Figure 7.15 shows the variations of R_m/R_o versus substrate area, A_w. The geometry of the plasma is assumed to be cylindrical with a radius, R, and height, L. The coefficients, K_S and K_w, are given as 0.0017 and 1.5 x 10^{-4} respectively [74]. The experimental results as shown in Table 7.2, in general, follow the trend predicted by equation (7.3). As the wafer size increases, the etch rate decreases. However, it is necessary to understand that this model may only apply to a flow limited conditions in which the amount of etch material exposed to the plasma will affect the dynamics of the chemical reaction.

Microloading is here defined as the variation of etch rate due to packing density of the features. It is an important issue when fabricating features of different sizes on a single wafer. Figure 7.16 shows the etch profile of two different features on the sample. As shown, the etch depth in the 500 nm line/500 nm spacing was the same as the 200 nm line/300 nm spacing. The result of another experiment which was run under exactly the same condition as in Figure 7.16, is shown in Figure 7.17. No microloading was observed in the 500 nm line/200 nm spacing, 100-150 nm line/200 nm spacing and the 100-150 nm line/500 nm spacing patterns. All SEM pictures show the submicron features with the intact 100 nm thick aluminum mask. Highly anisotropic (90°) etching was demonstrated. The etch condition was 500 Watts microwave power, -10 volts bias and 4% SF_6 at 0.6 mTorr located at 10 cm downstream. The total gas flow was 20 sccm.

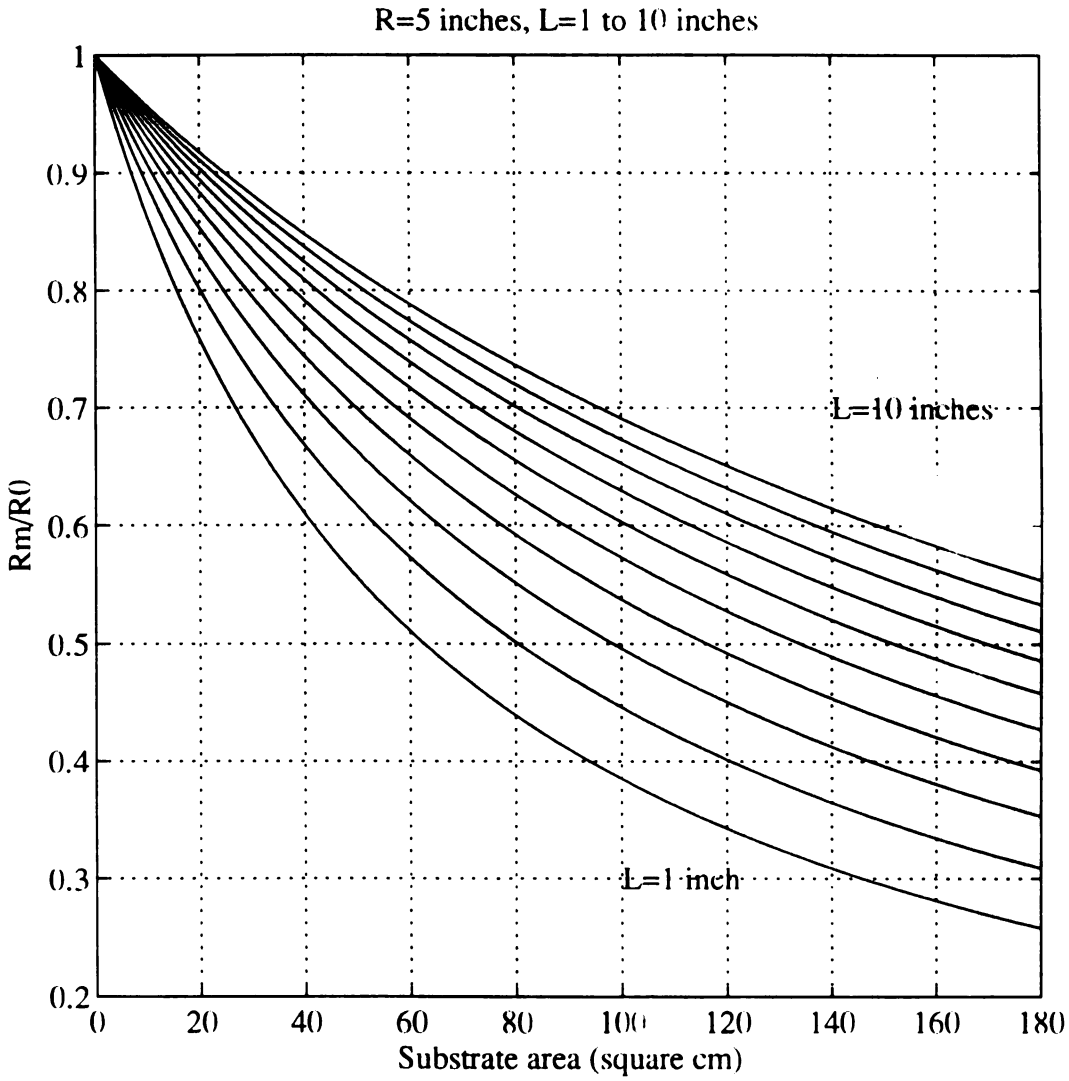

Figure 7.15 Loading effect according to equation (7.3)

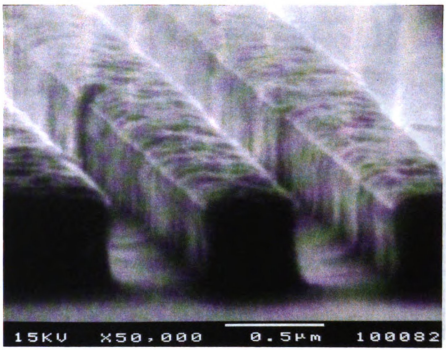

(a) 500 nm line/500 nm spacing

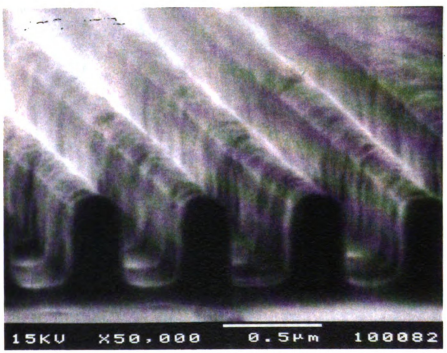

(b) 200 nm line/300 nm spacing

Figure 7.16 Anisotropic etching of silicon

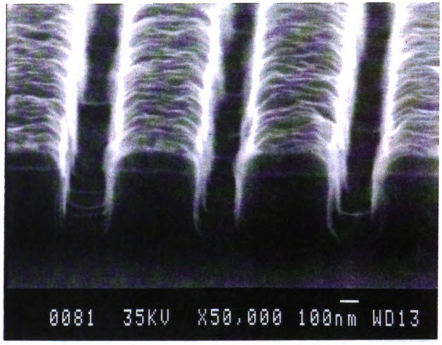

(a) 500 nm line/200 nm spacing

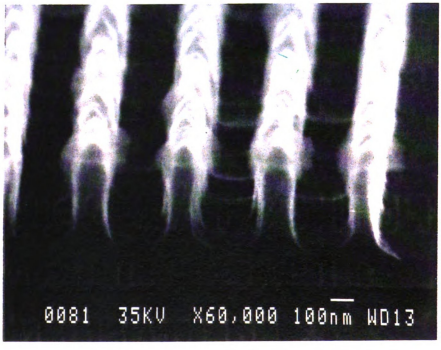

(b) 100-150 nm line/200 nm spacing

Figure 7.17 Anisotropic etching of silicon

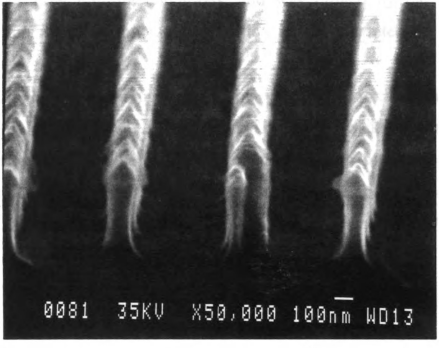

(c) 100-150 nm line/500 nm spacing

Figure 7.17 Anisotropic etching of silicon

§ 7.7 Summary

Highly anisotropic etching (≈ 90°) of submicron features from 500 nm to 100 nm on p-type <100> silicon has been achieved. The etch rate varied from 200 Å/min to 1120 Å/min depending on etching pressure. Etching was done under flow limiting conditions, and was limited by the supply of fluorine atoms. Higher flow rate would allow higher etch rate.

At high pressure, a high induced bias is needed to achieve anisotropic etch profile. In that case, a stronger mask such as nickel mask or other hardened resist has to be used other than aluminum mask. The induced substrate bias voltage is also a function of the chuck position. A positive bias voltage was obtained when the chuck was 4.5 cm downstream. A negative bias voltage can be obtained either by increasing the rf power or increasing the ground surface near the baseplate.

Etch rate increased dramatically with processing pressure, but increased slightly with rf bias and microwave power. The increases of etch rate with the flow rate indicates a higher pumping speed is needed to increase the etch rate when the operation pressure is decreased. As the substrate moved from 5 cm downstream to 17 cm downstream, the etch rate dropped from about 290 Å/min to 230 Å/min at 0.6 mTorr. Etch rate can be increased by placing the substrate closer to the source or change the gas composition. Uniformity of 4% (1σ) over 150 mm diameter and 1.4% (1σ) over 75 mm diameter without downstream confinement magnets were obtained. Loading effect was observed when the wafer size changed from 3-

inch to 6-inch in diameter. However, no microloading was observed in the experiments.

CHAPTER EIGHT

FUTURE RESEARCH

§ 8.1 Summary of research

A large diameter electron cyclotron resonant microwave plasma disk reactor, the MPDR 20, was designed, built and characterized as part of this Ph.D. thesis research. The source has a 45.7 cm diameter cavity and a 20 cm diameter discharge. It was the first MPDR operated at 915 MHz. At 500 watts, the source produced a plasma density of 10^{11} cm^{-3} at zero downstream, which was ten times of the critical density at 915 MHz. At 13 cm downstream, a 2.6% (1σ) uniformity over 18 cm in diameter was obtained. This highly uniform plasma is ideal for large diameter wafer processing. The plasma potential was low, between 7 to 10 volts. Measurements of ion energy distribution function revealed a small FWHM of 8 eV with average ion energies in the range of 8-10 eV. The plasma source was operated with TE_{211} excitation mode at 915 MHz. Initial experiments of operating the MPDR 20 at 2.45 GHz was also successful which lead to the construction of the MPDR 325 which is now sold as a commercial plasma processing source.

Characterization of the MPDR 325 was also investigated in this Ph.D. thesis. The MPDR 325 was the first large diameter commercial plasma source operated at 2.45 GHz microwave frequency. Multimode excitation was used to create the plasma. It has a 35.56 cm diameter cavity and a 24 cm diameter discharge. Unlike the other smaller MPDRs, the MPDR 325 has an opening which is larger than the cutoff radii of some cavity resonant modes. Plasma can be ignited at pressure at several mTorr while the other MPDRs have to ignited at pressure about 100 mTorr. The Experimental result showed that the source has all the advantages which the MPDR 20

processes. The plasma density was high at downstream position, about $6x10^{10}$ cm^{-3} at 14 cm downstream. A 3.1% (1σ) variation of plasma distribution over 18 cm at 14 cm downstream was obtained. Plasma potential was low about 10 volts at 14 cm downstream. The average ion energies were about 10 to 14 eV. The ion energy distribution functions had small FWHM of about 7 to 9 eV. Unlike the MPDR 20, this large diameter source is capable of operating at microwave up to 1500 watts.

The experimental performance of several different diameter MPDRs was also investigated to understand the difference in operation versus the size of the plasma source. Results showed that the MPDR 5, which has a 5 cm discharge, produced the highest density at zero downstream. The plasma potentials were high, about 23 volts at zero downstream and 20 volts at 5 cm downstream. The most interesting result in the MPDR 5 was its bimodal distribution in the ion energy distribution function, which was believed to be caused by resonant charge exchange. Four figures of merit were used to compare the performance of the MPDRs. They were the electron temperature versus the product of pressure-diffusion length, microwave coupling efficiency, ion production energy cost and power density. The coupling efficiencies of all MPDRs, which were excited by single cavity resonant modes, varied from 75% to 95%. Within a pressure between 1.0-1.2 mTorr and power between 200 to 300 watts, the MPDR 9 had the highest ion production energy cost, 640 eV per ion, while the MPDR 325 was the most efficient in the ion production with 220 eV per ion. In terms of power density, the MPDR 5 required a minimum of 2 watts/cm^3 to sustain the plasma while the MPDR 20 and MPDR 325 required only 0.06 watts/cm^3 and 0.1 watts/cm^3 respectively.

Submicron application of the large diameter MDPR was performed in a new etching and deposition system. Feature sizes varied from 0.5 μm down to 0.1 μm were patterned on a p-type <100> silicon wafer both by optical and electron-beam lithography. An aluminum mask was used as the etch mask. Optimal gas composition for anisotropic etching was 4% SF_6 in argon plasma. The pressure was 0.6 mTorr with a total flow of 20 sccm. Five hundred watts of microwave power at 2.45 GHz was used and the rf induced bias voltage was -10 volts. The etch rate varied from 200 Å/min to 1120 Å/min depending on discharge pressure. The etch process was limited by the supply of fluorine atoms. Higher pumping speeds would result higher etch rate. Etch uniformities were 4% (1σ) over 150 mm diameter and 1.4% (1σ) over 75 mm diameter without downstream confinement magnets.

§ 8.2 Future research

8.2.1 Plasma source development

Development of microwave plasma disk reactor can be divided into following categories:

(A) Structure of the MPDR

Magnetic configuration is the subject of interest in this category. As shown in Chapter Four, the idea magnetic configuration is one which matches with the transverse electric field of the cavity resonant mode. Study of variation of plasma properties versus magnetic configuration, in fact, has started. Initial results showed that there were improvements both in plasma

density and ion energy distribution. The work can be applied to the large MPDR 20 which was operated at TE $_{211}$ mode with 915 MHz excitation. The objective is thus to determine the optimal excitation mode and its magnetic configuration.

(B) Automation of the MPDR

All MPDRs can be operated by computer since all operation positions are repeatable. The task is to build a robust real-time program which can start the discharge, tune the cavity and monitor the process.

(C) Scale up of the MPDR 20

The performance of the MPDR 325 is better than the smaller MPDRs in terms of operation and ion production efficiency. If a higher power 915 MHz microwave source is available, the MPDR 20 can be scaled up to a larger reactor with discharge diameter larger than 34 cm. The immediate concern in this scale-up to large diameter is the cost of the components such as the quartz discharge chamber. A high power 915 MHz microwave source, which has a maximum of at least one thousand watts is needed for the operation of the scale-up source. Current commerical unit has a maximum of 500 watts.

8.2.2 Plasma etching

Etch rate is currently limited by the pumping speed. Without changing the hardware, the etch rate can be increased by using other etch

gas such as Hydrogen Bromide. Another method is to move the chuck upward, i.e. closer to the plasma source, where the plasma density is higher.

Anisotropic etching of silicon is only one of the fabrication processes [178]. The etching of silicon nitride is also an important process. Recently Tungsten has become an important material for metal contact in ULSI. It is because voids are less likely formed in via holes [179] than the aluminum. Both silicon nitride and tungsten can be etched by the SF_6-argon gas. All the end products, SiF_4, NF_3 and WF_6 have low boiling point [180] and therefore are volatile in vacuum environment.

Finally, process control is equally important in plasma processing. The end point detection is a crucial technique and yet has not been studied in the MPDR sources.

LIST OF REFERENCES

LIST OF REFERENCES

[1] N. Sakudo, K. Tokiguchi, H. Koike and I. Kanomata, Rev. Sci. Instrum., Vol. 48, No. 7, 762 (1977).

[2] K. Suzuki, S. Okudaira, N. Sakudo and I. Kanomata, Japan. J. Appl. Phys., Vol. 16, No. 11, 1979 (1977).

[3] K. Suzuki, S. Okudaira and I. Kanomata, J. Electrochem. Soc., Vol. 126, No. 6, 126 (1979).

[4] K. Ninomiya, K. Suzuki and S. Nishimatsu, Japan. J. Appl. Phys., Vol. 22, No. 4, 139 (1983).

[5] S. Matsuo and M. Kiuchi, Japan. J. Appl. Phys., Vol. 22, No. 4, L210 (1983).

[6] K. Suzuki, K. Ninomiya, S. Nishimatsu and S. Okudaira, J. Vac. Sci. Technol., B3 (4), 1025 (1985).

[7] K. Tokiguchi, N. Sakudo and H. Koike, Rev. Sci. Instrum., 57 (8), 1526 (1986).

[8] M. Matsuoka and K. Ono, Appl. Phys. Lett. 50 (26), 1864 (1987).

[9] K. Asakawa, N. Takadoh, M. Uchida and T. Yuasa, NEC Res. & Develop., 87, 1 (1987).

[10] S. Sugito, S. Ishida and Y. Iida, NEC Res. & Develop., 92, 18 (1989).

[11] K. Shirai, T. Iizuka and S. Gonda, Japan. J. Appl. Phys., Vol. 28, No. 5, 897 (1989).

[12] M. Matsuoka and K. Ono, Japan. J. Appl. Phys., Vol. 28, No. 3, L503 (1989).

[13] K. Tomotsune, Y. Yamamoto, M. Morita, K. Suzuki, Y. Shimizu, K. Fuji, N. Takadoh, K. Asakawa and K. Okada, NEC Res. & Develop., 95, 15 (1989).

[14] H. Nihei, J. Morikawa and N. Inoue, Japan. J. Appl. Phys., Vol. 29, No. 5, L822 (1990).

[15] K. Kamata, T Inoue, K Maruyama and I. Tanabe, Japan. J. Appl. Phys., Vol. 29, No. 7, L1203 (1990).

[16] S. Iizuka and N. Sato, J. Appl. Phys., 70(8), 4165 (1991).

[17] H. Abe, NEC Res. & Develop., Vol. 32, No. 2, 179 (1991).

[18] E. Ghanbari, I. Trigor and T. Nguyen, J. Vac. Sci. Technol. A7(3), 918 (1989).

[19] Y.H. Lee, J.E. Heidenreich III and G. Fortuno, J. Vac. Sci. Technol. A7(3), 903 (1989).

[20] O.A. Popov and H. Waldron, J. Vac. Sci. Technol. A7(3), 914 (1989).

[21] O.A. Popov, J. Vac. Sci. Technol. A7(3), 894 (1989).

[22] J. Forster and W. Holber, J. Vac. Sci. Technol. A7(3), 899 (1989).

[23] D.A. Carl, M.C. Wiliamson, M.A. Lieberman and A.J. Lichtenberg, J. Vac. Sci. Technol. B9(2), 339 (1991)

[24] R.R. Burke and C. Pomot, Solid State Tehnol., 67, Feb., 1988.

[25] J. Pelletier, Y. Arnal and L. Vallier, Rev. Sci. Instrum., 59(7), 1072 (1988).

[26] M. Geisler, J. Kieser, E. R•uchle and R. Wilhelm, J. Vac. Sci. Technol. A8(2), 908 (1990).

[27] K.H. Kretschmer, K. Matl, F. Lorenz, I. Kessler and B. Dumbacher, Solid State Tehnol., 53, Feb., 1990.

[28] G. Neumann, J. Vac. Sci. Technol., B9(2), 334 (1991).

[29] R.W. Boswell and D. Henry, Appl. Phys. Lett., 47 (10), 1095 (1985).

[30] A.J. Perry and R.W. Boswell, Appl. Phys. Lett. 55 (2), 148 (1989).

[31] A.J. Perry, D. Vender and R.W. Boswell, J. Vac. Sci. Technol., B9(2), 310 (1991).

[32a] J. Root and J. Asmussen, "MSU microwave ion source", presented at the MSU/NASA Workshop on Advanced Propulsion Concepts using Time Varying Electromagnetic Fields, East Lansing, Michigan, Feb (1982).

[32b] J. Asmussen and J. Root, Appl. Phys. Lett., 44(4), 396 (1984).

[32c] J. Asmussen, J. Root, "Ion generation apparatus and method for the use thereof", US patent No. 4507588, March (1985).

[33] J. Root and J. Asmussen, Rev. Sci. Instrum., 56(8), 1511 (1985).

[34] T. Roppel, D.K. Reinhard and J. Asmussen, J. Vac. Sci. Technol., B4(1), 295 (1986).

[35a] M. Dahimene and J. Asmussen, 19th EPIB conference, (1984).

[35b] M. Dahimene and J. Asmussen, J. Vac. Sci. Technol., B4(1), 126 (1986).

[36] J. Asmussen and M. Dahimene, J. Vac. Sci. Technol., B5(1), 328 (1987).

[37] L. Mahoney, M. Dahimene and J. Asmussen, Rev. Sci. Instrum., 59(3), 448 (1988).

[38] J. Hopwood, D.K. Reinhard and J. Asmussen, J. Vac. Sci. Technol., B6(6), 1896 (1988).

[39] J. Asmussen, J. Vac. Sci Technol., A7, 883 (1989).

[40] J. Asmussen, R. Fritz, L. Mahoney, G. Fournier and G. Demaggio, Rev. Sci. Instrum., 282 (1990).

[41] L. Mahoney and J. Asmussen, Rev. Sci. Instrum., 61(1), 285 (1990).

[42] J. Asmussen, J. Hopwood and F.C. Sze, Rev. Sci. Instrum., 61(1), 250 (1990).

[43] F.C. Sze, D.K. Reinhard, B. Musson, J. Asmussen and M. Dahimene J. Vac. Sci. Technol., B8(6), 1759 (1990).

[44] J. Hopwood and J. Asmussen, Appl. Phys. Lett., 58(22), 2473 (1991).

[45] B. Musson, F.C. Sze, D.K. Reinhard and J. Asmussen, J. Vac. Sci. Technol., B9(6), 3521 (1991).

[46] G. King, F.C. Sze, P. Mak, T.A. Grotjohn and J. Asmussen, J. Vac. Sci. Technol. A 10(4), 1265 (1992).

[47] P. Mak, G. King, T.A. Grotjohn and J. Asmussen, J. Vac. Sci. Technol. A 10(4), 1281 (1992).

[48] A.K. Srivastava, M. Dahimene, T.A. Grotjohn and J. Asmussen (to be published).

[49] J. Hopwood et al., IBM, (seminar presented in Michigan State Univeristy).

[50] Y. Sakamoto and Y. Ishibe, Japan. J. Appl. Phys., Vol. 19, No. 3, 839 (1980).

[51] K. Kamata, T. Inoue, K. Maruyama and I. Tanabe, Japan. J. Appl. Phys., Vol. 29, No. 7, L1203 (1990).

[52] S. Samujkawa, S. Mori and M. Sasaki, Japan. J. Appl. Phys., Vol. 29, No. 4, 792 (1990).

[53] S. Tachi, K. Tsujimoto and S. Okudaira, Appl. Phys. Lett., 52(8), 616 (1988).

[54] D.E. Post and R. Behrisch, Physics of Plasma-Wall Interactions in Controlled Fusion, NATO ASI series, Plenum Press, New York, p17, 1988.

[55] W. Lochte - Holtgreven, Plasma Diagnostics, North - Holland, Amsterdam, 705-725.

[56] E.O. Johnson and L. Malter, Phys. Rev., Vol. 80(1), 58 (1950).

[57] M.J. Druyvesteyn, Z. Phys., 64, 781 (1930).

[58] H.W. Rundle, D.R. Clark and J.M. Deckers, Can. J. Phys., Vol. 51, 144 (1973).

[59] J.E. Heidenreich III and J.R. Paraszczak, J. Vac. Sci. Technol., B6(1), 288 (1988).

[60] J. Hopwood, Macroscopic properties of a multipolar electron cyclotron resonance microwave-cavity plasma source for anisotropic silicon etching, Ph. D. Thesis, Dept. of Electrical Engineering, Michigan State University (1990).

[61] L. Mahoney, The design and testing of a compact electron cyclotron resonant microwave cavity ion source, M.S. Thesis, Dept. of Electrical Engineering, Michigan State University (1989).

[62] F.F. Chen, Plasma Diagnostic Technique, R.H. Huddlestone and S.L. Leonard, editors, Academic Press, New York, 113 (1965).

[63] H.R. Kaufman and R.S. Robinson, Operation of Broad-Beam Sources, Common-wealth Scientific Corporation, Virginia, (1987).

[64] F.P. McKelvey, Solid State and Semiconductor Physics, Robert E. Krieger Publishing Co. Inc., Florida (1986).

[65] D. Rapp and P. Englander-Golden, J. Chem. Phys., 43, 1464 (1965).

[66] R. F. Harrington, Time Harmonic Electromagnetic Fields, McGraw-Hill (1961).

[67] A. Theodore Forrester, Large Ion beams: Fundamentals of Generation and Propagation, John Wiley & Sons, 10 (1988).

[68] B.E. Cherrington, Gaseous electronics and gas lasers, Pergamon Press, New York (1979).

[69] J. L. Delcroix, Introduction to the theory of ionized gases, translated by M. Clark, D. J. BenDaniel and J. M. BenDaniel, Interscience publishers, Inc., New York (1964).

[70] J.A. Bittencourt, Fundamentals of plasma physics, Pergamon Press, (1988).

[71] P. C. Stangeby, Physics of Plasma-Wall Interactions in Controlled Fusion, D. E. Post and R. Behrisch, editors, Plenum Press, New York, 41 (1988).

[72] B, M. Smirnov, Physics of weakly ionized gases, translated by Oleg Glebov, Mir Publishers, Moscow (1981).

[73] D. R. Nicholson, Plasma theory, John Wiley and Sons, 1983.

[74] D.M. Manos and D. L. Flamm, Plasma Etching-An Introduction, Academic Press (1989).

[75] L.C. Shen and J.A. Kong, Applied Electromagnetism, Brooks/Cole Engineering Division (1983).

[76] M. Sadowski, Rev. Sci. Instrum., Dec., 1545 (1969).

[77] L. Pomathiod, R. Debrie, Y. Arnal and J. Pelletier, Phys. Lett., Dec., 301 (1984).

[78] R. Limpaecher and K.R. MacKenzie, Rev. Sci. Instrum., vol. 44, 6, June, 726 (1973).

[79] Seitaro Matsuo, Yumiko Takehara and Akira Ozawa, Japn. J. Appl. Phys., Vol. 17, No. 11, 2071 (1978).

[80] Kiyokatsu Jinno, Japan. J. Appl. Phys., Vol. 17, No. 7, 1281 (1978).

[81] Seitaro Matsuo and Yoshio Adachi, Japan. J. Appl. Phys., Vol. 21, No. 1, L4 (1982).

[82] D. L. Flamm, V. M. Donnelly and D.E. Ibbotson, J. Vac. Sci. Technol. B 1(1), 23 (1983).

[83] H.F. Winters, J.W. Coburn and T.J. Chuang, J. Vac. Sci. Technol. B 1(2), 469 (1983).

[84] Y. Arnal, J. Pelletier, C. Pomot, B. Petit, and A. Durandet, Appl. Phys. Lett., 45 (2), 132 (1984).

[85] C. Pomot, B. Mahi, B. Petit, Y. Arnal and J. Pelletier, J. Vac. Sci. Technol. B 4(1), 1 (1986).

[86] N.N. Efremow, M.W. Geis, R.W. Mountain, G.A. Lincoln, J.N. Randall and N.P. Economou, J. Vac. Sci. Technol. B 4(1), 337 (1986).

[87] Susumu Asada and Katsumi Mori, J. Vac. Sci. Technol. B 4(1), 318 (1986).

[88] J. Sugiura, W.J. Lu, K.C. Cadien and A.J. Steckl, J. Vac. Sci. Technol. B 4(1), 349 (1986).

[89] Yukinori Ochiai, Kazuhiko Shihoyama, Takao Shiokawa, Koichi Toyoda, Akio Masuyama, Kenji Gamo and Susumu Namba, J. Vac. Sci. Technol. B 4(1), 333 (1986).

[90] Gregory W. Grynkewich, T.H. Fedynyshyn and R.H. Dumas, J. Vac. Sci. Technol. B 8(1), 5 (1990).

[91] Wei-Xi Chen, L.M. Walpita, C.C. Sun and W.S.C. Ghang, J. Vac. Sci. Technol. B 4(3), 701 (1986).

[92] Toshiro Ono, Masatoshi Oda, Chiharu Takahashi and Seitaro Matsuo, J. Vac. Sci. Technol. B 4(3), 696 (1986).

[93] B. Mahi, Y. Arnal, C. Pomot, J. Vac. Sci. Technol. B 5(3), 657 (1987).

[94] N. Vodjdan and P. Parrens. J. Vac. Sci. Technol. B 5(6), 1591 (1987).

[95] J. Hopwood, M. Dahimene, D.K. Reinhard and J. Asmussen, J. Vac. Sci. Technol. B 6(1), 268 (1988).

[96] Y. Tobinaga, N. Hayashi, H. Araki, S. Nakayama and H. Kudoh, J. Vac. Sci. Technol. B 6(1), 272 (1988).

[97] S.W. Pang, M.W. Geis, W.D. Goodhue, N.N. Efremow, D.J. Ehrlich, R.B. Goodman and J.N. Randall, J. Vac. Sci. Technol. B 6(1), 249 (1988).

[98] Ahmed M. El-Masry, F-O. Fong, J.C. Wolfe and J.N. Randall, J. Vac. Sci. Technol. B 6(1), 257 (1988).

[99] S.W. Pang, W.D. Goodhue, T.M. Lyszczarz, D.J. Ehrilich, R.B. Goodman and G.D. Johnson, J. Vac. Sci. Technol. B 6(6), 1918 (1988).

[100] R. Cheung, Y.H. Lee, K.Y. Lee, T.P. Smith, III, D.P. Kern, S.P. Beaumont and C.D.W. Wikinson, J. Vac. Sci. Technol. B 7(6), 1462 (1989).

[101] T.R. Hayes, M.A. Dreisbach, P.M. Thomas, W.C. Dautremont-Smith and L.A. Heimbrook, J. Vac. Sci. Technol. B 7(5), 1130 (1989).

[102] S. J. Pearton, W.S. Hobson and K.S. Jones, J. Appl. Phys., 66 (10), 5009 (1989).

[103] S. J. Pearton and W.S. Hobson, J. Appl. Phys., 66 (10), 5018 (1989).

[104] A. Durandet, O. Joubert, J. Pelletier and M. Pichot, J. Appl. Phys., 67(8), 3862 (1990).

[105] S. Salimian, C.B. Cooper, III and A. Ellingboe, Appl. Phys. Lett., 56 (14), 1311 (1990).

[106] A. Scherer, B.P. Van der Gaag, E.D. Beebe and P.S.D. Lin, J. Vac. Sci. Technol. B 8(1), 28 (1990).

[107] J.M. Cook, D.E. Ibbotson and D.L. Flamm, J. Vac. Sci. Technol. B 8(1), 1 (1990).

[108] C. Constantine, D. Johnson, S.J. Pearton, U.K. Chakrabarti, A.B. Emerson, W.S. Hobson and A.P. Kinsella, J. Vac. Sci. Technol. B 8(4), 596 (1990).

[109] S. Salimian, C. Yuen, C. Shih and C.B Cooper, III, J. Vac. Sci. Technol. B 9(1), 114 (1991).

[110] Daniel L. Flamm, Solid State Technology, March, 47 (1991).

[111] S.W. Pang, K.T. Sung and K.K. Ko, J. Vac. Sci. Technol. B 10(3), 1118 (1992).

[112] Yoju Saito, Masahiro Hirabaru and Akira Yoshida, J. Vac. Sci. Technol. B 10 (1), 175 (1992).

[113] Seji Samukawa, Tomohiko Toyosato and Etsuo Wani, J. Vac. Sci. Technol. B 9(3), 1471 (1991).

[114] D. Dane, P. Gadgil, T.D. Mantei, M.A. Carlson and M.E. Weber, J. Vac. Sci. Technol. B 10(4), 1312 (1992).

[115] S.J. Pearton, F. Ren, J.R. Lothian, T.R. Fullowan, R.F. Kopf, U.K. Chakrabarti, S.P. Hui, A.B. Emerson, R. L. Kostelak and S.S. Pei, J. Vac. Sci. Technol. B 9(5), 2487 (1991).

[116] L.R. Lothian, J.M. Kuo, W.S. Hobson, E. Lane, F. Ren and S.J. Pearton, J. Vac. Sci. Technol. B 10(3), 1061 (1992).

[117] S.J. Pearton, U.K. Chakrabarti, A. Katz, A.P. Perley, W.S. Hobson and C. Constantine, J. Vac. Sci. Technol. B 9(3), 1421 (1991).

[118] K. Suzuki, S. Okudaira, S. Nishimatsu, K. Usami, and I. Kanomata, J. Electrochem. Soc., Solid-State Sci. and Technol., 129(12), 2764 (1982).

[119] Takashi Matsuura, Hiroaki Uetake, Tadahiro Ohmi, Junichi Murota, Koichi Fukuda, Nobuo Mikoshiba, Tadashi Kawashima and Yoshihiro Yamashita, Appl. Phys. Lett., 56 (14), 1339 (1990).

[120] Tohru Saitoh, Toshiya Yokogawa and Tadashi Narusawa, Appl. Phys. Lett., 56 (9), 839 (1990).

[121] Konstantinos P. Giapis, G.R. Scheller, R.A. Gottscho, W. S. Hobson and Y.H. Lee, Appl. Phys. Lett., 57(10), 983 (1990).

[122] Yasuhiro Yokota, H. Hashimoto, M. Song and M. Awaji, Japan. J. Appl. Phys., 29(4), 739 (1990).

[123] Shin'ichi Tachi and S. Okudaira, J. Vac. Sci. Technol. B 4(2), 459 (1986).

[124] Jer-Shen Maa, H. Gossenberger and L. Hammer, J. Vac. Sci. Technol. B 8(4), 581 (1990).

[125] Akira Shigetomi, S. Matsuda, K. Moriizumi, HJ. Kusunose, H. Onoda, T. Imai and Y. Watakabe, J. Vac. Sci. Technol. B 8(2), 117 (1990).

[126] Masaharu Watanabe, Solid State Technol., March, 39 (1991).

[127] Masaharu Watanabe, Solid State Technol., April, 133 (1991).

[128] Philippe Laporte, Y. Melaku and M. Goethals, Solid State Technol., April, 69 (1991).

[129] Mr. Hanhu Pu, private conversation.

[130] Seiji Samukawa, M. Sasaki and Y. Suzuki, J. Vac. Sci. Technol., B 8(5), 1062 (1990).

[131] O.J. Glembocki and E.A. Dobisz, J. Vac. Sci. Technol., B 9(2), 1403 (1991).

[132] R. Cheung, S. Thomas, I. McIntyre, C.D.W. Wilkinson and S.P. Beaumont, J. Vac. Sci. Technol., B 6(6), 1911 (1988).

[133] M. Surendra, D.B. Graves and I.J. Morey, Appl. Phys. Lett., 56 (11), 1022 (1990).

[134] J.L. Cecchi, J.E. Stevens, R.L. Jarechi, Jr., and Y.C. Huang, J. Vac. Sci. Technol., B 9(2), 318 (1991).

[135] Harold F. Winters and I.C. Plumb, J. Vac. Sci. Technol., B 9(2), 197 (1991).

[136] M. Haverlag, A. Kono, D. Passchier, G.M. W. Kroesen, W.J. Goedheer and F.J. de Hoog, J. Appl. Phys., 70(7), 3472 (1991).

[137] S. Vanhaelemeersch, J. Van Hoeymissen, D.Vermeylen and J. Peeters, J. Appl. Phys., 70(7), 3892 (1991).

[138] R. K.F. Teng and H.G. Yang, J. Vac. Sci. Technol., B 9(2), 380 (1991).

[139] R. Venkatasubramanian, M.L. Timmons and T.S. Colpitts, J. Appl. Lett., 59(17), 2153 (1991).

[140] R. J. Davis, Appl. Phys. Lett., 59(14), 1717 (1991).

[141] J.C. Arnold and H.H. Sawin, J. Appl. Phys., 70 (10), 5314 (1991).

[142] N. Sadeghi, H. Debontride, G. Turban and M.C. Peignon, Plasma Chemistry and Plasma Processing, 10(4), 553 (1990).

[143] Jérôme Perrin, J. Méot, J-M. Siéfert and J. Schmitt, Plasma Chemistry and Plasma Processing, 10(4), 571 (1990).

[144] K.R. Ryan and I.C. Plumb, Plasma Chemistry and Plasma Processing, 10(2), 207 (1990).

[145] N. Mutsukura and G. Turban, Plasma Chemistry and Plasma Processing, 10(1), 27 (1990)

[146] E.S. Aydil, J.A. Gregus and R.A. Gottscho, PS-ThA5, 39th AVS National Symposium, Chicago, Nov. (1992)

[147] Joel M. Cook and K.G. Donohoe, Solid State Technol., April, 119 (1991).

[148] Tatsuya Takeshita, T. Unagami and O. Kogure, Japan. J. Appl. Phys., 28(3), L358 (1989).

[149] T. Shibata, Y. Nanishi and M. Fujimoto, Japan. J. Appl. Phys., 29(7), L1181 (1990).

[150] Semiconductor International, June, 46 (1992)

[151] Carey Pico, Solid State Technology, May, 81 (1992)

[152] Solid State Technology, Dec., 22 (1991)

[153] Semiconductor International, May, 48 (1992)

[154] Peter Singer, Semiconductor International, July, 52 (1992)

[155] A. J. van Roosmalen, J. A. G. Baggerman and S. J. H. Brader, Dry Etching for VLSI, Plenum Press, New York (1991).

[156] B. Petti and J. Pelletier, Japan. J. Appl. Phys., 26(6), 825 (1987).

[157] A.J. Perry, H.Persing and R.W. Boswell, PS2-ThM10, 39th AVS National Symposium, Chicago, Nov. (1992).

[158] G. Giroult-Matlakowsk, S. Armand, R. W. Boswell, PS-MoP8, 39th AVS National Symposium, Chicago, Nov. (1992).

[159] R.W. Boswell and R.K. Porteous, PS-MoP9, 39th AVS National Symposium, Chicago, Nov. (1992).

[160] M.A. Jarnyk and R.W. Boswell, PS-WeP24, 39th AVS National Symposium, Chicago, Nov. (1992).

[161] C. Charles, A. Goullet, C. Cardinaud, G. Turbanand R.W. Boswell, EM-ThP36, 39th AVS National Symposium, Chicago, Nov. (1992).

[162] Jeffrey A. Tobin, Guifan Li, L. T. Mahoney, D.D. Denton and J. L. Shohet, J11-ThM11, 39th AVS National Symposium, Chicago, Nov. (1992).

[163] L.T. Mahoney, G.Li, A.E. Wendt, J.L. Shohet and H. Yu, PS-MoP7, 39th AVS National Symposium, Chicago, Nov. (1992).

[164] J. Hopwood, C.R. Guarnieri and J.J. Cuomo, PS-ThA8, 39th AVS National Symposium, Chicago, Nov. (1992).

[165] A.K. Srivastava and J. Asmussen, PS-ThA3, 39th AVS National Symposium, Chicago, Nov. (1992).

[166] E.B. Manring, An experimental investigation of the microwave heating of solid non-reactive materials in a circular cylindrical resonant cavity, M.S. thesis, Department of Electrical Engineering, Michigan State University (1988).

[167] John S. Mckilop, J.C. Forster, and W. M. Holber, J. Vac. Sci. Technol. A 7(3), 908 (1989).

[168] T.I. Cox, V.G. Deshmukh, D.A. Hoe, A. J. Hydes, N. St. J. Braithwaite and N. M. P. Benjamin, J. Phys. D: Appl. Phys. 20, 820 (1987).

[169] Edbertho Leal-Quiros and M.A. Prelas, Rev. Sci. Instrum. 61(6), 1708 (1990).

[170] J. A. Meyer, G-H. Kim and N. Hershkowitz, PS-ThA6, 39th AVS National Symposium, Chicago, Nov. (1992).

[171] R.A. Stewart, B. Troyanovsky and M.A. Lieberman, "Modeling of magnetic bucket confinement in an ECR processing reactor," IEEE Conference on Plasma Science, Williamsburg (1991).

[172] Masayuki Fukao and Yasuo Harada, J. Appl. Phys. 72(9), 3943 (1992).

[173] D. Henry, J.M. Francou and A. Inard, J. Vac. Sci. Technol. A10(6), 3426 (1992).

[174] M.E. Day, M. Delfino, and S. Salimian, J. Appl. Phys. 72 (11), 5467 (1992).

[175] R. A. Gottscho, C.W. Jurgensen and D.J. Vitkavage, J. Vac. Sci. Techol. B 10(5), 2133 (1992).

[176] F. Ren, T. R. Fullowan, S. J. Peraton, J. R. Lothian, R. Esagui, C. R. Abernathy and W.S. Hobson, J5-ThA6, 39th AVS National Symposium, Chicago, Nov. (1992).

[177] K.T. Kung, J.P. Fourier and S.W. Pang, PS-WeM7, 39th AVS National Symposium, Chicago, Nov. (1992).

[178] D.K. Reinhard, Introduction to Integrated Circuit Engineering, Houghton Mifflin Company, Boston, 181 (1987).

[179] Peter Singer, Semiconductor International, August, 36 (1992)

[180] Robert C. Weast, CRC Handbook of Chemistry and Physics, 1st student edition, B (1990).

[181] S.M. Gorbatkin and L.A. Berry, J. Vac. Sci. Technol. A 10(5), 3104, Sept. (1992).

[182] J. Hopwood, C.R. Guarnieri, S.J. Whitehair and J.J. Cuomo, J. Vac. Sci. Technol. A 11(1), 147 (1993).

[183] J. Hopwood, C.R. Guarnieri, S.J. Whitehair and J.J. Cuomo, J. Vac. Sci. Technol. A 11(1), 152 (1993).

[184] S.M. Gorbatkin, L.A. Berry, and J.B. Roberto, J. Vac. Sci Technol. A 8 (3), 2893 (1992).

[185] S. Whitehair and J. Asmussen, J. propulsion and power, 3 (2), 136 (1987).

[186] L. Mahoney, seminar given in Electrical Engineering Department, Michigan State University, Feb (1993).

[187] D. Peterson, The OSHA Compliance Manual. McGraw-Hill Book Company, New York, New York.

[188] F.C. Sze, G. Alers, D. K. Reinhard, B. Golding and J. Asmussen, "Etching of silicon with features to 0.2 micron using a multipolar ECR plasma reactor," 39th AVS National Symposium, Chicago, Nov., 1992 (to be published in J. Vac. Sci. Technol.)

[189] F.C. Sze and J. Asmussen, "Experimental scaling laws for ECR reactors," 39th AVS National Symposium, Chicago, Nov., 1992 (to be published in J. Vac. Sci. Technol.)

[190] F.C. Sze and J. Asmussen, "Downstream characterization of a 20 cm diameter 915MHz/2.45GHz multipolar electron cyclotron resonant plasma source," (presented at 1991 IEEE international conference on plasma science, Williamsburg, Virginia).

[191] J.R. Brophy and R.J. Wilbur, AIAA Journal, 23, 1731 (1985).

[192] J. Rogers, "Properties of steady-state high pressure argon microwave discharge", Ph.D. thesis, Michigan State University, East Lansing (1982).